eXPRESS Polymer Letters Vol.9, No.6 (2015) 489
Available online at www.expresspolymlett.com
DOI: 10.3144/expresspolymlett.2015.46

Editorial corner – a personal view
Added function – Added value: Multifunctional high-performance composites

A. Bismarck[1,2*]

[1]Polymer & Composite Engineering (PaCE) Group, Institute of Materials Chemistry and Research, Faculty of Chemistry, University of Vienna, Austria
[2]Department of Chemical Engineering, Imperial College of London, UK

All materials are functional materials. If not, why else would one develop materials? Materials carry load, can be used to produce or harvest, transmit and store electrical energy or are thermal and electrical conductors or insulators. Materials can be 'smart', 'responsive', 'reactive', 'self-healing', 'bio-inspired' etc. By combining structural properties with additional integrated optical, magnetic, electrical or thermal functionalities into a single material, multifunctional materials are created (DOI: 10.1016/j.compstruct.2010.05.003). A multitude of biological materials are multifunctional, for example bone – a structural, rigid, self-healing organ that also acts as bioreactor, producing red and white blood cells. Bones are living hierarchical composites with a layered structure. Composites are materials consisting of at least two identifiably different materials, which combined together, have an engineering performance that by far exceeds those of the individual constituents. High performance fibre reinforced polymer composites are now used in cars and (plastic) airplanes. In composites, fibres carry load and the fibre type, alignment, orientation determine the overall mechanical properties while the polymer matrix protects and holds the fibres in place, and transfers the load between the fibres. The structure of composites can be tailored for functionality by combining separate components; sensors, cables and even batteries can be integrated into composites (DOI: 10.1016/j.compscitech.2008.02.019). However, this comes at a cost; it adds additional weight. The more challenging approach is to design a single material to perform more functions, for instance to carry significant mechanical load and simultaneously store and deliver electrical energy (DOI: 10.1016/j.compositesa.2012.10.007). Carbon materials are both a structural composite reinforcement and a common electrode component. Moreover, both structural composites and electrochemical devices are often laminates but the requirements for structural fibres and electrode materials are different; one has to be strong and stiff while the other has to be electrically conducting with a high surface area to either allow for the formation of an electrochemical double layer (supercapacitors) or intercalate lithium (batteries). In batteries and supercapacitors, the electrodes need to be separated to avoid short-circuiting and the matrix is usually a liquid electrolyte. These requirements pose significant challenges for structural materials. Recent research (DOI: 10.1039/C4FD00055B) has been addressing some of the challenges aiming to develop structural electrodes and solid polymer electrolytes, which are both structural but also allow for sufficient ion conductivity. Successful structural energy storage systems could sacrifice some mechanical and electrical performance and yet offer attractive solutions to reduce the overall weight of a structural component.

Prof. Dr. Alexander Bismarck
Member of the International Advisory Board

*Corresponding author, e-mail: alexander.bismarck@univie.ac.at

eXPRESS Polymer Letters Vol.9, No.6 (2015) 490–495
Available online at www.expresspolymlett.com
DOI: 10.3144/expresspolymlett.2015.47

An excellent ozone-resistant polymethylvinylsiloxane coating on natural rubber by thiol-ene click chemistry

N. Y. Ning[1,2], *Z. P. Zheng*[1], *L. Q. Zhang*[1,2], *M. Tian*[1,2*]

[1]State Key Laboratory of Organic-Inorganic Composites, Beijing University of Chemical Technology, 100029 Beijing, China
[2]Key Laboratory of Carbon Fiber and Functional Polymers, Ministry of Education, Beijing University of Chemical Technology, 100029 Beijing, China

Received 30 September 2014; accepted in revised form 17 December 2014

Abstract. Natural rubber (NR) as renewable resource is a kind of cheap and versatile elastomer. A disadvantage of NR is that the ozone resistance is not good, which needs to be improved for its wider application. In this study, polymethylvinylsiloxane (PMVS) coating on natural rubber (NR) was realized for the first time by using thiol-ene click reaction under UV irradiation, simultaniously realizing the fast crosslinking of PMVS layer and the covalent crosslinking between PMVS layer and NR layer. As a result, a good interphase adhesion between PMVS coating and NR was obtained. The coating of the crosslinked PMVS layer on NR resulted in an obvious increase in the ozone resistance of NR. Our study provides a new and high efficient strategy to prepare elastomer materials with good ozone resistance.

Keywords: *coating, the thiol-ene click reaction, interphase adhesion, ozone resistance*

1. Introduction

Natural rubber (NR) is a cheap and versatile elastomer, and thus has been widely used in industry such as tires. Nowadays, NR as renewable resource has attracted more attention because of the requirement of environmental protection and resource saving. However, the ozone resistance of NR is not good because of its unsaturated chain structure [1]. Numerous works have been conducted to improve the ozone resistance of NR by adding paraffin or antioxidant in NR matrix or by blending NR with other rubbers with good ozone-resistance [2–4]. The disadvantages of these methods are the deterioration of processability and mechanical properties of NR. Hydrogenation of NR is also an effective method to improve the ozone resistance of NR [5]. A disadvantage of this method is that the hydrogenation reaction is complicated. Furthermore, the coating of hydrogenated carboxylated nitrile butadiene rubber (HXNBR) on NR by using the room temperature curing systems was also effective to improve the ozone resistance of NR [6]. But the traditional curing method at room temperature is inefficient.

Silicon rubber has excellent resistance to extremely low and high temperatures (–55 to 300°C), excellent elasticity and good ozone resistance. Thus, the coating of silicon rubber on the surface of substrates with good interphase adhesion has been prepared by room-temperature vulcanizing [7]. However, the adhesion strength between silicon rubber and NR is poor because of the extremely low surface tension of silicone rubber [8]. Thus, the coating of silicon rubber on NR has not been reported to improve the ozone resistance of NR.

The thiol-ene click reaction, which is extremely rapid and copper-free reaction with mild reaction condi-

*Corresponding author, e-mail: tianm@mail.buct.edu.cn

tions, good selectivity and high yields, has attracted considerable attention in the past few years [9–11]. In previous studies, UV-curing silicon rubber has been prepared by thiol-ene reaction [12, 13]. In addition, thiol functional groups were successfully introduced on polydimethylsiloxane (PDMS) elastomer, and the thiol-functionalized PDMS was modified with hydrophilic molecules containing enes by using the thiol-ene click reaction [14].

In this study, we used the thiol-ene reaction to simultaniously realize the crosslinking of polymethylvinylsiloxane (PMVS) layer and the covalent crosslinking between PMVS and NR to improve the interphase adhesion between PMVS coating and NR. We prepared PMVS coating on peroxide pre-crosslinked NR sheet by spraying PMVS/trimethylolpropane tris (3-mercaptopropionate) (TMPMP) solution on NR followed by crosslinking reaction via thiol-ene click chemistry under UV light. We aim to improve the ozone-resistance of NR by PMVS coating and the interphase adhesion between PMVS coating and NR.

2. Experimental

2.1. Materials

NR was purchased from Shenchi Petrochemical Company (Shandong Province, China). PMVS with vinyl content of 0.18 mol% was purchased from Chenguang Research Institute of Chemical Industry (Chengdu, China). Tetrahydrofuran (THF, 99%), Dicumyl peroxide (DCP, 99%), 2-methyl-4-(methylthio)-2-morpholinopropiophenone (MMMP, 98%) as the reaction initiator and trimethylolpropane tris (3-mercaptopropionate) (TMPMP, 95%) as the crosslinking agent were obtained from J & K Chemical Technology (Shanghai, China). The chemical structure of PMVS, DCP, MMMP and TMPMP is shown in Figure 1a–1c, and 1d, respectively.

2.2. Preparation of the samples

NR sheet with the thickness of 2 mm was prepared by melt blending of 100 g of NR and 0.8 g of DCP using open mill followed by compression molding at 150°C for 10 minutes using curing press. The coating of PMVS on NR sheet was as follows. First, 1 g of PMVS, 0.05 g of MMMP and 0.05 g of TMPMP were dissolved in 9 g of THF under stirring. The concentration of PMVS used is the optimized concentration (10 wt%). The as prepared PMVS solution was then coated on the surface of NR sheet by spraying. After the evaporation of THF, the PMVS coating was crosslinked under UV light (500 W, 320 nm < λ < 420 nm) for 15 minutes under nitrogen atmosphere. The distance between the lamp and the samples is 20 cm. We washed the crosslinked samples for several times by using THF to completely remove the unreacted TMPMP and MMMP, and then dried for 8 hours under vacuum.

2.3. Characterizations

The ester group and the thiol group were characterized by Fourier Transform Infrared Spectroscopy (Tensor 27, Bruker Optik GmBH, Germany) at a resolution of 1–0.4 cm^{-1}. The fractured surface of PMVS coated NR was studied using a S4700 scanning electron microscopy (SEM) (Hitachi Co. Japan) and energy dispersive X-ray spectroscopy (EDS). The sample of PMVS coated NR was first fractured in liquid nitrogen, and then the fractured surface was coated with a thin layer of gold and observed by SEM and EDS. The adhesion strength was studied by using a cross-cut tape test following ASTM D3359 standard. Ozone resistance of the samples was studied using an ozone test chamber (OZ-0500AH, Taiwan High Speed Rail, China) according to ISO 1431-1: 2004 standard. The samples were aged at the ozone concentration of 50 parts per hundred million [pphm] and 200 pphm in static stretching mode, and 50 pphm in dynamic stretching mode. In dynamic stretching mode, the samples were first elongated up to 20% of the length and then returned to their original length repeatedly with dynamic stretching frequency 0.5 Hz.

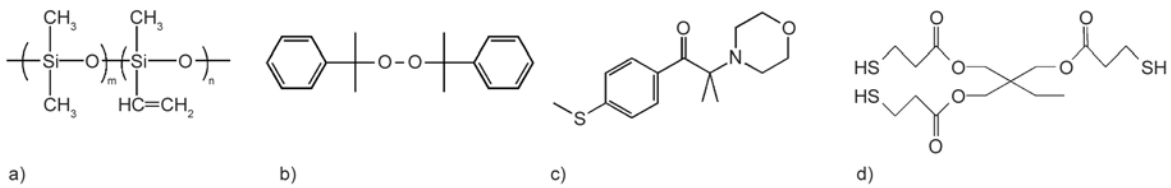

Figure 1. Chemical structure of PMVS (a), DCP (b), MMMP (c) and TMPMP (d)

3. Results and discussion

The reaction between TMPMP and PMVS was characterized by using FTIR, and the results are shown in Figure 2a. The peak at 1727 cm^{-1} represents the carbonyl group (C=O) of MMMP, which is a kind of photoinitiator and does not participate in the crosslinking reaction of polymer. Two typical characteristic peaks are observed for TMPMP. The peak at 2570 cm^{-1} represents the thiol group (–SH), whereas the peak at 1727 cm^{-1} represents the carbonyl group (C=O) of TMPMP. Comparing with the spectra of uncrosslinked PMVS (pure PMVS), the characteristic peak of C=O group appears on the spectra of crosslinked PMVS, indicating the successful reaction between TMPMP and PMVS by UV irradiation. Here, we should note that the crosslinked PMVS was washed by THF to remove the unreacted TMPMP and MMMP. The disappearance of the characteristic peak of thiol group further demonstrates the reaction between TMPMP and PMVS. Thus, FTIR results demonstrate that we can successfully crosslink PMVS by TMPMP via click chemistry under UV light. The direct evidence of the crosslink of PMVS by TMPMP is observed from Figure 2b. We can observe that crosslinked PMVS after UV irradiation is insoluble in THF.

SEM image of the fractured surface of PMVS coated NR is shown in Figure 3a. We can observe that a layer of PMVS with the thickness of 20–30 μm is coated on the surface of NR, and the interphase adhesion between PMVS and NR is good.

The mechanism for the crosslinking of PMVS by TMPMP and the good interphase adhesion between PVMS and NR was studied by using EDS. We selected three samples from PMVS layer (Point A), interphase (Point B) and NR layer (Point C) of the fractured surface of PMVS coated NR, as shown in Figure 3a. Then, we sequentially scanned these samples using EDS to study the content of sulfur element in these samples, and the results are shown in Figure 3b. The sulfur element is from TMPMP, and thus there is no sulfur element in both pure NR crosslinked by DCP and pure PMVS without crosslinking, as demonstrated by EDS results shown in Figure 3b. Before UV irradiation, there are some sulfur element in all the samples of PMVS coated NR because of the addition of TMPMP. The content of sulfur element is the highest at the interphase and the lowest at PMVS layer, indicating that TMPMP molecules migrate into NR layer. This is ascribed to the better thermodynamic compatibility between TMPMP and NR than that between TMPMP and PMVS. Interestingly, the content of sulfur element at PMVS layer is increased from 0.16% to 0.71% after UV irradiation, whereas that at the interphase is decreased from 0.58% to 0.1%, suggesting that TMPMP molecules migrate from interphase into PMVS layer during UV irradiation. This indicates the dynamic driving force of crosslinking reaction between thiol groups of TMPMP and double bonds of PMVS, as schematically shown in Figure 4. Meanwhile, the content of sulfur element at NR layer is even slightly increased to 0.34% after UV irradiation, suggesting the reaction between TMPMP molecules and some double bonds of NR. The lower content of sulfur element at NR layer than that at PMVS layer is ascribed that NR was crosslinked by DCP whereas PMVS was uncrosslinked, indicating the faster crosslink-

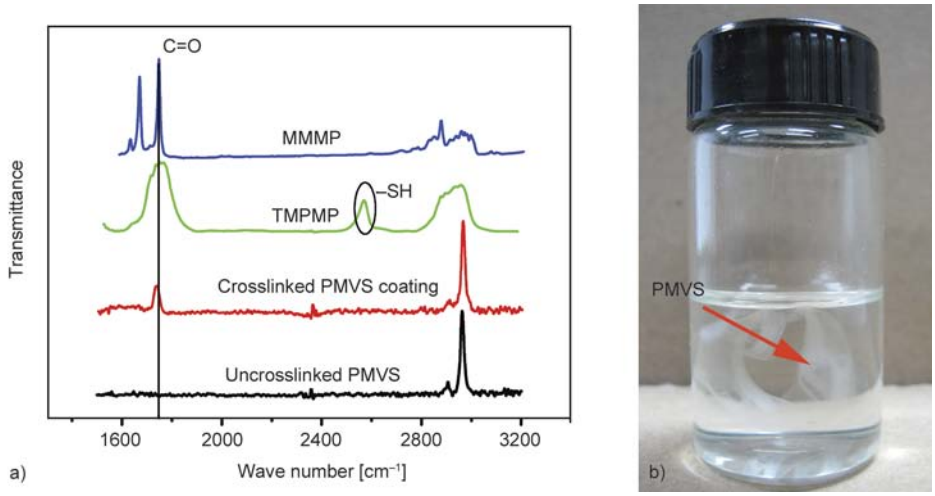

Figure 2. (a) FTIR spectra of uncrosslinked PMVS, TMPMP, MMMP and crosslinked PMVS coating; (b) the photograph of PMVS coating crosslinked by UV irradiation

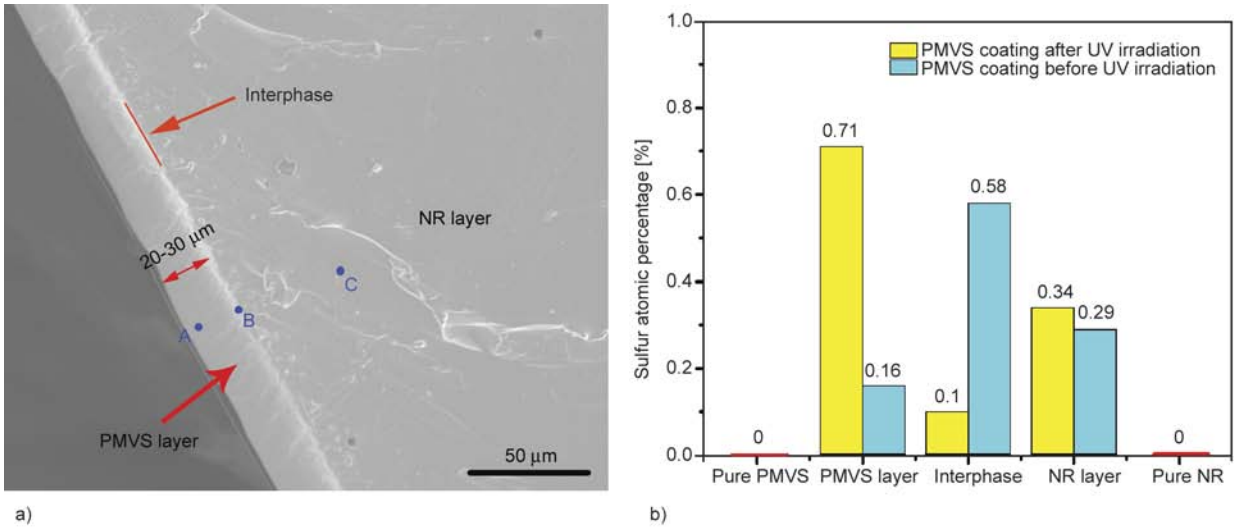

Figure 3. (a) SEM image of fractured surface of PMVS coated NR; (b) sulfur percentage of pure PMVS, pure NR and different layers of PMVS coated NR

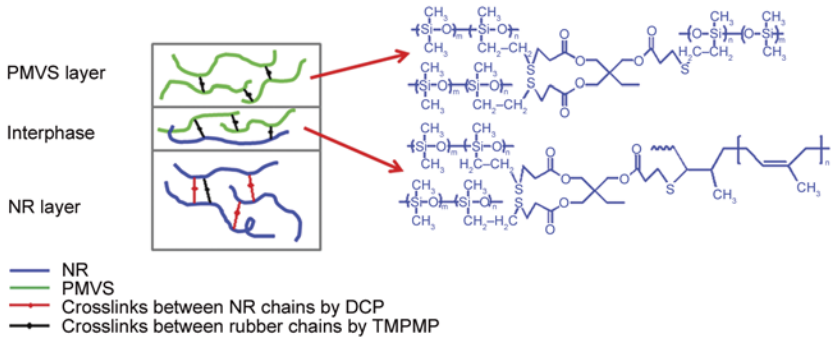

Figure 4. Schematic representation of the crosslinking of PMVS layer and the interface between PMVS coating and NR

ing of PMVS layer than that of NR layer. More importantly, some TMPMP molecules (0.1%) remained at the interphase after UV irradiation, which can simultaneously react with both of PMVS and NR, as demonstrated by the improved interphase adhesion strength between NR and PMVS (see below).

The adhesion strength of the PMVS coating on NR was characterized using cross-cut tape test, and the results are shown in Table 1. According to ASTM standard, 5B (100% adhesion) represents the best adhesion strength, whereas 0B represents no adhesion (0% adhesion). The grading of the adhesion of PMVS coating before UV irradiation is 0B, indicating that the sample does not have any adhesion. However, the grading of adhesion of PMVS coating after UV irradiation reaches 4B, indicating the good interphase adhesion between PMVS coating after UV irradiation and NR. The direct evidence of the poor adhesion between PMVS coating on NR before UV irradiation, and the good interphase adhesion between PMVS coating on NR after UV irradiation is shown in Figure 5. Severe detachment of PMVS coating before UV irradiation from NR is observed (see Figure 5a), whereas almost no detachment of PMVS

Table 1. The grading of the adhesion strength of PMVS coating

	Grading
PMVS coating on NR before UV irradiation	0B
PMVS coating on NR after UV irradiation	4B

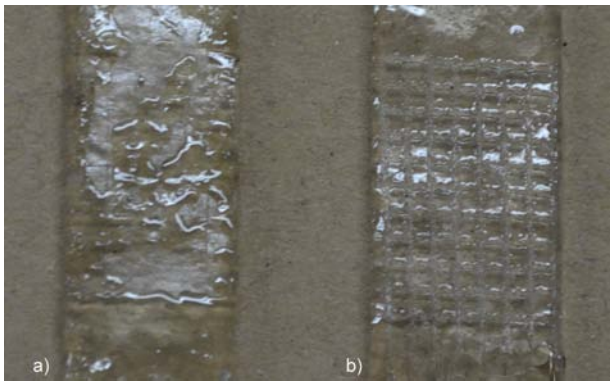

Figure 5. The photos of the surfaces of PMVS coated samples before UV irradiation (a) and after UV irradiation (b)

coating after UV irradiation from NR is observed (see Figure 5b). The reason is that TMPMP at the interphase can simultaneously react with double bonds of both PMVS and NR under UV irradiation. The ozone resistance of pure NR and PMVS coated NR was evaluated by the SEM images of these samples aged under different ozone aging conditions, as shown in Figure 6. The ozone resistance is shown in Table 2. We observe obvious cracks (B-3) in SEM image of pure NR aged at the ozone concentration of 50 pphm in static stretching mode, whereas we observe no cracks in PMVS coated NR aged at the same conditions, as shown in Figure 6a and Figure 6d, respectively. We observe wider cracks (B-3) on pure NR aged at the ozone concentration of 200 pphm in static stretching mode, whereas we observe only some micro-cracks (A-1) on PMVS coated NR aged at the same conditions, as shown in Figure 6b and Figure 6e, respectively. The cracks on the surface of pure NR aged at the ozone concentration of 50 pphm in dynamic stretching mode even become much wider (B-3), indicating the very poor ozone aging resistance of pure NR, as shown in Figure 6c and Table 2. More cracks (B-1) on PMVS coated NR aged at the same condition was observed, but they are still micro-cracks, as shown in Figure 6f. These results demonstrate that the coating of PMVS on NR by crosslinking via click chemistry can largely improve the ozone aging resistance of NR, facilitating the storage and application of NR. The poor ozone resistance of NR is because of its unsaturated chain structure of the polyisoprene backbone, which is easily attacked by oxygen or ozone. PMVS, with very low content of unsaturated bond, has a basic building block of silicon-oxygen bond with high bond energy, which is not easily attacked by oxygen or ozone, and thus shows a good ozone resistance. Therefore, the PMVS coating on NR can effectively protect NR from ozone attack. Com-

Table 2. The ozone resistance of the samples

	Testing conditions	Type of cracking
Pure NR	50 pphm in static stretching mode	B-3
	200 pphm in static stretching mode	B-3
	50 pphm in dynamic stretching mode	B-3
NR coated with PMVS	50 pphm in static stretching mode	nc[a]
	200 pphm in static stretching mode	A-1
	50 pphm in dynamic stretching mode	B-1

[a]The cracking was not appeared on the surface of rubber specimens.

Marking the types of cracking:

A: A small number of cracking.
B: A large of number cracking.
C: Numberless cracking.

1. That which cannot be seen with eyes but can be confirmed with 10 times magnifying glass.
2. That which can be confirmed with naked eyes.
3. That which the deep and comparatively long (below 1 mm).
4. That which the deep and long (above 1 mm and below 3 mm).
5. That which about to crack more than 3 mm or about to severe.

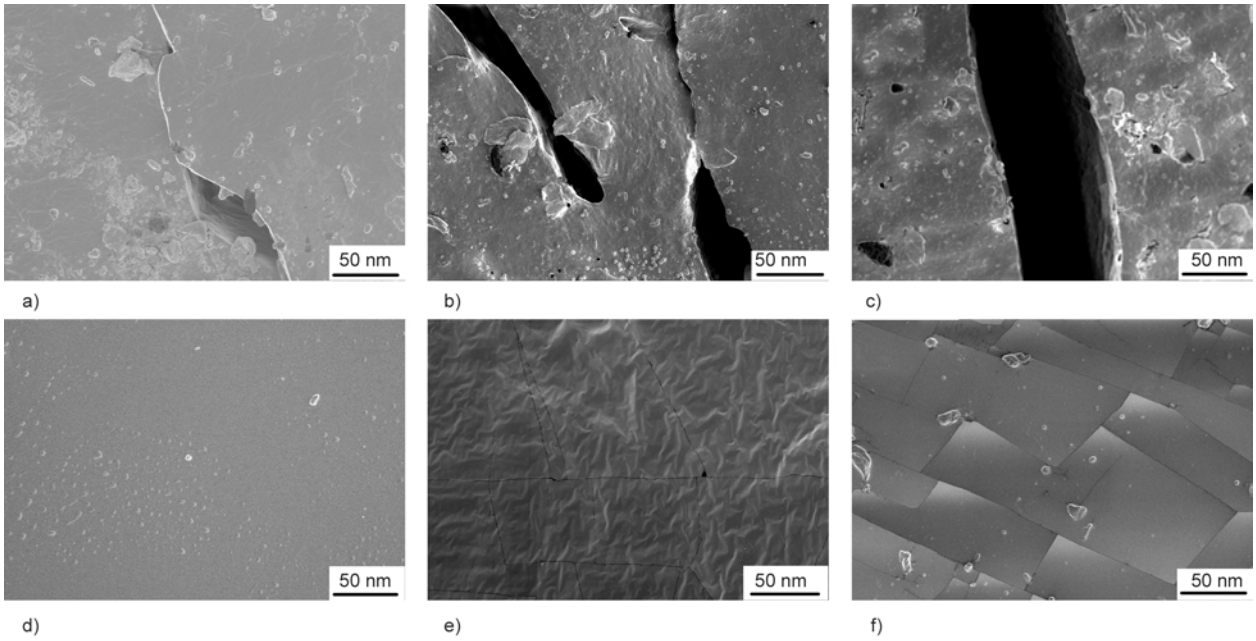

Figure 6. SEM images of pure NR (a, b, c) and PMVS coated NR (d, e, f) under different ozone aging conditions. (a) (d) at the ozone concentration of 50 pphm in static stretching mode; (b) (e) at the ozone concentration of 200 pphm in static stretching mode; (c) (f) at the ozone concentration of 50 pphm in dynamic stretching mode.

pared with the previous studies using the traditional methods to improve the ozone resistance [1, 15], our method also can achieve the good ozone resistance. The advantage of our method is the achievement of good interphase adhesion between PMVS coating and NR. Thus, the mechanical properties of NR are not affected by the PMVS coating in this study.

4. Conclusions

We have successfully prepared PMVS coating on NR via thiol-ene click reaction under UV irradiation, which simultaniously realized the crosslinking of PMVS layer and the covalent crosslinking between PMVS layer and NR layer. As a result, the ozone resistance of NR was improved by the coating of crosslinked PMVS layer on the surface of NR sheet. Meanwhile, we obtained a good interphase adhesion between PMVS coating and NR. Our study provides an effective technique to prepare polymer materials with good ozone-resistance.

Acknowledgements

We gratefully acknowledge the financial supports of the National Natural Science Foundation of China under Grant No. 51373012 and 51221002.

References

[1] Piya-areetham P., Rempel G. L., Prasassarakich P.: Hydrogenated nanosized polyisoprene as a thermal and ozone stabilizer for natural rubber blends. Polymer Degradation and Stability, **102**, 112–121 (2014). DOI: 10.1016/j.polymdegradstab.2014.01.032

[2] Saeed F., Ansarifar A., Ellis R. J., Haile-Meskel Y., Farid A. S.: Effect of the blooming of chemical curatives on the cyclic fatigue life of natural rubber filled with a silanized silica nanofiller. Journal of Applied Polymer Science, **120**, 2497–2507 (2011). DOI: 10.1002/app.33396

[3] Abdelwahab N. A., El-Nashar D. E., Abd El-Ghaffar M. A.: Polyfuran, polythiophene and their blend as novel antioxidants for styrene- butadiene rubber vulcanizates. Materials and Design, **32**, 238–245 (2011). DOI: 10.1016/j.matdes.2010.06.003

[4] Ramesan M. T., Alex R., Khanh N. V.: Studies on the cure and mechanical properties of blends of natural rubber with dichlorocarbene modified styrene–butadiene rubber and chloroprene rubber. Reactive and Functional Polymers, **62**, 41–50 (2005). DOI: 10.1016/j.reactfunctpolym.2004.08.002

[5] Hinchiran N., Lertweerasirikun W., Poonsawad W., Rempel G. L., Prasassarakich P.: Hydrogenated natural rubber blends: Aspect on thermal stability and oxidative behavior. Journal of Applied Polymer Science, **113**, 1566–1575 (2009). DOI: 10.1002/app.30034

[6] Joseph R.: HXNBR coating for improving aging resistance of natural rubber products. Rubber Chemistry and Technology, **79**, 553–560 (2006). DOI: 10.5254/1.3547951

[7] Momen G., Farzaneh M., Jafari R.: Wettability behaviour of RTV silicone rubber coated on nanostructured aluminium surface. Applied Surface Science, **257**, 6489–6493 (2011). DOI: 10.1016/j.apsusc.2011.02.049

[8] Kim E. S., Kim E. J., Lee T. H., Yoon J. S.: Improvement of the adhesion properties of silicone rubber by the incorporation of silane-modified montmorillonite. Journal of Applied Polymer Science, **128**, 2563–2570 (2013). DOI: 10.1002/app.38489

[9] Lowe A. B.: Thiol-ene 'click' reactions and recent applications in polymer and materials synthesis. Polymer Chemistry, **1**, 17–36 (2010). DOI: 10.1039/b9py00216b

[10] Li G. L., Xu L. Q., Tang X., Neoh K. G., Kang E. T.: Hairy hollow microspheres of fluorescent shell and temperature-responsive brushes via combined distillation-precipitation polymerization and thiol–ene click chemistry. Macromolecules, **43**, 5797–5803 (2010). DOI: 10.1021/ma1008012

[11] Li G. L., Wan D., Neoh K. G., Kang E. T.: Binary polymer brushes on silica@polymer hybrid nanospheres and hollow polymer nanospheres by combined alkyne–azide and thiol–ene surface click reactions. Macromolecules, **43**, 10275–10282 (2010). DOI: 10.1021/ma1020787

[12] Xue L., Zhang Y., Zuo Y., Diao S., Zhang J., Feng S.: Preparation and characterization of novel UV-curing silicone rubber via thiol-ene reaction. Materials Letters, **106**, 425–427 (2013). DOI: 10.1016/j.matlet.2013.05.084

[13] Campos L. M., Meinel I., Guino R. G., Schierhorn M., Gupta N., Stucky G. D., Hawker C. J.: Highly versatile and robust materials for soft imprint lithography based on thiol-ene click chemistry. Advanced Materials, **20**, 3728–3733 (2008). DOI: 10.1002/adma.200800330

[14] Zhang J., Chen Y., Brook M. A.: Facile functionalization of PDMS elastomer surfaces using thiol–ene click chemistry. Langmuir, **29**, 12432–12442 (2013). DOI: 10.1021/la403425d

[15] Simma K., Rempel G. L., Prasassarakich P.: Improving thermal and ozone stability of skim natural rubber by diimide reduction. Polymer Degradation and Stability, **94**, 1914–1923 (2009). DOI: 10.1016/j.polymdegradstab.2009.08.005

eXPRESS Polymer Letters Vol.9, No.6 (2015) 496–508
Available online at www.expresspolymlett.com
DOI: 10.3144/expresspolymlett.2015.48

Low band-gap polymers incorporating benzotriazole and 5,6-dialkoxy-benzothiadiazole as solution processable electrochromic materials

W. T. Neo[1], *Q. Ye*[1], *X. Wang*[1], *H. Yan*[1], *J. Xu*[1,2*]

[1]Institute of Materials Research and Engineering, 3 Research Link, Agency for Science, Technology and Research (A*STAR), 117602 Singapore, Singapore
[2]Department of Chemistry, National University of Singapore, 3 Science Drive 3, 117543 Singapore, Singapore

Received 10 October 2014; accepted in revised form 21 December 2014

Abstract. Two series of donor-acceptor type conjugated polymers bearing benzotriazole or 5,6-dialkoxy-benzothiadiazole as acceptors unit are synthesized via Stille coupling. The optical, electrochemical, spectroelectrochemical characterizations and theoretical calculations are carried out. The polymers display excellent solubility in common organic solvents upon the introduction of long aliphatic side chains. The electrochromic performances of the polymers are also studied. Upon oxidation, the polymers switch from magenta or blue to a transmissive light blue state. In particular, respectable optical contrasts of about 44 and 40% are obtained in the visible and near infrared (NIR) region respectively for **P2**. The polymers also reveal fast switching of about from one second to a few seconds. In addition, **P2** exhibits a high coloration efficiency of 518 and 561 cm^2/C in the visible and NIR region respectively. The promising electrochromic behaviour of these polymers, together with the enhanced solubility will allow large-scale processing and advancement towards real applications.

Keywords: *polymer synthesis, molecular engineering, donor-acceptor, electrochromic, solution processable*

1. Introduction

Electrochromic materials that display color changes upon an applied external bias have received widespread attention as they have been heralded as the next-generation color-changing technology. In this regard, conjugated polymers are one type of the most promising candidates as electrochromic materials. Researchers have ingeniously utilized the distinct advantage of conjugated polymers – ease of structural modifications, for color-tuning through bandgap manipulations [1]. One particular strategy that has been widely employed for the adjustment of frontier orbital energy levels is the donor-acceptor (D–A) approach [2]. Benzothiadiazole (BT) and related derivatives [3] have been intensively investigated as the acceptor moiety in donor-acceptor type conjugated polymers [4–11]. To tune the physical properties of the functional polymer, e.g., varying the frontier orbital energy level and absorption behaviour, a large number of electron-withdrawing building blocks have been synthesized based on the similar chemical structure of benzothiadiazole. Prevailing chemical strategies to modify the electronic property of BT unit include a) replacement of the S atoms to O [12–15], –NR [10, 16], $–CR_2$ [17, 18], Se [19, 20], Te [20]; b) replacement of the C–H part with N [21–23], C–F [24–26], $C–NO_2$ [27], C–OR [28, 29] and c) extension of the π-conjugation [30–37]. Out of all the building blocks available in the literatures, those with flexible chains for enhanced solubility of corre-

*Corresponding author, e-mail: jw-xu@imre.a-star.edu.sg

sponding polymers are typically employed for the preparation of solution processable D–A conjugated polymers [38].

As an on-going research progress on design and synthesis of EC materials [39–42], we are keen to incorporate BT based acceptor moieties into D–A polymers to prepare high performance solution processable EC polymers. In this regard, the acceptor building block needs suitable electron affinity for frontier orbital energy level control and functional sites for the attachment of solubilizing chains. Benzotriazole and 5,6-dialkoxy benzothiadiazole (Figure 1) are the target building blocks that contain both features. First of all, the highest-occupied molecular orbital (HOMO) energy level of the final electrochromic polymer is of great importance to control the oxidation of the polymer in the EC device, which thus controls the saturation working voltage of the device [1]. To lower the energy consumption and to enhance the lifetime of EC device, a lower working voltage is desired and hence a higher HOMO is more desirable. For these two building blocks, their electron affinity is lowered compared with that of BT, due to the replacement of the sulfur with –NR and addition of two electron donating alkoxyl groups. Secondly, both of the two building blocks have functional sites which allow facile attachment of solubilizing chains. Furthermore, both building blocks can be conveniently prepared in large quantities following established chemical synthesis, which allows large scale synthesis of the final polymers. Owing to these advantages, implementation of these two BT derived building blocks into D–A type conjugated polymer would be a very promising approach to prepare high performance solution processable electrochromic materials.

Herein, we report the synthesis of two series of benzotriazole or 5,6-dialkoxyl-benzothiadiazole-containing D–A type conjugated polymers via Stille cross coupling reactions. With the incorporation of long aliphatic side chains on the moieties, all the polymers **P1–P5** (Figure 1) exhibit good solubility, rendering solution processing techniques applicable. Their physical properties are well characterized, both experimentally and theoretically. The utilization of these materials as electrochromes in electrochromic devices is investigated. The polymers are found to be magenta or blue in their neutral states and partially transmissive in the fully oxidized states. The electrochromic properties of the polymers are promising, such as fast switching, respectable optical contrasts, coloration efficiencies and stabilities under ambient conditions.

2. Experimental section

2.1. Materials

All materials were purchased from Aldrich and used as received unless otherwise stated. Tetrahydrofuran (THF) and toluene were distilled over sodium/benzophenone. Triethylamine (TEA) was purified by refluxing with calcium hydride and then distilled. Dimethylformamide (DMF, 99%) from Tedia Company Inc. was dried with molecular sieves (4 Å) and used directly without filtration or distillation. Indium tin oxide (ITO, 60 Ω/sq) coated poly(ethylene terephthalate) (PET) was obtained from Aldrich and used as the substrate.

2.2. Instrumentation

^{1}H-NMR (400 MHz) and ^{13}C-NMR (100 MHz) were obtained in $CDCl_3$ with Tetramethylsilane (TMS) as the internal reference on Bruker spectrometers.

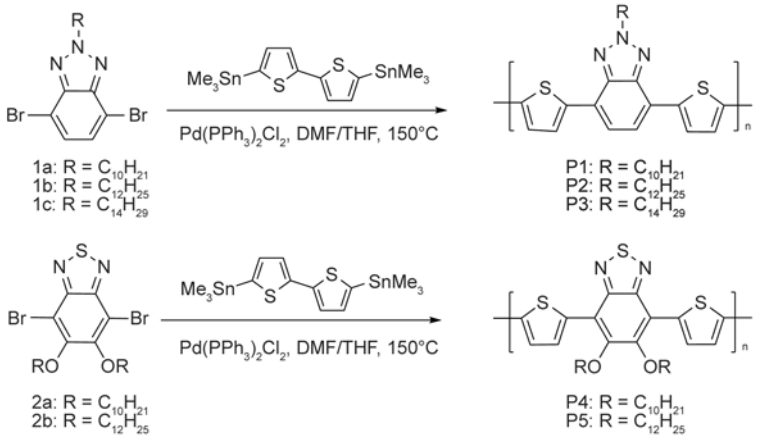

Figure 1. Synthetic routes leading to polymers **P1–P5**

Molecular weights were determined using Waters Model 2690 Gel Permeation Chromatography (GPC) in HPLC-grade tetrahydrofuran (THF) against polystyrene (PS) as standard. UV-vis absorption spectra were measured with a Shimadzu UV-3101 PC scanning spectrometer. The fluorescence measurements were conducted with Perkin Elmer LS55 fluorescence spectrometer. Modulated differential scanning calorimetry (DSC 2920) was used to evaluate the thermal behaviors of the polymers. Polymer deposition was carried out using a SCS G3P-8 spincoater, at a speed rate of 1000 rpm for 60 s, to yield film thicknesses of approximately 70–80 nm. An Autolab PGSTAT128N potentiostat/galvanostat was used for cyclic voltammetry experiments and in situ spectroelectrochemical studies. A Shimadzu UV-3600 UV-vis-NIR spectrophotometer was also employed for the spectroelectrochemical studies.

2.3. Synthesis of monomers

Dibromo-benzotriazole monomers **1a–1c**, 4,7-dibromo-5,6-dialkoxy-benzothiadiazole monomers **2a–2b** and the monomer 5,5′-bis(trimethylstannyl)-2,2′-bithiophene were prepared according to the reported procedures [39, 40, 43].

4,7-Dibromo-2-decylbenzotriazole (1a)

Yield 50%; ^{1}H-NMR ($CDCl_3$, 400 MHz): δ ppm = 7.44 (s, 2H), 4.78 (t, J = 7.2, 7.6 Hz, 2H), 2.15 (m, 2H), 1.37–1.25 (m, 14H), 0.88 (t, J = 6.8 Hz, 3H); ^{13}C-NMR (100 MHz, $CDCl_3$): δ =144.1, 129.8, 110.3, 57.8, 32.2, 30.5, 29.74, 29.65, 29.54, 29.28, 26.83, 22.95, 14.4; MS (EI): calc for $C_{16}H_{23}Br_2N_3$ $[M]^+$ 417.2, found 416.8.

4,7-Dibromo-2-dodecylbenzotriazole (1b)

Yield 62%; ^{1}H-NMR ($CDCl_3$, 400 MHz): δ ppm = 7.44 (s, 2H), 4.78 (t, J = 7.2, 7.6 Hz, 2H), 2.15 (m, 2H), 1.36–1.25 (m, 18H), 0.88 (t, J = 6.8 Hz, 3H).

4,7-Dibromo-2-tetradecylbenzotriazole (1c)

Yield 45%; ^{1}H-NMR ($CDCl_3$, 400 MHz): δ ppm = 7.44 (s, 2H), 4.77 (t, J = 7.2, 7.6 Hz, 2H), 2.15 (m, 2H), 1.36–1.25 (m, 22H), 0.88 (t, J = 6.8 Hz, 3H); ^{13}C-NMR (100 MHz, $CDCl_3$): δ = 144.1, 129.9, 110.4, 57.8, 32.3, 30.5, 30.01, 29.98, 29.93, 29.83, 29.69, 29.32 26.87, 23.03, 14.4; MS (EI): calc for $C_{20}H_{31}Br_2N_3$ $[M]^+$ 473.3, found 472.9.

4,7-Dibromo-5,6-bis(decyloxy)benzo-2,1,3-thiadiazole (2a)

Yield 85%; ^{1}H-NMR ($CDCl_3$, 400 MHz): δ ppm = 4.16 (t, J = 6.4 Hz, 4H), 1.88 (m, 4H), 1.28 (m, 28H), 0.89 (t, J = 6.4 Hz, 6H); ^{13}C-NMR (100 MHz, $CDCl_3$): δ = 154.9, 150.8, 106.6, 75.5, 32.3, 30.6, 29.96, 29.94, 29.79, 29.68, 26.4, 23.04, 14.4; MS (EI): calc for $C_{26}H_{42}Br_2N_2O_2S$ $[M]^+$ 606.5, found 606.1.

4,7-Dibromo-5,6-bis(dodecyloxy)benzo-2,1,3-thiadiazole (2b)

Yield 88%; ^{1}H-NMR ($CDCl_3$, 400 MHz): δ ppm = 4.16 (t, J = 6.8, 6.4Hz, 4H), 1.88 (m, 4H), 1.27 (m, 36H), 0.88 (t, J = 6.8, 6.4 Hz, 6H); ^{13}C-NMR (100 MHz, $CDCl_3$): δ = 154.9, 150.8, 106.6, 75.5, 32.3, 30.64, 30.04, 30.01, 29.99, 29.80, 29.72, 29.39, 26.4, 23.04, 14.4; MS (EI): calc for $C_{30}H_{50}Br_2N_2O_2S$ $[M]^+$ 662.6, found 662.2.

2.4. Synthesis of polymers (P1-P5)

Compound **1a–1c** (2 mmol) or **2a–2b** (2 mmol) and 5,5′-bis(trimethylstannyl)-2,2′-bithiophene (2 mmol) were dissolved in 50 mL dry DMF and 50 mL dry THF, which was purged with argon for 1 h. $Pd(PPh_3)_2Cl_2$ (30 mg) was added in one portion and the mixture was heated up to reflux at 150°C for 4 days. After cooling down to room temperature, the solvents were evaporated under reduced pressure and the residue was dissolved by small amount of hot chloroform, followed by precipitation in cold methanol. The resulting black particles after filtration were then purified by Soxhlet extraction with successively MeOH, hexane, and chlorobenzene. The chlorobenzene fraction was recovered and evaporated and the dark purple solid was obtained.

Polymer P1 *Poly{2-decyl-4,7-di(thiophen-2-yl)-2H-benzo[d][1,2,3]triazole}*

(Yield, 76%). ^{1}H-NMR ($CDCl_3$, 400 MHz): δ ppm = 7.53 (m) (benzotriazole), 7.37 (br) (thiophene), 7.07 (br) (thiophene), 4.86 (br) (–N–CH_2–), 1.68–0.87 (br) (pendant alkyl chain). GPC using PS in THF as standard: (M_n = 35.1 k, M_w = 49.5 k, PDI = 1.41); Anal. Calcd. for **P1**: $(C_{24}H_{27}N_3S_2)_n$: C, 68.37; H, 6.45; N, 9.97. Found: C 68.06; H, 6.77; N, 10.05.

Polymer P2 *Poly{2-dodecyl-4,7-di(thiophen-2-yl)-2H-benzo[d][1,2,3]triazole}*
(Yield, 64%). ^{1}H-NMR ($CDCl_3$, 400 MHz): δ ppm = 7.59–7.70 (benzotriazole), 7.33–7.45 (thiophene), 7.00–7.13 (thiophene), 4.72– 4.87 (–N–CH_2–), 1.53–0.83 (pendant alkyl chain). GPC using PS in THF as standard: (M_n = 119.5 k, M_w = 157.1 k, PDI = 1.31); Anal. Calcd. for **P2**: $(C_{26}H_{31}N_3S_2)_n$: C, 69.45; H, 6.95; N, 9.34. Found: C 69.36; H, 7.17; N, 9.15.

Polymer P3 *Poly{2-tetradecyl-4,7-di(thiophen-2-yl)-2H-benzo[d][1,2,3]triazole}*
(Yield, 72%). ^{1}H-NMR ($CDCl_3$, 400 MHz): δ ppm = 7.60–7.78 (benzotriazole), 7.22–7.35 (thiophene), 7.09–7.15 (thiophene), 4.78–4.89 (–N–CH_2–), 1.69–0.82 (pendant alkyl chain). GPC using PS in THF as standard: (M_n = 26.7 k, M_w = 45.2 k, 1.70); Anal. Calcd. for **P3**: $(C_{28}H_{35}N_3S_2)_n$: C, 70.40; H, 7.38; N, 8.80. Found: C 70.26; H, 7.57; N, 8.65.

Polymer P4 *Poly{5,6-bis(decyloxy)-4,7-di(thiophen-2-yl)benzo[c][1,2,5]thiadiazole}*
(Yield, 65%). ^{1}H-NMR ($CDCl_3$, 400 MHz): δ ppm = 8.6 (m), 7.4 (m), 4.2 (m), 2.04–1.12 (m), 0.88 (m). GPC using PS in THF as standard: (M_n = 32.9 k, M_w = 55.8 k, PDI = 1.70); Anal. Calcd. for **P4**: $(C_{34}H_{46}N_2O_2S_3)_n$: C, 66.84; H, 7.59; N, 4.59. Found: C 66.61; H, 7.83; N, 4.50.

Polymer P5 *Poly{5,6-bis(dodecyloxy)-4,7-di(thiophen-2-yl)benzo[c][1,2,5]thiadiazole}*
(Yield 61%). ^{1}H-NMR ($CDCl_3$, 400 MHz): δ ppm = 8.6 (m), 7.4 (m), 4.2 (m), 2.03–1.11 (m), 0.86 (m). GPC using PS in THF as standard: (M_n = 33.3 k, M_w = 61.9 k, PDI = 1.90); Anal. Calcd. for **P5**: $(C_{38}H_{56}N_2O_2S_3)_n$: C, 68.42; H, 8.16; N, 4.20. Found: C 68.72; H, 8.40; N, 4.13.

2.5. Cyclic voltammetry

The polymer solutions in *m*-xylene (10 mg/mL) were drop cast (2 μL) onto glassy carbon electrode to form electrochromic layers with an active area of around 0.03 cm^2. Cyclic voltammetry (CV) was performed in a three-electrode cell with polymer-coated glassy carbon electrode (CH Instruments, 2 mm diameter) as the working electrode, platinum wire (CH Instruments) as the counter electrode and silver wire (CH Instruments) as the reference electrode. A 0.1M $LiClO_4$ solution in acetonitrile was used. For CV measurements, the electrolyte solution was first bubbled with argon for 60 min to remove residual oxygen prior to characterization. A scan rate of 25 mV/s was employed for the studies. The pseudo-reference electrode was calibrated with respect to the ferrocene/ferrocenium redox couple $E_{1/2}$ (Fc/Fc^+) = +0.29 V (vs. Ag wire). For the approximation of HOMO levels, the ferrocene/ferrocenium redox couple was taken to occur at 4.8 eV below vacuum.

2.6. Spectroelectrochemistry

The solutions of **P1** to **P5** in *m*-xylene (10 mg/mL) were spin-coated (1000 rpm, 60 s) onto ITO coated PET to form electrochromic layers with an active area of 2.5 cm^2. In-situ spectroelectrochemical data for the polymer thin film were recorded using a three-electrode cell assembly, where the working electrode was the ITO coated PET substrate, the counter electrode was a platinum wire and a Ag wire was the pseudo-reference electrode. A 0.1M $LiClO_4$ solution in acetonitrile was used as prepared. The spectra were scanned after the potentials have been applied for 10 s, and held throughout the course of the scans.

2.7. Computational details

All theoretical calculations were carried out at the density functional theory (DFT) level with the B3LYP functional and the 6-31G(d) basis set using Gaussian 09 [44]. The vertical energy transition data and oscillator strengths were obtained by the time-dependent density functional theory (TD-DFT). Gauss View was used to generate the pictorial representations.

3. Results and discussion

3.1. Synthesis

The synthesis of the target polymers **P1–P5** is shown in Figure 1. The Stille cross coupling reaction was utilized as the polymerization tool to construct the copolymers **P1–P5**. All the five polymers were obtained in satisfactory yields and exhibited good solubility in common organic solvents such as chloroform and chlorobenzene. The molecular weight and polydispersity index of the synthesized polymers **P1–P5** are summarized in Table 1. Stille coupling reaction has been validated as a reliable polymerization technique to prepare conjugated copolymers with high molecular weight and low polydispersity compared to Yomamoto coupling reaction, chemi-

Table 1. Molecular weights and polydispersity of polymers **P1–P5**[a]

Polymer	M_w [Da]	M_n [Da]	Polydispersity index
P1	49 500	35 100	1.41
P2	157 100	119 500	1.31
P3	45 200	26 700	1.70
P4	55 800	32 900	1.70
P5	61 900	33 300	1.90

[a]M_w: the weight-average molecular weight. M_n: the number-average molecular weight.

cal oxidative polymerization or electrochemical polymerization methods [45–48]. As a representation of the polymers, **P2** and **P5** were chosen for the probing of the thermal stabilities. The polymers exhibit good thermal stability and no phase transition peaks are observed by differential scanning calorimetry study up to 200°C. The polymers also reveal high solubility in common organic solvents such as chloroform, toluene and xylene.

3.2. Optical properties

The UV-visible absorption and photoluminescence spectra of polymers **P1–P5** are plotted in Figure 2 and the results for all polymers are summarized in Table 2. As representative examples, the insert pictures in Figure 2 show the absorption and emission colour of the THF solutions of **P2** and **P5**. For **P1** to **P3**, as the length of the alkyl chains increases from octyl ($–C_8H_{17}$) to dodecyl ($–C_{12}H_{25}$), the absorption maximum remained essentially the same both in the solution (~500 nm) and in the film (~490 nm) while the absorption onset showed a slight bathochromic shift from 635 nm for **P1** to 653 nm for **P3**, indicating that variation of the aliphatic chains has minimal influence on the absorption behaviour of the polymers [49]. The absorption maxima of **P4** and **P5** is about 90 nm red shifted compared with those of **P1–P3**, mainly due to a stronger electron withdrawing ability of 5,6-dialkoxy-benzothiadiazole compared with benzotriazole. It is worthy to note that the series of benzotriazole based polymers (**P1–P3**) showed a bright orange emission with quantum yield of 0.4–0.6 while two dialkoxy-benzothiadiazole based polymers (**P4** and **P5**) exhibited low quantum yield of <0.1. This could perhaps be attributed to the presence of two long alkoxy chains in **P4** and **P5** which disrupt the planarity of the conjugated backbone. In highly rigid conjugated systems, high quantum yields have been observed [50]. The bright fluorescence of **P1–P3** rendered them potential as fluorescence based sensing materials [51].

3.3. Electrochemical and spectroelectrochemical behavior

The redox behaviours of the polymers were studied using cyclic voltammetry and the results are summarized in Table 2. Typical cyclic voltammograms of **P2** and **P5** are shown in Figure 3 as representation. The cyclic voltammograms of the other polymers can be found in the supporting information. **P1–P3** exhibited similar HOMO (~–5.4 eV) and LUMO (~–3.4 eV) energy levels. For **P4** and **P5**, the HOMO are slightly lower than that of **P1–P3**. This is mainly ascribed to the higher electron affinity of 5,6-dialkoxy-benzothiadiazole than benzotriazole moiety (*vide infra*). Length of the alkyl chains attached was found to have minimal influence on the electronic behavior of the polymers.

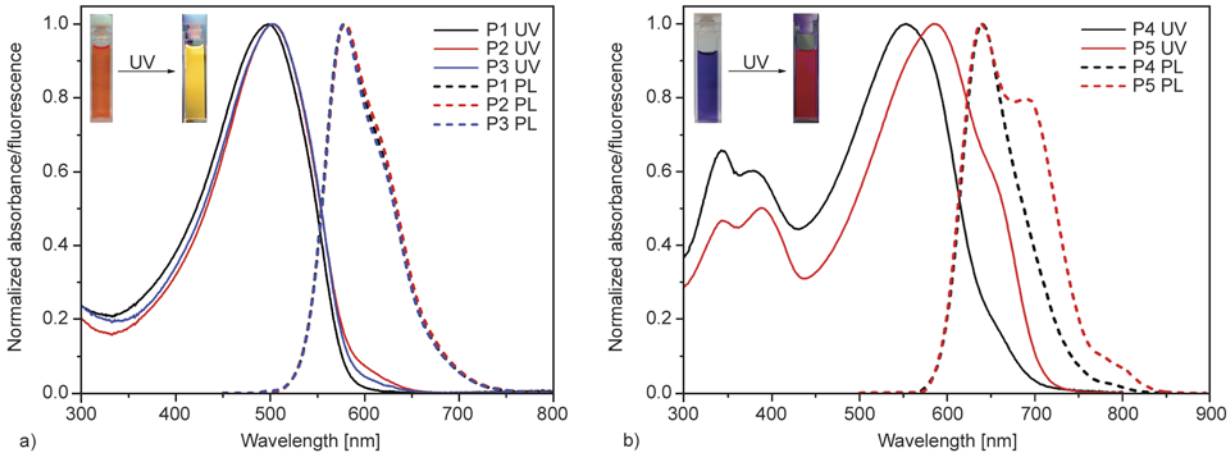

Figure 2. Absorption and emission spectra of (a) **P1–P**3 and (b) **P4** and **P5** in THF. The inserts show the color of **P2** and **P5** in THF solution under white light (left) and when exposed to UV light (366 nm) (right) at ambient temperature.

Table 2. Optical and electrochemical properties of polymers **P1–P5**

Polymer	λ_{max}(THF)[a] [nm]	λ_{max}(em)[b] [nm]	λ_{onset}(film)[c] [nm]	E_g^{op} [d] [eV]	HOMO[e] [eV]	LUMO[f] [eV]	Φ_{PL}(THF)[g]
P1	497	578.5	635	1.95	–5.35	–3.40	0.60
P2	501	579.0	645	1.92	–5.35	–3.43	0.42
P3	501	578.5	653	1.90	–5.37	–3.47	0.62
P4	586	638.5	696	1.78	–5.49	–3.71	0.10
P5	586	639.0	710	1.75	–5.37	–3.62	0.02

[a]Absorption maximum from the UV-vis spectrum in THF solution. [b]PL emission maximum in THF solution. [c]Absorption onset from the UV-vis spectrum. [d]Egop is calculated following the equation $E_g^{op} = 1240/\lambda_{onset}$ [eV]; [e]HOMO is calculated following the equation HOMO = –(4.8 + E_{onset}^{ox} vs Fc/Fc$^+$). [f]LUMO is calculated following the equation LUMO = HOMO – E_g^{op}. [d]The photoluminescence (*PL*) quantum yield (Φ_{PL}) of the polymer in THF solution was measured by using quinine sulphate (ca. $1 \cdot 10^{-5}$M solution in 0.1M H_2SO_4, assuming Φ_{PL} of 0.55) as a standard.

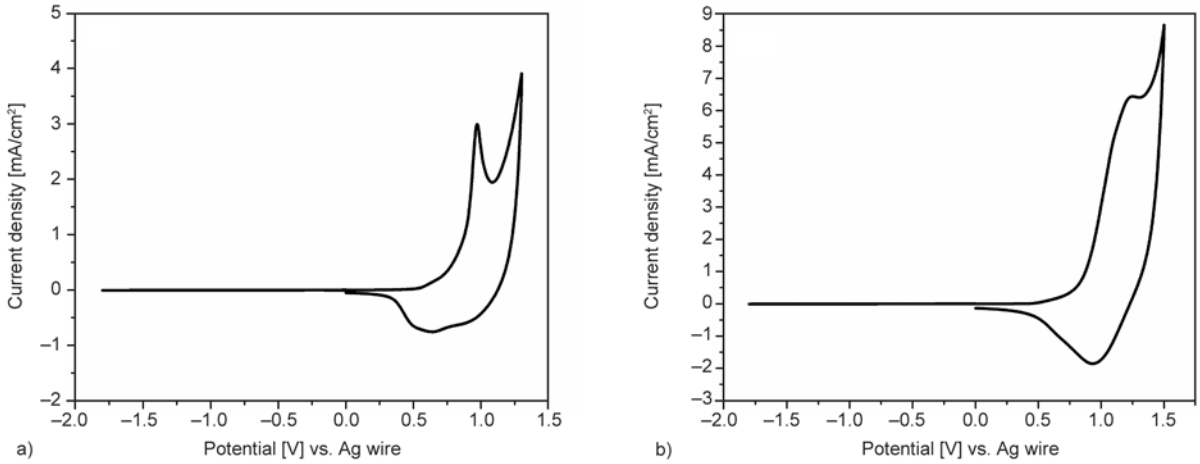

Figure 3. Cyclic voltammograms of (a) **P2** and (b) **P5** films in 0.1M $LiClO_4$ solution in acetonitrile at a scan rate of 25 mV/s

The electrochemical absorption spectra of the polymers were recorded upon progressive oxidation from 0.0 to around 1.5 V. At the neutral states, polymers **P1** to **P5** all reveal one broad absorption band in the visible region with absorption maximum of around 500–600 nm. The benzotriazole-based polymers **P1–P3** display a purple hue in their neutral states, whereas the benzothiadiazole-based polymers **P4** and **P5** are blue. As the polymers are gradually oxidized, the peaks at the visible region decrease while polaronic and bipolaronic bands start to appear in the NIR region. At the fully oxidized state, all the polymers turn transmissive blue due to the tailing absorption in the visible region. The color changes observed for the polymers are depicted in Figure 4. Such colored-to-transmissive electro-

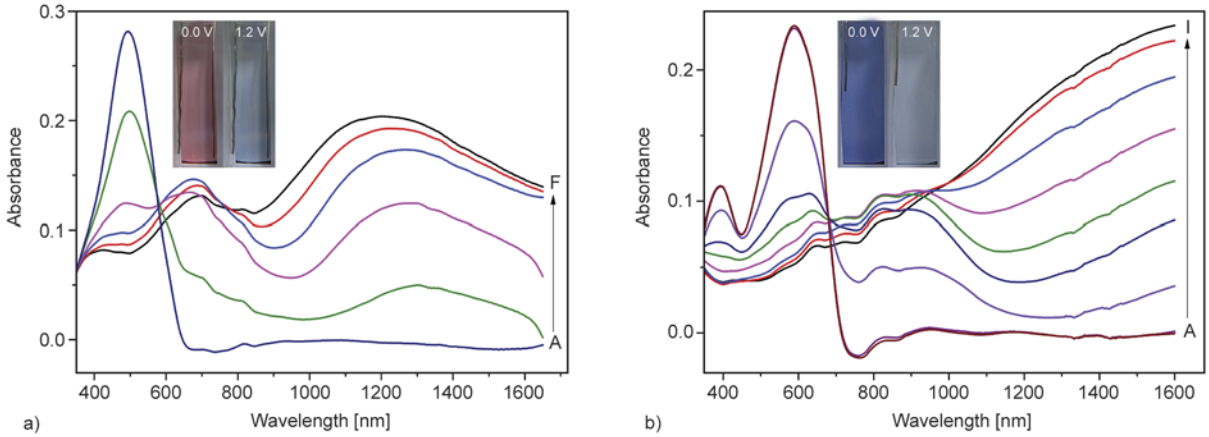

Figure 4. Spectroelectrochemistry of (a) **P2** and (b) **P5** film on an ITO coated PET in 0.1M $LiClO_4$ solution in acetonitrile at applied potentials [V]. Curves: (A) 0.0, (B) 0.5, (C) 0.8, (D) 1.0, (E) 1.1, (F) 1.2, (G) 1.3, (H) 1.4, (I) 1.5 V. Inserts show the colors of (a) **P2** and (b) **P5** films at 0.0 V and 1.2 V.

chromic changes are of particular interest in absorption/transmission devices such as smart windows, information displays etc [1].

3.4. TD-DFT computational analysis

To better understand the electronic properties of these two series of polymers, time-dependent density functional theory (TD-DFT at the B3LYP/6-31G(d) level) calculations were carried out for the oligomeric model compounds of these polymers. All the side chains are shortened to methyl groups in the model compounds to save calculation time as it has been found that the length of alkyl chains has minimal influence on the electronic properties of the polymers. The optimized structures and the HOMO/LUMO profiles of the trimeric model compounds of **P1–P5** are shown in Figure 5. Both frontier orbitals are found to distribute evenly over the whole conjugated system. It is noted that the –NR group in the benzotriazole moiety and the S atom in the 5,6-dialkoxy-benzothiadiazole moiety are only covered by the LUMO and the sulfur atom is more intensively involved in the LUMO electron density compared with the –NR moiety, which would be due to the larger polarizability of sulfur atom [37]. One more feature to highlight is the phase distribution of the HOMO and LUMO in the conjugated backbone. In the HOMO profile, the two carbons linking the thiophene and the acceptor unit is in the opposite phase while in the LUMO profile, these two carbons are in the same phase. Such patterns have been routinely observed in many D–A type conjugated systems [52–55], and this suggests that both the donor and the acceptor play an essential role in determining the energy levels. The energy levels of the HOMO and LUMO orbitals were computed for the monomer, dimer and oligomers, and the band gaps are plotted as a function of the inverse of the number of repeating monomer units [56, 57]. Through extrapolation of the curve, the estimated band gap of an infinitely long polymer chain is obtained (Table 3). It is estimated that the band gap of the 5,6-dialkoxy-

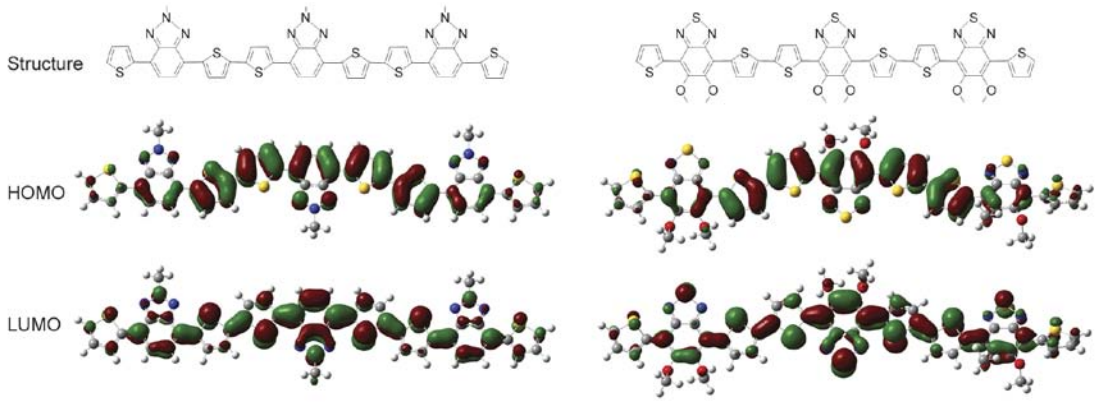

Figure 5. Electron distribution in HOMO and LUMO orbitals of benzotriazole and 5,6-dialkoxy-benzothiadiazole-based trimers

Table 3. TD-DFT calculated HOMO/LUMO energy levels of benzotriazole and 5,6-dialkoxy-benzothiadiazole based oligomers

Chemical structure	N	HOMO [eV]	LUMO [eV]	E_g [eV]
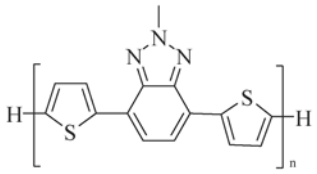	1	–5.094	–1.903	3.192
	2	–4.672	–2.233	2.439
	3	–4.544	–2.361	2.183
	4	–4.489	–2.422	2.067
	∞	–	–	1.686
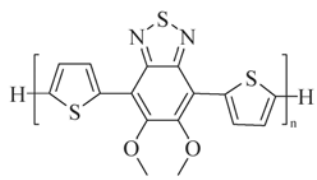	1	–5.276	–2.432	2.844
	2	–4.831	–2.613	2.217
	3	–4.699	–2.700	1.999
	4	–4.646	–2.739	1.907
	∞	–	–	1.587

benzothiadiazole based polymer (1.59 eV) is about 0.1 eV less than that of the benzotriazole based polymer (1.69 eV). This trend is in agreement with the experimental measurement. The electron-accepting ability of the benzotriazole and 5,6-dialkoxy-benzothiadiazole units is compared using the LUMO energy levels as a crude approximation. The LUMO level of the benzotriazole based monomer is calculated to be around –1.903 eV which is 0.5 eV higher than that of the 5,6-dialkoxy-benzothiadiazole based monomer at –2.432 eV, hence confirming the weaker electron affinity of the benzotriazole based monomer.

3.5. Electrochromic performance

A square-wave potential step absorptometry was carried out to characterize the degree of color changes of the polymers. The potentials were switched repeatedly between 1.2 and –1.2 V with a switching time of 10 s for 2 cycles, 5 s for 4 cycles, 2 s for 6 cycles and 1 s for 8 cycles at the absorption maximum in both the visible and NIR regions. The results are shown in Figure 6 and summarized in Table 4. Respectable contrasts were recorded for the polymers in the visible and NIR regions respectively. Among all the polymers, **P2** displayed the most promising contrasts of about 40% in both the visible and NIR regions. It was also found that the length of side chains influences the electrochromic performance to a considerable extent. Across the two series of polymers, it is interesting to note that the polymers with alkyl/alkoxy chain lengths of twelve carbon units appear to yield the best electrochromic performance. Further studies may involve the study and elucidation of the structure of side chains necessary to yield devices with optimal performances. In comparison to a similar polymer with a benzyl side group functionalized at the benzotriazole instead of an alkyl chain in this work, similar contrast in the visible region was observed [58]. The response times of the polymers were calculated as the time required to achieve 95% optical contrast of the full switch. This value is typically used as the human eye is unable to discern the difference in the last 5% [1]. The coloration and bleaching time in the visible and NIR regions for all the polymers are determined and given in Table 4. Among the benzotriazole and

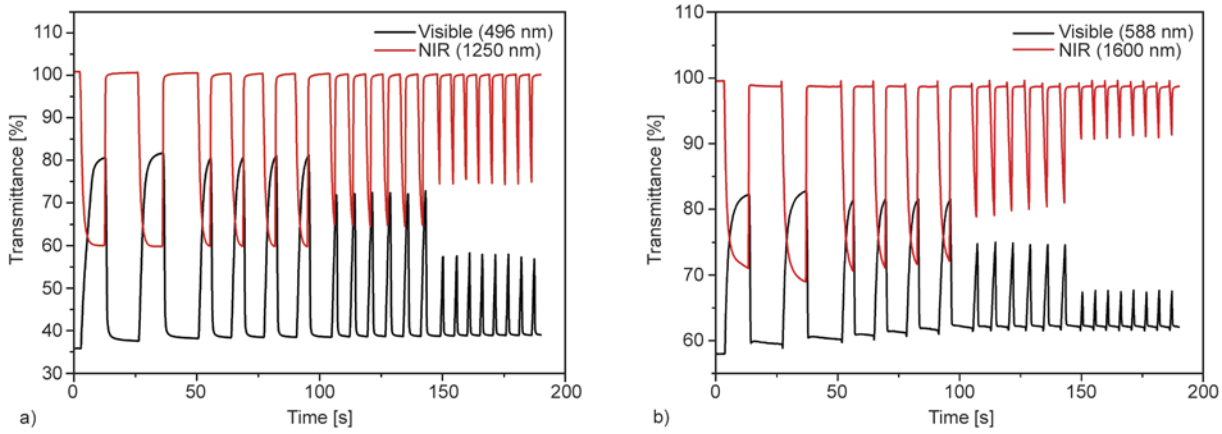

Figure 6. Square-wave potential step absorptometry of (a) **P2** and (b) **P5** film in the visible region and NIR region on an ITO coated PET in 0.1M $LiClO_4$/ACN electrolyte/solvent couple between –1.2 V and 1.2 V with a switch time of 10 s for 2 cycles, 5 s for 4 cycles, 2 s for 6 cycles and 1 s for 8 cycles

Table 4. Summary of electrochromic performance of polymers **P1–P5** in film state

Polymer	Optical contrast [ΔT%]		Switching time [s]				Coloration efficiency [cm^2/C]	
	At λ_{max}	At NIR	At λ_{max}		At NIR		At λ_{max}	At NIR
			Coloration[a]	Bleaching[b]	Coloration[a]	Bleaching[b]		
P1	22	25	1.2	3.2	2.9	0.8	191	234
P2	44	40	0.8	5.0	2.5	0.4	518	561
P3	23	24	1.3	1.3	1.2	0.9	273	333
P4	14	22	0.4	2.4	4.0	0.4	230	257
P5	23	30	0.6	5.4	5.0	0.3	403	275

[a]Coloration refers to the process in which the percent transmittance changes from a higher value to lower value; [b]Bleaching refers to the process in which the percent transmittance changes from a lower value to higher value.

5,6-dialkoxy-benzothiadiazole based polymers, **P2** exhibits the best switching behaviour during bleaching in the NIR region at 0.4 s. For all the five polymers, the oxidation process corresponding to the bleaching in the visible region and coloration in the NIR region is found to be slower than the reverse process corresponding to the coloration in the visible region and bleaching in the NIR region. This can be rationally explained by the different diffusion rates of the counter anions (ClO_4^-) and counter cations (Li^+) at different charged states of the polymer films [59]. The polymers were subjected to repeated potential switching between 1.2 and –1.2 V at 5 s switch. All the five polymers exhibited stable cycling behavior in the device and the stability cycling performance of **P2** is illustrated in Figure 7 as a demonstration. After about 200 cycling, the polymer film was still able to produce 90% of the original transmittance with switch time almost unchanged, indicating the high robustness of these copolymers under ambient conditions. The coloration efficiency is estimated from Equation (1) [60]:

$$CE(\eta) = \frac{\log\left(\frac{T_{ox}}{T_{red}}\right)}{Q_d} \quad (1)$$

where T_{ox} refers to the percent transmittance of the bleached state, T_{red} the percent transmittance of the colored state, and Q_d the injected/ejected charge per unit area (C/cm^2). The coloration efficiency for all the polymers the visible and NIR regions are calculated and tabulated in Table 4. Among all the polymers, **P2** reveals the best coloration efficiency of more than 500 cm^2/C in both visible and NIR regions. In general, the superior electrochromic performance for **P1–P3** compared to **P4–P5** may have arisen from the lower HOMO levels of **P1–P3**, which allows for ease of oxidation, lower working voltage and lower energy consumption.

4. Conclusions

Two series of benzotriazole and 5,6-dialkoxy-benzothiadiazole containing D–A type conjugated polymers (**P1–P5**) were synthesized via Stille coupling, affording magenta and blue polymers in their neutral states and partially transmissive in their oxidized states. All the prepared polymers have good solubility in common organic solvents and the films can thus be prepared by solution based processing methods. The effect of the electron-acceptor strength, as well as alkyl chain lengths on the optical, electrochemical and electrochromic properties of the polymers were also studied. Both theoretically and experimentally, it has been shown that the acceptor strength greatly affects the HOMO energy level and the band gap of the conjugated polymers. These polymers have been demonstrated as electrochromic materials which turn partially transmissive upon p-doping. Good contrast, fast switching, high coloration efficiency and high stability of the EC devices have been established using these polymers as the electrochromic layer, thus rendering promise of these benzotriazole and 5,6-dialkoxy-benzothiadiazole based polymers as high performance colored-to-transmissive electrochromes.

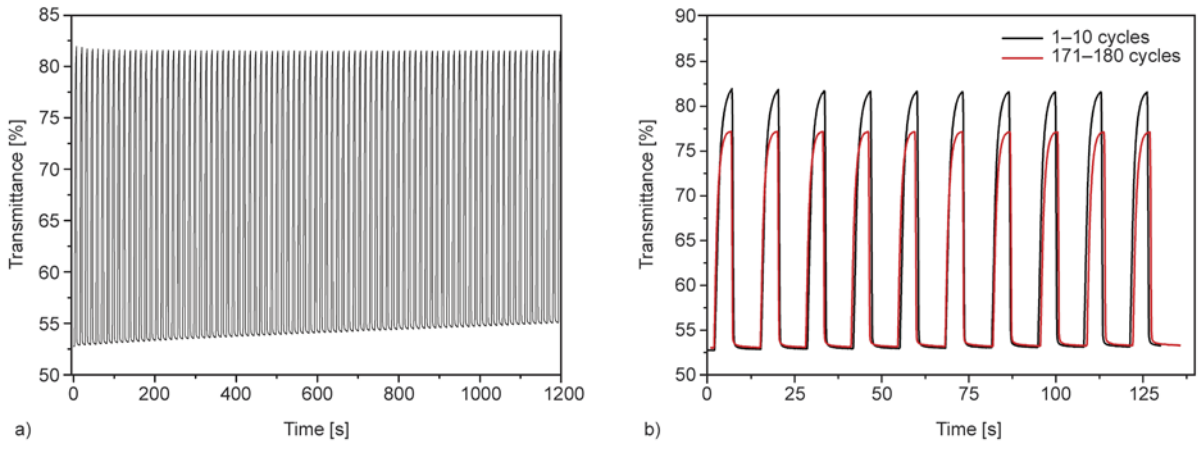

Figure 7. Stability testing of **P2** polymer film through square-wave potential step absorptometry at λ_{max} between 1.2 and –1.2 V with a switch time of 5 s, a) illustration of 90 continuous deep cycles, b) comparison in optical contrasts between cycles 1–10 and cycles 171–180

Acknowledgements

The authors would like to thank the Agency for Science, Technology and Research (A*STAR) for financial support (Grant no.:1321760011).

References

[1] Beaujuge P. M., Reynolds J. R.: Color control in π-conjugated organic polymers for use in electrochromic devices. Chemical Reviews, **110**, 268–320 (2010). DOI: 10.1021/cr900129a

[2] Havinga E. E., ten Hoeve W., Wynberg H.: A new class of small band gap organic polymer conductors. Polymer Bulletin, **29**, 119–126 (1992). DOI: 10.1007/BF00558045

[3] Neto B. A. D., Lapis A. A. M., da Silva Júnior E. N., Dupont J.: 2,1,3-Benzothiadiazole and derivatives: Synthesis, properties, reactions, and applications in light technology of small molecules. European Journal of Organic Chemistry, **2**, 228–255 (2013). DOI: 10.1002/ejoc.201201161

[4] Cheng Y-J., Yang S-H., Hsu C-S.: Synthesis of conjugated polymers for organic solar cell applications. Chemical Reviews, **109**, 5868–5923 (2009). DOI: 10.1021/cr900182s

[5] Beaujuge P. M., Fréchet J. M. J.: Molecular design and ordering effects in π-functional materials for transistor and solar cell applications. Journal of the American Chemical Society, **133**, 20009–20029 (2011). DOI: 10.1021/ja2073643

[6] Yen Y-S., Chou H-H., Chen Y-C., Hsu C-Y., Lin J. T.: Recent developments in molecule-based organic materials for dye-sensitized solar cells. Journal of Materials Chemistry, **22**, 8734–8747 (2012). DOI: 10.1039/C2JM30362K

[7] Blouin N., Michaud A., Gendron D., Wakim S., Blair E., Neagu-Plesu R., Belletête M., Durocher G., Tao Y., Leclerc M.: Toward a rational design of poly(2,7-carbazole) derivatives for solar cells. Journal of the American Chemical Society, **130**, 732–742 (2008). DOI: 10.1021/ja0771989

[8] Wang C., Dong H., Hu W., Liu Y., Zhu D.: Semiconducting π-conjugated systems in field-effect transistors: A material odyssey of organic electronics. Chemical Reviews, **112**, 2208–2267 (2012). DOI: 10.1021/cr100380z

[9] Biniek L., Schroeder B. C., Nielsen C. B., McCulloch I.: Recent advances in high mobility donor–acceptor semiconducting polymers. Journal of Materials Chemistry, **22**, 14803–14813 (2012). DOI: 10.1039/C2JM31943H

[10] Thakur V. K., Ding G., Ma J., Lee P. S., Lu X.: Hybrid materials and polymer electrolytes for electrochromic device applications. Advanced Materials, **24**, 4071–4096 (2012). DOI: 10.1002/adma.201200213

[11] Balan A., Baran D., Toppare L.: Benzotriazole containing conjugated polymers for multipurpose organic electronic applications. Polymer Chemistry, **2**, 1029–1043 (2011). DOI: 10.1039/C1PY00007A

[12] Karsten B. P., Bijleveld J. C., Viani L., Cornil J., Gierschner J., Janssen R. A.: Electronic structure of small band gap oligomers based on cyclopentadithiophenes and acceptor units. Journal of Materials Chemistry, **19**, 5343–5350 (2009). DOI: 10.1039/B901374A

[13] Jiang J-M., Yang P-A., Hsieh T-H., Wei K-H.: Crystalline low-band gap polymers comprising thiophene and 2,1,3-benzooxadiazole units for bulk heterojunction solar cells. Macromolecules, **44**, 9155–9163 (2011). DOI: 10.1021/ma201848z

[14] Pati P. B., Das S., Zade S. S.: Benzooxadiazaole-based D–A–D *co*-oligomers: Synthesis and electropolymerization. Journal of Polymer Science Part A: Polymer Chemistry, **50**, 3996–4003 (2012). DOI: 10.1002/pola.26195

[15] Ding P., Zhong C., Zou Y., Pan C., Wu H., Cao Y.: 5,6-bis(decyloxy)-2,1,3-benzooxadiazole-based polymers with different electron donors for bulk-heterojunction solar cells. Journal of Physical Chemistry C, **115**, 16211–16219 (2011). DOI: 10.1021/jp2031434

[16] Lee J-K., Gwinner M. C., Berger R., Newby C., Zentel R., Friend R. H., Sirringhaus H., Ober C. K.: High-performance electron-transporting polymers derived from a heteroaryl bis(trifluoroborate). Journal of the American Chemical Society, **133**, 9949–9951 (2011). DOI: 10.1021/ja201485p

[17] Song S., Jin Y., Park S. H., Cho S., Kim I., Lee K., Heeger A. J., Suh H.: A low-bandgap alternating copolymer containing the dimethylbenzimidazole moiety. Journal of Materials Chemistry, **20**, 6517–6523 (2010). DOI: 10.1039/C0JM00772B

[18] Shim J. Y., Lee B. H., Song S., Kim H., Kim J. A., Kim I., Lee K., Suh H.: Synthesis and properties of the conjugated polymers with indenoindene and benzimidazole units for organic photovoltaics. Journal of Polymer Science Part A: Polymer Chemistry, **51**, 241–249 (2013). DOI: 10.1002/pola.26385

[19] Shin S. A., Park J. B., Kim J-H., Hwang D-H.: Synthesis and characterization of 2,1,3-benzoselenadiazole-based conjugated polymers for organic photovoltaic cells. Synthetic Metals, **172**, 54–62 (2013). DOI: 10.1016/j.synthmet.2013.04.004

[20] Gibson G. L., McCormick T. M., Seferos D. S.: Atomistic band gap engineering in donor–acceptor polymers. Journal of the American Chemical Society, **134**, 539–547 (2012). DOI: 10.1021/ja208917m

[21] Welch G. C., Bazan G. C.: Lewis acid adducts of narrow band gap conjugated polymers. Journal of the American Chemical Society, **133**, 4632–4644 (2011). DOI: 10.1021/ja110968m

[22] Sun Y., Chien S-C., Yip H-L., Zhang Y., Chen K-S., Zeigler D. F., Chen F-C., Lin B., Jen A. K-Y.: High-mobility low-bandgap conjugated copolymers based on indacenodithiophene and thiadiazolo[3,4-*c*]pyridine units for thin film transistor and photovoltaic applications. Journal of Materials Chemistry, **21**, 13247–13255 (2011).
DOI: 10.1039/C1JM11564B

[23] Wen W., Ying L., Hsu B. B. Y., Zhang Y., Nguyen T-Q., Bazan G. C.: Regioregular pyridyl[2,1,3]thiadiazole-*co*-indacenodithiophene conjugated polymers. Chemical Communications, **49**, 7192–7194 (2013).
DOI: 10.1039/C3CC43229G

[24] Price S. C., Stuart A. C., Yang L., Zhou H., You W.: Fluorine substituted conjugated polymer of medium band gap yields 7% efficiency in polymer–fullerene solar cells. Journal of the American Chemical Society, **133**, 4625–4631 (2011).
DOI: 10.1021/ja1112595

[25] Albrecht S., Janietz S., Schindler W., Frisch J., Kurpiers J., Kniepert J., Inal S., Pingel P., Fostiropoulos K., Koch N., Neher D.: Fluorinated copolymer PCPDTBT with enhanced open-circuit voltage and reduced recombination for highly efficient polymer solar cells. Journal of the American Chemical Society, **134**, 14932–14944 (2012).
DOI: 10.1021/ja305039j

[26] Dou L., Chen C-C., Yoshimura K., Ohya K., Chang W-H., Gao J., Liu Y., Richard E., Yang Y.: Synthesis of 5*H*-dithieno[3,2-*b*:2′,3′-*d*]pyran as electron-rich building block for donor-acceptor type low-bandgap polymers. Macromolecules, **46**, 3384–3390 (2013).
DOI: 10.1021/ma400452j

[27] He Y., Wang X., Zhang J., Li Y.: Low bandgap polymers by copolymerization of thiophene with benzothiadiazole. Macromolecular Rapid Communications, **30**, 45–51 (2009).
DOI: 10.1002/marc.200800507

[28] Nagarjuna G., Kokil A., Kumar J., Venkataraman D.: A straightforward route to electron transporting conjugated polymers. Journal of Materials Chemistry, **22**, 16091–16094 (2012).
DOI: 10.1039/C2JM32217J

[29] Ku S-Y., Liman C. D., Burke D. J., Treat N. D., Cochran J. E., Amir E., Perez L. A., Chabinyc M. L., Hawker C. J.: A Facile synthesis of low-band-gap donor–acceptor copolymers based on dithieno[3,2-*b*:2′,3′-*d*]thiophene. Macromolecules, **44**, 9533–9538 (2011).
DOI: 10.1021/ma202095j

[30] Lee J., Cho S., Seo J. H., Anant P., Jacob J., Yang C.: Swapping field-effect transistor characteristics in polymeric diketopyrrolopyrrole semiconductors: Debut of an electron dominant transporting polymer. Journal of Materials Chemistry, **22**, 1504–1510 (2012).
DOI: 10.1039/C1JM14549E

[31] Li H., Tam T. L., Lam Y. M., Mhaisalkar S. G., Grimsdale A. C.: Synthesis of low band gap [1,2,5]-thiadiazolo[3,4-*g*]quinoxaline and pyrazino[2,3-*g*]quinoxaline derivatives by selective reduction of benzo[1,2-*c*; 4,5-*c*′]bis[1,2,5]thiadiazole. Organic Letters, **13**, 46–49 (2011).
DOI: 10.1021/ol102465a

[32] Zha D., Chen L., Wu F., Wang H., Chen Y.: Modulation of the molecular geometry of carbazolebis(thiadiazole)-based conjugated polymers for photovoltaic applications. Polymer Chemistry, **4**, 2480–2488 (2013).
DOI: 10.1039/C3PY21113D

[33] Dong Y., Hu X., Duan C., Liu P., Liu S., Lan L., Chen D., Ying L., Su S., Gong X., Huang F., Cao Y.: A series of new medium-bandgap conjugated polymers based on naphtho[1,2-c:5,6-c]bis(2-octyl-[1,2,3]triazole) for high-performance polymer solar cells. Advanced Materials, **25**, 3683–3688 (2013).
DOI: 10.1002/adma.201301547

[34] Wei P., Duan L., Zhang D., Qiao J., Wang L., Wang R., Dong G., Qiu Y.: A new type of light-emitting naphtho[2,3-*c*][1,2,5]thiadiazole derivatives: Synthesis, photophysical characterization and transporting properties. Journal of Materials Chemistry, **18**, 806–818 (2008).
DOI: 10.1039/B714539J

[35] Park H. J., Lee Y., Jo J. W., Jo W. H.: Synthesis of a low bandgap polymer based on a thiadiazolo-indolo [3,2-*b*]carbazole derivative for enhancement of open circuit voltage of polymer solar cells. Polymer Chemistry, **3**, 2928–2932 (2012).
DOI: 10.1039/C2PY20417G

[36] Yuen J. D., Fan J., Seifter J., Lim B., Hufschmid R., Heeger A. J., Wudl F.: High performance weak donor–acceptor polymers in thin film transistors: Effect of the acceptor on electronic properties, ambipolar conductivity, mobility, and thermal stability. Journal of the American Chemical Society, **133**, 20799–20807 (2011).
DOI: 10.1021/ja205566w

[37] Patel D. G., Feng F., Ohnishi Y-Y., Abboud K. A., Hirata S., Schanze K. S., Reynolds J. R.: It takes more than an imine: The role of the central atom on the electron-accepting ability of benzotriazole and benzothiadiazole oligomers. Journal of the American Chemical Society, **134**, 2599–2612 (2012).
DOI: 10.1021/ja207978v

[38] Arias A. C., MacKenzie J. D., McCulloch I., Rivnay J., Salleo A.: Materials and applications for large area electronics: Solution-based approaches. Chemical Reviews, **110**, 3–24 (2010).
DOI: 10.1021/cr900150b

[39] Neo W. T., Loo L. M., Song J., Wang X., Cho C. M., Chan H. S. O., Zong Y., Xu J.: Solution-processable blue-to-transmissive electrochromic benzotriazole-containing conjugated polymers. Polymer Chemistry, **4**, 4663–4675 (2013).
DOI: 10.1039/C3PY00677H

[40] Lim S. Z. H., Neo W. T., Cho C. M., Wang X., Tan A. Y. X., Chan H. S. O., Xu J.: Electrochromic π-conjugated copolymers derived from azulene, fluorene, and dialkyloxybenzothiadiazole. Australian Journal of Chemistry, **66**, 1048–1056 (2013).
DOI: 10.1071/CH13147

[41] Neo W. T., Cho C. M., Song J., Chin J. M., Wang X., He C., Chan H. S. O., Xu J.: Solution-processable multicolored dithienothiophene-based conjugated polymers for electrochromic applications. European Polymer Journal, **49**, 2446–2456 (2013).
DOI: 10.1016/j.eurpolymj.2013.02.026

[42] Ding G., Cho C. M., Chen C., Zhou D., Wang X., Tan A. Y. X., Xu J., Lu X.: Black-to-transmissive electrochromism of azulene-based donor–acceptor copolymers complemented by poly(4-styrene sulfonic acid)-doped poly(3,4-ethylenedioxythiophene). Organic Electronics, **14**, 2748–2755 (2013).
DOI: 10.1016/j.orgel.2013.07.037

[43] Chen M. S., Niskala J. R., Unruh D. A., Chu C. K., Lee O. P., Fréchet J. M. J.: Control of polymer-packing orientation in thin films through synthetic tailoring of backbone coplanarity. Chemistry of Materials, **25**, 4088–4096 (2013).
DOI: 10.1021/cm402489a

[44] Frisch M. J., Trucks G. W., Schlegel H. B., Scuseria G. E., Robb M. A., Cheeseman J. R., Scalmani G., Barone V., Mennucci B., Petersson G. A., Nakatsuji H., Caricato M., Li X., Hratchian H. P., Izmaylov A. F., Bloino J., Zheng G., Sonnenberg J. L., Hada M., Ehara M., Toyota K., Fukuda R., Hasegawa J., Ishida M., Nakajima T., Honda Y., Kitao O., Nakai H., Vreven T., Montgomery J. A., Peralta J. E. Jr., Ogliaro F., Bearpark M., Heyd J. J., Brothers E., Kudin K. N., Staroverov V. N., Kobayashi R., Normand J., Raghavachari K., Rendell A., Burant J. C., Iyengar S. S., Tomasi J., Cossi M., Rega N., Millam M. J., Klene M., Knox J. E., Cross J. B., Bakken V., Adamo C., Jaramillo J., Gomperts R., Stratmann R. E., Yazyev O., Austin A. J., Cammi R., Pomelli C., Ochterski J. W., Martin R. L., Morokuma K., Zakrzewski V. G., Voth G. A., Salvador P., Dannenberg J. J., Dapprich S., Daniels A. D., Farkas Ö., Foresman J. B., Ortiz J. V., Cioslowski J., Fox D. J.: Gaussian 09, Revision A.2. Gaussian Inc., Wallingford, USA (2009).

[45] Carsten B., He F., Son H. J., Xu T., Yu L.: Stille polycondensation for synthesis of functional materials. Chemical Reviews, **111**, 1493–1528 (2011).
DOI: 10.1021/cr100320w

[46] Balan A., Baran D., Gunbas G., Durmus A., Ozyurt F., Toppare L.: One polymer for all: Benzotriazole containing donor–acceptor type polymer as a multi-purpose material. Chemical Communications, **44**, 6768–6770 (2009).
DOI: 10.1039/B912482A

[47] Qiao X., Wang X., Mo Z.: The $FeCl_3$-doped poly(3-alkyithiophenes) in solid state. Synthetic Metals, **122**, 449–454 (2001).
DOI: 10.1016/S0379-6779(00)00587-7

[48] Helgesen M., Gevorgyan S. A., Krebs F. C., Janssen R. A. J.: Substituted 2,1,3-benzothiadiazole- and thiophene-based polymers for solar cells – Introducing a new thermocleavable precursor. Chemistry of Materials, **21**, 4669–4675 (2009).
DOI: 10.1021/cm901937d

[49] Pasker F. M., Le Blanc S. M., Schnakenburg G., Höger S.: Thiophene-2-aryl-2*H*-benzotriazole-thiophene oligomers with adjustable electronic properties. Organic Letters, **13**, 2338–2341 (2011).
DOI: 10.1021/ol2005853

[50] Davey A. P., Elliot S., O'Connor O., Blau W.: New rigid backbone conjugated organic polymers with large fluorescence quantum yields. Journal of the Chemical Society, Chemical Communications, **14**, 1433–1434 (1995).
DOI: 10.1039/C39950001433

[51] Ding G., Zhou H., Xu J., Lu X.: Electrofluorochromic detection of cyanide anions using a benzothiadiazole-containing conjugated copolymer. Chemical Communications, **50**, 655–657 (2014).
DOI: 10.1039/C3CC47732K

[52] Zhang Y., Zou J., Yip H-L., Sun Y., Davies J. A., Chen K-S., Acton O., Jen A. K-Y.: Conjugated polymers based on C, Si and N-bridged dithiophene and thienopyrroledione units: Synthesis, field-effect transistors and bulk heterojunction polymer solar cells. Journal of Materials Chemistry, **21**, 3895–3902 (2011).
DOI: 10.1039/C0JM03927F

[53] Chang H-H., Tsai C-E., Lai Y-Y., Chiou D-Y., Hsu S-L., Hsu C-S., Cheng Y-J.: Synthesis, molecular and photovoltaic properties of donor–acceptor conjugated polymers incorporating a new heptacylic indacenodithieno [3,2-*b*]thiophene arene. Macromolecules, **45**, 9282–9291 (2012).
DOI: 10.1021/ma3019552

[54] Azoulay J. D., Koretz Z. A., Wong B. M., Bazan G. C.: Bridgehead imine substituted cyclopentadithiophene derivatives: An effective strategy for band gap control in donor–acceptor polymers. Macromolecules, **46**, 1337–1342 (2013).
DOI: 10.1021/ma302569u

[55] Shi Q., Fan H., Liu Y., Chen J., Ma L., Hu W., Shuai Z., Li Y., Zhan X.: Side chain engineering of copolymers based on bithiazole and benzodithiophene for enhanced photovoltaic performance. Macromolecules, **44**, 4230–4240 (2011).
DOI: 10.1021/ma200576y

[56] Yang S., Olishevski P., Kertesz M.: Bandgap calculations for conjugated polymers. Synthetic Metals, **141**, 171–177 (2004).
DOI: 10.1016/j.synthmet.2003.08.019

[57] Ma J., Li S., Jiang Y.: A time-dependent DFT study on band gaps and effective conjugation lengths of polyacetylene, polyphenylene, polypentafulvene, polycyclopentadiene, polypyrrole, polyfuran, polysilole, polyphosphole, and polythiophene. Macromolecules, **35**, 1109–1115 (2002).
DOI: 10.1021/ma011279m

[58] Yigitsoy B., Karim S. M. A., Balan A., Baran D., Toppare L.: Multichromic polymers of benzotriazole derivatives: Effect of benzyl substitution. Electrochimica Acta, **56**, 2263–2268 (2011).
DOI: 10.1016/j.electacta.2010.11.052

[59] Haynes W. M.: CRC handbook of chemistry and physics. CRC Press, Boca Raton (2014).

[60] Sonmez G., Meng H., Wudl F.: Organic polymeric electrochromic devices: Polychromism with very high coloration efficiency. Chemistry of Materials, **16**, 574–580 (2004).
DOI: 10.1021/cm0301773

eXPRESS Polymer Letters Vol.9, No.6 (2015) 509–524
Available online at www.expresspolymlett.com
DOI: 10.3144/expresspolymlett.2015.49

Enhanced thermal and mechanical properties of poly(trimethylene terephthalate-*block*-poly(tetramethylene oxide) segmented copolymer based hybrid nanocomposites prepared by *in situ* polymerization via synergy effect between SWCNTs and graphene nanoplatelets

S. Paszkiewicz[1*], *A. Szymczyk*[2], *K. Livanov*[3], *H. D. Wagner*[3], *Z. Rosłaniec*[1]

[1]West Pomeranian University of Technology, Institute of Material Science and Engineering, Piastow Av. 19, PL-70310 Szczecin, Poland
[2]West Pomeranian University of Technology, Institute of Physics, Piastow Av. 19, PL-70310 Szczecin, Poland
[3]Department of Materials and Interfaces, Weizmann Institute of Science, 76100 Rehovot, Israel

Received 9 October 2014; accepted in revised form24 December 2014

Abstract. Graphene nanoplatelets/single walled carbon nanotubes/poly(trimethylene terephthalate-block-poly(tetramethylene oxide) segmented copolymer (GNP/SWCNT/PTT-PTMO) hybrid nanocomposites were synthesized via *in situ* polymerization. A remarkable synergistic effect between GNPs and SWCNTs on improving thermal and mechanical properties of nanocomposites based on segmented block copolymers was observed. Heterogeneous structure of the PTT-PTMO allowed for a better and more uniform distribution of both types of nanoparticles and stabilized the structure in question. This enabled us to observe a so-called 'synergistic effect', caused by the use of mixture of carbon nanotubes and graphene nanopletelets, on the enhancement of thermal and mechanical properties of the obtained polymer. In order to ascertain the influence of mentioned carbon nanostructures on the nano-phase-separated structure of the synthesized PTT-PTMO block copolymers, differential scanning calorimetric (DSC) and dynamic mechanical thermoanalysis (DMTA) measurements were performed. Scanning electron microscopic (SEM) and transmission electron microscopic (TEM) images of the PTT-PTMO nanocomposites displayed that hybrid nanofillers exhibited better distribution and compatibility than SWCNTs and GNPs did individually. The tensile modulus of 0.5SWCNT/0.1GNP/PTT-PTMO composites was 68% higher than that of the PTT-PTMO alone, compared to only a 10 and 28% increase in tensile modulus for 0.3GNP/PTT-PTMO and 0.3SWCNT/PTT-PTMO composites respectively (the highest concentration when single nanofiller was added).

Keywords: *nanocomposites, nanomaterials, mechanical properties, thermal properties, material testing*

1. Introduction

The field of nanocomposite and polymer nanocomposite research is currently one of the most rapidly developing domains of cognitive work and applied engineering. The materials in question are essentially complex systems with two or more phases (continuous and dispersed) with an explicit separation surface. The studies on interfacial interactions at the nano level which affect the composite's properties are among the most important subjects of research and development in the field of material science today [1, 2].

Up to and including now, nanocomposites enriched by an addition of carbon nanotubes have sparked great interest among scientists and innovative research groups [3]. Same has been the case for

*Corresponding author, e-mail: spaszkiewicz@zut.edu.pl

graphene, an allotropic form of carbon discovered in 2004, existence of which was earlier only predicted by complex theoretic models. Graphene itself is a one atom thick, two-dimensional (2D) sheet composed of sp^2 carbon atoms arranged in a honeycomb lattice [4] with a carbon–carbon bond length of 0.142 nm [5, 6]. It has proven to have a variety of exceptional intrinsic characteristics among which high electron mobility at room temperature (250 000 $cm^2/(V{\cdot}s)$) [7, 8], (where, unlike in the case of CNTs, chirality does not impede it's electrical conductivity), exceptional thermal conductivity (5000 W/(m·K)) [9], and superior mechanical properties with Young's modulus of ~1 TPa and ultimate strength of 130 GPa [8] can be distinguished. Aforementioned characteristics, along with an extremely high surface area (theoretical limit: 2630 m^2/g) and gas impermeability [10], demonstrate graphene's unique potential for improving electrical, mechanical, thermal and gas barrier properties of polymers [11, 12]. Taking all above into consideration, a simultaneous introduction of two types of carbon nanofillers such as graphene (a plate filler – 2D) and CNTs (a fibrous/linear filler – 1D) may seem desirable from the standpoint of their influence on electrical and mechanical qualities.

A controlled distribution of both nanoplatelets and linear nanoparticles throughout a polymer matrix may result in obtaining specified physical characteristics, most important being the enhancement of mechanical properties and obtaining electrically conductive materials. All at a very low total concentration of both nanofillers. This claim is substantiated by several cases i.e. thin polymer films have been fabricated from a mixture of single walled carbon nanotubes (SWCNTs) and multi walled carbon nanotubes [13, 14] and from a mixture of SWCNTs and carbon fibers [14]. In each mentioned case the examined samples displayed an array of significantly improved properties. Furthermore, another recent research has looked at the mixtures of oxidized nanotubes and graphene oxide [15]. Finally, Khan *et al*. [16] prepared hybrid films comprised of single walled carbon nanotubes and nano-graphite. It has been demonstrated that these hybrids displayed mechanical and electrical properties that were superior to those of either nanotube-only or graphene-only films.

Latest literature on the subject indicates that it was not yet possible to fully utilize the potential of applying a mixture of carbon nanotubes and graphene to observe a so-called 'synergistic effect' which in theory should result in a significant enhancement of properties of obtained materials. Indeed, a remarkable synergistic effect between multi-graphene platelets (MGPs) and multi walled carbon nanotubes (MWCNTs) causing an improvement of mechanical properties and thermal conductivity in epoxy composites has been studied [17]. However, obtaining similar results for thermoplastic polymer composites remains an unresolved and thus a noteworthy subject, hence it is widely undertaken by many research groups. Therefore, the addition of carbon nanoparticles to segmented block copolymers, composed of both flexible and rigid segments, seems particularly interesting as they demonstrate a behaviour similar to that of thermoplastic elastomers. Due to their excellent mechanical qualities, like strength and elastic properties in a wide temperature range, multiblock poly(ether–esters) (PEEs) have been intensely studied [18, 19]. A recent study on a novel family of polyester thermoplastic elastomers based on poly(trimethylene terephthalate) (PTT) has been conducted [20, 21]. The influence of organoclay [22], carbon nanotubes [23] and graphene oxide [24] on the structure and physical properties of PTT-PTMO copolymers has been previously described. This type of segmented block copolymers, based on poly(trimethylene terephthalate) (PTT) as rigid segments and polyether (PTMO) as flexible segments, displays a variety of remarkable qualities such as low glass transition temperature (T_g), high melting temperature of rigid phase (T_m) and a temperature independent rubbery plateau. An addition of carbon nanoparticles in mentioned block copolymers may influence the phase separation thus changing the elastic properties of the used polymer matrix. It is anticipated that the heterogeneity of the PTT-PTMO structure will allow for its stabilization and a better and more uniform dispersion of nanoparticles. Although the phase size of polyester thermoplastic elastomers is greater than the size of nanoparticles, it is believed that the multiphase structure of block copolymers will significantly improve both thermal and mechanical characteristics. Moreover, it will allow to observe a synergistic effect between carbon nanotubes and graphene nanoplatelets on properties enhancement

This work is a part of a wider project with an objective to fabricate electrically conductive polymer

nanocomposites containing carbon nanoparticles [25]. In this study, PTT- PTMO based nanocomposites with hybrid fillers comprising of SWCNTs and GNPs were developed in order to enhance thermal stability and mechanical characteristics. The thermal and mechanical properties of the obtained nanocomposites were thoroughly evaluated and favourably compared with those of neat block copolymer and those containing either SWCNTs or GNPs alone.

2. Experimental section

2.1. Materials

The single walled carbon nanotubes KNT 95 (SWCNTs) were purchased from Grafen Chemical Industries (Grafen Co., located in Ankara, Turtkey) a leader in the field of fabrication and application of carbon nanomaterials. According to manufacturers' data: diameter: <2 nm, electrical conductivity (*EC*): >100 S/cm, length: 5–30 μm, purity: >95%, surface area: 380 m^2/g. Graphene nanoplatelets (<1 nm) was purchased from ANGSTRON Materials (Dayton, Ohio, USA), it was bought in the form of a powder with less than three graphene layers and *x–y* dimensions of up to 10 μm. The carbon content is ~97.0%, and the oxygen content is ~2.10%. Graphene nanoplatelets have a specific surface area of 400–800 m^2/g and a true density of ≤2.20 g/cm^3.

The following materials were used in the course of fabrication of the PTT-PTMO block copolymer and PTT-PTMO/carbon nanoparticles nanocomposites: dimethyl terephtalate (DMT, Sigma-Aldrich) and poly(tetramethylene oxide) glycol with molecular mass of 1000 g/mol (PTMG, Terathane 1000, DuPont, USA) were used as received. 1,3-propanenediol (PDO, Sigma-Aldrich) was distilled before use. Tetrabutyl orthotitaniate (TBT, Fluka) was used as catalyst in transesterification and polycondensation. Irganox 1010 (Ciba-Geigy, Switzerland) was used as antioxidant.

2.2. Synthesis of PTT-PTMO based nanocomposites

Poly(trimethylene terephthate-*block*-poly(tetramethylene oxide) (PTT-PTMO) segmented block copolymer based nanocomposites with carbon nanotubes and/or graphene nanoplatelets were prepared by *in situ* polymerization according to a procedure described earlier for nanocomposites with MMT [22] and GO [24]. The PTT-PTMO block copolymer with the content of 50 wt% of PTT rigid segments and 50 wt% of PTMO soft segments was used as nanocomposite polymer matrix. The process of *in situ* polymerization was preceded by a stage of nanofillers dispersion. For that purpose a specified amount of graphene nanoplatelets was mixed in a liquid substrate (1,3-propylene glycol) during a 30 min period, alternately using a high speed stirrer and vibrations of an ultrasound stirrer. Subsequently, for the purpose of greater separation of graphene sheets an ultrasonic washer was used for a period of 8 hours. To a so prepared mixture of graphene nanoplatelets, in the case of hybrid nanocomposites, a specified amount of carbon nanotubes was added. However, due to the high fragility of nanotubes only an ultra-high speed stirrer high (Ultra-Turrax® T25) and ultrasonic homogenizer (*Sonopuls* HD 2200, Bandelin) were used in order to prepare their dispersion in an appropriate manner. A ready dispersion was then put into a polycondensation reactor (Autoclave Engineers, Pennsylvania, USA), preheated to 80°C, along with dimethyl terephtalate (DMT) and a first portion of catalyst. First stage of the reaction, the transesterification process, was performed in a 160–185°C temperature range. The course of the reaction was controlled by observing the secretion of its by-product – methanol. When its amount reached about 90% of the quantity computed by means of stoichiometric calculations, the second stage of synthesis, being the polycondensation process, was commenced. For this purpose PTMO mixed with thermal stabilizer (Irganox 1098), along with the second portion of catalyst were inserted. The temperature of the reaction was then gradually increased up to 250°C. However, unlike the first stage which was performed under atmospheric pressure, the polycondensation stage was carried out under reduced pressure (~20 Pa). In this case, the course of the reaction was monitored by observing the stirrer's torque. When the polymer/nanocomposite melt reached a high molecular mass, it was then extruded in the form of a thin wire. It was subsequently granulated and subjected to injection moulding procedure.

2.3. Preparation of test samples

The dumbbell shaped samples for density, DMTA, SEM and tensile tests were obtained using a Boy 15 (Dr BOY GmbH&Co., Germany) injection moulding machine with parameters as follows: injection pressure 55 MPa, melt temperature 225°C, mould temperature 30°C, holding down pressure of 20 MPa

for 15 s and cooling time 10 s. Prior to performing the above mentioned measurements, the dumbbell shaped samples were annealed at 80°C for a period of 2 h.

2.4. Methods of characterization

The intrinsic viscosity [η] of the obtained samples was determined using a phenol/1,1,2,2-tetrachloroethane mixture (60/40 by weight) at 30°C. The concentration of polymer in the solvent amounted to 0.5 dL/g. The measurement was performed using a capillary viscometer Ubbelohde (type Ic, K = 0.03294). In order to remove the influence of the nanofiller on the measured values, a procedure described earlier in [22, 25–27] was used.

Density measurement (d) was performed using a hydrostatic scales (Radwag WPE 600C, Poland), calibrated using working standards of known density.

The melt viscosity of the samples was measured using ARES rheometer (Rheometric Scientific Inc., USA). The measurement was performed at 220°C in frequency range 0.1–50 Hz, in a parallel-plate fixture (diameter = 25 mm) with a gap distance of 2 mm.

The structure of nanocomposites was observed using scanning electron microscopes (SEM, JEOL JSM 6100; SEM ULTRA-55 Zeiss and SEM SUPRA-55 VP Zeiss). Prior to testing, the samples were cryofractured in liquid nitrogen, and then vacuum coated with a thin gold film. SEM images were collected with an In-Lens detector at an acceleration voltage of 5 kV and working distance of 5–6 mm. Transmission electron microscopic (TEM) analysis was carried out by a PHILLIPS CM 120 Electron Microscope using an acceleration voltage of 80 kV. The specimens used in TEM examination (thickness about 100–150 nm) were obtained/cut from the central part of the dumbbell shaped sample using Reichert Ultracut R ultramicrotome with a diamond knife. The procedure was carried out only after the sample had been immersed in liquid nitrogen. The direction of the cut was perpendicular to the direction of flow in the mould.

Thermal and thermo-oxidative stability of investigated polymer nanocomposites were evaluated by thermogravimetry (TGA 92-16.18 Setaram) using the system to measure the simultaneous TG-DSC. Measurements were carried out in inert atmosphere (argon) an oxidizing atmosphere i.e. dry, synthetic air (N_2:O_2 = 80:20 vol%). The study was conducted at a heating rate of 10°C/min in the temperature range 20–700°C. Measurements were conducted in accordance with the principles contained in the PN-EN ISO 11358:2004.

The dynamic mechanical thermal (DMTA) measurements were performed using a Polymer Laboratories MK II apparatus working in a bending mode at a frequency of 1 Hz in a temperature range from –100°C to polymer melt temperature and heating rate of 3°C/min. Dynamic mechanical thermal analysis comprised of measurements of E' constituents (storage modulus) and E'' (loss modulus) complex elastic modulus and mechanical loss factor $\tan\delta = (E''/E')$. It is one of the relaxation methods, which allows to ascertain the structure and phase transformation of the researched materials. The examined sample is subjected to a sinusoidal alternating causing its' deformation, the properties are determined on the basis of modulus changes and the ability of attenuation as a function of temperature and frequency of load changes. Temperatures of α-relaxation (T_α) and β-relaxation (T_β) were designated from the maximum of the loss modulus change curve (E'') and the loss factor tangent ($\tan\delta$) of temperature curve.

Differential scanning calorimetry (DSC) measurements were carried out using a TA Q100 instrument under a nitrogen atmosphere in a temperature range from –100 to 250°C at the heating and cooling rate of 10°C/min and sample weight of 10±0.2 mg. Each DSC testing cycle consisted of heating, cooling and repeating of the scans. The first cooling and second heating scans were used to determine the melting and crystallization peaks. The heat of fusion has been determined by integration of the normalized area of melting endotherm. The glass transition temperature (T_g) of the polymer samples was taken as the midpoint of the change in heat capacity. The degree of crystallinity of the sample (X_c) was calculated using Equation (1):

$$X_c[\%] = \frac{\Delta H_m}{\Delta H_m^0} \tag{1}$$

where ΔH_m^0 is the enthalpy change of melting for a 100% crystalline sample, for PTT equals to 146 J/g [28] and ΔH_m is derived from melting peak area on DSC thermogram.

Tensile measurements were performed on an Instron 5566 universal tensile testing frame, equipped with a 5 kN Instron load cell, a contact optical long travel extensometer and the Bluehill 2 software. Pneu-

matic 1 kN Instron side action grips were used to clamp the test samples. The measurements were carried out at room temperature using a cross-head speed of 100 mm/min and a grip distance of 20 mm. The tensile properties, being the Young's modulus, yield stress and yield strain, stress and elongation at break, were determined using injection moulded dumbbell-shaped bars (ISO 37 type 3). The results for each polymer are based on data collected from 6 samples (per polymer), for which the mean values and standard deviations were calculated. Moreover, the tensile deformation recovery properties of the samples were investigated. The dumbbell sample was stretched to a predetermined strain at a speed of 100 mm/min at room temperature, and then the imposed strength was released. The residual strain was then measured to calculate the deformation recovery rate. The predetermined strain of 100% was utilized in our testing.

3. Results and discussion

3.1. Rheological properties

A series of hybrid nanocomposites based on multiblock poly(ether-ester) copolymer with PTT as a rigid segment were synthesized via *in situ* polymerization. The values of intrinsic viscosity, melt viscosity and density (Table 1) are dependent on the sample composition. The measured values of intrinsic viscosity for PTT-PTMO copolymer (1.325 dL/g) and PTT-PTMO hybrid nanocomposites (1.299–1.322) [dL/g] (for three hybrids with increasing content of SWCNTs) suggest that molecular weights of studied polymers should be reasonably high. The value of [η] decreased slightly along with addition of nanofillers. However, an increase was observed together with a rise in number of SWCNTs and graphene platelets.

It can clearly be seen that the addition of SWCNTs strongly affected the melt viscosity of PTT-PTMO nanocomposites (Figure 1). On the other hand however, no such behaviour was observed when graphene nanoplatelets were added to the polymer (Table 1). A much stronger effect of the addition of carbon nanotubes on the viscosity of the composition was observed when compared to the hybrid nanocomposite PTT-PTMO/0.1 SWCNTs+0.3 GNPs with the same amount of SWCNTs (0.1 wt%). Same was observed for the nanocomposite with 0.3 wt% of SWCNTs. It can therefore be concluded, that in case of PTT-PTMO hybrid nanocomposites, the mixture of both nanofillers affected the polymer's melt viscosity much stronger than either graphene or nanotubes alone (Figure 1). A similar effect was noticed in the case of nanocomposites based on polycarbonate with carbon black/carbon nanotube systems [29]. It has also been observed that an increase in pure MWCNT/CB content leads to respectively highest/lowest increase rate of melt viscosity. Additionally, the melt viscosity value for composites with mixed filler systems were in between those of pure/singe fillers. In the case described herein, addition of carbon nanoparticles with a 0.5 wt% nanotube content caused a substantial increase in viscos-

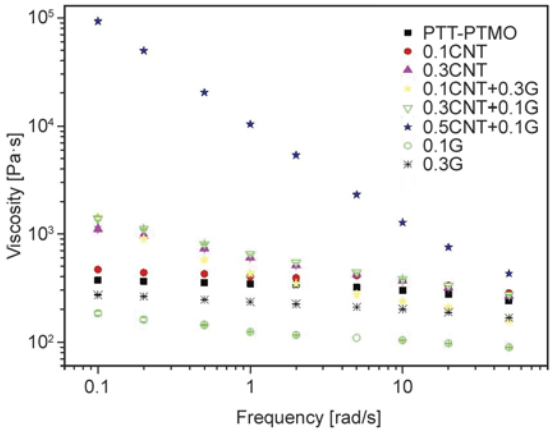

Figure 1. Melt viscosity versus frequency for neat PTT-PTMO and PTT-PTMO/SWCNTs+GNPs nanocomposites at temperature of 220°C

Table 1. Intrinsic viscosity, density and melt viscosity of PTT-PTMO/SWCNTs+GNPs nanocomposites

Sample	Nanofiller [wt%]	[η] [dL/g]	d [g/cm^3]	Melt viscosity^M [Pa·s]
PTT-PTMO	0	1.325	1.174	340.02±0.76
PTT-PTMO/0.1 G	0.1	1.315	1.174	124.38±0.93
PTT-PTMO/0.3 G	0.3	1.327	1.175	232.66±0.84
PTT-PTMO/0.1 SWCNT+0.3 G	0.1+0.3	1.299	1.173	428.76±1.22
PTT-PTMO/0.3 SWCNT+0.1 G	0.3+0.1	1.319	1.177	648.65±1.31
PTT-PTMO/0.5 SWCNT+0.1 G	0.5+0.1	1.322	1.176	10 409.07±18.84
PTT-PTMO/0.1 SWCNT	0.1	1.325	1.181	398.52±1.08
PTT-PTMO/0.3 SWCNT	0.3	1.324	1.176	602.11±1.60

[η] – intrinsic viscosity; *d* – density; η – melt viscosity measured at 220°C at 1 Hz

ity value (over a 30 time increase relative to neat copolymer). The aforementioned concentration of nanofillers should be considered as a critical value for the used *in situ* polymerization method. When surpassed, extrusion of polymer from the reactor would be impossible. This indicates that despite an enhancement of mechanical and thermal qualities which is caused by the synergistic effect between SWCNTs and GNPs, the system comprised of 0.5 SWCNTs+0.1 GNPs provides the highest melt viscosity values along with the greatest improvement in tensile properties and thermal stability. However, such a high rise in viscosity may prove unsuitable for processing purposes.

The density of PTT-PTMO hybrid nanocomposites has increased slightly with the addition of nanofillers. Obtained density values depend strongly on the crystallite content as well as on the content of the nanofiller in the polymer matrix. As the obtained hybrid nanocomposites displayed density values comparable to those of nanotubes only, it may be concluded that an addition of nanotubes alone has a greater impact of the density.

3.2. Morphology

Single walled carbon nanotubes and graphene nanoplatelets used in this study were characterized using scanning electron microscopy (SEM), which provided visual information on the ratio of carbon nanofiller to carbonaceous impurities (Figure 2a and 2b). In case of SWCNTs it was presumed that fiber-like areas correspond to bundled SWCNTs, while the other particles and lumps correspond to carbonaceous impurities. Figure 2b displays the photomicrograph of the loose structures of graphene nanoplatelets in sequentially larger magnifications. Obviously, in the case of graphene nanoplatelets loose structures containing multi-pores can be observed. This micrograph also suggests the thickness of the graphene platelet layer is less than 100 nm.

As mentioned in the introduction, the natural tendency of carbon nanostructures to agglomerate (due to van der Waals interactions) is the underlying reason for difficulties in preparation of composites based on thermoplastic matrices, which can be characterized by a high degree of homogeneity of the nanophase. Effectiveness of using the *in situ* polycondensation method, preceded by a dispersion of the carbon nanotubes and/or graphene nanoplatelets in a substrate, can be assessed qualitatively by means of structure analysis using microscopic techniques. Taking into consideration the development of methods of *in situ* polymer composite preparation, it was assumed that dispersing SWCNTs/GNPs in one of the substrates by means of mechanical forces and vibrations at the ultrasonic frequency, and then carrying out the synthesis of the polymer matrix in the presence of the nanoparticles, would allow to obtain uniform distribution in the mass. The uniform distribution itself is owed to intercalation of growing polymer chains between nanotube bundles and graphene nanoplatelet, causing them to separate even further. One of the main problems encountered during dispersion of CNTs, limiting the effective use of carbon nanotubes as nanofillers in a polymer matrix, is the strong inter-tube attraction between CNTs. Many approaches to overcome this issue have been made, however they mostly result in an excessive modification or even damage to the unique morphology of CNTs. An efficient alternative allowing to tailor the polymer/CNT interface and at the same time preserving the integrity of the tubes is mixing them together with a different shaped nanofiller (i.e. platelike shape). In the discussed study, it was assumed that application of graphene nanoplatelets might be a suitable solution. A uniform distribution of SWCNTs on graphene's surface should cause a synergistic effect and thus enable them to act together as stronger reinforcing agent for the polymer, resulting in a substantial enhancement of thermal and mechanical properties (Figure 2c–2g). The evenly spaced bright dots and lines are attributed to the ends and edges of the broken SWCNTs/GNPs covered in PTT-PTMO. They are clearly visible due to their high electrical conductivity. A good connection between graphene nanoplatelets, contained in the SWCNTs and GNPs mixture, along with a good compatibility with the polymer matrix were due to residual oxide groups on GNPs' surface [25]. The dual-filler strategy appears to yield a more efficient dispersion of SWCNTs+GNPs/PTT-PTMO. The SEM images of the PTT-PTMO/0.3 SWCNT+0.1 GNPs are shown in Figure 2e–2g. Both the SWCNTs and GNPS show fairly good distribution which can be seen in Figure 2e and 2g. The graphene nanosheets in Figure 2e appear to show better dispersion than those previously observed when only graphene was added to copolymer matrix (incompletely exfoliated structure of nanocomposites based on PTT-PTMO with

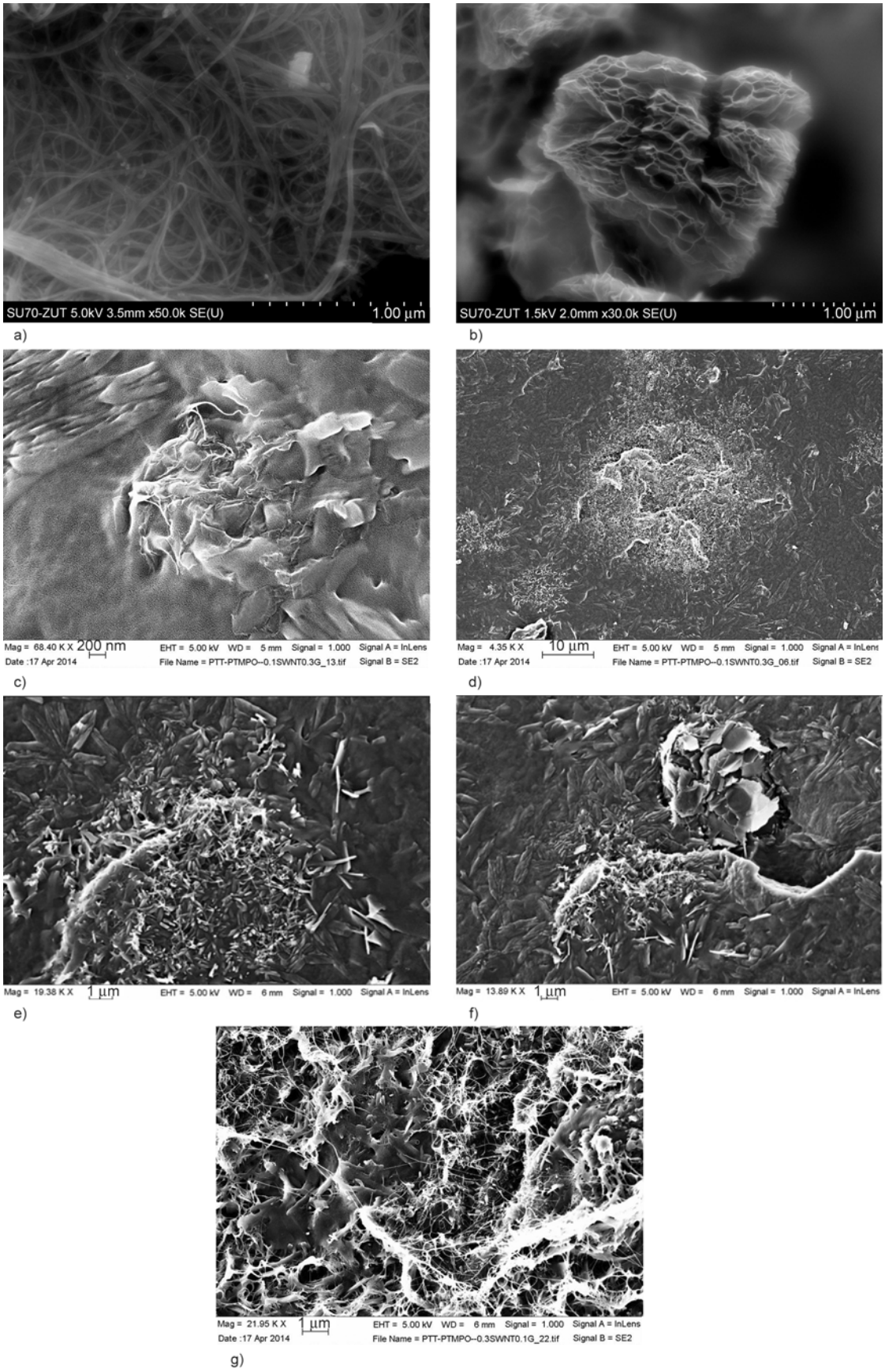

Figure 2. (a) and (b) SEM micrographs of SWCNTs and GNPs as received; (c) and (d) SEM micrographs of PTT-PTMO/0.1 SWCNTs+0.3 GNPs hybrid nanocomposites; (e)–(g) SEM micrographs of PTT-PTMO/0.3 SWCNT+ 0.1 GNPs hybrid nanocomposites

GNP observed in TEM micrographs, Figure 3a, 3b). A detailed study on the influence of GNPs and GO on the morphology of PTT-PTMO matrix was previously described in [25] and [24] respectively. In that particular case this indicates that an addition of SWCNTs improves the dispersion of graphene nanoplatelets, which agrees with the tensile results which exhibit an improvement in mechanical qualities. However, because of the van der Waals interactions the graphene sheets tend to form irreversible agglom-

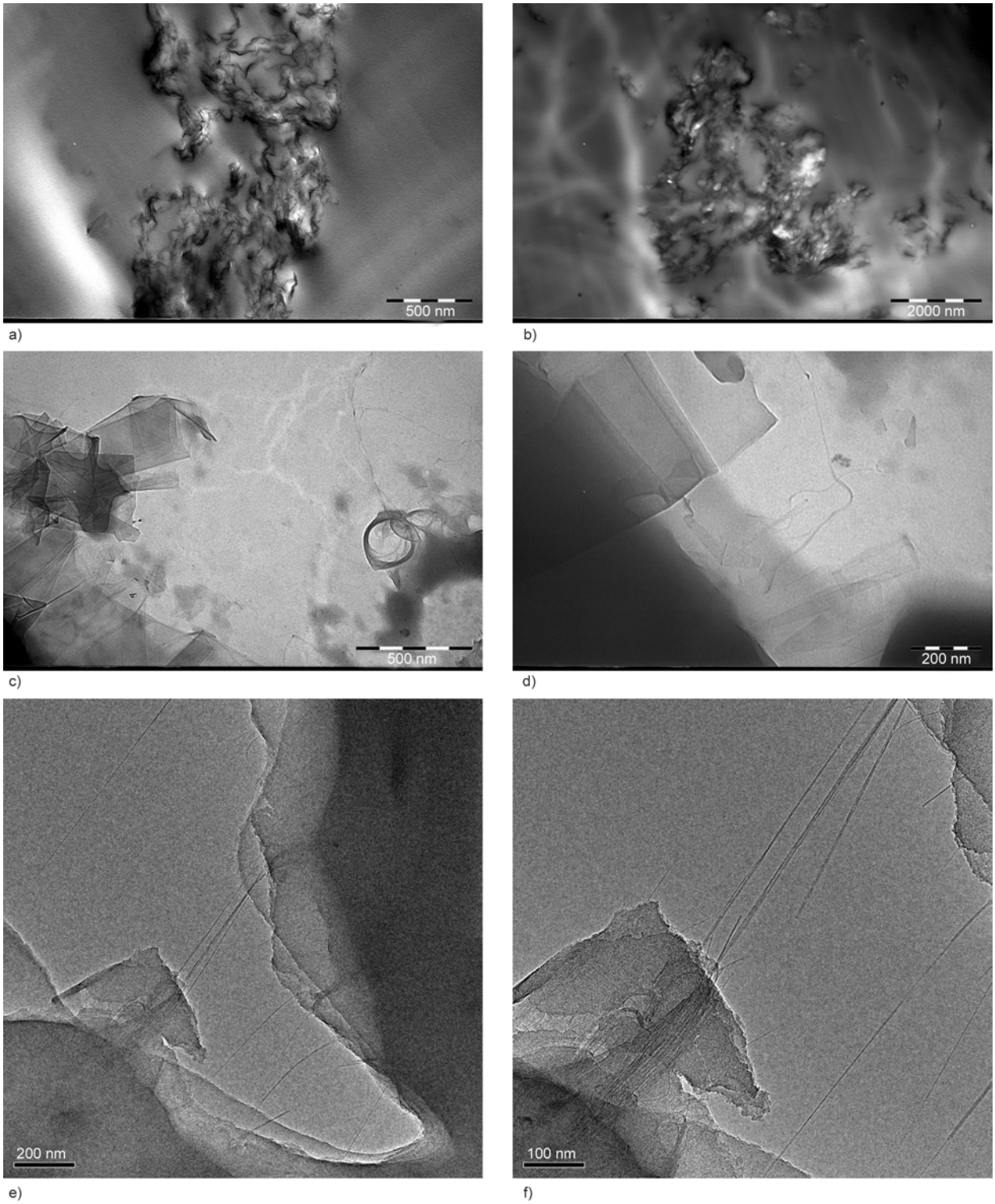

Figure 3. (a)–(d) TEM micrographs of PTT-PTMO/GNPs nanocomposites with: (a) 0.1 GNPs, 75 000×, (b) 0.3 GNPs, 20 000×, (c) and (d) TEM micrographs of PTT-PTMO/0.1 SWCNT+0.3 GNPs nanocomposites at (c) 100 000× and (d) 150 000×; (e) and (f) TEM micrographs of PTT-PTMO/0.3 SWCNT+0.1 GNPs nanocomposites (e) 150 000× and (f) 175 000×

erates and even restack to form graphite (Figure 2f). Additionally, the SEM images of PTT-PTMO/SWCNT+GNPs in Figures 2g and 2h show that the SWCNTs and graphene nanoplatelets form a kind of network structure. The SWCNTs appear to a have good affinity for GNPs. Aforementioned formation of nanofiller-nanofiller interactions may explain the good thermal stability and mechanical characteristics of PTT-PTMO/0.3 SWCNT+0.GNPs. The dispersion state in the composites with hybrid CNTs/graphene particles was further confirmed by transmission microscopy.

The TEM images (Figure 3c and 3d, with two different magnifications of PTT-PTMO/0.1 SWCNTs+0.3 GNPs) display the real distribution of conductive fillers in the respective nanocomposites. They may provide valuable insight into the mechanisms behind the synergy between the hybrid fillers of CNT and graphene platelets in enhancing the conductivity [25] of nanocomposites. Figure 3c depicts both randomly dispersed individual SWCNTs and a round SWCNT agglomerate, also well-dispersed graphene sheets can be seen. In some places carbon nanotubes and graphene plates seem to be connected to one another. This can be better seen in Figure 3d where the dispersion of both nanofillers is even better and only nanotubes attached to graphene planes were observed.

In order to examine the dispersion of SWCNTs/GNPs (with 0.3 wt% of SWCNTs and 0.1 wt% of GNPs) in the polymer hybrids in detail, TEM studies were carried out. They allow a qualitative understanding of the internal structure through direct observation. Typical TEM photographs of hybrids with 0.3 wt% of SWCNT and 0.1 wt% of GNPs are shown in Figure 3e and 3f. They show that both nanofillers were well dispersed in the polymer matrix, meaning that single nanotubes along with homogenously distributed GNPs were observed. Interestingly, the 'pull-out' mechanism of SWCNTs has been also shown as carbon nanotubes counteracted the break of the polymer matrix, which can clearly be seen at a higher magnification. As observed in the figures, the CNT-to-CNT and CNT-to-GNPs interactions by the surface contact (or tunnelling) should increase the mechanical strength of the composite, which will be discussed further.

3.3. Phase structure

An introduction of a carbon nanofiller into the multiphase system (block copolymer) may initiate the formation of a heterophase structure. The newly formed structure stabilizes the distribution of nanoparticles in the polymer matrix. The poly(ether-ester) multiblock copolymer composed of PTT as rigid segment and poly(tetramethylene oxide) PTMO as flexible segment with hardness of 51 Shore D [21, 23], was used as polymer matrix in nanocomposites described herein. During cooling from the melt, mentioned segmented block copolymer's microphase separated into high meting crystalline PTT hard domains and relatively low glass transition soft PTMO-rich domains. The elastic characteristics of this segmented block copolymer is a consequence of aforementioned microseparated phase structure, which is a result of the chemical nature and incompatibility between the rigid and flexible blocks/segments build into the polymer chains. Here, in order to investigate the effect of the addition of carbon nanostructures, which differ in shape, on the nanoseparated phase structure of the synthesized PTT-PTMO block copolymers, DSC and DMTA measurements were performed.

Forming of above mentioned separation occurs together with the formation of a soft (PTMO-rich) phase and a hard semicrystalline polyester (PTT) phase with characteristic temperatures T_g and T_m, respectively. Existence of such a structure was confirmed by DSC measurement (Figure 4a and 4b). Since the size of domains of the hard phase (few nm, [20]) is comparable to the size of SWCNTs and graphene nanoplatelets which were used to obtain the hybrid nanocomposites, it is difficult to explain the influence of hybrid nanofillers on the microstructure of the resulting nanocomposites. The glass transition temperatures (T_{g1} and T_{g2}) of nanocomposites were not affected by the incorporation of SWCNTs together with graphene nanoplatelets. Both nanofillers, despite good interactions with the polymer matrix (confirmed by SEM analysis), showed no effect on glass transition temperatures of both soft (T_{g1}) and amorphous polyester phase (T_{g2}).

In contrast, the crystallization process was stronger affected in the obtained nanocomposites. A notable rise in the crystallization temperature has been observed along with an increase in content of both

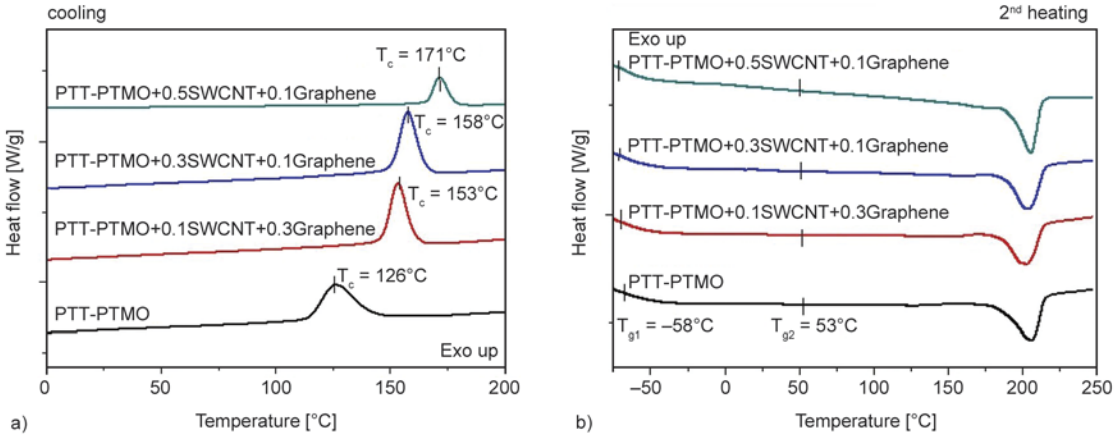

Figure 4. DSC thermograms for PTT-PTMO and PTT-PTMO/SWCNTs+GNPs nanocomposites during the cooling (a) and 2nd heating (b)

SWCNTs and graphene nanoplatelets. The highest shift toward higher T_c temperature was observed in the case of PTT-PTMO/0.5 SWCNT+0.1 GNP, the value in question reached as high as 45°C. Surprisingly, a stronger influence on crystallization behaviour seems to occur in the presence of carbon nanotubes in PTT-PTMO matrix. It can be well observed for hybrid nanocomposites where, with increasing loading of SWCNT (from 0.1 to 0.5), an increase in T_c was observed. However, all values of ΔH_c were comparable to neat PTT-PTMO segmented block copolymer. In addition, the melting temperature remains unchanged for all nanocomposites. Based on the obtained results it can be also concluded that the composition of SWCNT:GNP of 5:1 accelerated the rate of crystallization probably due to larger amount of crystallization agents. It can clearly be seen that the T_c value increased along with an increase in SWCNTs content. The degree of crystallinity of obtained nanocomposites estimated basis DSC changes significantly (1–2%) compared to neat block copolymer (Table 2). At first slight a decrease can be observed, but with increasing loading of both nanofillers a rise in comparison to neat PTT-PTMO emerges.

The DMTA analysis (Figure 5) has shown that PTT-PTMO based nanocomposites are multiphase systems having one crystalline and two amorphous phases which confirmed the results obtained from DSC measurements. On the storage modulus E' curve at low temperatures an inflection (corresponding to the β_1 maximum in the loss modulus E'') associated with the glass transition of the soft polyether-rich phase can be observed. A decrease and a subsequent rise of the storage modulus value in the temperature range 20–120°C is related to amorphous PTT glass transition which is immediately followed by cold crystallization. (A completely amorphous PTT has a glass transition temperature of 40°C, exceeding that value will cause its crystallization). Above 20°C, the storage modulus depends on the type and content of carbon nanofiller. In the curve presenting the loss

Table 2. Thermal properties of neat PTT-PTMO and PTT-PTMO/SWCNTs+GNPs nanocomposites determined by DSC

Sample	T_{g1} [°C]	T_{g2} [°C]	T_m [°C]	ΔH_m [J/g]	T_c [°C]	ΔH_c [J/g]	x_c [%]	$T_{\beta1}$ [°C]	$T_{\beta2}$ [°C]
PTT-PTMO	–58	53	206	30.9	126	28.3	21.2	–31	43
PTT-PTMO/0.1 G	–61	52	204	28.1	149	27.3	19.2	–35	–
PTT-PTMO/0.3 G	–59	50	205	29.1	149	27.8	19.9	–36	–
PTT-PTMO/0.1 SWCNT+0.3G	–61	51	203	31.1	153	27.8	21.4	–41	70
PTT-PTMO/0.3 SWCNT+0.1G	–62	51	203	31.7	158	28.8	21.7	–41	75
PTT-PTMO/0.5 SWCNT+0.1G	–63	54	206	34.6	171	34.5	23.7	–41	60
PTT-PTMO/0.1 SWCNT	–59	50	208	29.9	155	29.9	20.5	–37	57
PTT-PTMO/0.3 SWCNT	–61	51	204	31.3	157	29.2	21.4	–40	60

T_{g1} – glass transition temperature of soft phase, T_{g2} – glass transition temperature of amorphous polyester phase, T_m – melting temperature of polyester crystalline phase; T_c – crystallization temperature of polyester crystalline phase; ΔH_m, ΔH_c – enthalpy of melting and crystallization of polyester crystals, respectively; x_c – mass fraction of crystallinity, $T_{\beta1}$, $T_{\beta2}$ – temperature of β_1- and β_2 – relaxations corresponding to the glass transition temperatures determined from maximum of tan δ

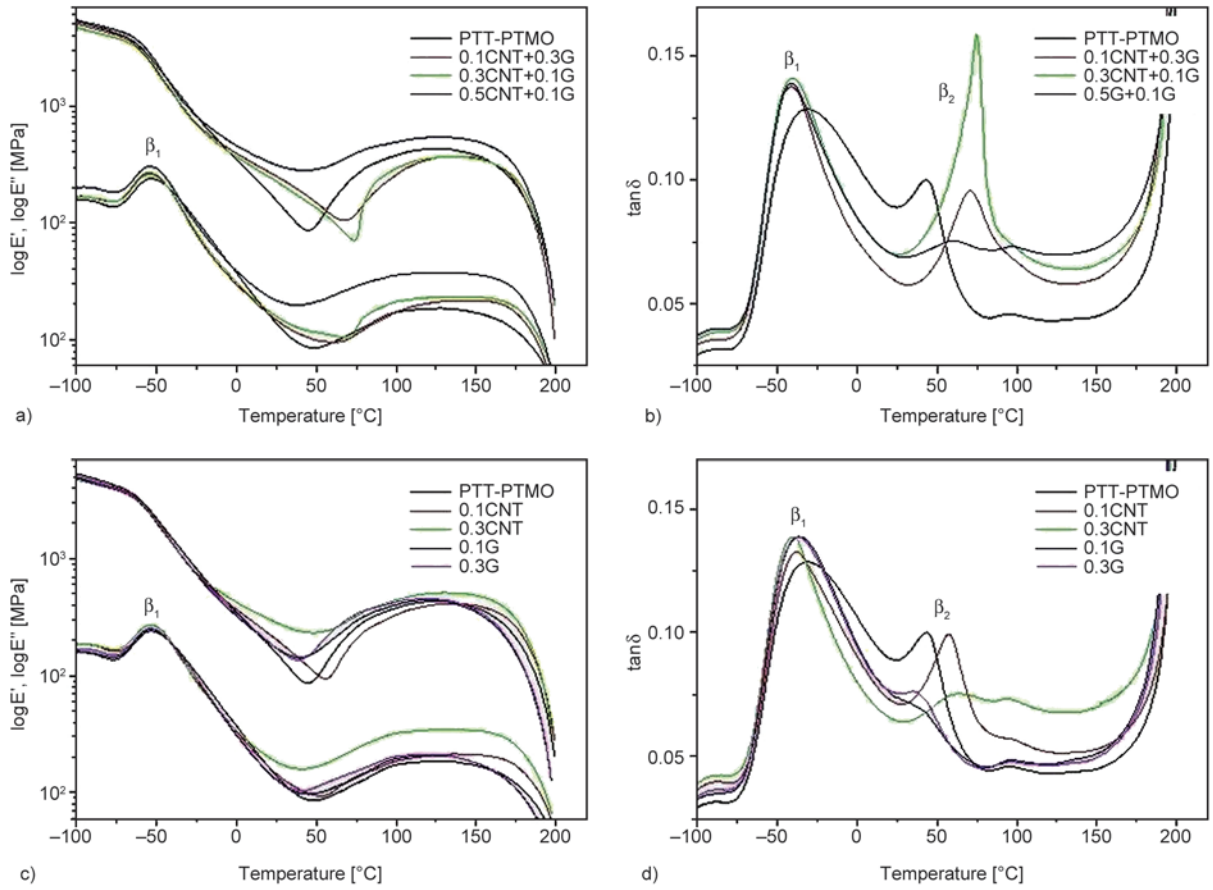

Figure 5. The dependence of storage modulus E', loss modulus E'' and tan δ on temperature for PTT-PTMO/SWCNT+G (a)–(b) and PTT–PTMO/SWCNT and PTT-PTMO/G (c)–(d) nanocomposites

factor tangent of the temperature dependency (Figures 5b, 5c), two relaxations (β_1, β_2) can clearly be seen. These relaxations are attributed to the glass transition of amorphous polyether-rich phase (β_1) and amorphous polyester phase (β_2). When a hybrid nanofiller in the form of a SWCNTs and GNPs mixture has been added (marked on the plot as *G*), a clear phase separation occurred. As a result two parts emerged, a PTMO-rich amorphous part (low temperature peak, β_1) and an amorphous PTT part (high temperature peak, β_2). Moreover, the β_1 peak has shifted towards lower temperatures and has become slimmer and narrower than the one corresponding to the neat PTT-PTMO, which proves that the presence of SWCNTs and GNPs influences the phase separation of the examined system. Also, the β_2 peak (max tan δ) has shifted towards higher temperatures and a change in its intensity can be observed, i.e. in the case of composites containing only graphene nanoplatelets (0.1 and 0.3) or (0.3 CNT, 0.5 CNT+0.1 G) a decrease of β_2 peak's intensity can be seen, which is a clear evidence for a drop in PTT chain mobility.

3.4. Thermal stability

Thermogravimetric analysis (TGA) was used to analyze the effect of the hybrid system of nanofillers (1D+2D) dispersed in PTT-PTMO block copolymer matrix on its thermal and thermo-oxidative stability. The TGA curves for PTT-PTMO/ hybrid nanoparticles nanocomposites in air and an inert (argon) atmosphere are presented in Figure 6. No improvement in thermal stability has been observed in an inert atmosphere, as compared to the neat PTT-PTMO block copolymer, but also to PTT-PTMO/SWCNTs and PTT-PTMO/GNPs nanocomposites (Table 3). What is more, a slight decrease in the temperatures of 5 and 10% weight loss ($T_{5\%}$, $T_{10\%}$) was observed. However, in an oxidizing atmosphere for all hybrid nanocomposites the noticeable improvement of thermo-oxidative stability of nanofillers has been found. When comparing the temperature of 5% weight loss for neat PTT-PTMO block copolymer and the hybrid composites, a significant shift of 24°C towards higher temperatures was observed. Interestingly enough, the addition of carbon nanofillers of different shapes and aspect ratios

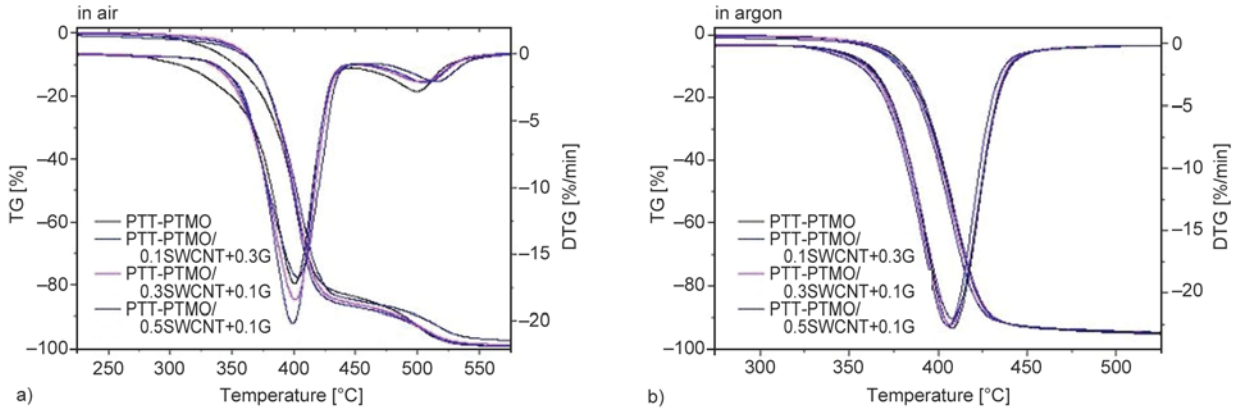

Figure 6. Weight loss and derivative weight loss versus temperature for the PTT-PTMO/SWCNTs+GNPs nanocomposites in air (a) and in argon (b) at a heating rate of 10°C/min

causes a substantial improvement in the thermo-oxidative stability of the thermoplastic elastomer in question. The thermal stability enhancement does not seem to depend upon a particular shape of the nanofiller as similar results were obtained in the case of SWCNTs and graphene nanosheets individually, as well as for the mixture of both. Apparently, both types of nanoparticles (carbon nanotubes and graphene nanoplatelets) affect the thermal stability of polymers in a similar manner. This can clearly be seen in Figure 6 where all the curves are close each other. Thus, it can be assumed that the morphology differences in PTT-PTMO/SWCNTs+GNPs nanocomposites do not appear to make a noticeable difference in the thermal stability of the nanocomposites. The possible explanation for such behaviour is that both the SWCNTs and graphene nanoplatelets have high electron affinities and as such seem to be capturing free radicals [30, 31]. Discussed TGA results suggest that by incorporating either SWCNTs or graphene nanoplatelets or the mixture of both into the polymer, its thermo-oxidative stability should be improved.

Table 3. Temperatures corresponding to 5 and 10% weight loss and the temperature at maximum of weight loss rate for the PTT-PTMO/ SWCNT+GNPs (G) nanocomposites obtained in air and argon atmosphere

Symbol	$T_{5\%}$ [°C]	$T_{10\%}$ [°C]	T_{DTG1} [°C]	T_{DTG2} [°C]
Measurement carried out in an oxidizing atmosphere				
PTT-PTMO	331	352	400	499
PTT-PTMO/0.1 G	322	342	398	500
PTT-PTMO/0.3 G	357	368	397	499
PTT-PTMO/0.1 SWCNT+0.1 G	355	368	399	507
PTT-PTMO/0.3 SWCNT+0.3 G	355	358	401	504
PTT-PTMO/0.5 SWCNT+0.3 G	350	369	403	515
PTT-PTMO/0.1 SWCNT	363	376	402	510
PTT-PTMO/0.3 SWCNT	358	372	406	515
Measurement carried out in argon				
PTT-PTMO	371	382	408	–
PTT-PTMO/0.1 G	366	383	406	–
PTT-PTMO/0.3 G	374	382	408	–
PTT-PTMO/0.1 SWCNT+0.1 G	366	377	406	–
PTT-PTMO/0.3 SWCNT+0.3 G	368	379	407	–
PTT-PTMO/0.5 SWCNT+0.3 G	367	380	409	–
PTT-PTMO/0.1 SWCNT	372	382	408	–
PTT-PTMO/0.3 SWCNT	369	380	408	–

3.5. Mechanical properties

The use of new carbon nanomaterials with excellent mechanical properties has opened a new and exciting chapter in today's material science. A better understanding of chemistry and the intrinsic properties of both graphene and carbon nanotubes, along with new and innovative approaches to polymer fabrication has led scientists to developing composites with GNPs and SWCNTs and thus creating new materials with substantially enhanced mechanical, electrical, thermal and barrier properties. Similarly to traditional composites, the range of the obtained improvements is referred to using factors such as reinforcement phase concentration, distribution in the host matrix, interface bonding and the reinforcement phase aspect ratio.

The tensile properties of the PTT-PTMO/SWCNTs+GNPs hybrid nanocomposites were examined. Typical stress–strain curves for PTT-PTMO block copolymers were plotted in Figure 7. In order to make the plots more comprehensible, the obtained data is presented in two separate figures where the results obtained for hybrid nanocomposites have been compared to those for graphene (a) and carbon nanotubes (b). A clear tendency for an increase in tensile modulus and a decrease in elongation, caused by a

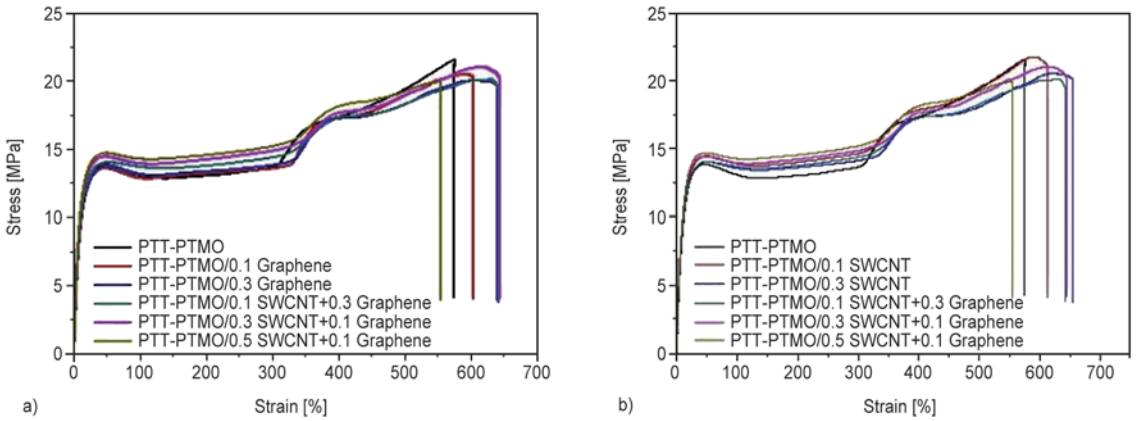

Figure 7. Representative stress-strain curves of PTT-PTMO/SWCNTs+GNPs hybrid nanocomposites (a) in comparison to PTT-PTMO/GNPs and (b) in comparison to PTT-PTMO/SWCNTs nanocomposites

rise in the hybrid system content has been observed (Table 4). Carbon nanofillers (SWCNTs and GNPs) added in small amounts to PTT-PTMO elastomer increase the tension related to deformation, limiting the free length of chains located between physical nodes of the network/matrix (they create additional physical nodes). This effect was significantly stronger when two nanofillers were used. For pristine PTT-PTMO the tensile modulus was 118 MPa. With the incorporation of up to 0.3 wt% of graphene, the tensile modulus decreased to ca. 131 MPa, which is ca. 11% more compared to neat PTT-PTMO block copolymer. However, in the case of PTT-PTMO/SWCNTs a substantial rise up to 162 MPa has been noted. The increase in the modulus was accompanied by lower values of elongation at break for nanocomposites with graphene and with 0.1 wt% of SWCNTs. Only a slight increase in εb for PTT-PTMO/0.3 SWCNT to 639% was observed. An addition of the hybrid system has further increased the modulus to 149, 178 and 212 MPa, for 0.1 SWCNTs+0.3 G, 0.3 SWCNTs+0.1 GNPs and 0.5 SWCNTs+0.1 GNPs respectively. Hybrid nanocomposite with a concentration of 0.5 wt% of nanotubes and 0.1 wt% of graphene reached a modulus value which is ca. 68% higher than the pristine elastomer. Thus, the tensile measurements revealed that the effect of hybrid nanofillers system is more pronounced on the tensile modulus. The noticeable increase in the tensile modulus reflects the reinforcement effect attained by the dispersion of the nanotubes and graphene platelets in PTT-PTMO matrix. Calorimetric studies for obtained PTT-PTMO/hybrid nanocomposites (Table 4) showed only minute differences in the polymer melt enthalpy and negligible increase in degree of crystallinity. Therefore, the improvement in the tensile properties at low nanofillers' loading observed herein, cannot be due to a change in crystallinity and is more likely caused by the presence of SWCNTs and graphene nanoplatelets next to PTT hard domains dispersed in PTMO-rich soft phase. Similar results have been also previously observed for PTT-PTMO nanocomposites with graphene oxide (GO) [24] and montmorillonite (MMT) [22].

Elongation at break, on the other hand, decreased significantly for PTT-PTMO/0.5 SWCNTs+0.1 GNPs. At the same time, a rise in the permanent set accom-

Table 4. Tensile properties of PTT-PTMO/SWCNTs+GNPs nanocomposites

Sample	E [MPa]	σ(100%) [MPa]	σ_y [MPa]	ε_y [%]	σ_b [MPa]	ε_b [%]
PTT-PTMO	118.3±1.5	12.7±0.1	13.6±0.2	44.8±0.9	20.3±0.7	625±12
PTT-PTMO/0.1 GNPs	123.0±1.3	12.8±0.1	13.4±0.2	50.4±1.3	20.3±0.1	594±12
PTT-PTMO/0.3 GNPs	131.7±4.1	13.1±0.1	13.7±0.1	49.6±0.1	19.8±0.2	594±14
PTT-PTMO/0.1 SWCNT+0.3 GNPs	149.2±2.7	13.6±0.1	14.0±0.1	49.8±0.8	19.2±0.3	634±29
PTT-PTMO/0.3 SWCNT+0.1 GNPs	178.3±6.9	13.9±0.1	14.4±0.1	48.1±1.1	20.4±0.2	642±21
PTT-PTMO/0.5 SWCNT+0.1 GNPs	212.2±6.5	14.1±0.1	14.6±0.9	47.6±1.2	18.5±1.2	542±59
PTT-PTMO/0.1 SWCNT	145.1±3.9	13.6±0.3	14.2±0.2	47.8±0.8	20.7±0.6	617±24
PTT-PTMO/0.3 SWCNT	162.5±2.5	13.7±0.1	14.1±0.1	49.7±0.5	19.9±0.2	639±13

E – tensile modulus; σ(100%) – stress at strain of 100%; σ_y, ε_y – yield stress and strain respectively, σ_b, ε_b – stress and strain at break respectively

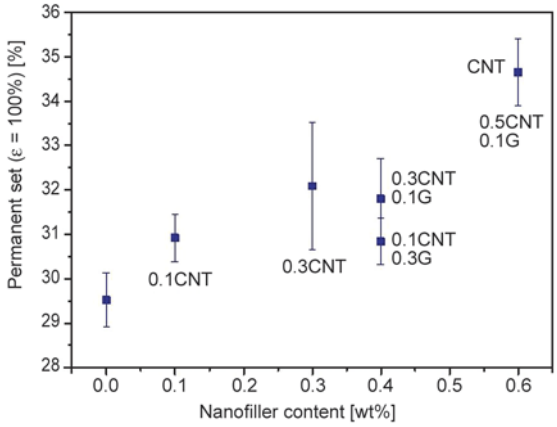

Figure 8. Permanent set accompanying the 100% deformation as a function of total content of carbon nanofillers for nanocomposites based on PTT-PTMO

panying the 100% deformation was observed in a limited reversible deformation range. Analysis of the permanent set, created after a 100% deflection for the examined PTT-PTMO composites (Figure 8) proved that content of nanofillers in the amount of up to 0.6 wt% cause only a slight deterioration of elasticity as they cause just a few percent decrease in relaxation from 100% deflection. It can be said however, that nanofillers greatly impede the elasticity, because at 0.6 wt% content an average of the permanent set increased by 20%. The synergistic toughening mechanisms of a combination of SWCNTs and graphene has been observed for PTT-PTMO block copolymer.

4. Conclusions

The present research and experiments focused mainly on the preparation and characterization of polymer composites containing SWCNTs, GNPs and hybrid systems comprising of both SWCNTs/GNPs, in which PTT-PTMO constituted the matrix. The use of *in situ* synthesis allowed to obtain composites with a high degree of homogeneity, which is a key issue for further industrial applications. At the same time, the analysis of the properties of obtained materials showed a strong effect of the addition of carbon nanotubes and graphene nanoplatelets on their structure, physical transitions, thermal stability and mechanical strength. The presence of SWCNTs and GNPs in the polymer melt during cooling substantially speeds up the crystallization process as is evidenced by a shift of the crystallization peak to up to 45°C, which was recorded for PTT-PTMO/0.5 SWCNT+ 0.1 GNP hybrid nanocomposite. The introduction of carbon nanoparticles into the polymer matrix did not have a significant effect on the thermal stability of obtained nanocomposites in an inert atmosphere. However, addition of SWCNTs and graphene nanoplatelets individually, as well as the mixture of both caused substantial enhancement of thermo-oxidative stability, shifting the beginning of the chemical decomposition temperature by 20–25°C. Remarkably, in the case of mechanical properties of presented nanocomposites a synergistic hybrid effect has been observed. The addition of carbon nanotubes together with graphene nanosheets caused an increase in strength of up to 68% for the highest concentration of nanofillers. Results of the experiments contained herein indicate a remarkable potential of the new group of materials, the polymer hybrid nanocomposites, which and might be of extreme importance for further development and possible industrial applications. Determination of the appropriate conditions for obtaining hybrid nanocomposites during the polymer matrix synthesis process is paramount in order to develop new technologies for their production on the pilot and industrial scale. Moreover, the observed positive hybrid effect in the case of segmented block copolymers will allow to lower the final price of the finished product (suitable selection of properties at the optimum price), which can be characterized by good thermal properties with, at the same time, improved mechanical properties.

Acknowledgements

This work was financially supported by National Science Center in Poland, project Preludium 2013/11/N/ST8/00404. Authors would like to thank Dr Ronit Popovitz for preparing TEM micrographs.

References

[1] Thomas S., Zaikow G. E.: Progress in polymer nanocomposite research. Nova Science, New York (2008).
[2] Wang Z. M.: Toward functional nanomaterials. Springer, New York (2009).
[3] Kingston C., Zepp R., Andrady A., Boverhof A., Fehir R., Hawkins D., Roberts J., Sayre P., Shelton B., Sultan Y., Vejins V., Wohlleben W.: Release characteristics of selected carbon nanotube polymer composites. Carbon, **1**, 33–57 (2014).
DOI: 10.1016/j.carbon.2013.11.042
[4] Kim H., Abdala A. A., Macosko C. W.: Graphene/polymer nanocomposites. Macromolecules, **43**, 6515–6530 (2010).
DOI: 10.1021/ma100572e

[5] Slonczewski J. C., Weiss P. R.: Band structure of graphite. Physical Review Letters, **109**, 272–279 (1958). DOI: 10.1103/PhysRev.109.272

[6] Soldano C., Mahmood A., Dujardin E.: Production, properties and potential of graphene. Carbon, **48**, 2127–2150 (2010). DOI: 10.1016/j.carbon.2010.01.058

[7] Novoselov K. S., Geim A. K., Morozov S. V., Jiang D., Zhang Y., Dubonos S. V., Grigorieva I. V., Firsov A. A.: Electric field effect in atomically thin carbon films. Science, **306**, 666–669 (2004). DOI: 10.1126/science.1102896

[8] Lee C., Wei X., Kysar J. W., Hone J.: Measurement of the elastic properties and intrinsic strength of monolayer graphene. Science, **321**, 385–388 (2008). DOI: 10.1126/science.1157996

[9] Balandin A. A., Ghosh S., Bao W., Calizo I., Teweldebrhan D., Miao F., Lau C. N.: Superior thermal conductivity of single-layer graphene. Nano Letters, **8**, 902–907 (2008). DOI: 10.1021/nl0731872

[10] Bunch J. S., Verbridge S. S., Alden J. S ., van der Zande A. M., Parpia J. M., Craighead H. G., McEuen P. L.: Impermeable atomic membranes from graphene sheets. Nano Letters, **8**, 2458–2462 (2008). DOI: 10.1021/nl801457b

[11] Kim H., Miura Y., Macosko C. W.: Graphene/polyurethane nanocomposites for improved gas barrier and electrical conductivity. Chemistry of Materials, **22**, 3441–3450 (2010). DOI: 10.1021/cm100477v

[12] El Achaby M., Arrakhiz F-A., Vaudreuil S., el Kacem Qaiss A., Bousmina M., Fassi-Fehri O.: Mechanical, thermal, and rheological properties of graphene-based polypropylene nanocomposites prepared by melt mixing. Polymer Composites, **33**, 733–744 (2012). DOI: 10.1002/pc.22198

[13] Hall L. J., Coluci V. R., Galvão D. S., Kozlov M. E., Zhang M., Dantas S. O., Baughman R. H.: Sign change of Poisson's ratio for carbon nanotube sheets. Science, **320**, 504–507 (2008). DOI: 10.1126/science.1149815

[14] Park J. G., Li S., Liang R., Fan X., Zhang C., Wang B.: The high current-carrying capacity of various carbon nanotube-based buckypapers. Nanotechnology, **19**, 185710/1–185710/7 (2008). DOI: 10.1088/0957-4484/19/18/185710

[15] Cai D., Song M., Xu C.: Highly conductive carbon-nanotube/graphite-oxide hybrid films. Advanced Materials, **20**, 1706–1709 (2008). DOI: 10.1002/adma.200702602

[16] Khan U., O'Connor I., Gun'ko Y. K., Coleman J. N.: The preparation of hybrid films of carbon nanotubes and nano-graphite/graphene with excellent mechanical and electrical properties. Carbon, **48**, 2825–2830 (2010). DOI: 10.1016/j.carbon.2010.04.014

[17] Yang S-Y., Lin W-N., Huang Y-L., Tien H-W., Wang J-Y., Ma C-C. M., Li S-M., Wang Y-S.: Synergetic effects of graphene platelets and carbon nanotubes on the mechanical and thermal properties of epoxy composites. Carbon, **49**, 793–803 (2011). DOI: 10.1016/j.carbon.2010.10.014

[18] Gabriëlse W., Soliman M., Dijkstra K.: Microstructure and phase behavior of block copoly(ether ester) thermoplastic elastomers. Macromolecules, **34**, 1685–1693 (2001). DOI: 10.1021/ma0012696

[19] Schmalz H., Abetz V., Lange R., Soliman M.: New thermoplastic elastomers by incorporation of nonpolar soft segments in PBT-based copolyesters. Macromolecules, **34**, 795–800 (2001). DOI: 10.1021/ma001226p

[20] Szymczyk A., Senderek E., Nastalczyk J., Roslaniec Z.: New multiblock poly(ether-ester)s based on poly(trimethylene terephthalate) as rigid segments. European Polymer Journal, **44**, 436–443 (2008). DOI: 10.1016/j.eurpolymj.2007.11.005

[21] Szymczyk A., Nastalczyk J., Sablong R. J., Roslaniec Z.: The influence of soft segment length on structure and properties of poly(trimethylene terephthalate)-*block*-poly(tetramethylene oxide) segmented random copolymers. Polymers for Advanced Technologies, **22**, 72–83 (2011). DOI: 10.1002/pat.1858

[22] Szymczyk A., Paszkiewicz S., Roslaniec Z.: Influence of intercalated organoclay on the phase structure and physical properties of PTT–PTMO block copolymers. Polymer Bulletin, **70**, 1575–1590 (2013). DOI: 10.1007/s00289-012-0859-y

[23] Szymczyk A.: Poly(trimethylene terephthalate-block-tetramethylene oxide) elastomer/single-walled carbon nanotubes nanocomposites: Synthesis, structure, and properties. Journal of Applied Polymer Science, **126**, 796–807 (2012). DOI: 10.1002/app.36961

[24] Paszkiewicz S., Szymczyk A., Špitalski Z., Mosnáček J., Kwiatkowski K., Rosłaniec Z.: Structure and properties of nanocomposites based on PTT-block-PTMO copolymer and graphene oxide prepared by *in situ* polymerization. European Polymer Journal, **50**, 69–77 (2014). DOI: 10.1016/j.eurpolymj.2013.10.031

[25] Paszkiewicz S.: Polymer hybrid nanocomposites containing carbon nanoparticles. *In situ* synthesis and physical properties. PhD thesis, West Pomeranian University of Technology in Szczecin, Institute of Materials Science and Engineering, Poland (2014).

[26] Paszkiewicz S., Rosłaniec Z., Szymczyk A., Spitalsky Z., Mosnácek J.: Morphology and thermal properties of expanded graphite (EG)/Poly(ethylene terephthalate) (PET) nanocomposites. Chemik, **66**, 21–30 (2012).

[27] Paszkiewicz S., Szymczyk A., Špitalský Z., Soccio M., Mosnáček J., Ezquerra T. A., Rosłaniec Z.: Electrical conductivity of poly(ethylene terephthalate)/expanded graphite nanocomposites prepared by *in situ* polymerization. Journal of Polymer Science Part B: Polymer Physics, **50**, 1645–1652 (2012).
DOI: 10.1002/polb.23176

[28] Scheirs J., Long T. E.: Modern polyesters. Chemistry and technology of polyesters and copolyesters. Wiley, Chichester (2003).

[29] Pötschke P., Arnaldo M. H., Radusch H-J.: Percolation behavior and mehanical properties of polycarbonate composites filled with carbon black/carbon nanotube systems. Polimery, **3**, 204–211 (2012).
DOI: 10.14314/polimery.2012.204

[30] Yu J., Huang X., Wu C., Jiang P.: Permittivity, thermal conductivity and thermal stability of poly(vinylidene fluoride)/graphene nanocomposites. IEEE Transactions on Dielectrics and Electrical Insulation, **18**, 478–484 (2011).
DOI: 10.1109/TDEI.2011.5739452

[31] Kuan C-F., Chen W-J., Li Y-L., Chen C-H., Kuan H-C., Chiang C-L.: Flame retardance and thermal stability of carbon nanotube epoxy composite prepared from sol–gel method. Journal of Physics and Chemistry of Solids, **71**, 539–543 (2010).
DOI: 10.1016/j.jpcs.2009.12.031

eXPRESS Polymer Letters Vol.9, No.6 (2015) 525–535
Available online at www.expresspolymlett.com
DOI: 10.3144/expresspolymlett.2015.50

Effect of annealing and UV-radiation time over micropore architecture of self-assembled block copolymer thin film

G. del C. Pizarro[1*], *O. G. Marambio*[1], *M. Jeria-Orell*[1], *C. M. González-Henríquez*[1], *M. Sarabia-Vallejos*[2], *K. E. Geckeler*[3,4]

[1]Departamento de Química, Universidad Tecnológica Metropolitana. J. P. Alessandri, 1242 Santiago, Chile
[2]Facultad de Física, Pontificia Universidad Católica de Chile, Vicuña Mackenna, 4860 Santiago, Chile
[3]Laboratory of Applied Macromolecular Chemistry, School of Materials Science and Engineering, Gwangju Institute of Science and Technology (GIST), 500-712 Gwangju, South Korea
[4]Department of Nanobio Materials and Electronics (WCU), Gwangju Institute of Science and Technology (GIST), 500-712Gwangju, South Korea

Received 13 October 2014; accepted in revised form 25 December 2014

Abstract. Block copolymers have been recognized as versatile materials to prepare nanoporous polymer films or membranes, but their potential has not been completely explored. This study focuses on the formation and characterization of nanoporous polymer films based on poly(styrene)-*block*-(methylmethacrylate/methacrylic acid); (PS-*b*-MMA/MAA) were obtained through atom transfer radical polymerization (ATRP), by using two different protocols: annealing and annealing-irradiation; for improving the formation of microporous surface. The composition, crystallinity and structural order of the films were studied by Raman spectroscopy. The film polymer thickness was obtained through very high resolution ellipsometry (VHRE). Finally, atomic force microcopy (AFM) and scanning electron microscopy (SEM) techniques were used to detect changes in the porous-structure. These results show that the morphological properties of the block copolymer were affected via the modification of two variables, UV-radiation time and annealing. SEM and AFM micrographs showed that the morphology exhibit a porous ordered structure. Contact angle measurement suggests additional interactions between hydrophilic functional groups that influence the film wettability.

Keywords: *polymer membranes, self-assembled diblock copolymers, thin films, irradiation, annealing*

1. Introduction

Thin films prepared from different materials have recently been interesting for many fields such as electronic semiconductor devices, optical coatings, and pharmaceuticals drug delivery [1, 2]. An increasing interest has aroused about preparing polymeric materials with ordered microstructures. The growing demand for films or membranes with controlled nanostructures for different applications, for example molecular electronics [3], optical devices [4], biological [5] and chemical sensors [6], including water desalination and other alternative technologies, have brought new perspectives to membrane science.

Structural changes at molecular level, in combination with surface chemistry, allow the manipulation of material intrinsic properties for some specific applications [7]. A large number of methods has been used to produce ordered periodic arrays of various materials with sizes from nanometer to micrometer such as conventional lithography, soft lithography [8, 9], etc.

The last decade, some inexpensive non-lithographical techniques such as phase separation [10], dewet-

*Corresponding author, e-mail: pizarroguadalupe048@gmail.com

ting [11], air bubble [12] and convection [13] provide other routes for patterning polymeric materials.

Furthermore, the properties of amphiphilic diblock copolymers produce great interest in industrial fields due to their micro- or macro- phase-separated morphologies. Phase separation in thin block copolymer film can be lead to various morphologies such as islands, bicontinuous structure, etc.; this is a new way of patterning polymeric materials through controlling phase separation morphologies of thin polymer films varying the block domain length [14]. These self-assembled domains are essentially monodisperse, with nanometer dimensions, in which its morphology and sizes are controlled by altering each block length and the total molecular mass [15].

The thermodynamic reasons for block copolymer patterns have been the topic of several classical papers in the field. For example, Guarini *et al*. [16] used UV light (185 and 254 nm) to etch methyl methacrylate blocks of PS-*b*-MMA copolymers, followed by removal in acetic acid to form a porous structure to yield nanoporous membranes. Yang *et al*., [17] prepared thin films of poly(styrene-*b*-methyl methacrylate) and poly(methyl methacrylate) on silicon oxide substrates to give an ordered morphology. Phillips and co-workers [18, 19] and Jackson and Hillmyer [20] prepared dense thin films of poly (styrene-*b*-polylacticide) on the top of a microporous support treated with UV to improve adhesion and promote cross-linking. The lactic acid block domain was etched by immersion in methanol/water and NaOH to form pores. Development of nanoporous templates from block copolymers for optoelectronics and other applications is a fast-growing field. Recent reviews with a large number of examples are available. [21–23].

This work focuses on the microporous structured films formation prepared by solvent casting with annealing above the glass temperature and UV irradiation using the self-assembled amphiphilic PS-*b*-MMA/MAA block copolymer synthesized by ATRP [24]. With the analysis realized in this work it was possible to investigate the role of physical and chemical interactions between PMAA segments, increasing film surface hydrophilicity, due to hydrogen bonding generated between these chains. Also, annealing process produced an ordering change in the arrangement of the functional groups.

On the other hand, it is known that polystyrene and polymethyl methacrylate are amorphous thermoplastics materials, these fact implies that physical properties are also influenced by macromolecular orientation caused by shaping, resulting from the presence of special interactions between these chains. Last, but not least, the quality is influenced by additives, for example plasticizers, UV light and heat stabilizers, among others. Low fraction of PMAA exposed to ambient air absorb some % moisture, water acts as a plasticizer, a decreasing T_g is expected when the amount of absorbed water increases, affecting the spatial conformation of the macromolecule. Also, annealing process at 120°C, above the glass transition temperature (65°C) produces polymers that have not yet reached their crystallinity, forming crystals when molecule mobility is sufficiently high (polymer mobility increases with temperature). In addition, possible hydrogen bonding generated between carboxylic acid groups affects polymer molecular arrangement, favors certain structural ordering into the system, this behavior was observed by Raman spectroscopy.

The films were characterized by FT-IR and Raman spectroscopy, thermogravimetric analysis (TGA), differential scanning calorimetry (DSC), UV-Vis spectroscopy, fluorescence, scanning electron microscopy (SEM), potentiodynamic electrochemical measurement, transmission electron microscopy (TEM) and atomic force microcopy (AFM) techniques.

According to preliminary studies, two different series of thin films were prepared: the first with annealing at 120°C for 2 hours and the second with annealing and subsequent UV irradiation at 254 nm for 2, 4, 6 and 8 h. The time series was used to understand the porosity change at surface level over time. The thin films thickness was determined using very high resolution ellipsometry (VHRE). Raman spectroscopy was used to study changes in crystallinity and possible polymer chains ordering into the system. Atomic force microscopy (AFM) and scanning electronic microscopy (SEM) were performed to detect morphology changes at surface level and to determine pore dimensions (shape, depth and diameter).

2. Experimental section

2.1. Materials

Styrene (purchased from Sigma-Aldrich chemicals, CHEMIE, Germany) was washed with 5% aqueous NaOH to remove inhibitor and distilled under reduced pressure before use. Methylmethacrylate

(MMA) (obtained from Merck-Schuchardt Chemicals, Germany) was purified by distillation under reduced pressure. Benzoyl peroxide (BPO) (Merck-Schuchardt, with 25% H_2O, CHEMIE, Germany) was used as received. Copper(I) bromide (Aldrich, 98%) was purified by stirring overnight over CH_3COOH at room temperature, followed by washing with ethanol and diethyl ether prior to drying at 50°C under vacuum for 1 day. 2, 2′-Bipyridyl (Sigma-Aldrich, 99%) was used as received.

2.2. Methods and equipment

The number-average (M_n) and weight-average (M_w) molecular weights and the molecular weight distribution (polydispersity, M_w/M_n) of polymers were determined using size exclusion chromatography (SEC) under the following conditions: WATERS 600E instrument equipped with UV and RI detectors using THF as solvent (flow rate: 1.0 mL/min). The samples were measured at 30°C with a concentration of 6 mg/mL, calibration was performed using polystyrene.

Infrared spectra were measured on a Bruker Vector 22 FT-IR spectrometer (Bruker Optics GmbH, Inc., Ettlingen, Germany) using OPUS 3.14 software to control the measurements. In previous work [24], this polymeric structure was characterized by ^1H and ^{13}C NMR analysis studied on a Bruker 400 MHz spectrometer using $CDCl_3$ the solvent. The structural chemical composition of copolymer films were characterized using Raman spectroscopy with a LabRam 010 instrument from ISA equipped with a 5.5 mW, 632.8 nm He-Ne laser without a filter. The Raman microscope uses back-scattering geometry, in where incident beam is linearly polarized at a 500:1 ratio. The microscope objective lens was an Olympus Mplan 100× (numerical aperture 0.9).

TG and DSC thermograms were recorded under nitrogen atmosphere. Studies of thermal stability were performed using a Star System 1 thermogravimetric analyzer (TGA) with a heating rate of 10°C/min. DSC measurements were performed with a Mettler Toledo Star System 822e in order to determine the copolymer glass transition temperature (T_g). The T_g was measured with 10°C/min heating rate; to eliminate the effect of thermal history on the phase transitions, all samples were heated to 150°C, held that temperature for 5 min and then cooled to 30°C.

The absorption spectra of PS-*b*-MMA/MAA were recorded at 25°C between 250–400 nm using a Perkin Elmer Lambda 35 spectrophotometer, intensity of 3.5 mW/cm^2 since 365 nm. Photoluminescence (PL) spectra of solid samples were recorded at room temperature with a Perkin Elmer L55 spectrofluorimeter, using an excitation wavelength of 320 nm. Both analyses were recorded using THF as solvent for the copolymer dissolution.

Cyclic voltammetry was carried out using an Aut 302 Ecochimie Autolab potentiostat/galvanostat recorded in DMF (ca $1.0 \cdot 10^{-3}$ mol/L) under nitrogen atmosphere with TBAP (ca 0.1 mol/L) using three-electrode cells. A hanging-drop mercury electrode (HDME) was used as working electrode, a platinum wire as auxiliary electrode, and saturated calomel (SCE) as reference electrode. The electrolyte support was a solution of 0.1 M (dissolved in DMF) LiCl. The experiments were carried out under nitrogen atmosphere at room temperature for the entire range of sweep rates. The DMF solvent was used without previous treatment.

The polymer morphology was examined using a SEM model LEO 1420VP with 100 μA beam current and working distance of 12–14 mm. The microscope was operated at high vacuum (system vacuum ~10^{-6} mbar and chamber 10^{-3} mbar). TEM observations were performed using a JEOL JEM 1200EX instrument operated at 120 kV, with a point resolution of approx. 4 Å. These images were taken by placing a drop of block copolymer dissolved in THF over carbon-coated copper grid. The equipment was operated at high vacuum (~10^{-5} mbar). Also, block copolymers surface characterization was performed using an AFM Digital Instruments Nano-Scope IIIA Series in 'tapping' mode. The polymer powder was dissolved in THF and cast on glass slides using spin coating technique with rotation frequency of 500 rpm for approximately 10 s and 1600 rpm for approximately 10 s. Contact angle was corroborated by sample roughness test using AFM technique.

Very High Resolution Ellipsometry (VHRE) with single wavelength laser (He-Ne, 632.8 nm) in PCSA null configuration was used to determine the film thickness. Laser beam incidence angle was 60.5° respect to sample normal. The film thicknesses were calculated using the Drude model for single layers with ellipsometric parameters Δ and ψ, which

are related to the measured polarizer P ($\Delta = 2P + 90°$) and analyzer A ($A = \psi$) angles. The refractive index value for poly(methylacrylate) was $n = 1.5343$, and polystyrene $n_{PS} = 1.5894$, and for the amphiphilic PS-*b*-MMA/MAA block copolymer was used the average of these last ones, $n_{PS\text{-}b\text{-}MMA/MAA} = 1.5662$ [25].

2.3. PS-*b*-MMA/MAA block copolymer

The PS-*b*-MMA/MAA was synthesized by ATRP using MMA/PS-Br /CuBr/BPy, in a molar ratio of 100/1/1/2, previously published by our research group [24]. The molecular weight and polydispersity were $10.2 \cdot 10^4$ g/mol and 1.30, respectively. The polymerization degree of PS and PMMA were calculated from molecular weight using SEC were $DP_n = 699$ for PS and $DP_n = 290$ for PMMA. PS-*b*-MMA/MAA was obtained by acidic hydrolysis of methyl ester linkages in the MMA blocks (see Figure 1). According to these results, the ^1H NMR spectra of hydrolyzed block copolymer show a 20% decrease in signal intensity at 3.5–3.6 ppm [$-CH_3$ ester protons of the MMA block], which corresponds to the percent hydrolysis of methyl ester, indicating the formation of COOH groups, given the Poly(S_{699}-*block*-MMA_{232}/MAA_{58}) block copolymer.

2.4. Preparation of polymer films

The PS-*b*-MMA/MAA was dissolved in THF at concentrations of 0.5 mg/mL at room temperature. Thin films were prepared using silicon wafers ($Si_{(100)}$/SiO_2) as substrate by spin-coating (360 rpm/18 s and 1480 rpm/60 s). According to this method, a film series were prepared to investigate the effect of irradiation time on surface porosity. One film was annealed at 120°C for 2 hours to produce certain molecular arrangement; the second film series were annealed for the same temperature and time. Afterwards these films were exposed to UV light (254 nm) for 2, 4, 6, and 8 hours.

3. Results and discussion

3.1. Structural studies of the polymeric films: FTIR and Raman analysis

Molecular structure was confirmed and corroborated by FT-IR and Raman spectroscopy, as shown in Figure 2. The absorption bands (double peak) between 1731 and 1601 cm^{-1} correspond to both symmetric and asymmetric C=O stretching of carboxylic acid carbonyl and ester carbonyl groups, the band at 3446 cm^{-1} correspond to OH– stretching of carboxylic acids that usually exist as hydrogen-bonded dimers (see Figure 2 curve a).

The Raman spectra also exhibited a strong peak at 3052–3039 cm^{-1} assigned to the aromatic protons (C–H stretching in plane bending), at 2952–2900 cm^{-1} assigned to the alkane (C–H anti-symmetric stretching $-CH_3$), and a band of low intensity at 1720 cm^{-1} assigned to the C=O (stretching). This same vibration appears intensely by infrared spectroscopy near 1730 cm^{-1}. The strong bands obtained by Raman spectroscopy at 1602–1583 cm^{-1} were assigned to C=C aromatic (stretching), (see Figure 2 curve b). The band at 1451 cm^{-1} was assigned to alkenes ($-CH_2$ bending). The same vibration appears in infrared spectroscopy (1450 cm^{-1}). However, IR shows only the frequency near 1490 cm^{-1}, corresponding to C=C stretching of the aromatic ring. The band at 1200–1154 cm^{-1} was assigned to C–O stretching of ester group. A strong signal at 1000 cm^{-1} was assigned to C–C aromatic (stretching), and the band at 619 cm^{-1} was assigned to C–H aromatic (stretching out of plane in opposite direction). Both signals were observed with very low intensity by IR spectroscopy.

3.2. Thermal analysis

The thermal decomposition temperature and the value of glass transition temperature (T_g) of PS-*b*-MMA/MAA was investigated by TGA and DSC, respectively (see Figure 3). The TGA curve exhibited slight weight loss approximately 76°C, with 5%

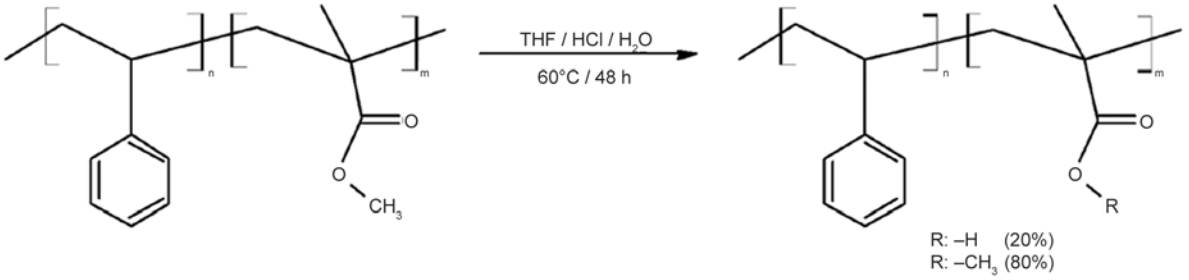

Figure 1. Representation of hydrolysis process for functional hydrophilic microdomains of PS-*b*-MMA/MAA block polymer

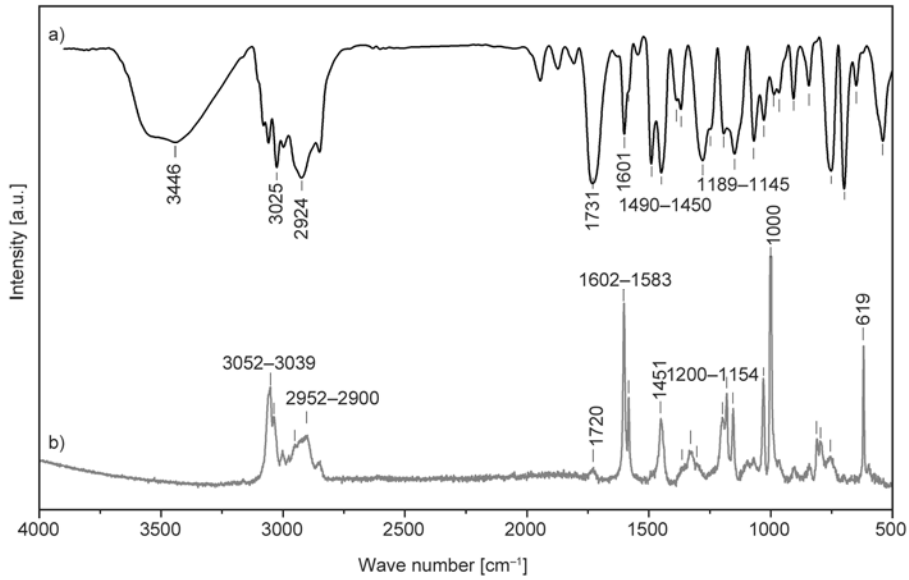

Figure 2. a) FT-IR spectrum and b) Raman spectrum of PS-*b*-MMA/MAA block copolymer films

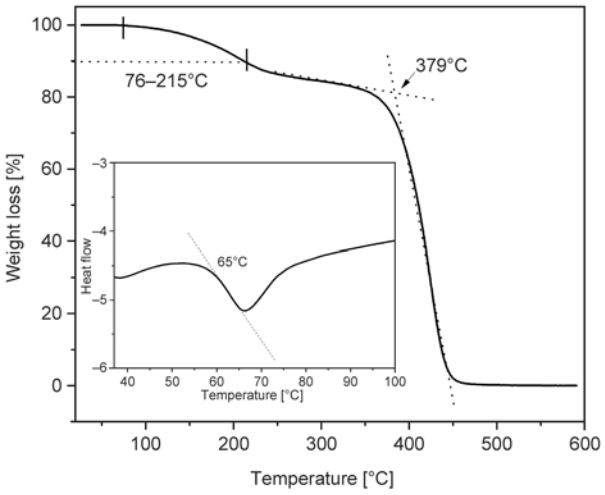

Figure 3. TGA / DSC thermogram of PS-*b*-MMA/MAA block copolymer. Heating rate 10°C/min

weight loss at 215°C. This temperature range is attributed to water loss (dehydration) associated with functional groups (COOH groups) of hydrophilic segment PMAA. The second weight change is attributable to decomposition of material from 330–379°C. The resulting material has an extrapolated thermal decomposition temperature (TDT) of approximately 379°C, when decomposition of backbone chain occurs.

T_g value reflects the change in the DSC slope curve after the second heating run. The result show that the copolymers have a low glass transition temperature in relation to previously studied systems [25]. This behavior is attributed to the moisture entrapped in the sample, because –COOH functional groups, in which moisture would be acting as a plasticizer, decrease the T_g. It is known that T_g depends very much on the moisture content. Therefore, moisture is an efficient plasticizer.

3.3. Optical properties

The UV-Vis absorption and fluorescence emission spectra were recorded at room temperature. UV-Vis spectrum of dilute PS-*b*-MMA/MAA copolymers solutions (Figure 4) exhibit four characteristic bands at 220, 261, 270 and 293 nm. The band near at 220 nm is related to the cut-off of tetrahydrofuran used as solvent. An intense absorption at 261 nm could be attributed to the π-π* transition due to electron delocalization in the aromatic ring (inter-molecular transfer change). At 270 nm, the band of medium intensity may be related to the non-conjugated π-systems of the main chain ester pendant groups. Finally, the small band at 293 nm is related to overlapping of atomic orbitals produced from the inter-molecular interaction between aromatic rings. The luminescence spectra of the copolymer are also shown in Figure 4 (left side). When the compound is excited with a wavelength of 320 nm, the sample presents blue emission with a peak maximum at 337 nm. This color is related to the poorly conjugated system of the copolymer that can be only attributed to the aromatic ring and the double bond ester groups.

Finally, copolymer solution used in optical studies was highly transparent, which can be attributed to

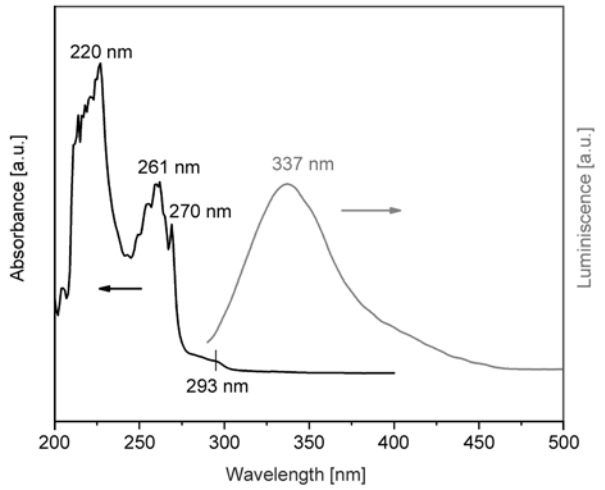

Figure 4. UV-Vis spectra (right) and photoluminescence spectrum of PS-*b*-MMA/MAA block copolymer films (left)

the lower fraction of PMAA segment owing to the reduced chain packing resulting from the presence of special interactions between these chains.

3.4. Cyclic voltammetry

The sample electrochemical behaviors were tested under potential range from –1.0 to +1.0 V and from –1.5 to 1.5 V (scan rate 100 mV/s). The block copolymer cyclic voltammetry (CV) characterization is shown in Figure 5. In these voltammograms, it is observed that the block copolymer did not exhibit oxidation-reduction process under CV analysis conditions. In all cases an oxidation small wave was observed; this could correspond to the peroxide oxidation generated in the oxygen reduction, which was observed at low potential (electrocatalysis) (approximately from –0.7 to –0.5 V). The range of electrochemical inertia can be extended to –1.0 V. The oxidation-reduction process obtained corresponds to the oxygen reduction and peroxide oxidation. A redox process was not observed for the copolymer under tested conditions. This copolymer shows electrochemical stability and thus provides an ideal platform for fabricating novel functional nanostructured materials for potential applications in advanced technologies such as optical coatings and information storage.

3.5. Morphological analysis

Morphological characterizations of polymer films were realized by AFM and SEM. The samples were prepared in films without further processing. The copolymer was dissolved in THF (0.5 mg/mL) and

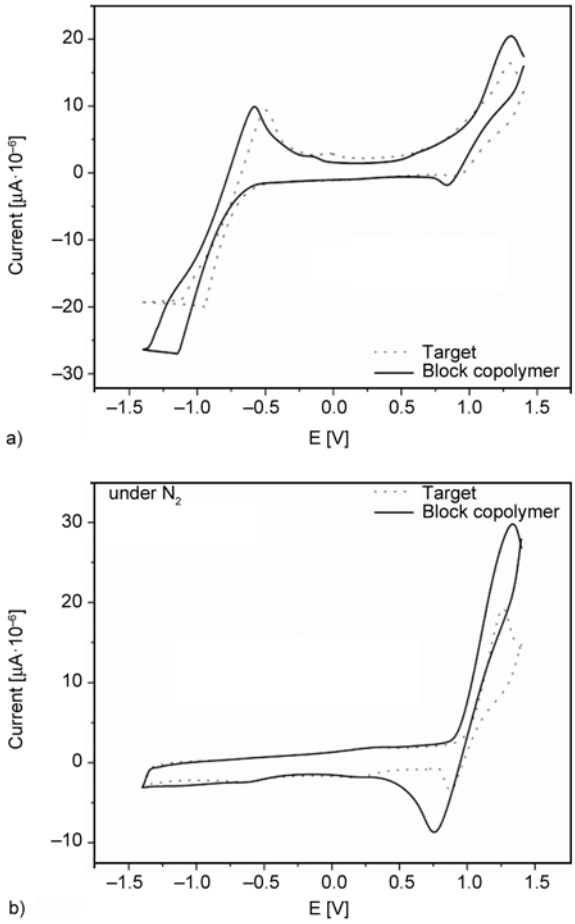

Figure 5. Cyclic voltammetric response of glassy carbon electrode cycled in a solution containing PS-*b*-MMA/MAA block copolymer and target. Scan rate: a) 100 mV/s and b) under nitrogen.

deposited over silicon wafer (Si_{100}/SiO_2) using spin coating. Typical SEM microphotographs of PS-*b*-MMA/MAA block copolymer at different concentration are shown in Figure 6. SEM images give additional information about size and dispersion of block copolymer at 0.5 mg/mL in THF, which form a porous-structure, see Figure 6a. The microphase separation between both domains occurs due to the different block and block copolymer lengths, the structure tend to adopt a spherical shape via nucleation growth manner; also, aggregation arises with increasing concentration (1.0 mg/mL), see Figure 6b. SEM images show that the block copolymer form micelles spherical aggregates in THF/MeOH (drops). The micelles can assume different forms depending on solvent-block interactions and block sizes [26]. The particles size dispersion measure by DLS was relatively narrow ($Đ = 0.347$) with an effective particle diameter of 32 nm (0.5 mg/mL). As the block copolymer concentration increased (1.0 mg/mL)

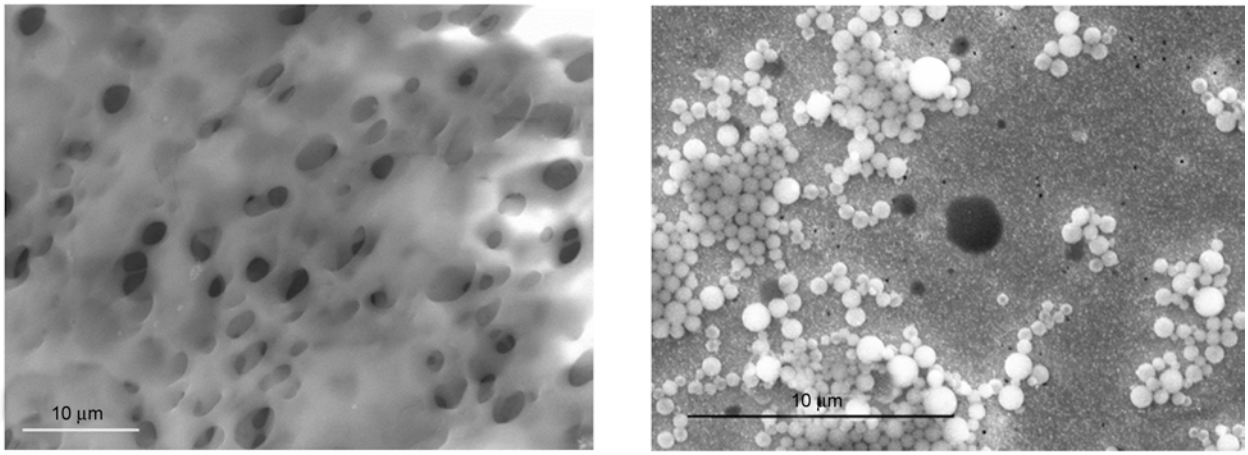

Figure 6. SEM microphotographs obtained from spin-coated films of PS-*b*-MMA/MAA block copolymer a) 0.5 mg/mL and b) 1.0 mg/mL

large spherical aggregates were detected with a narrow size distribution ($Đ$ = 0.352) and an effective diameter of 120.2 nm. The particle size range showed that the micelles tended to self-assemble into much larger micellar aggregates that finally predominate.

3.6. Characterization of the polymeric films

The copolymer was dissolved in THF and spin-coated on $Si_{(100)}/SiO_2$ wafers. Silicon wafers of 0.5×0.5 cm were used for polymer films fabrication by copolymer dissolution in THF and spin-coating (360 rpm/18 s and 1480 rpm/60 s). Two types of films were prepared: The first series was subjected to annealing (120°C for 2 h) and the second series films were annealed and exposed to UV light at 254 nm for 2, 4, 6, and 8 h. Both series of films were studied with techniques such as VHRE for film thickness measures, Raman spectroscopy for crystallinity degree, AFM and SEM for the effect of UV irradiation on the microstructure and pore diameter size. The annealing temperature (120°C) is related to the intrinsic properties of the copolymer (T_g = 65°C, Figure 3). Beyond this temperature, localized bond movements favor changes in order and homogeneity at the surface level. Radiation with wavelength of 254 nm is related to the optical properties of the material and a possible π-π* transition. The low thickness of the polymer films and good homogeneity produced by spin-coating did not change the optical properties of the silicon wafer (n = 1.46). The refractive indexes of poly(methylacrylate) and polystyrene are n_{PMA} = 1.4793 and n_{PS} = 1.5894, respectively. Thus, average refractive index of the film was n = 1.465. The results for thin film thickness obtained by VHRE are shown in Table 1. Five samples were annealed at 120°C/2 h, and four of the films were irradiated for 2, 4, 6, and 8 h at 254 nm.

3.7. Studies of the polymeric films by Raman spectroscopy

According to the results, Raman spectrum shown in the Figure 7 a is totally different to those presented in Figure 2, this behavior could be related to the annealing process effected on the films, producing a change in the functional group arrangement that form the copolymers and therefore a restructuration in the porous layer.

When the thin films were annealed at 120°C (2 h) above the glass transition temperature (65°C), the

Table 1. Thin films thickness obtained using VHRE

Samples	Thickness of the thin films [nm]	Pore diameter [nm]	Pore depth [nm]
Annealed at 120°C for 2 h	27.4	791	25
Annealed at 120°C and UV irradiated at 254 nm.			
2 h under irradiation	29.1	1149	21
4 h under irradiation	26.2	1136	25
6 h under irradiation	27.4	1099	25
8 h under irradiation	28.2	1138	25

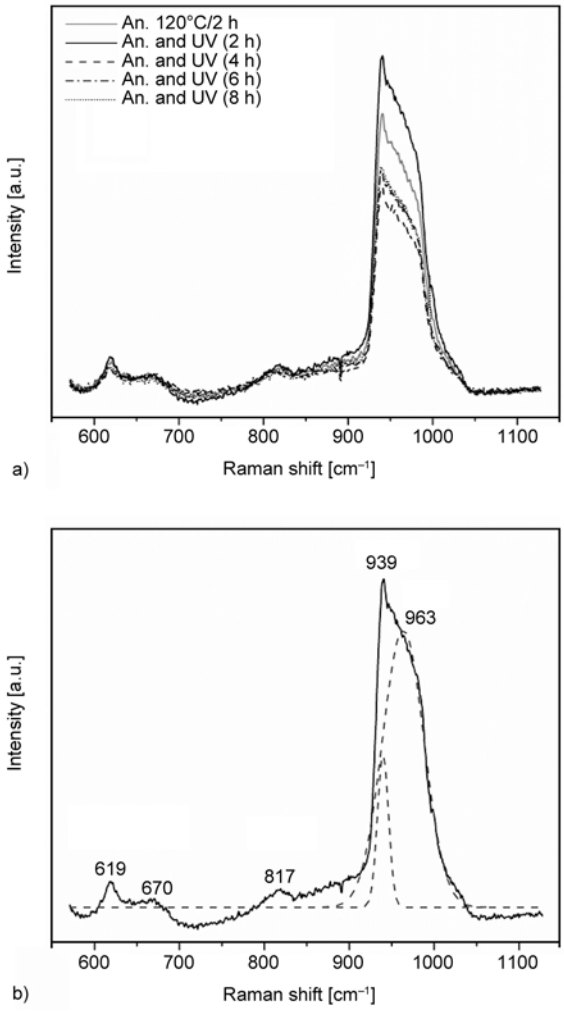

Figure 7. Raman shifts of thin films as a function of annealing and irradiation time, and b) spectral band deconvolution analysis of one sample annealed at 120°C and irradiated at 254 nm for 2 h

Raman spectrum showed five bands at 619, 670, 817, 939, and 963 cm^{-1} representative of the aromatic group. These values were obtained from the band deconvolution analysis (see Figure 7b). Thus, bands near 619–817 cm^{-1} are low intensity, possibly related to the aromatic ring C–H out of plane. The high-intensity band with overlap of two vibrations at 939 and 963 cm^{-1} respectively, were assigned to aromatic ring C–C and C–O stretching of the copolymer pendant ester group.

3.8. Measurements of contact angle on the polymeric film

Two films were prepared, the first was not subjected to annealing and the second film was annealed (120°C) and exposed to UV light at 254 nm for 2 h. Even in an almost perfectly smooth surface obtained by spin coating, a drop will assume a wide spectrum of contact angles between the highest (advancing) contact angle, θ_A, and the lowest (receding) contact angle, θ_R. The roughness effect on the contact angle was determined from the area project (25 μm^2) and real area (28 μm^2) data obtained by AFM. When the thin films were annealed at 120°C (2 h) above the glass transition temperature (65°C), the contact angle value of the film was approximately 80° (corrected from AFM data) and without annealing the contact angle value of the film was 72°; according with these results, is possible to conclude that the film increases the surface hydrophilicity. This behavior was attributed to the annealing process that produces a change in the order and, also, in the functional group arrangement; therefore, porous film will form. This provides some information regarding the hydrogen bonding interactions between carboxylic acids and carbonyl ester groups on the surface of prepared films, where these functional groups increase surface hydrophilicity. The increase in the contact angle value suggests additional interactions that influence the wettability of the film [27].

3.9. Morphological analysis by AFM and SEM

Figure 8 shows the AFM/SEM image of the polymer films. All the thin films were annealed at 120°C; however, only one was taken as base (2 h) (Figure 8a) and four were irradiated with UV light of 245 nm for 2, 4, 6, and 8 h (Figure 8b–8c). The AFM reveals that the surface monolayer has circular pores or individual cavities that are directly connected. The sample that was annealed at 120°C for 2 h displays pore dimensions of ~791 nm (diameter) and ~25 nm (depth) (Figure 8a). This behavior was mainly modified by UV irradiation at different time of exposition (Figure 8b–8c). Accordingly, samples that were irradiated at 2, 4, 6, and 8 hours showed an increase in pore diameter size compared to the sample base without radiation. Their values were 1149, 1136, 1099, and 1138 nm, respectively. All the samples, except the one irradiated for 2 hours (21 nm), displayed pore depth of 25 nm. The last thin film (8 h, UV irradiation) showed a possible fluctuation of density that affects the clarity of the image, producing a distortion of the porous-structure real topography. Moreover, SEM results show that the diameter pore size of these sample film was around ~1000 nm. Notably, irradiation time does not strongly affect particle diameter pore size. On the other hand, if it is compare samples with similar

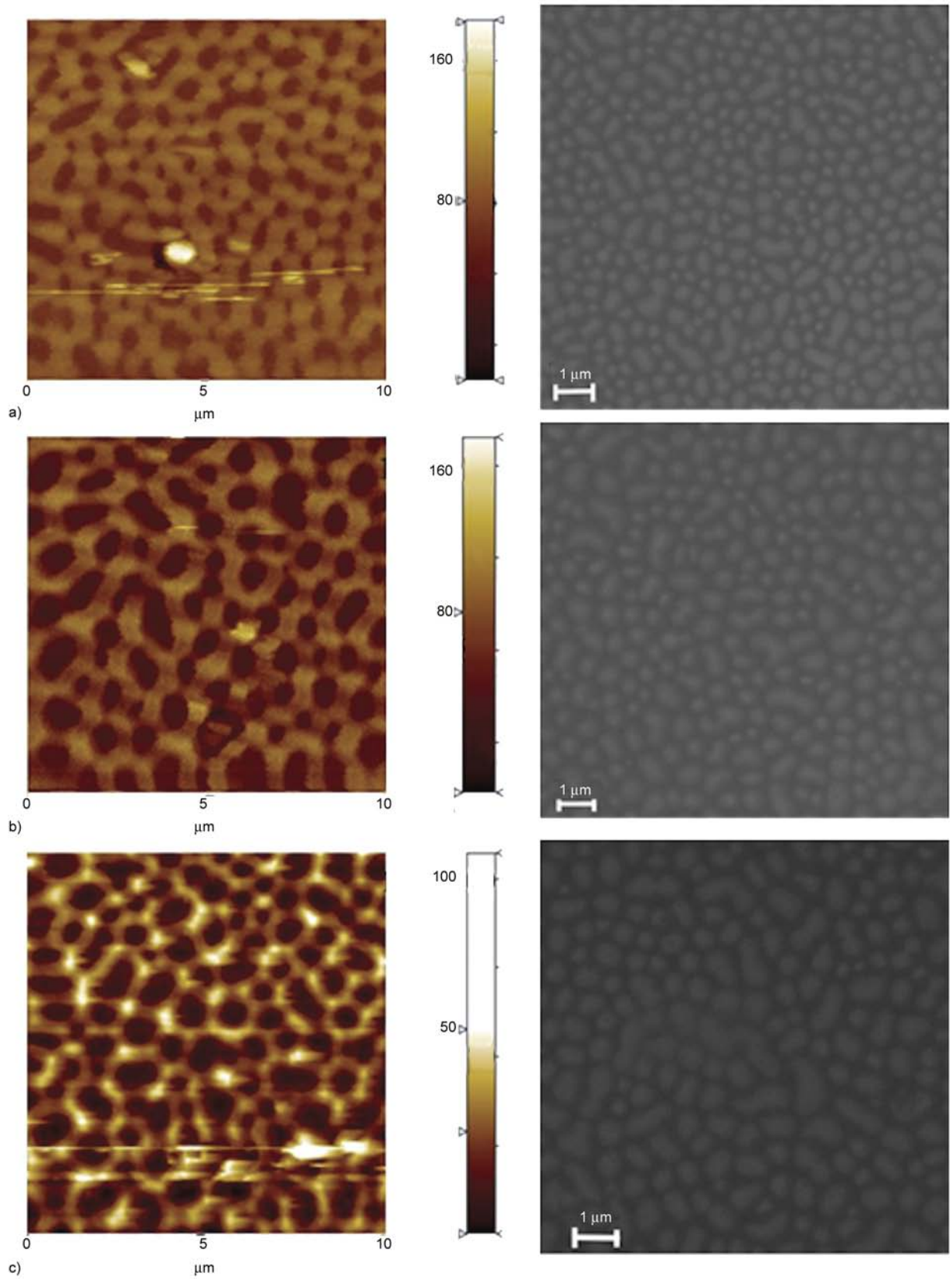

Figure 8. AFM and SEM of copolymers obtained through annealing at 120°C (2 h) and irradiation at 254 nm: a) annealing at 120°C, b) annealing at 120°C and 4 h irradiation; c) annealing at 120°C and 6 h irradiation

thickness at 0, 2, 4, and 6 h of irradiation, it is possible to conclude that non-irradiated samples possess smaller pore diameter size that the UV-irradiated samples and these last exhibited approximately the same pore diameter size, greater than the sample film base.

For a high molecular weight block copolymer, as the used in this study, carboxylic acid end-groups allows the generation of polar segments, increasing macromolecular chains amphiphilic character. They must exhibit chemical and physical star-like structures due to macromolecule polar end-chain insolubility [28].

4. Conclusions

Thin films based on a well-controlled structure of a single amphiphilic block copolymer with relatively low dispersity ($Đ < 1.28$) were obtained by spin-coating. The films exhibited UV absorption in the blue region of the spectrum and high transparency that can be attributed to a smaller fraction of PMAA, owing to reduced chain packing from special interactions between these chains. Electrochemical analysis did not show oxide-reduction process under these conditions. The curves indicate no electro-activity. This electrochemical stability provides an ideal platform for fabricating novel functional nanostructured materials, for potential applications in advanced technologies such as optical coatings and information storage. The films exhibit thermal stability because to their high extrapolated thermal decomposition temperature (TDT = 379°C). The films annealing and exposed to UV light showed a porous structure based on this self-assembled amphiphilic block copolymer. AFM images of the film show a uniform rough surface morphology due to microphase separation of the block copolymer. This behavior was attributed to a self-assembling effect of PMAA in the microstructure.

Finally, it can be concluded that when the copolymer is annealed over the glass transition temperature, the functional groups of the compound are rearranged. Therefore, different vibrational groups in the Raman spectroscopy were observed, particularly the aromatic group that formed the copolymer. AFM reveals that the nanopores or individual cavities are directly open to the surface. The pore dimensions are controlled by UV irradiation on the sample. Thus, a decrease in pore diameter was observed without UV irradiation and the pore depth is directly related to film thickness.

Acknowledgements

The authors acknowledge the financial support of this work by *Fondo Nacional de Investigación Científica y Tecnológica*, FONDECYT Grant 1110836 and 11121281, UTEM Grant, and the WCU Program funded by MEST (R31-10026). Also, Mr. Sarabia acknowledges the Master studies grant give by CONICYT.

References

[1] Wang D., Wang X.: Amphiphilic azo polymers: Molecular engineering, self-assembly and photoresponsive properties. Progress in Polymer Science, **38**, 271–301 (2013).
DOI: 10.1016/j.progpolymsci.2012.07.003

[2] Lee L-H., Chen W-C.: High-refractive-index thin films prepared from trialkoxysilane-capped poly(methyl methacrylate)–titania materials. Chemistry of Materials, **13**, 1137–1142 (2001).
DOI: 10.1021/cm000937z

[3] Karthaus O., Adachi C., Kurimura S., Oyamada T.: Electroluminescence from self-organized 'microdomes'. Applied Physics Letters, **84**, 4696–4698 (2004).
DOI: 10.1063/1.1760592

[4] Chari K., Lander C. W., Sudol R. J.: Anamorphic microlens arrays based on breath-figure template with adaptive surface reconstruction. Applied Physics Letters, **92**, 111916/1–111916/4 (2008).
DOI: 10.1063/1.2901027

[5] Chaudhuri J. B., Davidson M. G., Ellis M. J., Jones M. D., Wu X. J.: Fabrication of honeycomb-structured poly(DL-lactide) and poly[(DL-lactide)-*co*-glycolide)] films and their use as scaffolds for osteoblast-like cell culture. Macromolecular Symposia, **272**, 52–57 (2008).
DOI: 10.1002/masy.200851206

[6] Xu X., Zhuang J., Wang X.: SnO_2 quantum dots and quantum wires: Controllable synthesis, self-assembled 2D architectures, and gas-sensing properties. Journal of the American Chemical Society, **130**, 12527–12535 (2008).
DOI: 10.1021/ja8040527

[7] Hamley I. W.: Ordering in thin films of block copolymers: Fundamentals to potential applications. Progress in Polymer Science, **34**, 1161–1210 (2009).
DOI: 10.1016/j.progpolymsci.2009.06.003

[8] Xia Y., Kim E., Zhao X-M., Rogers J. A., Prentiss M., Whitesides G. M.: Complex optical surfaces formed by replica molding against elastomeric masters. Science, **273**, 347–349 (1996).
DOI: 10.1126/science.273.5273.347

[9] Kim E., Xia Y., Whitesides G. M.: Polymer microstructures formed by moulding in capillaries. Nature, **376**, 581–584 (1995).
DOI: 10.1038/376581a0

[10] Yamaguchi T., Inagawa T., Nakasumi H., Irie S., Irie M.: Photoinduced pitch changes in chiral nematic liquid crystals formed by doping with chiral diarylethene. Journal of Materials Chemistry, **11**, 2453–2458 (2001). DOI: 10.1039/B103925N

[11] Luo C., Xing R., Han Y.: Ordered pattern formation from dewetting of polymer thin film with surface disturbance by capillary force lithography. Surface Science, **552**, 139–148 (2004). DOI: 10.1016/j.susc.2004.01.042

[12] Widawski G., Rawiso M., François B.: Self-organized honeycomb morphology of star-polymer polystyrene films. Nature, **369**, 387–389 (1994). DOI: 10.1038/369387a0

[13] Mitov Z., Kumacheva E.: Convection-induced patterns in phase-separating polymeric fluids. Physical Review Letters, **81**, 3427–3430 (1998). DOI: 10.1103/PhysRevLett.81.3427

[14] Affrossman S., Jerome R., O'Neill S. A., Schmitt T., Stamm M.: Surface structure of thin film blends of polystyrene and poly(*n*-butyl methacrylate). Colloid and Polymer Science, **278**, 993–999 (2000). DOI: 10.1007/s003960000358

[15] Sun P., Zhang Y., Shi L., Gan Z.: Thermosensitive nanoparticles self-assembled from PCL-*b*-PEO-*b*-PNIPAAm triblock copolymers and their potential for controlled drug release. Macromolecular Bioscience, **10**, 621–631 (2010). DOI: 10.1002/mabi.200900434

[16] Guarini K. W., Black C. T., Yeung S. H. I.: Optimization of diblock copolymer thin film self assembly. Advanced Materials, **14**, 1290–1294 (2002). DOI: 10.1002/1521-4095(20020916)14:18<1290::AID-ADMA1290>3.0.CO;2-N

[17] Yang S. Y., Ryu I., Kim H. Y., Kim J. K., Jang S. K., Russell T. P.: Nanoporous membranes with ultrahigh selectivity and flux for the filtration of viruses. Advanced Materials, **18**, 709–712 (2006). DOI: 10.1002/adma.200501500

[18] Phillip W. A., O'Neill B., Rodwogin M., Hillmyer M. A., Cussler E. L.: Self-assembled block copolymer thin films as water filtration membranes. ACS Applied Materials and Interfaces, **2**, 847–853 (2010). DOI: 10.1021/am900882t

[19] Phillip W. A., Hillmyer M. A., Cussler E. L.: Cylinder orientation mechanism in block copolymer thin films upon solvent evaporation. Macromolecules, **43**, 7763–7770 (2010). DOI: 10.1021/ma1012946

[20] Jackson E. A., Hillmyer M. A.: Nanoporous membranes derived from block copolymers: From drug delivery to water filtration. ACS Nano, **4**, 3548–3553 (2010). DOI: 10.1021/nn1014006

[21] Zhao H., Gu W., Sterner E., Russell T. P., Coughlin E. B., Theato P.: Highly ordered nanoporous thin films from photocleavable block copolymers. Macromolecules, **44**, 6433–6440 (2011). DOI: 10.1021/ma201416b

[22] Wang Y., He C., Xing W., Li F., Tong L., Chen Z., Liao X., Steinhart M.: Nanoporous metal membranes with bicontinuous morphology from recyclable block-copolymer templates. Advanced Materials, **22**, 2068–2072 (2010). DOI: 10.1002/adma.200903655

[23] Cheng J. Y., Ross C. A., Smith H. I., Thomas E. L.: Templated self-assembly of block copolymers: Top-down helps bottom-up. Advanced Materials, **18**, 2505–2521 (2006). DOI: 10.1002/adma.200502651

[24] del C. Pizarro G.: Jeria-Orell M., Marambio O. G., Olea A. F., Valdés D. T., Geckeler K. E.: Synthesis of functional poly(styrene)-*block*-(methyl methacrylate/methacrylic acid) by homogeneous reverse atom transfer radical polymerization: Spherical nanoparticles, thermal behavior, self-aggregation, and morphological properties. Journal Applied Polymer Science, **129**, 2076–2085 (2013). DOI: 10.1002/app.38923

[25] Wypych G.: Handbook of polymers. ChemTec Publishing, Toronto (2012).

[26] Israelachvili J. N.: Intermolecular and surface forces. Academic Press, Waltham (2011).

[27] Tamada Y., Ikada Y.: Fibroblast growth on polymer surfaces and biosynthesis of collagen. Journal of Biomedical Materials Research, **28**, 783–789 (1994). DOI: 10.1002/jbm.820280705

[28] Zhong X. F., Eisenberg A.: Aggregation and critical micellization behavior of carboxylate-terminated monochelic polystyrene. Macromolecules, **27**, 1751–1758 (1994). DOI: 10.1021/ma00085a013

eXPRESS Polymer Letters Vol.9, No.6 (2015) 536–553
Available online at www.expresspolymlett.com
DOI: 10.3144/expresspolymlett.2015.51

Combined main-chain/side-chain ionic liquid crystalline polymer based on 'jacketing' effect: Design, synthesis, supra-molecular self-assembly and photophysical properties

L. Weng[1], *H. L. Xie*[1*], *C. G. Arges*[3], *J. Tang*[1], *G. Q. Zhong*[1], *H. L. Zhang*[1], *E. Q. Chen*[2]

[1]Key Laboratory of Special Functional Polymer Materials of Hunan Province, Key Laboratory of Advanced Functional Polymer Materials of Colleges and Universities of Hunan Province and Key Lab of Environment-friendly Chemistry and Application in Ministry of Education, College of Chemistry, Xiangtan University, 411105 Xiangtan, Hunan Province, China
[2]Beijing National Laboratory for Molecular Sciences, College of Chemistry and Molecular Engineering, Peking University, 100871 Beijing, China
[3]Institute for Molecular Engineering, The University of Chicago, Chicago, 60637 Illinois, United States

Received 23 October 2014; accepted in revised form 31 December 2014

Abstract. Reasonably fabricating ordered structures of ionic polymers is very important for the development of novel functional materials. By combining the ions and liquid cry stalline polymer, we successfully designed and synthesized a series of novel combined main-chain/side-chain ionic liquid crystalline polymer (MCSC-ILCPs) containing imidazolium groups and different counter-anions, poly (2,5-bis{[6-(4-butoxy-4′-imidazolium biphenyl)hexyl]oxycarbonyl}styrene salts) poly(BImBHCS-X) with the following types of counter-anions (Br^-, BF_4^-, PF_6^- and $TFSI^-$). Combined technologies confirmed the chemical structures of the monomers and polymers with imidazolium cation and different counter-anions. Differential scanning calorimetry (DSC), polarized light microscopy (PLM) and one- and two-dimensional wide-angle X-ray diffraction (1D and 2D WAXD) results illustrated that the LC structures and the transitions of ordered structures depended on the nature of the counter-anion employed. The polymers with Br^- and BF_4^- counter-anions exhibited smectic A (SmA) LC behavior below the isotropic temperature. The another one, poly(BImBHCS–TFSI) with the large volume of the $TFSI^-$ anion destroyed the packing of the LC ordered structure resulting in an amorphous structure. The photophysical properties of the polymers prepared can be adjusted by tuning the ionic interaction of the polymers by switching the counter-anion.

Keywords: *polymer synthesis, molecular engineering, ionic liquid crystalline polymer, phase behavior, supermolecular structure*

1. Introduction

Ionic liquid crystalline polymers (ILCPs) are a class of macromolecular architectures with mesogenic groups and ionic species and they have attracted great interest in the fields of polymer chemistry and materials science lately [1–3]. The combination of electrostatic interaction with liquid crystalline (LC) ordering yields ILCPs with excellent mechanical properties, rheological processability, piezoelectric performance, and optical variable performance [1–7]. Generally, ionic interaction promotes the ILCPs to form ionic clusters resulting in a reversible physical gelation [1, 8, 9]. Moreover, incorporation of the ions and selection of the type of ion chemistry can effectively improve the miscibility with other polymers. Therefore, ILCPs are versatile candidates to construct new high-performance functional mate-

*Corresponding author, e-mail: xhl20040731@163.com

rials and micrometer/nanometer composite materials [10–20].

In terms of the chemical structure, ILCPs can be classified as a main-chain ionic liquid crystalline polymer (MC-ILCP) or a side-chain ionic liquid crystalline polymer (SC-ILCP) [1, 3, 6]. For the MC-ILCPs, the ionic liquid crystals (ILCs) are located in the main chain of polymer. Usually, this type polymer can be synthesized by a polycondensation reaction or non-covalent bond (such as hydrogen bonding, ionic bonds etc.). Incorporation of ion groups yields significant improvement in the polymer's transverse strength, compressive strength, and miscibility of polymers or other species in MC-ILCPs when compared to traditional main-chain liquid crystalline polymers (MCLCPs) [21, 22]. At the same time, the implementation of the ionic groups leads to better and more diverse thermal behavior, liquid crystal behavior, and photoelectric properties [23–26]. For example, the content of sulfonic acid in ILCPs not only dictates their glass transition temperature (T_g) and melting point (T_m), but also has been demonstrated to play an important role in their supramoleculer structures [27, 28]. For MC-ILCPs with viologen, the LC properties can be controlled via tuning the main chain linkage position resulting in both thermotropic and lyotropic smectic phases [29]. For SC-ILCPs, their ILC mesogens are pendants located in the side chain or the ions are placed in the main chain and LC mesogens are situated in the side chain. Both of these ILCPs can be synthesized or assembled through free radical polymerization, silicon hydrogen addition, or non-covalent bond assembly [30–32]. Similarly to MC-ILCPs, the T_g, isotropic temperature (T_i), and LC behavior of the SC-ILCPs becomes varied due to the incorporation of the different cations and anions. For instance, SC-ILCPs with sulfonic groups and carboxylic groups can self-assemble to sandwich thermotropic smectic phase structure, but a similar structure with bromide anions displays nematic phase only [33, 34].

Side chain liquid crystalline polymers (SCLCPs) without ions can be divided into two classes according to the linkage type of mesogenic groups to the polymer backbone. These two classes are: i) terminally (end-on) SCLCPs [35, 36] or ii) laterally (side-on) SCLCPs [37, 38]. Normally, it is necessary to employ flexible spacers to decouple the interaction between the side chain and the backbone of SCLCPs [39, 40]. However, when the flexible spacers were very short or a single carbon-carbon bond in the side-on in SCLCPs was utilized, these polymers still exhibited LC behaviors [41]. The typical example of such systems are the mesogen-jacketed LC polymers (MJLCPs), [42-46] whose bulky mesogenic units are laterally attached to the polymer backbone via non- or only short spacers. The significantly high steric hindrance forces the polymer chain to become stiff. In fact, the mesogens may not be necessary as long as the bulky side groups around the backbone are large enough. For example, poly[dialkyl vinylterephthalate] (PDAVT) with an appropriate alkyl length could form a 2D hexagonal columnar LC phase (Φ_H) [47]. Based on the PDAVT, a combined main-chain/side-chain LC polymer (MCSCLCP) poly(2,5-bis{[6-(4-butoxy-4′-oxy biphenyl) hexyl] oxy carbonyl} styrene) (PBBHCS) have been designed and synthesized. It is found that the MCSCLCP can exhibit hierarchical supra-molecular structures with orderings on both the nanometer and subnanometer length scales [48]. Herein, we intend to incorporate ions into this kind of MCSCLCP to construct a novel combined main-chain/side-chain ionic liquid crystalline polymer (MCSC-ILCPs). The introduction of ions adds additional interactions to the existing interaction of chain biphenyl mesogens and the polymer backbone leading to more complex behavior of the system. Thus, it is hypothesized that the resulting materials could display a larger array of structural configurations when processing as a function of temperature. Ultimately, our intention is to investigate these new materials to help us to understand the supra-molecule hierarchical assembly process and structure in ILCPs. The chemical structures of the system and the corresponding model are as shown in Figure 1. It is worth mentioning that previous work has revealed that the side chains with ions and the main chain of ILCPs cannot be totally phase separated. The two entities act as a whole to form a column type structure – specifically, the hexagonal columnar LC ordered structure form [49]. In this work, the PILC prepared derives from the MCSCLCP. This system differs from previous works because not only does the spacer induce side chain and main chain phase separation, but its unique characteristics can create different LC phases due to the ionic mesogens in side chain.

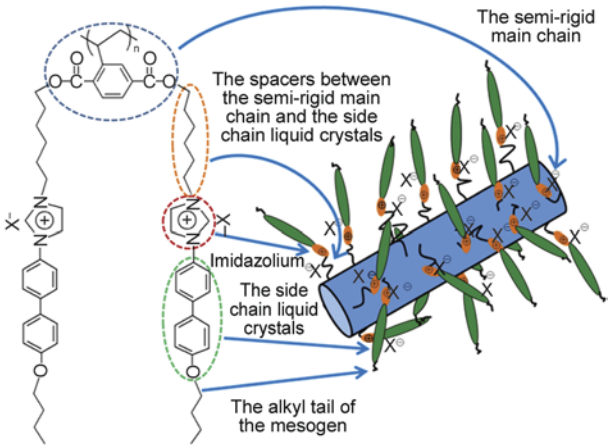

Figure 1. Chemical structures of MCSC-ILCPs poly(BImBHCS–X) (X^- = Br^-, BF_4^-, PF_6^- and $TFSI^-$)

Herein, we report the design and synthesis of the novel MCSC-ILCPs poly(2,5-bis{[6-(4-butoxy-4′-imidazolium biphenyl) hexyl] oxy carbonyl} styrene salts) [denoted as poly (BImBHCS–X), X^- = Br^-, BF_4^-, PF_6^- and $TFSI^-$) via radical polymerization. Detailed characterization of the thermal stability, phase transitions and LC ordered structures of ILCPs with different counter-anions were performed. The results showed that all the samples with varying counter-anions exhibited lamellar LC phase (SmA phase) except for the sample with $TFSI^-$. Additionally, these MCSC-ILCPs exhibited unique and enhanced fluorescence properties, which is able to promise a material for nanoscale technologies.

2. Experimental section

2.1. Instruments and measurements

Elemental analysis was carried out with an Elementar Vario EL instrument. ^{1}H NMR spectrum was taken at ambient temperature on a Bruker ARX400 spectrometer with chloroform-*d* ($CDCl_3$) as the solvent and tetramethylsilane (TMS) as the internal reference. Infrared spectroscopy was recorded on a PE Spectrum One FTIR spectrophotometer in KBr pellets over a range of 500–4000 cm^{-1}.

The apparent number-average M_w (M_n) and M_w distribution (M_w/M_n) were measured by a gel permeation chromatography (PL-GPC120). The μ-styragel columns used DMF as an eluent (1.0 mL/min) at 35°C. The calibration curve was obtained with linear polystyrene as standards.

Thermogravimetric analysis (TGA) was performed on a TA SDT 2960 instrument from room temperature to 600°C under nitrogen at a heating rate of 20°C/min. Differential scanning calorimetry (DSC) was performed on a TA DSC Q100 calorimeter under a continuous nitrogen purge and was recorded with a typical sample mass of 3~10 mg on the standard materials (indium and zinc) at different cooling and heating rates. LC texture was examined under polarized light microscopy (PLM) (Leica DM-LM-P) coupled with a Mettler-Toledo hot stage (FP82HT). The film was casted from chloroform solution and the thickness was approximately ~10 μm.

1D wide-angle X-ray diffraction (1D WAXD) experiments were performed on a Philips X′ Pert Pro diffractometer with a 3 kW ceramic tube as the X-ray source (Cu Ka) and an X′ celerator detector. The reflection peak positions were calibrated with silicon powder (2θ > 15°) and silver behenate (2θ < 10°). The sample stage was set horizontally and a temperature control unit (Paar Physica TCU 100) in conjunction with the diffractometer was employed to study the structure evolutions as a function of temperature. The heating and cooling rates in the WAXD experiments were 10°C/min. The 2D WAXD experiments were performed with a Bruker D8Discover in a transmission mode using a GADDS detector. The point-focused X-ray beam was aligned perpendicular to both the shear direction and the shear gradient. For both diffractometers, the X-ray sources (Cu KR) were provided by 3 kW ceramic tubes, and the diffraction peak positions were calibrated with silicon powder (2θ > 15°) and silver behenate (2θ < 10°).

UV-Vis absorption spectra were recorded with a Shimadzu MultiSpec-1501 spectrophotometer. All fluorescence measurements were carried out on a Perkin-Elmer LS55 luminescence spectrometer with excitation slit set at 5.0 nm and emission slit set at 3.0 nm.

2.2. Materials

Tetrahydrofuran (THF), acetonitrile and N-methyl-2-pyrrolidone(NMP) were desiccated by anhydrous magnesium sulfate, then filtered and purified with vacuum distillation before use. N, N-dimethylformamide (DMF) was heated circumfluence with calcium hydride for 48 hours, then filtered and obtained with vacuum distillation. Azobisisobutyronitrile (AIBN) was purified by recrystallization from ethanol before use. Lithium bis(trifluoromethanesulfonyl)imide (LiTFSI) obtained from Aladdin was

dried under vacuum overnight. Other solvents and reagents were used as received from commercial sources.

2.3. Synthesis

The synthetic route of the monomers and polymers MCSC-ILCPs is given in Figure 2. The detailed synthesis and characterization of intermediates, monomers, and polymers are provided as following.

2.4. Synthesis of MCSC-PILCs

2.4.1. Synthesis of 4-bromo-4′-butoxy biphenyl

4-bromo-4′-hydroxy biphenyl 2.49 g (10 mmol), 1-butyl bromide 2.05 g (15 mmol), K_2CO_3 2.76 g (20 mmol), and with KI 0.33 g (2 mmol) were refluxed in DMF until TLC indicated full conversion. Reaction mixture was cooled and filtered, the filter residue was washed with acetone. Filtrate was collected and removed with rotating vaporizer apparatus. The amount of DMF was reduced to 25% by vacuum distillation and the concentrated solution was precipitated in a mass of distilled water and the precipitate was filtered and collected. The product was dried in a vacuum oven over night and purified by recrystallization from ethanol, yield 82% of a white solid.^{1}H NMR ($CDCl_3$) δ (ppm): 7.56–7.54 (d, 2H, Ar–*H*), 7.50–7.48 (d, 2H, Ar–*H*), 7.44–7.42 (d, 2H, Ar–*H*), 6.99–6.97(d, 2H, Ar–*H*), 4.02 (t, 2H, –O*CH*$_2$–), 1.81 (m, 2H, –C*H*$_2$–), 1.54 (m, 2H, –C*H*$_2$–), 1.02–0.99 (t, 3H, –C*H*$_3$).

2.4.2. Synthesis of 4-butoxy-4′-imidazolyl biphenyl

4-bromo-4′-butoxy biphenyl 3.05 g (10 mmol), imidazole 1.02 g (15 mmol), K_2CO_3 2.76 g (20 mmol), and together with CuI 0.382 g (2 mmol) were put into a three-necked round bottom flask and stirred in dry N-methy-2-pyrrolidone under nitrogen atmosphere at 190°C for 24 h. The mixture was cooled down, filtered and washed with dichloromethane, and then the solvent was removed with rotate vaporizing apparatus. The remainder flowed through a short column filled with neutral aluminum oxide powder, and the residual liquid was precipitated in water and filter residue was collected. The solid product was dried in a vacuum oven over night, and then purified by recrystallization from hexane, yield 40.5% of a white or silver grey solid. ^{1}H NMR ($CDCl_3$) δ (ppm): 8.03 (s, 1H, Im–*H*2), 7.70–7.68 (d, 2H, Ar–*H*), 7.56–7.54 (d, 2H, Ar–*H*), 7.48–7.46 (d, 2H, Ar–*H*), 7.37 (br s, 1H, Im–*H*4), 7.28 (br s, 1H, Im–*H*5), 7.03–7.01 (d, 2H, Ar–*H*), 4.04 (t, 2H, –O*CH*$_2$–), 1.82–1.81 (m, 2H, –C*H*$_2$–), 1.55 (m, 2H, –C*H*$_2$–), 1.03–1.02 (t, 3H, –C*H*$_3$).

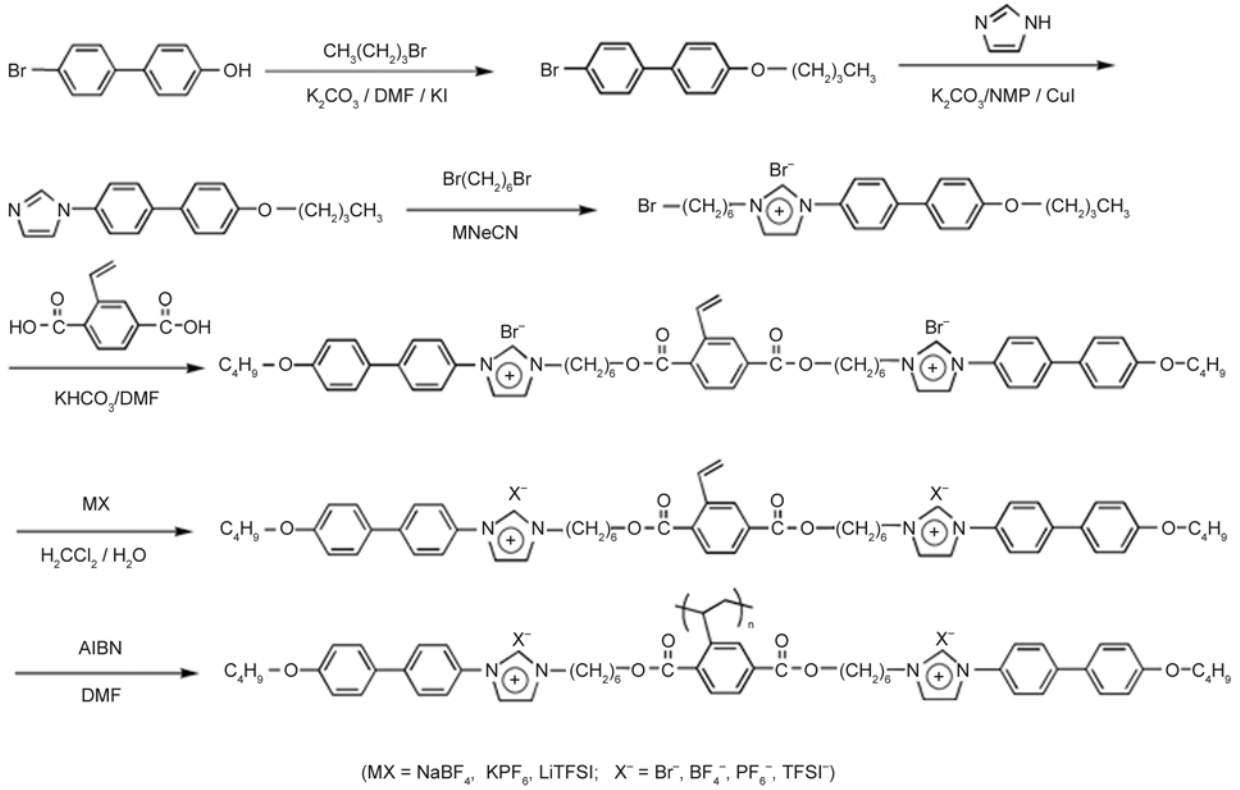

Figure 2. Synthetic route of the ILCs and the corresponding MCSC-ILCPs

2.4.3. Synthesis of ω-(4-butoxy biphenyl-4′-imidazolium)-1-bromo hexane bromide

4-butoxy-4′-imidazolyl biphenyl 2.92 g (10 mmol), 1,6-dibromohexane 7.32 g (30 mmol), and together with dry acetonitrile were added into a round bottom flask and refluxed until TLC indicated full conversion. The mixture was cooled down and the solvent was removed by rotating vaporizer apparatus. The residual liquid was precipitated in ethyl acetate, and the solid was washed with THF at least three times and then dried in a vacuum oven over night. The collected product was dissolved in a little dichloromethane and purified by the silicon column using mixed solvent (dichloromethane:methanol = 10:1) as the eluent. The first ingredient was collected and the eluent was removed with rotate vaporizing apparatus, then the product dried in a vacuum oven gave a pale-grey viscous solid. Yield: 80.2%. ^{1}H NMR ($CDCl_3$) δ (ppm): 11.15 (s, 1H, Im–*H*2), 7.78–7.76 (d, 2H, Ar–*H*), 7.68–7.66 (d, 2H, Ar–*H*), 7.62 (br s, 1H, Im–*H*4), 7.50 (br s, 1H, Im–*H*5), 7.46–7.43 (d, 2H, Ar–*H*), 6.94–6.92 (d, 2H, Ar–*H*), 4.58–4.55 (t, 2H, –N$^+$CH_2–), 3.97–3.94 (t, 2H, –OCH_2–), 3.37–3.34 (t, 2H, –CH_2Br), 2.00–1.97(m, 2H, –CH_2–), 1.83–1.71 (m, 4H, –CH_2–), 1.49–1.41 (m, 6H, –CH_2–), 0.96–0.92 (t, 3H, –CH_3).

2.4.4. Synthesis of 2-vinyl p-biphthalic acid

2-vinyl p-biphthalic acid was obtained by using the previous method from Zhang *et al*. [70]. ^{1}H NMR (DMSO-d_6) δ (ppm): 8.24 (s, 1H, Ar–*H*), 7.92 (d, 2H, Ar–*H*), 6.67 (d, 1H, =C*H*–), 5.75 (d, 1H, =CH_2), 5.42 (d, 1H, =CH_2).

2.4.5. Synthesis of monomers

2, 5-bis{[6-(4-butoxy-4'-imidazolium-biphenyl) hexyl] oxy carbonyl} styrene bis(bromide) (BImBHCS–Br)

2-vinyl p-biphthalic acid 0.96 g (5 mmol) and potassium hydrogen carbonate 1.0 g (10 mmol) were added into a 250 mL round bottom flask and stirred in DMF about 30 min until the vinyl p-biphthalic acid was dissolved completely. Then the ω-(4-butoxy biphenyl-4′-imidazolium)-1-bromo hexane bromide 6.70 g (12.5 mmol) and nitrobenzene 0.02 g (0.18 mmol) were input the flask and the mixture was stirred at 100°C until TLC indicated full conversion. After the reaction was over, the mixture was cooled down, filtered and the filtrate was added to ethyl acetate for precipitating. The resulting precipitate was collected and washed with THF five times. The crude product was separated through a silicon column by using the ethanol solution as the eluent until the first deserted ingredient outflow completely, and then exchanging mixed solvent (dichloromethane:methanol = 5:1) as the eluent. The previous outflowing ingredient was collected. By removing the solvent with rotate vaporizing apparatus, the product dried in a freeze drying gave a pale-yellow solid. Yield: 63.8%. ^{1}H NMR ($CDCl_3$) δ (ppm): 11.07 (s, 2H, Im–*H*2), 8.18 (s, 1H, Ar–*H*), 7.96–7.89 (d, 2H, Ar–*H*), 7.81–7.79 (d, 4H, Ar–*H*), 7.73 (s, 2H, Im–*H*4), 7.69–7.66 (d, 4H, Ar–*H*), 7.64 (s, 2H, Im–*H*5), 7.49–7.43 (d, 4H, Ar–*H*), 6.95 (d, 1H, =C*H*–), 6.93 (d, 4H, Ar–*H*), 5.74–5.70 (d, 1H, =CH*H*), 5.41–5.38 (d, 1H, =CH*H*), 4.61–4.57 (t, 4H, –N$^+$CH_2–), 4.30–4.28 (t, 4H, –COOCH_2–), 4.00–3.96 (t, 4H, –OCH_2–), 2.04 (m, 4H, –CH_2–), 1.79–1.76 (m, 8H, –CH_2–), 1.50 (m, 12H, –CH_2–), 0.99–0.96 (t, 6H, –CH_3).

FTIR (KBr): ν O–H/Br ···H 3441 (s), Ar C–H 3054 (w), Im C–H 2957 (s), Ar C–H 2929 (s), –CH_2– 2868 (s), –COO 1718 (s), Ar C–H 1651 (m), C=C 1608 (m), Ar skeletal vibration 1560 (m), Im C=N 1499 (m), –CH_2– 1465 (m), –CH_3 1384 (m), Im C–N 1288 (m), C–O–C 1248 (s), Im skeletal vibration 1180 (w), Im C–N 1115 (m), Im C–N 1072 (m), C–O–C 1036 (w), Ar–CH=CH_2 972 (w), Ar–CH=CH_2 916 (w), Ar C–H 824 (m), Im C–H 760 (m), Ar C–H 618 (m) cm^{-1}.

Anal. Calcd for $C_{60}H_{70}N_4O_6Br_2$: C, 65.43; H, 6.41; N, 5.09; Found: C, 64.79; H, 6.54; N, 5.08.

Anion exchange reaction for other three monomers

Because the used anion-exchange reactions of the ILC monomers are similar, herein, we took the monomer BImBHCS–BF_4 as an example to illustrate the process. The monomer BImBHCS–Br 3.30 g (3 mmol) was dissolved in dichloromethane and sodium fluoroborate ($NaBF_4$) 1.65 g (15 mmol) dissolved in deionized water were mixed at a 250 mL round bottom flask under vigorous stirring for nearly 10 hours. After the reaction complete, the mixed solution was extracted with dichloromethane 50 mL by twice, and washed with deionized water 50 mL by five times until the eluent remained clear with the addition of an aqueous solution of $AgNO_3$. The organic phase was collected and dried with $MgSO_4$ and filtered. The solvent was removed with rotate

vaporizing apparatus. The product was dried in a freeze dryer.

2,5-bis{[6-(4-butoxy-4′-imidazolium-biphenyl) hexyl] oxy carbonyl} styrene bis(fluoroborate) (BImBHCS–BF_4) Yield: 89.5% of an off-white solid.

^{1}H NMR ($CDCl_3$) δ (ppm): 9.25 (s, 2H, Im–*H*2), 8.18 (s, 1H, Ar–*H*), 7.99–7.93 (d, 2H, Ar–*H*), 7.68 (d, 4H, Ar–*H*), 7.63 (s, 2H, Im–*H*4), 7.58–7.56 (d, 4H, Ar–*H*), 7.47 (s, 2H, Im–*H*5), 7.45–7.43 (d, 4H, Ar–*H*), 6.95 (d, 1H, =C*H*–), 6.93 (d, 4H, Ar–*H*), 5.75–5.71 (d, 1H, =CH*H*), 5.41–5.38 (d, 1H, =CH*H*), 4.35–4.32 (t, 4H, –N^+CH_2–), 4.30–4.28 (t, 4H, –COOCH_2–), 4.00–3.97 (t, 4H, –OCH_2–), 1.98 (m, 4H, –CH_2–), 1.80–1.74 (m, 8H, –CH_2–), 1.52–1.49 (m, 12H, –CH_2–), 1.01–0.98 (t, 6H, –CH_3).

FTIR (KBr): ν O–H 3437 (s), Im C–H 3152 (w), Ar C–H 3042 (w), Im C–H 2956 (s), Ar C–H 2927 (s), –CH_2– 2869 (s), –COO 1718 (s), Ar C–H 1640 (w), C=C 1607 (m), Ar skeletal vibration 1563 (m), Im C=N 1499 (w), –CH_2– 1465 (s), –CH_3 1382 (m), Im C–N 1289 (m),C–O–C 1248 (s), Im skeletal vibration 1180 (m), Im C–N 1114 (m), BF_4^-1068 (s), Ar–CH=CH_2 972 (w), Ar–CH=CH_2 917 (w), Ar C–H 823(s), Im C–H 761 (m), Ar C–H 621 (m) cm^{-1}.

Anal. Calcd for $C_{60}H_{70}N_4O_6B_2F_8$: C, 64.49; H, 6.32; N, 5.02; Found: C, 64.79; H, 6.53; N, 4.82.

2,5-bis{[6-(4-butoxy-4′-imidazolium-biphenyl) hexyl] oxy carbonyl} styrene bis(hexafluorophosphate) (BImBHCS–PF_6) Yield: 88.2% of a light red solid.

^{1}H NMR ($CDCl_3$) δ (ppm): 8.86 (s, 2H, Im–*H*2), 8.18 (s, 1H, Ar–*H*), 7.99–7.92 (d, 2H, Ar–*H*), 7.61–7.59 (d, 4H, Ar–*H*), 7.51 (s, 2H, Im–*H*4), 7.48 (d, 4H, Ar–*H*), 7.44 (s, 2H, Im–*H*5), 7.42 (d, 4H, Ar–*H*), 6.95 (d, 1H, =C*H*–), 6.93 (d, 4H, Ar–*H*), 5.74–5.70 (d, 1H, =CH*H*), 5.40–5.37 (d, 1H, =CH*H*), 4.28 (t, 4H, –N^+CH_2–), 4.28 (t, 4H, –COOCH_2–), 4.00–3.97 (t, 4H, –OCH_2–), 1.97 (m, 4H, –CH_2–), 1.81–1.74 (m, 8H, –CH_2–), 1.55–1.47 (m, 12H, –CH_2–), 1.01–0.98 (t, 6H, –CH_3).

FTIR (KBr): ν O–H 3445 (s), Im C–H 3160 (w), Im C–H 2957 (m), Ar C–H 2931 (m), –CH_2– 2870 (m), –COO 1717 (s), Ar C–H 1670(s), C=C 1607 (m), Ar skeletal vibration 1564 (w), Im C=N 1499 (s), –CH_2– 1467 (w), –CH_3 1383 (w), Im C–N 1291 (w),C–O–C 1248 (s), Im skeletal vibration 1181 (w), Im C–N 1119 (m), Im C–N 1076 (m), Ar–CH=CH_2 972 (w), Ar–CH=CH_2 919 (w), PF_6^- 842 (vs), Im C–H 762 (w), Ar C–H 622 (m) cm^{-1}.

Anal. Calcd for $C_{60}H_{70}N_4O_6F_{12}P_2$: C, 58.42; H, 5.72; N, 4.54; Found: C, 58.78; H, 5.62; N, 4.48.

2,5-bis{[6-(4-butoxy-4′-imidazolium-biphenyl) hexyl] oxy carbonyl}styrene bis [bis (trifluoromethanesulfonyl) imide] (BImBHCS–TFSI) Yield: 88.0% of a yellowish solid.

^{1}H NMR ($CDCl_3$) δ (ppm): 9.12 (s, 2H, Im–H_2), 8.21 (s, 1H, Ar–*H*), 7.94–7.89 (d, 2H, Ar–*H*), 7.69–7.67 (d, 4H, Ar–*H*), 7.58 (s, 2H, Im–*H*4), 7.56–7.54 (d, 4H, Ar–*H*), 7.50 (s, 2H, Im–*H*5), 7.48 (d, 4H, Ar–*H*), 6.98 (d, 1H, =C*H*–), 6.96 (d, 4H, Ar–*H*), 5.75–5.71 (d, 1H, =CH*H*), 5.40–5.38 (d, 1H, =CH*H*), 4.33 (t, 4H, –N^+CH_2–), 4.32 (t, 4H, –COOCH_2–), 4.01–3.98 (t, 4H, –OCH_2–), 1.99 (m, 4H, –CH_2–), 1.78–1.77 (m, 8H, –CH_2–), 1.56–1.48 (m, 12H, –CH_2–), 1.01–0.97 (t, 6H, –CH_3).

FTIR (KBr): ν O–H 3450 (s), Im C–H 3139 (w), Im C–H 2954 (m), Ar C–H 2926 (s), –CH_2– 2867 (m), –COO 1700 (s), Ar C–H 1673(w), C=C 1605 (m), Ar skeletal vibration 1566 (w), Im C=N 1499 (m), –CH_2– 1465 (m), –CH_3 1384 (w), $TFSI^-$ 1354 (s), Im C–N 1280 (m), C–O–C 1242 (m), $TFSI^-$ 1178 (s), Im C–N 1135 (m), $TFSI^-$ 1056 (s), Ar–CH=CH_2 973 (w), Ar–CH=CH_2 916 (w), Ar C–H 824 (s), Im C–H 760 (w), $TFSI^-$ 738 (w), Ar C–H 614 (s) cm^{-1}.

Anal. Calcd for $C_{64}H_{70}N_6O_{14}F_{12}S_4$: C, 51.12; H, 4.70; N, 5.59; Found: C, 51.44; H, 4.77; N, 5.56.

2.4.6. Synthesis of MCSC-PILCs

Poly (2, 5-bis {[6-(4-butoxy-4′-imidazolium-biphenyl) hexyl] oxy carbonyl} styrene salts) [poly(BImBHCS–X)] (X^- = Br^-, BF_4^-, PF_6^- and $TFSI^-$). Via conventional radical polymerization, all of the MCSC-PILCs were obtained. And due to all the polymer reaction process was similar. So, a typical polymerization procedure for poly(BImBHCS–Br) was carried out as an example. The monomer BImBHCS–Br 1.10 g (1 mmol), 1 mg/mL DMF solution of AIBN 1.65 mL and together with the purified DMF 1.05 mL were input a polymerization tube. After three freeze-pump-thaw cycles, the tube was sealed off under vacuum. Polymerization was carried out at 70°C for 40 h. Then the tube was opened, and the reaction mixture was diluted with a few dichloromethane, and then it was precipitated in methanol. The polymer was purified by washed with methanol three times and frozen for drying to a constant weight. The other counter-anions polymers were obtained by the same way

except the precipitator and purification reagent of poly(BImBHCS–TFSI) was diethyl ether.

3. Results and discussion

3.1. Synthesis of monomers

In this work, we have successfully designed and synthesized the targeted MCSC-ILCPs via a multistep reactions route. The monomers with different counter-anions were synthesized as shown in the Figure 2. First, we synthesized the monomer with Br^- counter-anion, and then the other monomers with different counter-anions were obtained by an anion-exchange process. [50]. Figure 3 shows the ^1H NMR spectra of the monomers with different counter-anions. It was evident that the chemical shifts present at 6.95, 5.74–5.70, and 5.41–5.38 ppm (denoted j, l and m, respectively) represented the characteristic resonance peaks of the vinyl substituent of monomers. Completion of the anion-exchange step was determined by the changes in the assigned peaks. For example, the 2-substituent proton hydrogen in imidazolium (denoted a) of the monomers with different counter-anions exhibited different chemical shifts depending on the type of counter-anion used. The chemical shift of the 2-substituent proton hydrogen in imidazolium were presented at 11.07, 9.25, 8.86, and 9.12 ppm for the monomers contained Br^-, BF_4^-, PF_6^- and $TFSI^-$, respectively. The order of the chemical shifts of the 2-substituent proton hydrogen in imidazolium monomers was monomer with Br^- > monomer with BF_4^- > monomer with PF_6^- > monomer with $TFSI^-$. Because large counter-anions provided better shielding, it resulted in the chemical shift being moved towards the high-field after the anion exchange step [51, 52].

At the same time, FTIR was utilized to confirm the NMR results and the chemical structure of the mate-

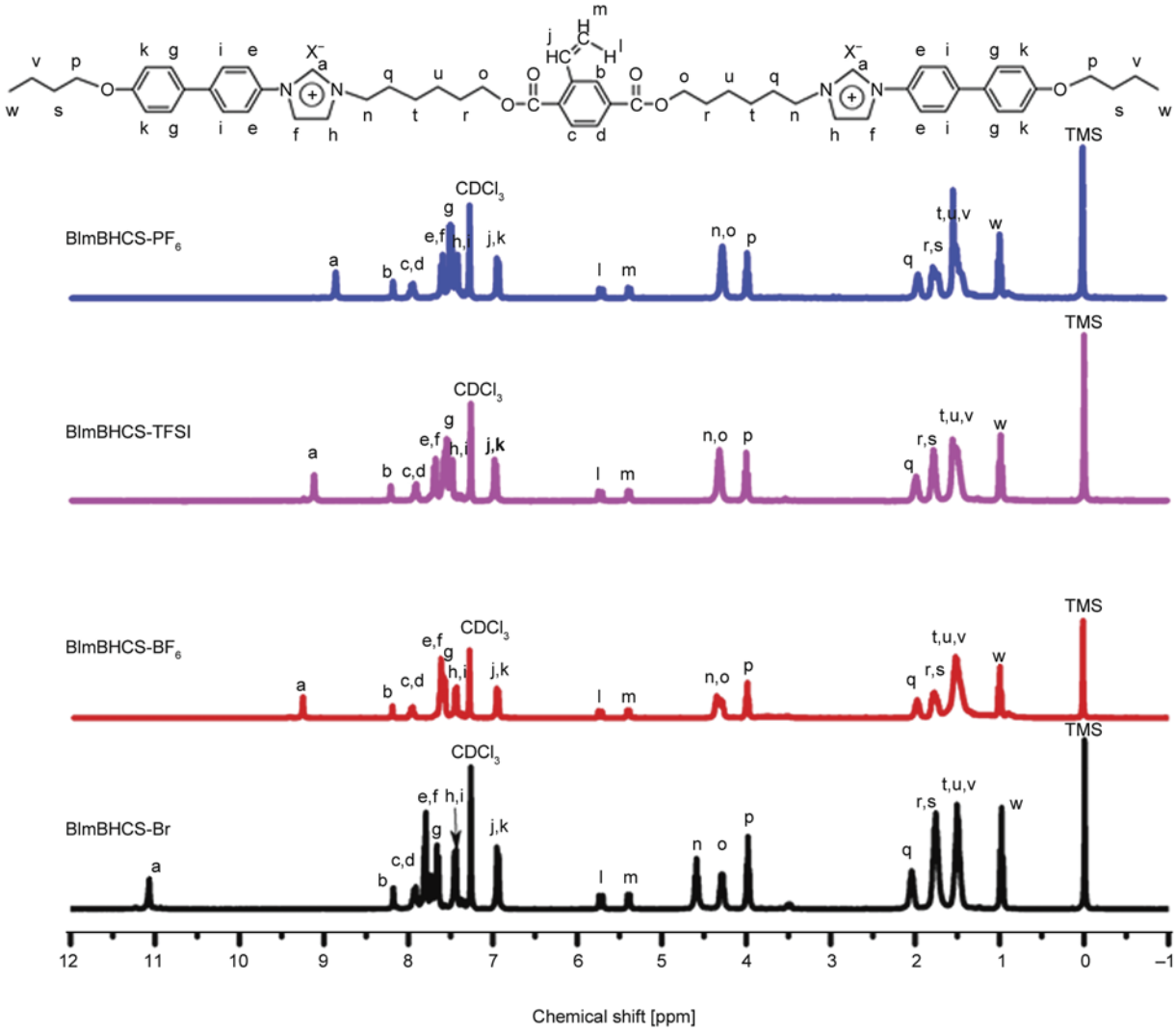

Figure 3. ^1H NMR spectra of ILC monomers BImBHCS–X (X^- = Br^-, BF_4^-, PF_6^- and $TFSI^-$)

rials prepared. The characteristic stretching vibration peaks observed for the different counter-anions were as follows: 1068 cm^{-1} for $BF4^{-}$, 842 cm^{-1} for $PF6^{-}$, and 1354, and 1178, 1056, 738 cm^{-1} for $TFSI^{-}$. Because residual water was present in the sample, the stretching for Br^{-} could not be discerned from the FTIR spectrum. Both the NMR and FTIR results were in good agreement with data found in the literatures [53, 54]. To recap, the combination of ^1H NMR and FTIR experiments demonstrated that the ionic liquid crystals side chain monomers with different anions were successfully prepared and the anion-exchange step was successfully achieved.

3.2. Synthesis of MCSC-ILCPs poly(BImBHCS–X) with different counter-anions

In this study, all monomers with vinyl substituent were polymerized via a simple radical polymerization method. Herein, the polymer poly(BImBHCS–BF_4) was used as an example to describe the process. ^1H NMR spectra of ILC monomer BImBHCS–BF_4 and the corresponding MCSC-PILC poly(BImBHCS–BF_4) are depicted in Figure 4. It was observed that the characteristic chemical shifts of the vinyl substituent of BImBHCS–BF_4 were present at 6.95, 5.75–5.71 and 5.41–5.38 ppm (denoted as j, l and m respectively). After polymerization these characteristic resonance peaks disappeared completely. Moreover, compared to the ILC monomer BImBHCS–BF_4, the chemical shift peaks of poly(BImBHCS–BF_4) became quite broad, which was consistent with the anticipated polymer structure.

To further confirm the chemical structures of the MCSC-ILCPs, we carried out the experiment of FTIR spectroscopic to analyze the materials. As mentioned above, we used the same monomer BImBHCS–BF_4 and the corresponding polymer poly(BImBHCS–BF_4) as the example to illustrate the process. The characteristic peaks of the monomer BImBHCS–BF_4, such as 1607 cm^{-1}, was assigned to C=C stretching-vibration, the peaks of 972 and 916 cm^{-1} was assigned to C–H out-of-plane bending vibration of the vinyl which completely disappeared after polymerization. In addition, restraint of the intra-molecular motion within the polymer material

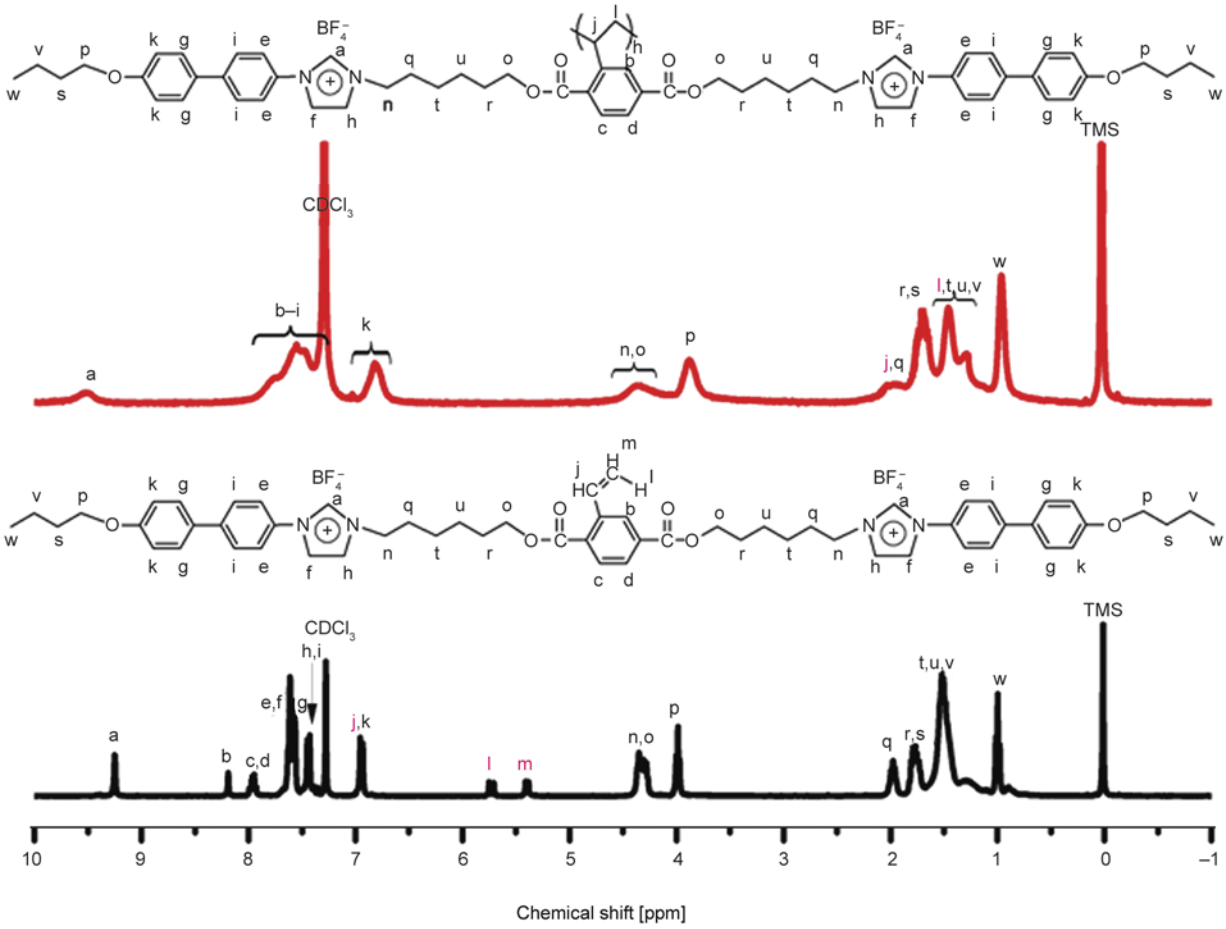

Figure 4. ^1H NMR spectra of BImBHCS–BF_4 and the corresponding poly(BImBHCS–BF_4)

Table 1. Molecular characteristics and the phase transition temperatures of poly(BImBHCS–X)

Sample	M_n ($\cdot 10^4$)[a]	M_w/M_n[a]	T_g[b] [°C]	T_i[b] [°C]
poly(BImBHCS–Br)	6.7	2.15	93	–
poly(BImBHCS–BF_4)	5.0	1.59	72	–
poly(BImBHCS–PF_6)	4.2	1.32	85	182
poly(BImBHCS–PTFSI)	4.0	1.21	36	–

[a]Determined from GPC results, linear PS as standards.
[b]Evaluated by DSC at a rate of 10°C/min under cooling.

resulted in a reduction of the intensity of the infrared peaks when compared to the corresponding monomer after polymerization. The FTIR spectra were in good agreement with the results from ^{1}H NMR spectroscopy. Moreover, the molecular weight and number distribution and polydispersity of MCSC-ILCPs poly (BImBHCS–X) with different counter-anions were determined using gel permeation chromatography (GPC). The results from gel permeation chromatography are shown in Table 1.

3.3. Thermal properties and liquid crystal ordered structures

Before studying phase behavior and phase structure, we first investigated the thermal stability of MCSC-ILPC. Figure 5 depicts the thermal stability of the materials with different counter-anions under a nitrogen atmosphere. The results indicated that all the samples had excellent thermal stability because the samples' decomposition temperatures were above 320°C except that of poly(BImBHCS–Br) at about 275°C. The thermal stability order for the series of polymers with different counter-anions was: poly (BImBHCS–TFSI), poly(BImBHCS–PF_6), poly (BImBHCS–BF_4) and poly(BImBHCS–Br), and this ordering was consistent with the nature of the type of counter-anions in poly(BImBHCS–X) [55]. DSC was used to investigate the phase transitions of the MCSC-ILCPs. Figure 6a gives a set of DSC traces for MCSC-ILCPs that correspond to the first cooling and second heating (which were recorded at the rate of 10°C/min). These curves were collected after erasing the initial thermal history of the sample. Only one T_g for these MCSC-ILCPs could be observed during the whole cooling and heating process except for the sample poly(BImBHCS–PF_6), which exhibited an additional phase transition temperature. Moreover, we used the sample poly (BImBHCS–BF_4) as an example to further investigate the phase transition behavior with different heating and cooling rates of 2.5, 5, 10, and 20°C/min. However, the data in Figure 6b only showed a single glass transitions T_g. Based on the DSC results, the order of the T_g is poly(BImBHCS–Br) > poly (BImBHCS–PF_6) > poly(BImBHCS–BF_4) > poly (BImBHCS–TFSI). The observed T_g trend resulted from the different nucleophilicity and steric effect of counter-anions [56]. For example, the $TFSI^-$ anion, which has relatively large steric hindrance and weak nucleophilicity, aided in the segment-movement strengthening of the material [57, 58], and thus this material (poly(BImBHCS–TFSI)) gave the lowest T_g temperature among the four samples.

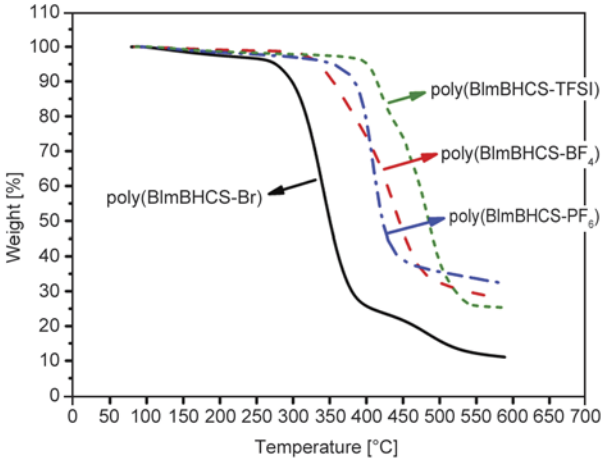

Figure 5. TGA thermograms of poly(BImBHCS–X) (X^- = Br^-, BF_4^-, PF_6^- and $TFSI^-$) at a rate of 10°C/min in nitrogen flow

To study the LC properties of the class of MCSC-ILCPs prepared herein, we performed PLM to investigate their birefringence phenomena. First, the thin film of poly(BImBHCS–X) (X^- = Br^-, BF_4^-, PF_6^- and $TFSI^-$) were drop casted from chloroform solution. As shown in Figure 7, each of the polymers exhibited strong birefringences upon heating except for poly(BImBHCS–TFSI), which indicated the existence of LC phases. Moreover, the samples MCSC-ILCPs poly(BImBHCS–Br) and poly(BImBHCS–BF_4) always maintained their birefringences during heating and cooling process until decomposition. For the sample poly(BImBHCS–PF_6), the birefringences disappeared after the temperature exceeded 182°C during the heating process. Subsequently, the texture would reappear again during the cooling process. For sample poly(BImBHCS–TFSI), no birefringences were found during the whole consecutive heating and cooling process. The appropriate volume size of the counter-anions Br^-,

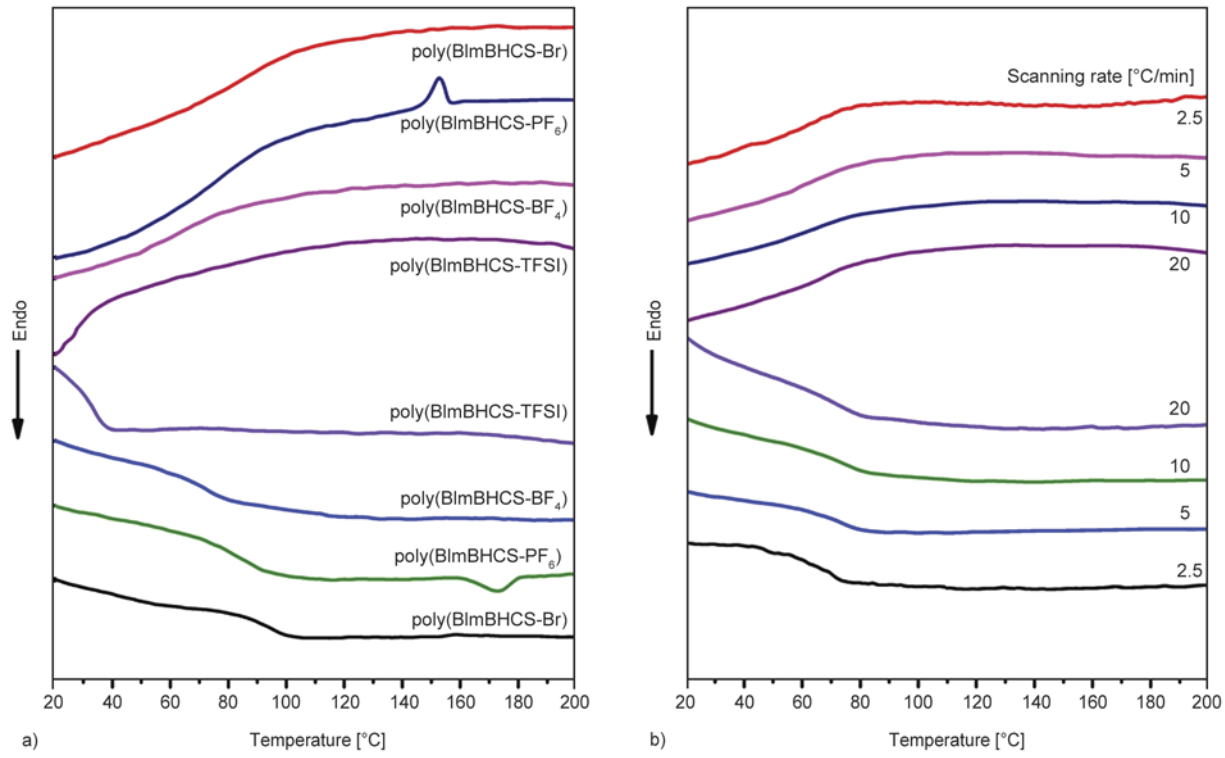

Figure 6. DSC thermograms of poly(BImBHCS–X) (X^- = Br^-, BF_4^-, PF_6^- and $TFSI^-$) at a rate of 10 °C/min (a) and poly(BImBHCS–BF_4) at different rates (b)

BF_4^- and PF_6^- facilitated LC formation, but the $TFSI^-$ counter-anion hindered the polymer to form the ordered structure because of its large volume. [59]. Note that the polymer PBBHCS with similar chemical structure of MCSC-ILCPs poly(BImBHCS–X) could exhibit typical different color fan texture, indicating highly ordered structure, but none of the poly(BImBHCS–X) samples exhibited any typical texture. It was obvious that the incorporation of counter-anions significantly restrained the formation of textures.

1D WAXD experiment was performed to identify the LC ordered structures of MCSC-ILCPs. Figure 8 presents the X-ray patterns of these polymers with different counter-anions. It was clearly found that all of the samples rendered an amorphous halo near 22° in high-angle region. This observation was attributed to the lack of long-range order at the sub-nanometer length scale. On the other hand, there were other three sharp diffractions at 2θ of 1.77, 3.56 and 5.34° for poly(BImBHCS–Br) and at 2θ of 1.85, 3.72 and 5.58° for poly(BImBHCS–BF_4) in the low-angle region. The q ratio ($q = 4\pi\cdot\sin(\theta/\lambda)$) of the diffractions were 1:2:3, so these peaks were assigned to the (001), (002) and (003) plane of smectic phase (lamellar structure). Furthermore, there were two diffractions peaks at 2θ of 1.94 and 3.89° for the sample poly(BImBHCS–PF_6) and its q ratio remained 1:2 ratio, which was attributed to (001) and (002) plane. Meanwhile, we roughly estimated the spacing of the layer was 6.00 nm for these MCSC-ILCPs according to the all-trans conformation, but according to 1D WAXD data it revealed that the d-spacings were 4.98, 4.77 and 4.55 nm for poly(BImBHCS–Br), poly(BImBHCS–BF_4) and poly(BImBHCS–PF_6), respectively. Therefore, we speculated that the SmA or SmC phases had formed. However, no sharp diffraction peak was detected in the low-angle and high-angle region for poly (BImBHCS–TFSI), only two scattering halos in the 2θ region between 2 and 35° were observed, which indicated the absence of the highly ordered structures.

Variable-temperature WAXD experiments were performed to elucidate LC ordered structures of MCSC-ILCPs under different temperatures. The previous discussed WAXD results established that poly(BImBHCS–BF_4) had similar LC properties and ordered structure to that of poly(BImBHCS–Br). Therefore, we used the polymer poly(BImBHCS–BF_4) as a model sample to describe the LC ordered structure transition upon temperature evolution. As

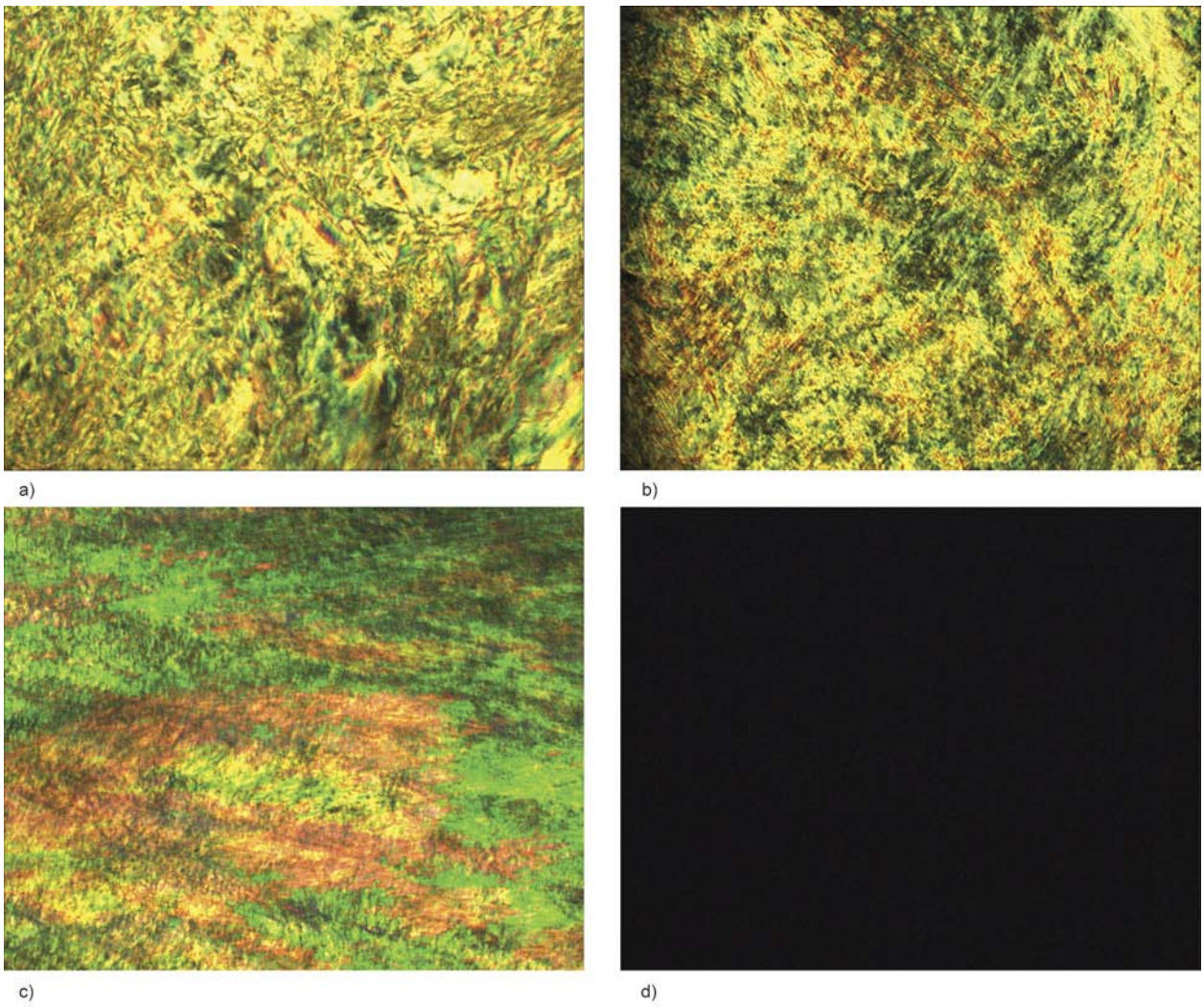

Figure 7. Representative textures of poly(BImBHCS–Br) (a), poly(BImBHCS–BF_4) (b), poly(BImBHCS–PF_6) (c) and poly(BImBHCS–TFSI) (d) during heating (200× magnification)

shown in Figure 9a, the sample of poly(BImBHCS–BF_4) rendered an amorphous halo in the high angle region and two sharp peaks at 2θ of 1.85 and 3.72° assigned to (001) and (002) in the low angle region at low temperature during the heating process. With the increasing of temperature, the peaks become sharper and their intensity gradually became stronger but there was relatively no shift in the peak position. At the same time, a new peak at 5.58° was observed and it was assigned to (003). Furthermore, none of the diffraction peaks disappeared until heating the sample to the decomposition temperature. This observed behavior mimicked the known transitional behavior of MJLCPs. However, in the case of the sample poly(BImBHCS–PF_6), there were some differences with the WAXD experiment results. As shown in Figure 9b, only two shape diffraction peaks of 1.94 and 3.89° in the low angle region assigned to (001) and (002) remained when changing the temperature and the third diffraction peak did not always appear when increasing the temperature. When the temperature exceeded 182°C, all of the diffraction peaks disappeared indicating the arrival of isotropic phase. During the cooling process, the

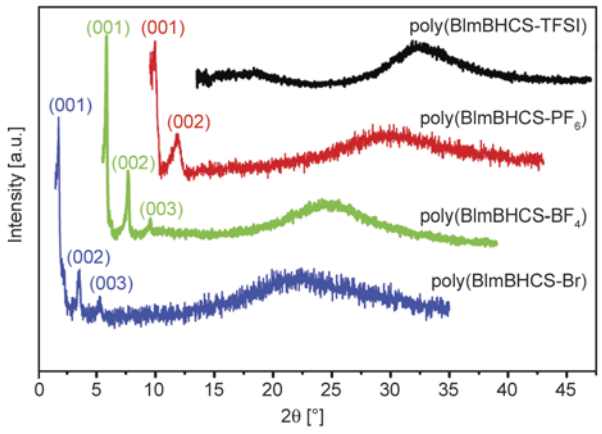

Figure 8. 1D WAXD powder patterns of poly(BImBHCS–X) (X^- = Br^-, BF_4^-, PF_6^- and $TFSI^-$)

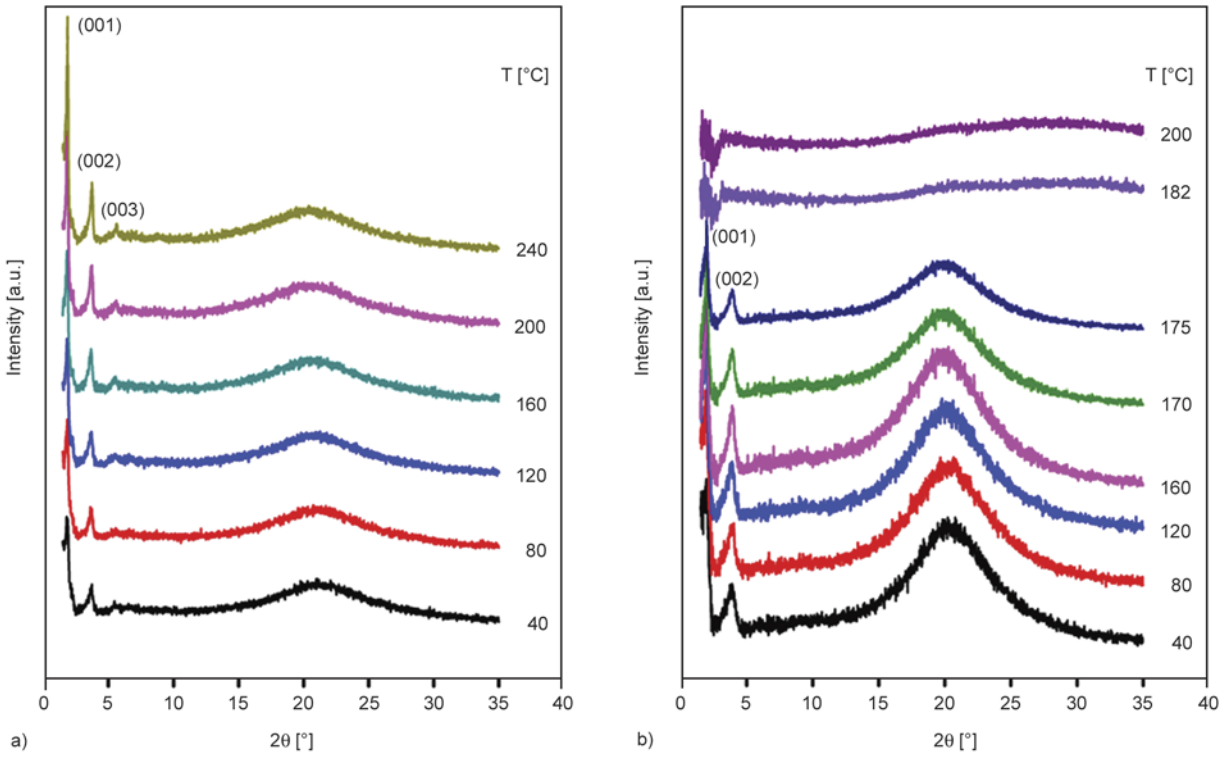

Figure 9. 1D WAXD powder patterns of poly(BImBHCS–BF_4) (a) and poly(BImBHCS–PF_6) (b) under heating

process was observed to be reversible because the sample poly(BImBHCS–PF_6) displayed lamellar diffraction peaks upon cooling. As for the sample poly(BImBHCS–TFSI), no diffraction peaks were observed during both the heating and cooling processes. The X-ray scattering results were consistent with the results of DSC and PLM.

To confirm the precise LC ordered structure of the MCSC-ILCPs poly(BImBHCS–X) (X^- = Br^-, BF_4^- and PF_6^-), 2D WAXD experiments were performed. Figure 10a schematically shows the sheared sample with the shear direction and shear gradient. The pattern for this sample poly(BImBHCS–PF_6) is shown in Figure 10b. From the result, it was found that there are two pairs of sharp diffraction arcs at 2θ of 1.94 and 3.89° assigned to (001) and (002) in the equator and the *q* ratio remains 1:2, which corresponded to the *d*-spacing of 4.55 and 2.27 nm, respectively. Meanwhile, a pair of diffuse halos displayed in the meridian region, indicated that the side-chain was laterally aligned. We can speculate the layer normal of the LC phase was perpendicular to the shear

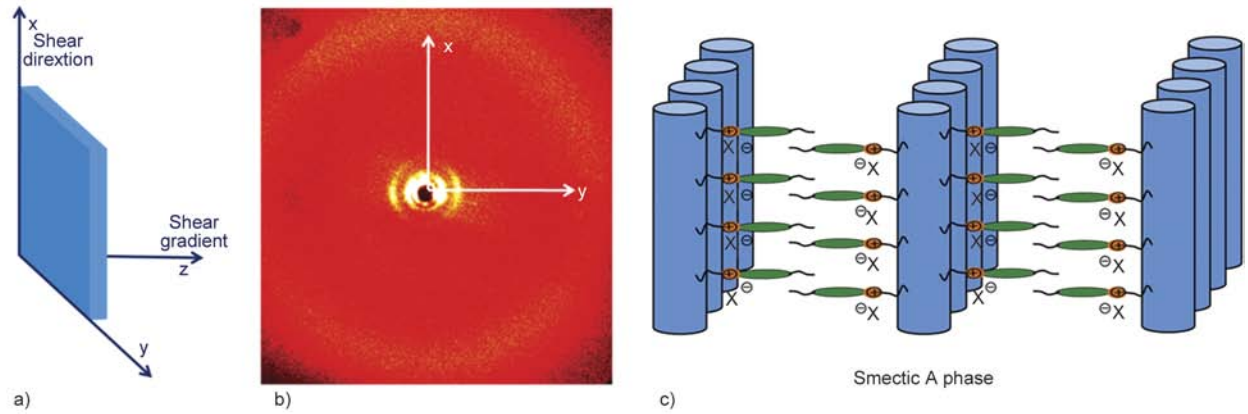

Figure 10. (a) Schematic drawing of the sheared sample with the shear direction and shear gradient, respectively; (b) 2D WAXD pattern of the oriented sample poly(BImBHCS–PF_6) obtained at room temperature; (c) schematic drawing of the proposed supra-molecular structures for MCSC-ILCPs poly(BImBHCS–X) with counter-anions Br^-, BF_4^-, PF_6^-

direction. This result strongly demonstrated that the polymer formed SmA phase ordered structure, and the side chain partially overlapped between each other. Unfortunately, the other samples poly (BImBHCS–Br) and poly(BImBHCS–BF_4) did not display any orientation during the heating process up to decomposition. The lack of observed orientation was ascribed to the softening of the material. Based on this result, we did not obtain the 2D WAXD patterns of these two samples.

The previous MCSCLCP PBBHCS displayed a fascinating hierarchical ordered structure with both double orderings on the nanometer and subnanometer scales. The nanoscale length structure in PBBHCS was assigned to the main chain, and the subnanoscle length structure resulted from the biphenyl side group being orthogonal to the main chain [48]. However, it was not unexpected to find no high-ordered structures in the MCSC-ILCPs samples because the biphenyl mesogen were directly attached to imidazole moieties in the side groups. Usually, this attachment should be helpful for enhancing the order structure, but the results demonstrated the opposite result. This effect was ascribed to the incorporated ions, which have weakened the construction of the LC phase. When the counter-anions inserted themselves in the imidazole group, the intermolecular space increased resulting in a decreased of the molecular stacking interaction. Based on these results, we propose that high-ordered structures cannot manifest themselves in this system. Therefore, the volume of the counter-anions in these polymers demonstrated a strong influence on the stability of LC ordered structure. For example, the samples poly (BImBHCS–Br) and poly(BImBHCS–BF_4) with relative small volume have stable LC ordered structure when varying the temperature. The volume of PF_6^- is bigger than that of Br^- and BF_4^- [57, 58] and the poly(BImBHCS–PF_6) exhibited an isotropic transition temperature during the heating process. The counter-anion $TFSI^-$ had the largest volume and not only can it weaken the intramolecular stacking of biphenyl but it was shown to destroy the scaffold of main chain LC properties. Thus, the LC ordered structures in the polymer with counter-anion $TFSI^-$ did not always appear during the heating and cooling process in DSC scans.

Combined with the aforementioned results, it was easy to identify the three distinct classes of phase behavior in poly(BImBHCS–X) (X^- = Br^-, BF_4^-, PF_6^- and $TFSI^-$) samples. The changes in phase behavior occurred by changing the counter-anion in poly(BImBHCS–X). As for MCSC-ILCPs poly (BImBHCS–X) with counter-anions Br^- and BF_4^-, the smectic phase always remained during the heating and cooling process except when they thermally decomposed. This result was consistent with the traditional MJLCPs. When the counter-anion was PF_6^-, this kind of MCSC-PILC still maintained its smectic phase, but revealed an isotropic phase at the higher temperature. For the poly(BImBHCS–X) sample with counter-anion $TFSI^-$, it was determined that this sample cannot exhibit a LC phase and it only presented the isotropic status during the heating and cooling process. It is worth noting that the main chain of these MCSC-ILCPs should be columnar in spite of the incorporation of counter-anions. A number of studies have proved that MJLCPs had a rod-like columnar main chain due to the steric hindrance originating from the bulky side groups [41]. Although there was no direct evidence to indicate a columnar main chain in our MCSC-ILCPs system, the polyethylene main chain directly linked to the terephthalate unit was expected to impose a strong steric hindrance on the sample leading to a rod-like columnar structure [48, 49]. Therefore, the main chain of these MCSC-ILCPs should be rod-like columnar because of the 'Jacketing' effect. The proposed smectic structures for this class of polymers prepared herein are depicted in Figure 10c.

3.4. The photophysical properties of MCSC-ILCPs poly(BImBHCS–X)

Ultraviolet-Visible (UV-Vis) and fluorescence experiments were carried out to investigate the photophysical properties of MCSC-ILCPs poly (BImBHCS–X). Figure 11 is the UV-Vis spectra of the MCSC-ILCPs poly(BImBHCS–X) (X^- = Br^-, BF_4^-, PF_6^- and $TFSI^-$) and MCSCLCP PBBHCS in thin films. It can be found that PBBHCS without ions incorporated into them displayed a sharp absorption maximum at 285 nm, which was indicative of π-π* transitions of aromatic rings [26, 60]. However, the samples poly(BImBHCS–X) (X^- = Br^-, BF_4^-, PF_6^- and $TFSI^-$) yielded a broad absorption maxima at 290 nm, which were essentially independent of the structures of counter-anions [61, 62]. It indicates that the absorption bands of the samples originate from the same electronic transitions [63]. Compared to PBBHCS, the slight bathochromic

shift of the characteristic absorption peak for the poly(BImBHCS–X) was found. The results come from the extended planarization of the imidazole heterocycle and biphenyl group [64, 65].

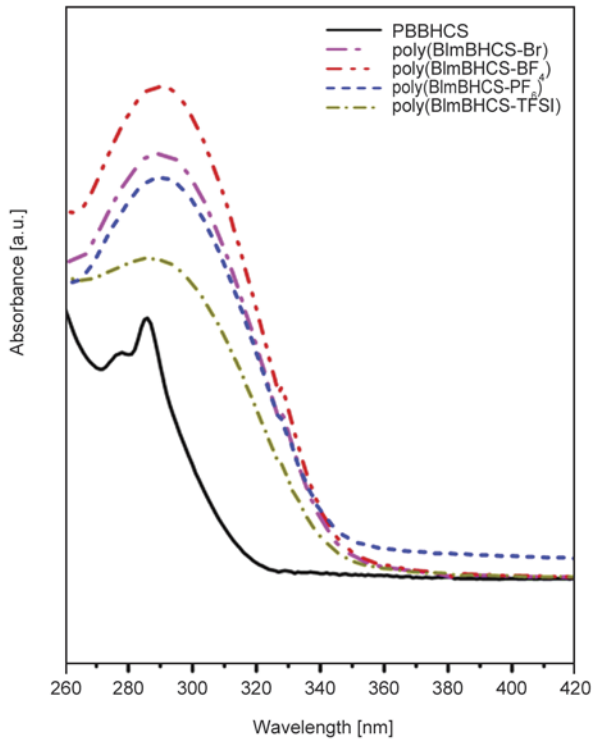

Figure 11. UV-Vis spectra of the MCSC-ILCPs poly (BImBHCS–X) in thin films. For comparison, the UV-Vis spectrum of PBBHCS is also included

The fluorescence emission spectra of the MCSC-ILCPs poly(BImBHCS–X) (X^- = Br^-, BF_4^-, PF_6^- and $TFSI^-$) and MCSCLCP PBBHCS in CH_2Cl_2 and in thin films at excitation wavelength of 290 nm are given in Figures 12a and 12b, respectively. In Figure 12a, we found that the sample MCSCLCP PBBHCS only gave two weak emission peaks located at 410 and 435 nm in CH_2Cl_2. However, the emission spectra of MCSC-ILCPs poly(BImBHCS–X) (X^- = Br^-, BF_4^-, PF_6^- and $TFSI^-$) displayed some difference from that of PBBHCS. For instance, the emission peak positions for the poly(BImBHCS–X) (X^- = Br^-, BF_4^-, PF_6^- and $TFSI^-$) samples were located at 420 and 435 nm indicating an obvious bathochromic shift when compared to PBBHCS. This shift originated from the extended planar conjugated system of imidazole heterocycle and biphenyl group [64, 65]. In Figure 12b, the spectra of these samples in thin films showed some new transitions which corresponded to the obvious emission peaks at 360, 420 and 485 nm, respectively. However, for poly(BImBHCS–X), there were some interesting changes. Emission signals were observed at 393, 390, 393 and 393 nm for poly(BImBHCS–Br), poly (BImBHCS–BF_4), poly(BImBHCS–PF_6) and poly (BImBHCS–TFSI), respectively. Compared to the emission of PBBHCS, the emissions from poly (BImBHCS–X) were obviously red-shifted which

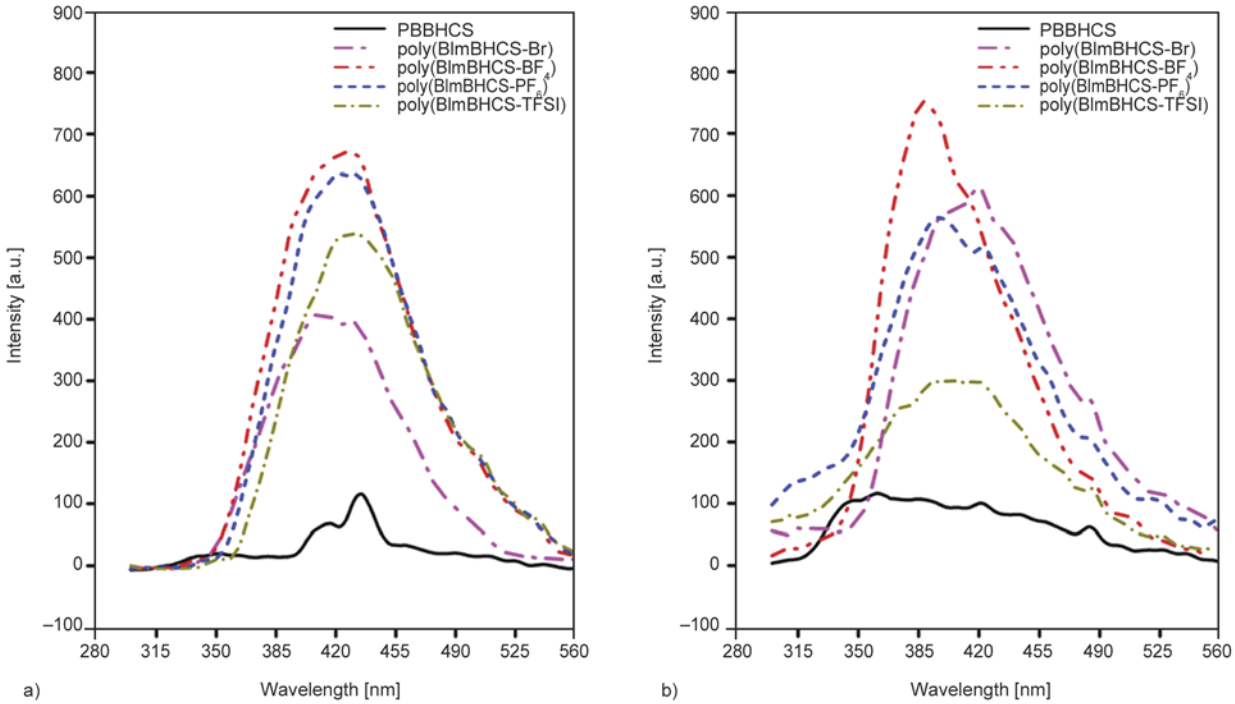

Figure 12. Emission spectra of MCSC-ILCPs poly(BImBHCS–X) (X^- =Br^-, BF_4^-, PF_6^- and $TFSI^-$) and PBBHCS at excitation wavelength of 290 nm: (a) in CH_2Cl_2 and (b) in thin films

derived from the electron richness of the imidazole heterocycle [64, 65]. In addition, the positions of the other two emission peaks present at 420 and 485 nm for poly(BImBHCS–Br), poly(BImBHCS–BF_4), poly(BImBHCS–PF_6) and poly(BImBHCS–TFSI) changed little compared to that of PBBHCS. Meanwhile, the emission peak intensity of poly (BImBHCS–X) (X^- = Br^-, BF_4^-, PF_6^- and $TFSI^-$) was much stronger than that of PBBHCS. This indicated that the counter-anions inserted into the polymer samples hindered the strong high-ordering packing of the side chain biphenyl mesogens, which resulted in the absence of fluorescence quenching [66–69]. The fluorescence emission spectra results were consistent with the previous results describing the structures of the MCSC-ILCPs poly(BImBHCS–X).

4. Conclusions

In this article, we successfully designed and synthesized a series of novel MCSC-ILCPs poly (BImBHCS–X) (X^- = Br^-, BF_4^-, PF_6^- and $TFSI^-$) via radical polymerization. Each synthesized MCSC-ILCPs displayed phase transitions and LC properties and these material characteristics were strongly influenced by the type of counter-anion used. Due to the strong intermolecular interplay, MCSC-ILCPs formed lamellar ordered structures except for the poly(BImBHCS–TFSI) sample Additionally, the poly(BImBHCS–PF_6) sample had isotropic phase besides the LC phase. Moreover, we found that the photophysical properties of poly(BImBHCS–X) were well-consistent with their chemical structure but practically independent on the types of counter-anions they contained. The LC property of MJLCPs depended on their molecular weight [48]. Herein, all monomers of the MCSC-ILCPs poly(BImBHCS–X) (X^- = Br^-, BF_4^-, PF_6^- and $TFSI^-$) having vinyl substituent were polymerized to control the polymer molecule chain length utilizing the 'controlled/living' radical polymerization method. This approach offered a new method to investigate the influence of the side chain length of the MCSC-ILCPs on the supra-molecular construction, LC behavior and photophysical properties. Continued studies with these materials (e.g., examining ion and electrical conductivity properties, optical properties, etc.) are underway and the relative results will be reported in subsequent articles.

Acknowledgements

This research is financially supported by the National Nature Science Foundation of China (21104062 and 21374092), the Doctoral Foundation of Ministry of Education of China (20114301120005), the project of Hunan Provincial Education Department (YB2013B032), Innovation Platform Open Foundation of University of Hunan Province (14K093) and Beijing National Laboratory for Molecular Sciences (BNLMS).

References

[1] Binnemans K.: Ionic liquid crystals. Chemical Reviews, **105**, 4148–4204 (2005). DOI: 10.1021/cr0400919

[2] Green M. D., Long T. E.: Designing imidazole-based ionic liquids and ionic liquid monomers for emerging technologies. Polymer Reviews, **49**, 291–314 (2009). DOI: 10.1080/15583720903288914

[3] Green O., Grubjesic S., Lee S., Firestone M. A.: The design of polymeric ionic liquids for the preparation of functional materials. Polymer Reviews, **49**, 339–360 (2009). DOI: 10.1080/15583720903291116

[4] Gohy J. F., Vanhoorne P., Jérôme R.: Synthesis and preliminary characterization of model liquid crystalline ionomers. Macromolecules, **29**, 3376–3383 (1996). DOI: 10.1021/ma951303u

[5] Jaeger W., Bohrisch J., Laschewsky A.: Synthetic polymers with quaternary nitrogen atoms – Synthesis and structure of the most used type of cationic polyelectrolytes. Progress in Polymer Science, **35**, 511–577 (2010). DOI: 10.1016/j.progpolymsci.2010.01.002

[6] Mecerreyes D.: Polymeric ionic liquids: Broadening the properties and applications of polyelectrolytes. Progress in Polymer Science, **36**, 1629–1648 (2011). DOI: 10.1016/j.progpolymsci.2011.05.007

[7] Shi X., Shen M., Möhwald H.: Polyelectrolyte multilayer nanoreactors toward the synthesis of diverse nanostructured materials. Progress in Polymer Science, **29**, 987–1019 (2004). DOI: 10.1016/j.progpolymsci.2004.07.001

[8] Maciejewska M., Zaborski M.: Effect of ionic liquids on the dispersion of zinc oxide and silica nanoparticles, vulcanisation behaviour and properties of NBR composites. Express Polymer Letters, **8**, 932–940 (2014). DOI: 10.3144/expresspolymlett.2014.94

[9] Jazkewitsch O., Ritter H.: Polymerizable ionic liquid crystals. Macromolecular Rapid Communications, **30**, 1554–1558 (2009). DOI: 10.1002/marc.200900187

[10] Paraknowitsch J. P., Zhang J., Su D., Thomas A., Antonietti M.: Ionic liquids as precursors for nitrogen-doped graphitic carbon. Advanced Materials, **22**, 87–92 (2010). DOI: 10.1002/adma.200900965

[11] Yoshio M., Mukai T., Kanie K., Yoshizawa M., Ohno H., Kato T.: Layered ionic liquids: Anisotropic ion conduction in new self-organized liquid-crystalline materials. Advanced Materials, **14**, 351–354 (2002). DOI: 10.1002/1521-4095(20020304)14:5<351::AID-ADMA351>3.0.CO;2-D

[12] Kato T.: From nanostructured liquid crystals to polymer-based electrolytes. Angewandte Chemie International Edition, **49**, 7847–7848 (2010). DOI: 10.1002/anie.201000707

[13] Li W., Zhang J., Li B., Zhang M., Wu L.: Branched quaternary ammoniumamphiphiles: Nematic ionic liquid crystals near room temperature. Chemical Communications, **2009**, 5269–5271 (2009). DOI: 10.1039/B909605A

[14] Mao Y., Zhang X-A., Xu H-P., Yuan W-Z., Zhao H., Qin A-J., Sun J-Z., Tang B. Z.: Synthesis of polyelectrolytic polyacetylene derivatives by quaternization of poly(pyridylacetylene). Chinese Journal of Polymer Science, **29**, 133–140 (2011). DOI: 10.1007/s10118-011-1032-z

[15] Wen Y-P., Li D., Lu Y., He H-H., Xu J-K., Duan X-M., Liu M.: Poly(3,4-ethylenedioxythiophene methanol)/ascorbate oxidase/nafion-single-walled carbon nanotubes biosensor for voltammetric detection of vitamin C. Chinese Journal of Polymer Science, **30**, 460–469 (2012). DOI: 10.1007/s10118-012-1140-4

[16] Zhang H-Y., Li X-Y., Wang X-G.: Nanomechanical properties of polyaniline and azo polyelectrolyte multilayer films. Chinese Journal of Polymer Science, **28**, 269–275 (2010). DOI: 10.1007/s10118-010-9066-1

[17] Shimura H., Yoshio M., Hoshino K., Mukai T., Ohno H., Kato T.: Noncovalent approach to one-dimensional ion conductors: Enhancement of ionic conductivities in nanostructured columnar liquid crystals. Journal of the American Chemical Society, **130**, 1759–1765 (2008). DOI: 10.1021/ja0775220

[18] Percec V., Johansson G., Ungar G., Zhou J.: Fluorophobic effect induces the self-assembly of semifluorinated tapered monodendrons containing crown ethers into supramolecular columnar dendrimers which exhibit a homeotropic hexagonal columnar liquid crystalline phase. Journal of the American Chemical Society, **118**, 9855–9866 (1996). DOI: 10.1021/ja9615738

[19] Liu F., Wang L., Sun Q., Zhu L., Meng X., Xiao F-S.: Transesterification catalyzed by ionic liquids on superhydrophobic mesoporous polymers: Heterogeneous catalysts that are faster than homogeneous catalysts. Journal of the American Chemical Society, **134**, 16948–16950 (2012). DOI: 10.1021/ja307455w

[20] Ichikawa T., Yoshio M., Hamasaki A., Mukai T., Ohno H., Kato T.: Self-organization of room-temperature ionic liquids exhibiting liquid-crystalline bicontinuous cubic phases: Formation of nano-ion channel networks. Journal of the American Chemical Society, **129**, 10662–10663 (2007). DOI: 10.1021/ja0740418

[21] Xue Y., Hara M., Yoon H.: Ionic naphthalene thermotropic copolyesters: Enhanced compressive properties of fibers. Macromolecules, **34**, 844–851 (2001). DOI: 10.1021/ma000984c

[22] Xue Y., Hara M.: Ionic naphthalene thermotropic copolyesters: Effect of ionic content. Macromolecules, **30**, 3803–3812 (1997). DOI: 10.1021/ma961703x

[23] Zhang A., Zhang B., Feng Z.: Compatibilization by main-chain thermotropic liquid crystalline ionomer of blends of PBT/PP. Journal of Applied Polymer Science, **85**, 1110–1117 (2002). DOI: 10.1002/app.10629

[24] González-Bellavista A., Macanás J., Muñoz M., Fabregas E.: Sulfonated poly(ether ether ketone), an ion conducting polymer, as alternative polymeric membrane for the construction of anion-selective electrodes. Sensors and Actuators B: Chemical, **125**, 100–105 (2007). DOI: 10.1016/j.snb.2007.01.051

[25] Bhowmik P. K., Akhter S., Han H.: Thermotropic liquid crystalline main-chain viologen polymers. Journal of Polymer Science Part A: Polymer Chemistry, **33**, 1927–1933 (1995). DOI: 10.1002/pola.1995.080331123

[26] Bhowmik P. K., Molla A. H., Han H., Gangoda M. E., Bose R. N.: Lyotropic liquid crystalline main-chain viologen polymers: Homopolymer of 4,4′-bipyridyl with the ditosylate of *trans*-1,4-cyclohexanedimethanol and its copolymers with the ditosylate of 1,8-octanediol. Macromolecules, **31**, 621–630 (1998). DOI: 10.1021/ma971115z

[27] Bockstaller M., Köhler W., Wegner G., Vlassopoulos D., Fytas G.: Hierarchical structures of a synthetic rodlike polyelectrolyte in water. Macromolecules, **33**, 3951–3953 (2000). DOI: 10.1021/ma000190y

[28] Bockstaller M., Köhler W., Wegner G., Vlassopoulos D., Fytas G.: Levels of structure formation in aqueous solutions of anisotropic association colloids consisting of rodlike polyelectrolytes. Macromolecules, **34**, 6359–6366 (2001). DOI: 10.1021/ma010027i

[29] Bhowmik P. K., Han H., Cebe J. J., Burchett R. A., Sarker A. M.: Main-chain viologen polymers with organic counterions exhibiting thermotropic liquid-crystalline and fluorescent properties. Journal of Polymer Science Part A: Polymer Chemistry, **40**, 659–674 (2002). DOI: 10.1002/pola.10134

[30] Roche P., ZhaoY.: Side-chain liquid crystalline ionomers. 2. Orientation in a magnetic field. Macromolecules, **28**, 2819–2824 (1995).
DOI: 10.1021/ma00112a029

[31] Ruokolainen J., Mäkinen R., Torkkeli M., Mäkelä T., Serimaa R., ten Brinke G., Ikkala O.: Switching supramolecular polymeric materials with multiple length scales. Science, **280**, 557–560 (1998).
DOI: 10.1126/science.280.5363.557

[32] Zhang B-Y., Sun Q-J., Tian M., Ren S-C.: Synthesis and mesomorphic properties of side-chain liquid crystalline ionomers containing sulfonic acid groups. Journal of Applied Polymer Science, **104**, 304–309 (2007).
DOI: 10.1002/app.25730

[33] Ujiie S., Iimura K.: Thermal properties and ferroelectric like behavior of liquid-crystalline ionic polyethylenimine derivative. Chemistry Letters, **20**, 1969–1972 (1991).
DOI: 10.1246/cl.1991.1969

[34] Chovino C., Frere Y., Guillon D., Gramain P.: Effect of smectogenicity of the ionic groups on the thermotropic liquid crystalline behavior of pyridinium and poly(4-vinylpyridinium) salts quaternized with mesogenic groups. Journal of Polymer Science Part A: Polymer Chemistry, **35**, 2569–2577 (1997).
DOI: 10.1002/(SICI)1099-0518(19970930)35:13<2569::AID-POLA4>3.0.CO;2-M

[35] Bazuin C. G., Brandys F. A.: Novel liquid-crystalline polymeric materials via noncovalent 'grafting'. Chemistry of Materials, **4**, 970–972 (1992).
DOI: 10.1021/cm00023a005

[36] KatoT., Kihara H., Ujiie S., Uryu T., Fréchet J. M. J.: Structures and properties of supramolecular liquid-crystalline side-chain polymers built through intermolecular hydrogen bonds. Macromolecules, **29**, 8734–8739 (1996).
DOI: 10.1021/ma9609341

[37] Qi B., Lu S. R., Xiao X. E., Pan L. L., Tan F. Z., Yu, J. H.: Enhanced thermal and mechanical properties of epoxy composites by mixing thermotropic liquid crystalline epoxy grafted graphene oxide. Express Polymer Letters, **8**, 467–479 (2014).
DOI: 10.3144/expresspolymlett.2014.51

[38] Percec V., Hahn B.: Liquid crystalline polymers containing heterocycloalkanediyl groups as mesogens. 7. Molecular weight and composition effects on the phase transitions of poly(methylsiloxane)s and poly (methylsiloxane-*co*-dimethylsiloxane)s containing 2-[4-(2(S)-methyl-1-butoxy)phenyl]-5-(11-undecanyl)-1,3,2-dioxaborinane side groups. Macromolecules, **22**, 1588–1599 (1989).
DOI: 10.1021/ma00194a014

[39] Finkelmann H., Ringsdorf H., Wendorff J. H.: Model considerations and examples of enantiotropic liquid crystalline polymers. Polyreactions in ordered systems. Die Makromolekulare Chemie, **179**, 273–276 (1978).
DOI: 10.1002/macp.1978.021790129

[40] Finkelmann H., Happ M., Portugal M., Ringsdorf H.: Liquid crystalline polymers with biphenyl-moieties as mesogenic group. Die Makromolekulare Chemie, **179**, 2541–2544 (1978).
DOI: 10.1002/macp.1978.021791018

[41] Chen X-F., Shen Z., Wan X-H., Fan X-H., Chen E-Q., Ma Y., Zhou Q-F.: Mesogen-jacketed liquid crystalline polymers. Chemical Society Reviews, **39**, 3072–3101 (2010).
DOI: 10.1039/B814540G

[42] Zhou Q. F., Li H. M., Feng X. D.: Synthesis of liquid-crystalline polyacrylates with laterally substituted mesogens. Macromolecules, **20**, 233–234 (1987).
DOI: 10.1021/ma00167a042

[43] Zhou Q., Li Z., Zhang Z., Pei X.: Studies on the post-polymerization of a liquid-crystal polymer with x-shaped mesogens. Macromolecules, **22**, 3821–3823 (1989).
DOI: 10.1021/ma00199a062

[44] Yang Q., Xu Y., Jin H., Shen Z., Chen X., Zou D., Fan X., Zhou Q.: A novel mesogen-jacketed liquid crystalline electroluminescent polymer with both thiophene and oxadiazole in conjugated side chain. Journal of Polymer Science Part A: Polymer Chemistry, **48**, 1502–1515 (2010).
DOI: 10.1002/pola.23908

[45] Wen G-H., Zhang B., Xie H-L., Liu X., Zhong G-Q., Zhang H-L., Chen E-Q.: Microphase separation facilitating and stabilizing hierarchical segment self-assembly of combined main-chain/side-chain liquid crystalline polymer in diblock copolymer. Macromolecules, **46**, 5249–5259 (2013).
DOI: 10.1021/ma400325g

[46] Yu Z-Q., Lam J. W. Y., Zhao K., Zhu C-Z., Yang S., Lin J-S., Li B. S., Liu J-H., Chen E-Q., Tang B. Z.: Mesogen jacketed liquid crystalline polyacetylene containing triphenylene discogen: Synthesis and phase structure. Polymer Chemistry, **4**, 996–1005 (2013).
DOI: 10.1039/c2py20535a

[47] Yin X-Y., Ye C., Ma X., Chen E-Q., Qi X-Y., Duan X-F., Wan X-H., Cheng S. Z. D., Zhou Q-F.: Manipulating supramolecular self-assembly via tailoring pendant group size of linear vinyl polymers. Journal of the American Chemical Society, **125**, 6854–6855 (2003).
DOI: 10.1021/ja034462z

[48] Xie H-L., Jie C-K., Yu Z-Q., Liu X-B., Zhang H-L., Shen Z., Chen E-Q., Zhou Q-F.: Hierarchical supramolecular ordering with biaxial orientation of a combined main-chain/side-chain liquid-crystalline polymer obtained from radical polymerization of 2-vinylterephthalate. Journal of the American Chemical Society, **132**, 8071–8080 (2010).
DOI: 10.1021/ja101184u

[49] Weng L., Yan J-J., Xie H-L., Zhong G-Q., Zhu S-Q., Zhang H-L., Chen E-Q.: Design, synthesis, and self-assembly manipulating of polymerized ionic liquids contained imidazolium based on 'Jacketing' effect. Journal of Polymer Science Part A: Polymer Chemistry, **51**, 1912–1923 (2013).
DOI: 10.1002/pola.26585

[50] Kouwer P. H. J., Swager T. M.: Synthesis and mesomorphic properties of rigid-core ionic liquid crystals. Journal of the American Chemical Society, **129**, 14042–14052 (2007).
DOI: 10.1021/ja075651a

[51] Tezuka Y., Goethals E. J.: Ion exchange and ring-opening reactions of telechelic poly(tetrahydrofuran)s containing terminal cyclic quaternary ammonium salts. Die Makromolekulare Chemie, **188**, 783–789 (1987).
DOI: 10.1002/macp.1987.021880412

[52] Cheng S., Zhang M., Wu T., Hemp S. T., Mather B. D., Moore R. B., Long T. E.: Ionic aggregation in random copolymers containing phosphonium ionic liquid monomers. Journal of Polymer Science Part A: Polymer Chemistry, **50**, 166–173 (2012).
DOI: 10.1002/pola.25022

[53] Ye Y., Elabd Y. A.: Anion exchanged polymerized ionic liquids: High free volume single ion conductors. Polymer, **52**, 1309–1317 (2011).
DOI: 10.1016/j.polymer.2011.01.031

[54] Lee M., Choi U. H., Salas-de la Cruz D., Mittal A., Winey K. I., Colby R. H., Gibson H. W.: Imidazolium polyesters: Structure–property relationships in thermal behavior, ionic conductivity, and morphology. Advanced Functional Materials, **21**, 708–717 (2011).
DOI: 10.1002/adfm.201001878

[55] Rajendran S., Prabhu M. R., Rani M. U.: Ionic conduction in poly(vinyl chloride)/poly(ethyl methacrylate)-based polymer blend electrolytes complexed with different lithium salts. Journal of Power Sources, **180**, 880–883 (2008).
DOI: 10.1016/j.jpowsour.2008.02.063

[56] Yoshizawa M., Ohno H.: Synthesis of molten salt-type polymer brush and effect of brush structure on the ionic conductivity. Electrochimica Acta, **46**, 1723–1728 (2001).
DOI: 10.1016/S0013-4686(00)00777-5

[57] Vygodskii Y. S., Mel'nik O. A., Shaplov A. S., Lozinskaya E. I., Malyshkina I. A., Gavrilova N. D.: Synthesis and ionic conductivity of polymer ionic liquids. Polymer Science Series A, **49**, 256–261 (2007).
DOI: 10.1134/S0965545X07030042

[58] Hunley M. T., England J. P., Long T. E.: Influence of counteranion on the thermal and solution behavior of poly(2-(dimethylamino)ethyl methacrylate)-based polyelectrolytes. Macromolecules, **43**, 9998–10005 (2010).
DOI: 10.1021/ma1017499

[59] Pont A-L., Marcilla R., De Meatza I., Grande H., Mecerreyes D.: Pyrrolidinium-based polymeric ionic liquids as mechanically and electrochemically stable polymer electrolytes. Journal of Power Sources, **188**, 558–563 (2009).
DOI: 10.1016/j.jpowsour.2008.11.115

[60] Pu K-Y., Fang Z., Liu B.: Effect of charge density on energy-transfer properties of cationic conjugated polymers. Advanced Functional Materials, **18**, 1321–1328 (2008).
DOI: 10.1002/adfm.200701018

[61] Spiliopoulos I. K., Mikroyannidis J. A.: Blue-light-emitting poly(phenylenevinylene)s with alkoxyphenyl substituents: Synthesis and optical properties. Macromolecules, **35**, 2149–2156 (2002).
DOI: 10.1021/ma011409r

[62] Goudreault T., He Z., Guo Y., Ho C-L., Zhan H., Wang Q., Ho K. Y-F., Wong K-L., Fortin D., Yao B., Xie Z., Wang L., Kwok W-M., Harvey P. D., Wong W-Y.: Synthesis, light-emitting, and two-photon absorption properties of platinum-containing poly(arylene-ethynylene)s linked by 1,3,4-oxadiazole units. Macromolecules, **43**, 7936–7949 (2010).
DOI: 10.1021/ma1009319

[63] Itami K., Yamazaki D., Yoshida J-I.: Pyrimidine-core extended π-systems: General synthesis and interesting fluorescent properties. Journal of the American Chemical Society, **126**, 15396–15397 (2004).
DOI: 10.1021/ja044923w

[64] Barik S., Bletzacker T., Skene W. G.: π-conjugated fluorescent azomethine copolymers: Opto-electronic, halochromic, and doping properties. Macromolecules, **45**, 1165–1173 (2012).
DOI: 10.1021/ma2024304

[65] Bhowmik P. K., Han H., Cebe J. J., Nedeltchev I. K., Kang S-W., Kumar S.: Synthesis and characterization of poly(pyridinium salt)s with organic counterions exhibiting both thermotropic liquid-crystalline and light-emitting properties. Macromolecules, **37**, 2688–2694 (2004).
DOI: 10.1021/ma030460n

[66] Yang J., He G. S., Zhang B., Luo W. A., Chen X. D., Fu R. W., Zhang M. Q.: Interfacial adhesion of nanoparticles in polymer blends by intrinsic fluorescence spectra. Express Polymer Letters, **5**, 799–808 (2011).
DOI: 10.3144/expresspolymlett.2011.78

[67] Geddes C. D., Lakowicz J. R.: Advanced concepts in fluorescence sensing: Part A: Small molecule sensing. Springer, New York (2007).

[68] Yang J., Liu M. K., Zhang B., Chen X. D., Fu R. W., Zhang M. Q.: Intrinsic fluorescence studies of compatibility in thermoplastic phenol formaldehyde resin/poly (ε-caprolactone) blends. Express Polymer Letters, **8**, 698–707 (2011).
DOI: 10.3144/expresspolymlett.2011.68

[69] Zhelev Z., Ohba H., Bakalova R.: Single quantum dot-micelles coated with silica shell as potentially non-cytotoxic fluorescent cell tracers. Journal of the American Chemical Society, **128**, 6324–6325 (2006).
DOI: 10.1021/ja061137d

[70] Zhang D., Liu Y., Wan X., Zhou Q-F.: Synthesis of a new side-chain type liquid crystal polymer poly[dicyclohexyl vinylterephthalate]. Macromolecules, **32**, 4494–4496 (1999).
DOI: 10.1021/ma9901386

eXPRESS Polymer Letters Vol.9, No.6 (2015) 554–566
Available online at www.expresspolymlett.com
DOI: 10.3144/expresspolymlett.2015.52

Evaluation of pH-sensitive poly(2-hydroxyethyl methacrylate-co-2-(diisopropylamino)ethyl methacrylate) copolymers as drug delivery systems for potential applications in ophthalmic therapies/ocular delivery of drugs

P. A. Faccia[1], *F. M. Pardini*[2], *J. I. Amalvy*[1,2,3,4*]

[1]Instituto de Investigaciones Fisicoquímicas Teóricas y Aplicadas (INIFTA), (CCT La Plata CONICET- UNLP), Diag. 113 y 64. La Plata, Argentina
[2]Centro de Investigación y Desarrollo en Tecnología de Pinturas (CIDEPINT, CIC-CCT La Plata CONICET), Av. 52 entre 121 y 122; La Plata, Argentina
[3]Cátedra de Materiales Poliméricos de la Facultad de Ingeniería, Universidad Nacional de La Plata, Calle 1 y 47. La Plata, Argentina
[4]CITEMA. Facultad Regional La Plata (Universidad Tecnológica Nacional) 60 y 124, La Plata, Argentina

Received 29 October 2014; accepted in revised form 1 January 2015

Abstract. Smart polymers like pH sensitive systems can improve different pharmacological treatment. In this work the behavior of copolymers containing 2-hydroxyethyl methacrylate (HEMA) with different proportions of 2-(diisopropylamino)ethyl methacrylate (DPA) and different amounts of cross-linker agent, ethylene glycol dimethacrylate (EGDMA) are evaluated as pH-sensitive drug delivery systems for potential application in ophthalmic therapies. A detailed characterization of the pH-responsive behavior was performed by swelling studies and scanning electron microscopy (SEM) analysis. Drug loading and release studies at different pH values were evaluated using Rhodamine 6G (Rh6G) as a model drug. The interaction between Rh6G and hydrogels was studied by Fourier Transform Infrared (FTIR) spectroscopy and scanning electron microscopy (SEM). The results show that the presence of DPA in the copolymers confers pH-responsive properties to the polymer, as noted in swelling and SEM studies, when the pH decreases below 7.40 the swelling degree increases and a porous morphology is observed. The apparent pK_a of copolymers was estimated between 6.80 and 7.17 depending on the composition. The amount of Rh6G loaded depends mainly on the medium pH and the interaction between the drug and the copolymers, observed by SEM and FTIR spectrum. The release of Rh6G of copolymers p(HEMA/DPA) show a normal Fickian or anomalous diffusion behavior at different pH values, depending on the HEMA/DPA ratio.

Keywords: *smart polymers, 2-hydroxyethyl methacrylate, 2-(diisoproylamino)ethyl methacrylate, pH-sensitive hydrogels, drug delivery systems*

1. Introduction

Hydrogels formed by chemical or physical cross-linking are three dimensional structures made from hydrophilic polymers that can imbibe a considerable amount of water while maintaining their integrity. The study of hydrogels as drug delivery systems and biomedical devices has been extensive over the last few decades because of their biocompatibility properties and control of solute transport [1–3]. More recently, sensitive hydrogels prepared with additional functions have gained considerable attention. In this way, the incorporation of stimuli-sensitive monomers in the chain of the hydrogel can improve the performance of these materials by increasing

*Corresponding author, e-mail: jamalvy@inifta.unlp.edu.ar

responsiveness in a particular medium [4]. These hydrogels, often called 'intelligent' or 'smart' hydrogels, can undergo relatively large and abrupt, physical or chemical modification in response to changes in environmental conditions such as pH, ionic strength, temperature or in presence of specific chemical compounds [5, 6]. For this reason, they are usually known as environmentally sensitive hydrogels. These types of stimuli-responsive polymers have the property to swell, shrink, bend, or degrade in response to changes in the environmental conditions.

Due to its properties, sensitive hydrogels have been proposed for a number of applications like drug delivery, separation techniques and sensors [7–9]. Recently sensitive hydrogels have been also proposed for ocular drug delivery systems in order to improve the ocular bioavailability of drugs, and to reduce the appearance of side effects [10]. In this case, within topical application of drugs, the presence of ocular compact barrier in the corneal and conjunctival epithelia of the eye, along with the dynamics of the lacrimal system, hinder the drug absorption into the intraocular area [11, 12]. The use of sensitive polymeric hydrogel allows to extend the residence time in the eye and to increase the percentage of drug absorbed [13].

In recent years research was mainly focusing to the technological innovations in this field with the aim to design hydrogels for a specific use as ocular drug delivery systems or in order to improve the uptake capacity and the release performance of these systems [8, 11, 14] although few works have been published using intelligent systems.

Of particular interest in this work it is the use of smart polymers as ocular drug delivery systems, and specifically the use of pH-sensitive hydrogels. This kind of material has been extensively studied as drug delivery systems for different applications, mainly due to the fact that they can release the drug selectively according to the pH of the medium [15]. In the human body there are variations in the physiologic pH values in both normal and pathological conditions, for example the gastrointestinal tract presents heterogeneous environments with different pH values ranging from 1 to 7.5 [16]. These conditions allow pH-sensitive hydrogels to release the desired drug in the right place [17]. In case of ophthalmologic therapies the release should be close to the medium ocular pH of 7.45 [18, 19].

The potential use of stimuli-sensitive hydrogels allow not only a spatial control but also a temporal control; i.e. during the period of time when the pH value is outside the normal range. These pH-sensitive hydrogels as drug delivery systems are potentially useful in ophthalmic therapies due to the fact that deviations from normal pH were observed in some disease processes, for example in ocular rosacea (an inflammation of the eye) [20]. Ocular pH change also in allergy and other conditions such as dry eye and bacterial infections [21]. Therefore these systems may be useful for controlling drug release in response to the pathological conditions.

Moreover, pH-sensitive hydrogels are normally prepared by adding pendant acidic or basic functional groups to the polymer backbone by including during the polymerization monomers like N-(3-aminopropyl)methacrylamide, 2-(dimethylamino) ethyl methacrylate, methacrylic acid and 2-aminoethyl methacrylate and 2-hidroxyethyl methacrylate (HEMA) for ionic type and butyl methacrylate, allyl diglycol carbonate, diallyl phthalate, and methyl methacrylate as neutral hydrophobic types [22–27]. Recently, we have reported the synthesis of a new pH-sensitive hydrogel based on 2-(diisopropylamino) ethyl methacrylate (DPA) and 2-hidroxyethyl methacrylate (HEMA), p(HEMA-co-DPA) [28] with good film properties depending on the monomer ratio.

In this contribution, we evaluate the properties of these pH-sensitive hydrogels with different proportions of HEMA and DPA and two degrees of crosslinking as potential materials for using in ocular drug delivery systems. Owing to this material, physical or chemical modifications can undergo in response to changes in environmental conditions, it is necessary to characterize the morphology and swelling behavior in function of the pH to understand and predict the drug's release rate. In this work we studied the swelling behavior of hydrogels in a range of pH from 5.5 to 8.4 which is the used range in eye drop solutions, and at the average ocular temperature of 34.5±0.5°C [29, 30]. We have determined pK_a values of different copolymers' compositions, and also we have studied morphological changes on hydrated samples at different medium pH values using Scanning Electron Microscopy (SEM). Their potential for ophthalmological application as pH-sensitive control drug release system was investigated in vitro using Rhodamine 6G Chloride (Rh6G, M_w = 479.01) as a model drug, because it is stable in

aqueous solutions (water solubility at 25°C = 20 mg·L^{-1}) and it is easily detected by its UV absorption. Effects of HEMA/DPA contents and different cross-linking degrees on drug uptake and release behavior were studied at different pH values under ocular conditions. Despite the number of recent studies incorporating active agent into hydrogels [31], the interaction between the matrix and the drug receive limited attention in the literature and it is often overlooked [4]. That is why in this work we intended to analyze also hydrogels' performance and their interactions with the model drug by using FTIR and SEM analysis.

2. Experimental section

2.1. Materials

2-Hydroxyethyl methacrylate (HEMA, 97%) and the cross-linker, ethylene glycol dimethacrylate (EGDMA, 98%), were purchased from Sigma-Aldrich, USA, while 2-(diisopropylamino)ethyl methacrylate (DPA) were purchased from Scientific Polymers Products, USA. Darocur TPO (97%) from Sigma-Aldrich, USA, was used as the initiator. The phosphate buffer solutions (PBS) were prepared from standard chemicals. The study of the hydrogels as drug delivery systems was performing using Rhodamine 6G Chloride (Rh6G, 95%), from Sigma-Aldrich, USA, as model drug (Figure 1). This molecule is frequently used for those studies because it has a similar chemical structure compared to drugs [32, 33]. Additionally Rh6G have good solubility in water (20 g/L at 25°C), chemical stability and it is easy detectable with UV-visible spectroscopy.

2.2. Polymer synthesis

The synthesis of DPA homopolymer and copolymers was performed in bulk by free radical polymerization using diphenyl (2,4,6-trimethylbenzoyl)-phosphine oxide (Darocur® TPO) as photo-initiator. Different ratios of HEMA/DPA monomers (namely 100/0, 90/10 and 70/30) and 1 and 3 wt% of cross-linker (relative to the whole monomer) were mixed with 1% w/v of photo-initiator and irradiated with an UV-lamp (Rayonet RPR3500, USA). Films with 180±30 μm of thickness were cut into circular pieces of 13 mm of diameter with a cork borer and dried at 25.0°C for 48 h before use. Film samples were denoted by using a short-hand notation HDX/Y-n, where X and Y denote the HEMA (H) and DPA (D) ratio respectively, and n denote the amount of cross-linker. More details of synthesis and experimental procedures can be found in a previous paper [28]. The experimental composition ratios in copolymers HD90/10-1, HD90/10-3, HD70/30-1 and HD70/30-3 are 82/18, 85/15, 66/34 and 65/35, respectively and they were determined by IR spectroscopy following the reported method by Canto and Pessan [34].

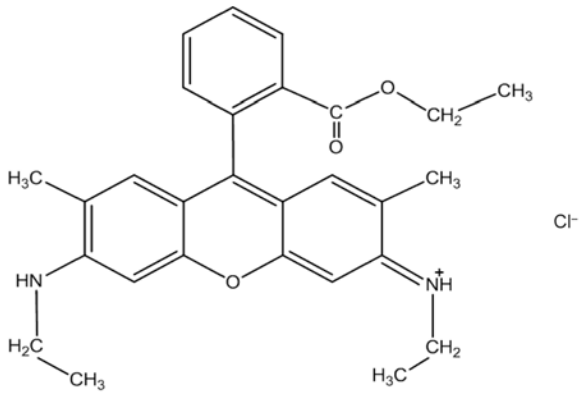

Figure 1. Chemical structure of Rhodamine 6G

2.3. Swelling degree

For the determination of the swelling degree, dry samples were immersed in phosphate buffer solutions (PBS, 0.1 M) at the desired pH (ranging from 5.5 to 8.4) at the average ocular temperature of 34.5°C [30]. At regular periods of time samples were removed from the aqueous solution, blotted with filter paper to remove surface liquid, weighed and returned to the same container until reaching a constant weight. The equilibrium swelling degree (Q_e) was calculated using Equation (1):

$$Q_e\,[\,\%\,] = \frac{W_e - W_d}{W_d} \cdot 100 \qquad (1)$$

where W_d is the weight of the dry film and W_e is the weight of swollen film at equilibrium. Experiments were performed in triplicate.

2.4. Drug loading

Films were loaded with Rh6G by soaking the dry films into 20 mL of the drug solution (50 mg/L) in PBS at pH 6.5 and 8.4, and at 25.0°C, until the equilibrium was reached (see below). For practical purposes the loading time was unified in 7 days for all samples. Drug uptake kinetics were followed by measuring the absorbance of the solution by UV-visible spectroscopy at 348 nm using a Fluorat®-02-Panorama spectrophotometer, Lumex, Russia. Samples loaded with Rh6G were denoted by adding the

letter R in brackets to the name of the sample (e.g. HD90/10-1(R)).

The partition coefficient of the drug through the hydrogel was calculated using the modified method of Sato and Kim [35, 36], as shown by Equation (2):

$$K_d = \frac{V_s(C_0 - C_e)}{V_m C_e} \quad (2)$$

where V_s is the volume of solution, V_m is the volume of polymer film, C_0 is the initial solute concentration and C_e is the solute concentration in the solution at the equilibrium time.

2.5. Scanning electron microscopy (SEM)

Hydrogels' morphology and drug distribution were observed by Scanning Electron Microscopy (SEM) with an FEI – Quanta 200 (The Netherlands) instrument, in high vacuum mode and operated at 15 or 20 kV acceleration voltage. p(HEMA-co-DPA) and pHEMA hydrogels were equilibrated during 24 h in different buffer solutions and then were frozen at –40°C in an alcoholic solution followed lyophilization under vacuum for 24 h. In order to prevent sample-charging effects during the observation, fractured pieces of samples were mounted onto the surface of an aluminum SEM specimen holder and sputter-coated with a thin overlayer of gold before observation. Films loaded with Rh6G were prepared in the same way.

2.6. Infrared spectroscopy (FTIR)

FTIR spectra were measured in transmission mode using a FTIR Nicolet 380 spectrometer, Thermo Scientific, USA. Samples were loaded with Rh6G until the equilibrium was reached and then powdered and mixed with KBr; disks were formed by pressing. FTIR spectra were obtained by recording 64 scans between 4000 and 400 cm^{-1} with a resolution of 4 cm^{-1}. Spectra processing was performed using the software EZ Omnic.

2.7. Drug release experiments

Release experiments of Rh6G loaded p(HEMA-co-DPA) films were conducted in media of different pH values. Drug loaded films were removed from the loading solution, wiped with filter paper to remove surface liquid and placed directly into the release solution. Drug release experiments were performed by immersing p(HEMA-co-DPA) films into 20 mL of PBS (0.1 M) at 34.5°C. The dynamic drug concentration in the PBS solution was monitored by measuring the absorbance at 526 nm. The Rh6G concentration released as a function of time (t) was adjusted to a power-law type relationship [37, 38] using the equation of Ritger-Peppas (Equation (3)):

$$\frac{M_t}{M_e} = kt^n \quad (3)$$

Here M_t and M_e are the cumulative amount of drug released after a time t and at infinite time, respectively, while k is a constant related to kinetic behavior and experimental conditions and n is the exponent depending on the release process. Data were fitted only up to 60% of drug release in order to apply Equation (3).

Parameters k and n were calculated from the intercept and the slope of Equation (4):

$$\ln\frac{M_t}{M_e} = \ln k + n\ln t \quad (4)$$

For Fickian diffusion processes, Equation (5) applies to calculate the diffusion coefficient (D_{ip}), where L is the thickness of the film:

$$\frac{M_t}{M_e} = 4\left(\frac{D_{ip}t}{\pi L^2}\right)^{1/2} \quad (5)$$

3. Results and discussion

3.1. Swelling studies

In pH-sensitive systems the release rate of the drug is regulated by several factors as swelling degree, drug-matrix interaction, water content and the initial PA concentration [39, 40]. However the swelling behavior as a function of pH has a principal role in drug release regulation, which makes this technique to be an important tool to predict the drug's rate release. In this section swelling results of hydrogels in a range of pH from 5.5 to 8.4 and the determination of pK_a values corresponding to the different compositions of the copolymers are presented. Figure 2 shows the equilibrium swelling degree for different HEMA/DPA ratios with 1 and 3 wt% of cross-linker at different pH values.

Hydrogels of pHEMA show a slight increase in the swelling degree when increasing the pH from 5.5 to 8.4. However, the difference of swelling degree over the pH range studied in this work is rather low. Similar results were observed by Brannon-Peppas and Peppas [41]. On the other hand, hydrogels of p(HEMA-co-DPA) show a significant increase of

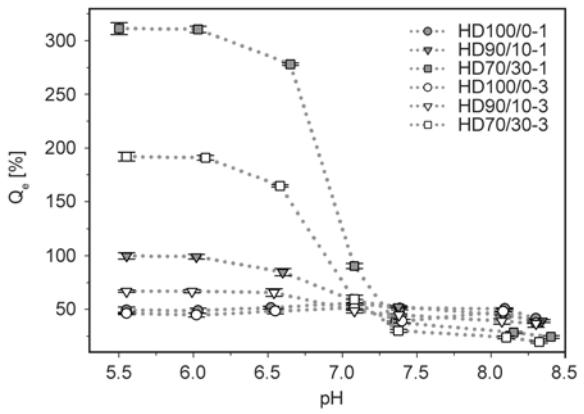

Figure 2. Equilibrium swelling degree for copolymers with different HEMA/DPA ratios, with 1 and 3 wt% of cross-linker as a function of pH at 34.5°C

the swelling when the pH decrease below 7.40. This effect is directly proportional to the amount of DPA co-monomer present in copolymers, and is mainly attributed to the protonation of the tertiary amino groups. At pH below 7.40, amino groups become protonated and the electrostatic repulsion, between these ionized groups, expands the network space and increases its internal volume, allowing water to get into the matrix [14, 42, 43]. The equilibrium of swelling is reached around pH 6.0. At basic pH, above 7.40, the effect is reversed, the swelling degree decreases with the amount of DPA present in the hydrogel. In this case functional groups of HEMA and DPA are able to form hydrogen-bonds [28], which in turn generate a proximity between polymer chains and consequently reduce the free space available for water molecules. Additionally, swelling values decrease also due to the hydrophobic nature of the unprotonated DPA moiety at basic pH.

For all HEMA/DPA ratios the cross-linking density does not modify the sensitivity to respond to pH changes but it affects the swelling degree. For high proportion of cross-linking, the swelling decreases for a given pH. This behavior is due mainly to two factors: first a matrix with higher crosslink density has less free space to be occupied by water; and second the crosslink degree generates a more rigid tridimensional structure which limits the chains' mobility and increases the elastic force that opposes to the expansion of the hydrogel's internal space [44].

The apparent copolymers' pK_a can be estimated by using swelling experiments at different pHs. In the pH range of 6.5 to 7.4 the swelling of the hydrogel decreases almost linear when increasing pH. In this range of pH, both the protonated and unprotonated form of the DPA moiety are present inside the polymer matrix acting as a buffer system in the hydrogel. Under these conditions, the Handeson-Hasselbalch equation (Equation (6)) can be applied to determine the apparent pK_a:

$$\mathrm{pH} = pK_a + \\ + \log\left[\frac{\text{unprotonated state of tertiary amine group}}{\text{protonated state of tertiary amine group}}\right] \quad (6)$$

The apparent pK_a of the hydrogel buffer system can be determined from the pH value for which the fraction between these two ionic forms is one. This corresponds to the point located in the middle of the swelling curve presented in Figure 2. The apparent pK_a values are show in Table 1 and range from 6.80 to 7.17 depending on polymers' composition and their crosslinking degree due to the availability of hydrogel's ionic groups to act as buffer system [29].

3.2. Drug uptake

Figure 3 shows the cumulative uptake of Rh6G as a function of immersion time for pHEMA and p(HEMA-co-DPA) films in PBS at pH 6.5 (Figure 3a) and 8.4 (Figure 3b).

At pH 6.5 by increasing the DPA content, the Rh6G kinetic uptake increases (Figure 3a). At this pH the swelling degree of hydrogels containing DPA (see above) favors the incoming of the drug into the film due to the increase of the network space and the diffusion of the aqueous solution, allowing the water soluble drug to get into the matrix. However, the final uptake and the partition coefficient at acid pH for pure pHEMA films are higher than that for the copolymer films (Table 2). This behavior can be explained in terms of an increased electrostatic repulsive interaction between the protonated tertiary amine groups of the polymer matrix and the positive charge on the Rh6G cation when increasing DPA content (see Figure 1 for the Rh6G chemical structure).

Table 1. Apparent pK_a values for copolymers at 34.5°C

Copolymers	pK_a	SD
HD70/30-1	7.01	0.06
HD70/30-3	6.94	0.07
HD90/10-1	6.87	0.08
HD90/10-3	6.80	0.06

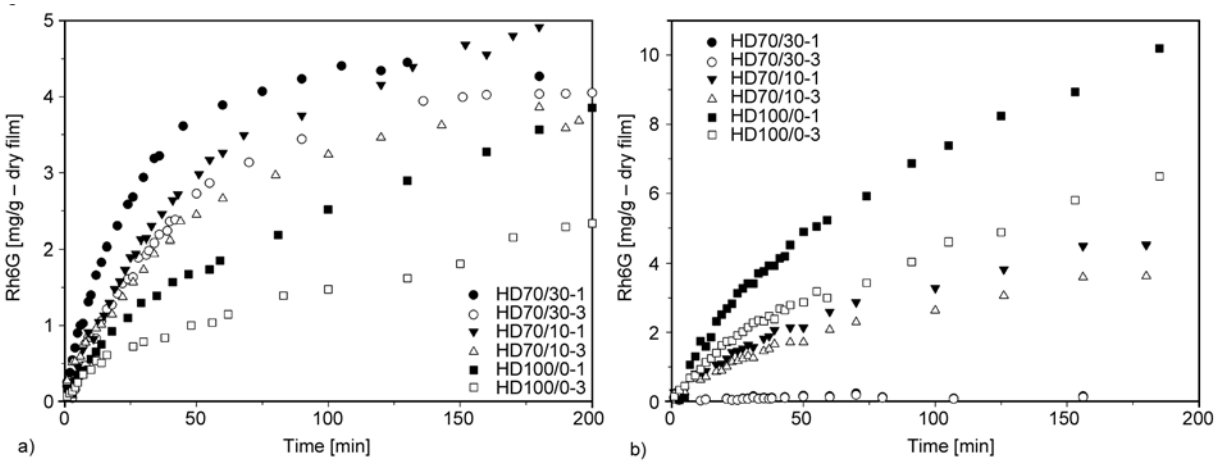

Figure 3. Cumulative uptake of Rh6G as a function of immersion time for pHEMA and p(HEMA-co-DPA) films in PBS at pH 6.5 (a) and 8.4 (b)

Table 2. Final mass uptake and partition coefficient (K_d) of Rh6G at pH 6.5 and 8.4

HEMA/DPA	Crosslinking [wt%]	Rh6G uptake (mg/g-dryfilm)					
		pH 6.5			pH 8.4		
		Mean	SD	K_d	Mean	SD	K_d
100/0	1	27.4	0.1	902	31.8	0.3	1210
	3	24.6	2.0	761	31.4	0.9	1066
90/10	1	6.3	0.6	101	23.7	0.8	694
	3	5.2	1.6	76	20.0	0.2	509
70/30	1	4.7	1.1	26	18.0	0.9	491
	3	3.7	0.9	28	15.1	0.2	358

SD: standard deviation; n: number of measure between 2–4.

On the opposite, at pH 8.4, by increasing the DPA content, the Rh6G kinetic uptake decreases (Figure 3b), and it is slower than at acid pH. The equilibrium time ranges from 150 minutes for HD70/30 to 6 days for HD100/0, when loading is at pH 6.5; and 2 days for HD70/30 and 6 days for HD100/0, when loading is at pH 8.4.

At pH 8.4 the increment on the DPA content causes a decrease in the swelling degree and consequently a decrease in the network space that retard the drug incorporation. However, the final uptake of Rh6G at pH 8.4 is higher than at pH 6.5. At acidic pH, the swelling increases due to the protonation of the functional group of the DPA, but the incorporation of Rh6G decreased by the electrostatic repulsion between the tertiary amine of DPA (partially protonated) and the cation of Rhodamine 6G. At basic pH, the electrostatic repulsion is less pronounced due to the decrease in the degree of ionization of the matrix, and hence the incorporation of Rh6G in the copolymers is higher. In conclusion, the amount of Rh6G incorporated into the polymer is inversely proportional with the swelling of the hydrogel, and depends mainly on the medium pH and the interaction between the drug and the copolymers' matrix.

At both pH values the total uptake Rh6G is higher for pure pHEMA homopolymer than for the copolymers. By including DPA monomer, the total amount of OH groups present in the hydrogel is reduced (as verified by FTIR) and, consequently, the available interaction sites decrease and then the number of Rh6G molecules incorporated also decreases (see Table 2).

As expected from the swelling data, increasing the degree of cross-linking from 1 to 3 wt% reduces the amount of Rh6G incorporated in all cases. Thus it is possible to modify the final incorporation of Rh6G changing the pH of the load medium instead of modifying the loading time. This allows regulating the amount of loaded drug into the hydrogel depending on the dose that is to be released.

3.3. SEM characterization

SEM is probably the best method for characterizing the hydrogel structure, especially in drug delivery systems because it offers information of surface

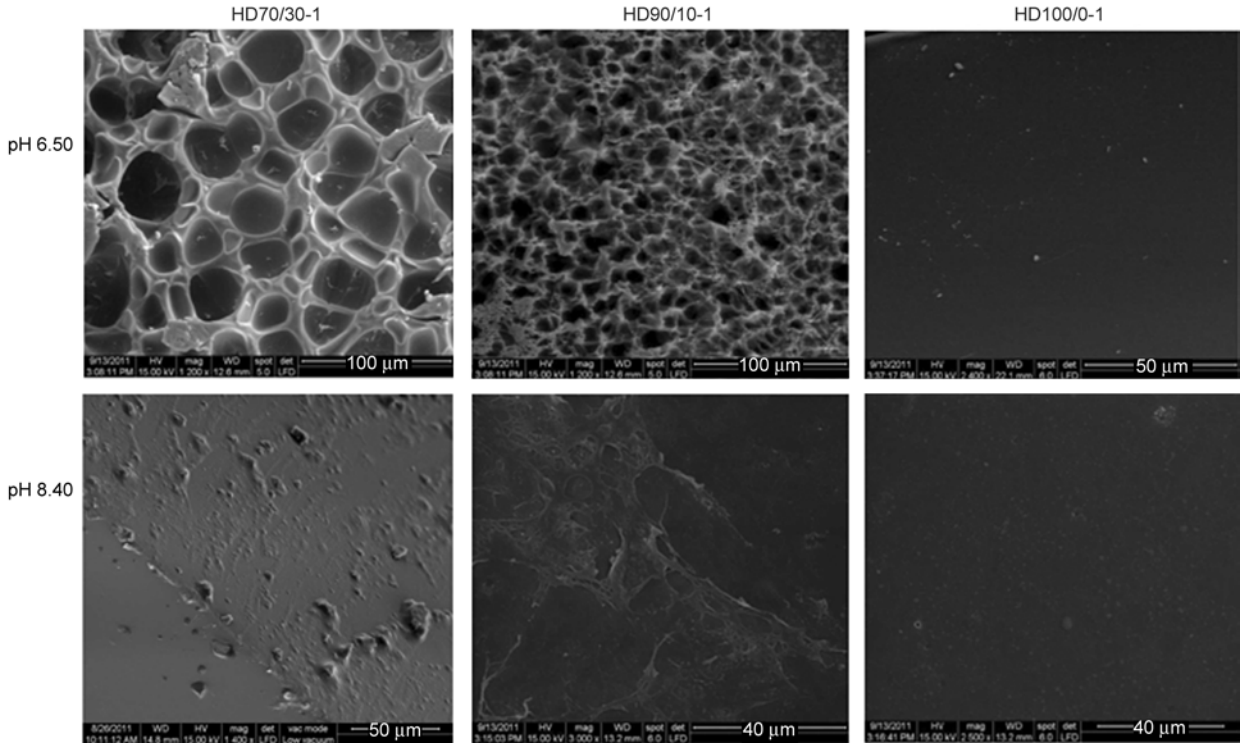

Figure 4. SEM images of hydrogel HD70/30-1, HD90/10-1 and HD100/0-1 at pH 6.5 and pH 8.4

porosity, amorphous and crystalline characterization, particle size, phase separation and in particular the active principle ingredient distribution in the structure [45]. Morphologic changes of lyophilized pH-responsive hydrogels, after exposure them to aqueous solutions of different pH values (6.5 and 8.4), have been examined by SEM technique. Images are shown in Figure 4.

The surface of the hydrogel HD70/30-1 at pH 6.5 shows an open morphology state with a porous structure, thin walls and a predominant free space as a consequence of the matrix expansion at this pH. At pH to 8.40 a collapsed state is observed with almost a featureless structure due to lower swelling degree and a more hydrophobic polymer at this pH. For hydrogel HD90/10-1 the surface also shows a morphologic change with the pH value. At pH 6.50 a homogeneous pore distribution on the surface is observed, while at pH 8.40 a non-porous and compact surface is appreciated. When the DPA content is higher, the equilibrium swelling increases, which led to more and larger pores in hydrogels as obtained from lyophilization, being 5±2 µm for 10 wt% and 7±2 µm for the 30% of DPA. By comparing those values with the mesh sizes of conventional hydrogels, smaller than 100 nm [46, 47], both systems have a higher pore size. For hydrogel HD100/0-1 no changes with pH are appreciated and in all cases a compact surface is observed. The incorporation of DPA confers pH-responsive properties to the polymer, as noted in swelling studies; therefore changing the medium pH not only changes the film volume but also the morphology. In the case of sample with higher concentration of cross-linker (3 wt%) the same trend in

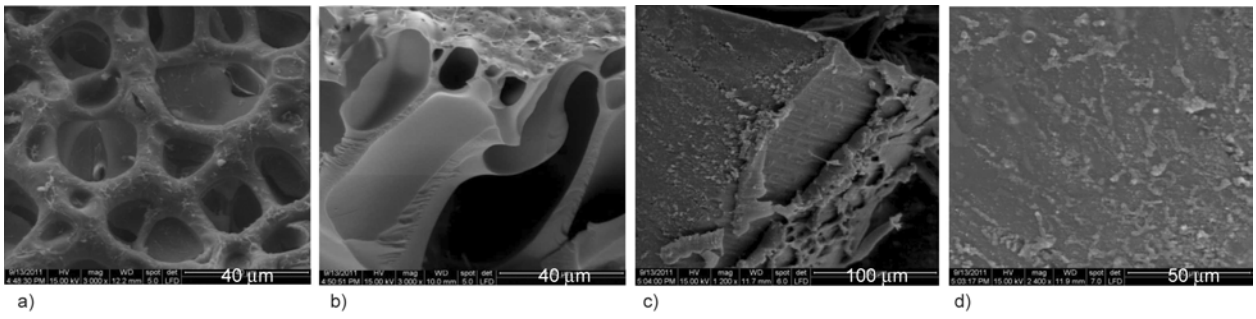

Figure 5. SEM images of hydrogel HD70/30-1(R) loaded at pH 6.5: a) surface, b) inside the matrix; and at pH 8.4: c) inside the matrix, d) surface

morphological changes with the medium pH is observed (data not shown).

In Figure 5 are presented SEM images of samples HD70/30-1(R), loaded with RhG6 at pH 6.5 and 8.4.

SEM images of the hydrogel 70/30-1(R) loaded at both pHs (6.5 and 8.4) show the presence of Rh6G. In the case of loading at pH 6.5, the surface (Figure 5a) shows a greater accumulation of Rh6G unlike inside the matrix (Figure 5b). While at pH 8.4 the Rh6G is observed both inside the matrix and on the surface (Figure 5c and 5d respectively). Rh6G molecules have lower affinity for the matrix of the copolymer HD70/30-1 at acidic pH, and therefore incorporation is lower and mainly superficial.

3.4. FTIR spectroscopy

Figure 6 shows the FTIR spectra of HD70/30-1 and HD100/0-1 with (samples labeled R) and without Rh6G. The main differences in the high wavenumbers region of the spectrum are the increasing intensity of the stretching band of the O–H group (3414 cm^{-1}). The existence of an interaction between Rh6G and-OH groups through the group =N+(H) is known, therefore interactions between Rh6G and pHEMA [48] are also expected. The C–H stretching region is also different. Upon the copolymerization with DPA, the $–CH_2–$ and $–CH_3$ bands of the stretching modes of pure pHEMA observed at 2986, 2951 and 2882 cm^{-1} (Figure 6) are overlapped with those of the DPA monomer and peaks become broader. In the C–H stretching region of the HD70/30-1 copolymer spectrum, a broad band centered at 2965 cm^{-1} is observed. These wavenumbers correspond to the characteristic peak of the methine group in the isopropyl moiety ($(CH_3)_2–CH–$) [49]. However after Rh6G loading the peak pattern of the FTIR changed showing peaks at 2985, 2950 and 2888 cm^{-1}. These

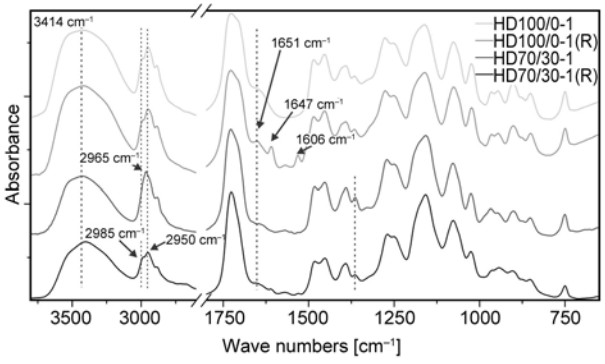

Figure 6. FTIR spectra for films: HD100/0-1, HD100/0-1(R), HD70/30-1 y HD70/30-1(R)

peaks values are close to the C–H stretching of the pure pHEMA, suggesting that the peak of the stretching of the methine group at 2965 cm^{-1} shifted, probably to higher wavenumbers and overlapping with the 2985 cm^{-1} peak due to the loss of interaction between the lone electron pair of tertiary amine group of DPA with the OH of pHEMA [28] and the formation of new hydrogen bonds with the Rh6G molecules [48].

In the 2000–400 cm^{-1} region the new features after Rh6G loading are mainly in low wavenumbers side of the C=O (free) stretching band (located at 1730 cm^{-1}), namely a band at 1651 cm^{-1} from the contribution of bonded carbonyl groups of Rh6G, and small peaks at 1647 and 1606 cm^{-1} from the xanthene ring of this molecule (see [50, 51] for more details of Rh6G spectrum). These contributions are more evident in HD100/0-1 film due to its higher loading of Rh6G. In HD70/30-1 film, the band of the isopropyl group ($(CH_3)_2–CH–$) of DPA moiety, observed at 1336 cm^{-1} in the unloading film, shows lower intensity after Rh6G loading. Minor differences are also observed in the 1000–880 cm^{-1} region, where the contribution of the absorption bands of Rh6G is negligible. This region is associated to C–C modes of the carbon backbone of the polymer.

In summary, observed differences in the FTIR spectra between loaded and unloaded films indicate that Rh6G molecules are interacting with polymer chains, probably with both parts of the copolymer (HEMA and DPA moieties) by hydrogen bonding or through dipole–dipole interaction [52].

3.5. Drug release

3.5.1. Effect of medium pH

Figure 7 shows the cumulative concentration of Rh6G released at 34.5°C in PBS for different pH values as a function of time for HD70/10-1, HD90/10-1 and HD100/0-1 loaded at pH 8.4. This pH was chosen because the drug uptake is the highest found in this work (see section 3.2 and Table 2.)

In copolymers of HEMA/DPA release kinetics of Rh6G varies significantly with changing the pH of the medium, as the pH increases the release becomes faster. This effect is related to the swelling property of these hydrogels when changing the medium pH. At basic pH the matrix is closed and the swelling is low, by acidifying the medium, the hydrogel swells and the release rate of the Rh6G increases as well as

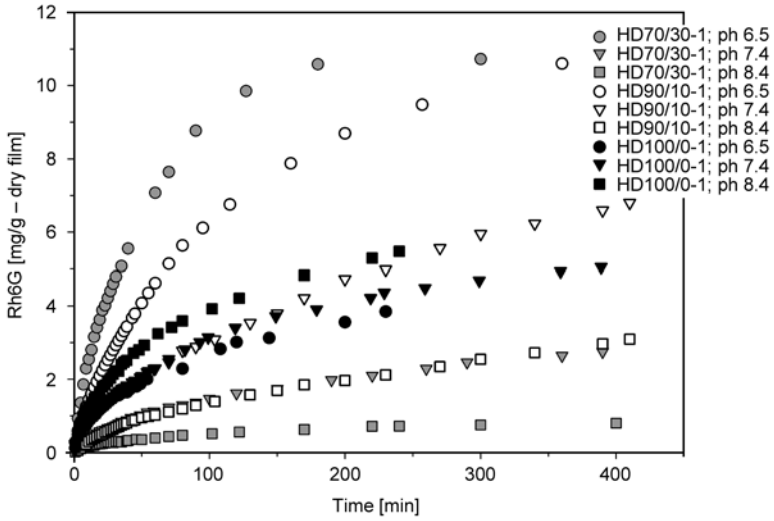

Figure 7. Cumulative concentration of Rh6G released as a function of time for HD70/10-1, HD90/10-1 and HD100/0-1 (loaded at pH 8.4) at 34.5°C in PBS for different pH values

the pore size of the hydrogel [53]. In the case of HD70/30-1 the effect of the pH on the release kinetics is much more pronounced than in HD90/10-1 copolymer due to the higher amount of DPA. At acid pH, the electrostatic repulsion between the tertiary amine groups of the DPA partially protonated and the Rh6G cation favors the released of this drug.

Drug release behavior at different pH values is also consistent with morphologic characteristics observed in SEM images (Figure 3), the higher the pore size of the hydrogel, the faster is the released of the drug.

The total amount of Rh6G released from pHEMA film is incomplete (about 30% is released) and it is almost pH independent as a consequence of the interaction of the Rh6G molecule with the polymer functional groups, as observed by FTIR spectroscopy. Similar results were obtained in other cases of interaction between the drug and the matrix [54–56]. Although, for DPA containing polymers, the total Rh6G released at pH 6.5 (about 90%) is higher than at pH 8.4 (about 40%). At acidic pH, the tertiary amine groups are partially protonated and the electrostatic interaction with the Rh6G cation impels the release from the matrix. At pH 8.4, the electrostatic repulsion is no longer acting and, therefore, the driving force is reduced.

Table 3 shows the kinetics parameters (k and n) of the experimental data of Figure 7, calculated using Equation (4), and the diffusion coefficient (D_{ip}), using Equation (5).

For pure pHEMA samples n values indicate a Fickian transport from pH 6.5 to 8.4. Highly soluble drugs, like Rh6G, typically exhibit Fickian release from hydrogels, and the release profile is mainly dependent upon the solubility and diffusion kinetics of the drug. For the hydrogel HD90/10-1, the n values are between 0.5 and 1, indicating anomalous transport, and a domination of relaxation process over diffusion. In the case of HD70/30-1, n values varies significantly with the pH, at pH 6.5 and 7.4 are between 0.5 and 1 while at pH 8.4 is low than 0.5. For higher pHs experimental values suggest a different mechanism transport, that is, the presence of another process besides passive diffusion. Above pK_a the deprotonation is accompanied by a deswelling of the hydrogel (see Figure 2).

The D_{ip} value of Rh6G in water at 25°C is $4.14 \cdot 10^{-6}$ cm^2/s and as expected, all values found in this work for Fickian diffusion are lower than this one [57].

Table 3. Parameters (k, n) calculated from the fit of Equation (4), and diffusion coefficients (D_{ip}) calculated from Equation (5) for the Rh6G release curves from Figure 7

Samples	pH	R^2	$k \cdot 10^2$ [cm^{-1}]	n	$D_{ip} \cdot 10^9$ [cm^2·seg^{-1}]
HD100/0-1	6.5	0.996	2.75	0.51	0.82
	7.4	0.986	2.73	0.51	0.94
	8.4	0.998	3.31	0.50	1.23
HD90/10-1	6.5	0.995	2.10	0.67	–
	7.4	0.995	1.58	0.63	–
	8.4	0.993	1.42	0.61	–
HD70/30-1	6.5	0.978	3.17	0.78	–
	7.4	0.993	1.57	0.56	–
	8.4	0.988	1.84	0.48	–

In principle the relation between the pH and the percentage of released R6G indicate that, while the release mechanism can be similar for different pHs, the final amount of drug released depends on the medium's pH and on the material's swelling degree. This behavior demonstrates the ability of such copolymers to achieve a control of drug released as a function of the pH of the medium.

3.5.2 Effect of cross-linking density

To evaluate the effect of cross-linker concentration on the mechanism of the drug transport at pH 7.4 and 34.5°C, parameters (n, k) of the power law model in Equation (3) are calculated (Table 4).

The release of Rh6G in pHEMA homopolymer at pH 7.4 seems to follow a Fickian diffusion behavior as suggested by values of n. However, by incorporating DPA, n values are close to 0.6 for all contents and cross-linking densities, suggesting a non-Fickian behavior.

The mechanism of Rh6G release does not seem to be affected by increasing the cross-linking density for the same copolymer composition, as judged by n values. However, a reduction in the k parameter is the most important effect of higher cross-linker concentration. The decrease in kinetic constant values reflects the decrease in the rate of drug release, which might be due to the dominance of chain entanglement and the decrease in the water content of polymers with different cross-linking densities. By increasing the cross-linking density, pores are smaller and less water is allowed to enter the matrix. Since Rh6G is a water soluble molecule, this factor has an important impact on drug rate. The larger pore in the 1 wt% cross-linked copolymers allows Rh6G diffusion with no or little resistance compared to smaller one. Pore size is significantly impacted by the extent of cross-linking and their increasing values result in lower released kinetic.

Table 4. Parameters (k, n) calculated from the fit of Equation (4) for the Rh6G release from different cross-linking densities at pH 7.4 and 34.5°C

Samples	Cross-linking [wt%]	R^2	$k \cdot 10^3$ [min^{-1}]	n
HD100/0	1	0.990	27.28	0.51
	3	0.989	20.72	0.51
HD90/10	1	0.997	15.82	0.61
	3	0.994	10.87	0.59
HD70/30	1	0.996	15.16	0.57
	3	0.980	7.67	0.61

This behavior could be an advantage in the case of treatments where a prolonged therapy is required.

4. Conclusions

The incorporation of DPA confers pH-responsive properties to the polymer, copolymers show a significant increase of the swelling degree when the pH decrease below 7.40 and reach the equilibrium around pH 6.0. This effect is directly proportional to the amount of present DPA in copolymers and inversely proportional with the amount of cross-linker. The apparent pK_a of copolymers depend on the composition of HEMA/DPA and the crosslinking degree of hydrogels, and estimated values are between 6.80 and 7.17. SEM images of copolymers show important morphological changes when varying the medium pH according to swelling results. At acid pH SEM imagines show an open morphology state with a porous structure as a consequence of the matrix expansion at this pH, while at basic pH show a collapsed state due to lower swelling degree and a more hydrophobic polymer. Hydrogels with 30 wt% of DPA show higher pores than hydrogels with 10 wt%. For hydrogel HD100/0-1 no changes with pH are appreciated and in all cases a compact surface is observed.

Copolymers of HEMA and DPA, having good film forming and physicochemical properties, were tested as drug delivery systems using Rh6G as model drug. The amount of Rh6G incorporated is higher for pure pHEMA than for copolymers and depends mainly on the medium pH and the interaction between the drug and the copolymers' matrix. The comparison of FTIR spectra between loaded and unloaded films indicates that Rh6G molecules interact with the OH group of the HEMA by hydrogen bonding or through dipole–dipole interaction. At pH 6.5, the total Rh6G uptake is lower than at pH 8.4, and SEM imagines show a greater accumulation on the surface at this pH. Thus the loaded Rh6G is inversely proportional with the swelling of the hydrogel and mainly depends on the interaction between the drug and the matrix of the copolymers. The total release of the drug depends on the polymer composition and medium pH. For pure pHEMA, the drug remains strongly associated with the polymer chains inside the matrix and, therefore, its release is very slow. On the other hand, for copolymers, the total Rh6G released at acid pH is higher than at basic pH, and it increases as the proportion of DPA monomer increases. The

pore size observed from SEM images is highly correlated with the drug release behavior when varying the medium pH. For copolymers, the release of the Rh6G model drug in PBS follows a non-Fickian diffusion process for pHs values less than or equal to 7.4. The change of the polymer´s cross-linking density affects only the drug release rate.

In conclusion, by changing the DPA content and the degree of cross-linking density it is possible to modify kinetic parameters and, therefore, to control the release kinetics depending on the medium pH. Results show that copolymers of HEMA/DPA are potentially useful as drug delivery systems for ophthalmic therapies.

Acknowledgements

We are grateful to CICPBA and ANPCyT (PICT 2011-0238) for their financial assistance. PAF is a postdoctoral student from CONICET (Argentina), FMP is Ph. D. student from CICPBA, and JIA is member of CICPBA. The authors thank Professor Piatti Guillermina for her assistance in reviewing and correcting the article.

References

[1] Jagur-Grodzinski J.: Polymeric gels and hydrogels for biomedical and pharmaceutical applications. Polymers for Advanced Technologies, **21**, 27–47 (2010). DOI: 10.1002/pat.1504

[2] Alvarez-Lorenzo C., Concheiro A.: Molecularly imprinted materials as advanced excipients for drug delivery systems. Biotechnology Annual Review, **12**, 225–268 (2006). DOI: 10.1016/s1387-2656(06)12007-4

[3] Geever L. M., Cooney C. C., Lyons J. G., Kennedy J. E., Nugent M. J., Devery S., Higginbotham C. L.: Characterisation and controlled drug release from novel drug-loaded hydrogels. European Journal of Pharmaceutics and Biopharmaceutics, **69**, 1147–1159 (2008). DOI: 10.1016/j.ejpb.2007.12.021

[4] García D. M., Escobar J. L., Noa Y., Bada N., Hernáez E., Katime I.: Timolol maleate release from pH-sensible poly(2-hydroxyethyl methacrylate-*co*-methacrylic acid) hydrogels. European Polymer Journal, **40**, 1683–1690 (2004). DOI: 10.1016/j.eurpolymj.2004.03.012

[5] Bettini R., Colombo P., Peppas N. A.: Solubility effects on drug transport through pH-sensitive, swelling-controlled release systems: Transport of theophylline and metoclopramide monohydrochloride. Journal of Controlled Release, **37**, 105–111 (1995). DOI: 10.1016/0168-3659(95)00069-K

[6] Atta A. M., Arndt K-F.: Swelling behavior of pH- and temperature-sensitive copolymers containing 2-hydroxyethyl methacrylate and *N*-vinyl-2-pyrrolidone crosslinked with new crosslinkers. Polymer International, **53**, 1870–1881 (2004). DOI: 10.1002/pi.1606

[7] Peppas N. A., Khare A. R.: Preparation, structure and diffusional behavior of hydrogels in controlled release. Advanced Drug Delivery Reviews, **11**, 1–35 (1993). DOI: 10.1016/0169-409X(93)90025-Y

[8] Xinming L., Yingde C., Lloyd A. W., Mikhalovsky S. V., Sandeman S. R., Howel C. A., Liewen L.: Polymeric hydrogels for novel contact lens-based ophthalmic drug delivery systems: A review. Contact Lens and Anterior Eye, **31**, 57–64 (2008). DOI: 10.1016/j.clae.2007.09.002

[9] Richter A., Paschew G., Klatt S., Lienig J., Arndt K-F., Adler H-J.: Review on hydrogel-based pH sensors and microsensors. Sensors, **8**, 561–581 (2008). DOI: 10.3390/s8010561

[10] Casolaro M., Casolaro I., Lamponi S.: Stimuli-responsive hydrogels for controlled pilocarpine ocular delivery. European Journal of Pharmaceutics and Biopharmaceutics, **80**, 553–561 (2012). DOI: 10.1016/j.ejpb.2011.11.013

[11] Alvarez-Lorenzo C., Hiratani H., Concheiro A.: Contact lenses for drug delivery. American Journal of Drug Delivery, **4**, 131–151 (2006). DOI: 10.2165/00137696-200604030-00002

[12] Urtti A., Salminen L.: Minimizing systemic absorption of topically administered ophthalmic drugs. Survey of Ophthalmology, **37**, 435–456 (1993). DOI: 10.1016/0039-6257(93)90141-S

[13] del Amo E. M., Urtti A.: Current and future ophthalmic drug delivery systems: A shift to the posterior segment. Drug Discovery Today, **13**, 135–143 (2008). DOI: 10.1016/j.drudis.2007.11.002

[14] Lin C-C., Metters A. T.: Hydrogels in controlled release formulations: Network design and mathematical modeling. Advanced Drug Delivery Reviews, **58**, 1379–1408 (2006). DOI: 10.1016/j.addr.2006.09.004

[15] Wang K., Xu X., Wang Y., Yan X., Guo G., Huang M., Luo F., Zhao X., Wei Y., Qian Z.: Synthesis and characterization of poly(methoxyl ethylene glycol-caprolactone-*co*-methacrylic acid-*co*-poly(ethylene glycol) methyl ether methacrylate) pH-sensitive hydrogel for delivery of dexamethasone. International Journal of Pharmaceutics, **389**, 130–138 (2010). DOI: 10.1016/j.ijpharm.2010.01.026

[16] Evans D. F., Pye G., Bramley R., Clark A. G., Dyson T. J., Hardcastle J. D.: Measurement of gastrointestinal pH profiles in normal ambulant human subjects. Gut, **29**, 1035–1041 (1988). DOI: 10.1136/gut.29.8.1035

[17] Wang Y., Chen L., Tan L., Zhao Q., Luo F., Wei Y., Qian Z.: PEG–PCL based micelle hydrogels as oral docetaxel delivery systems for breast cancer therapy. Biomaterials, **35**, 6972–6985 (2014).
DOI: 10.1016/j.biomaterials.2014.04.099

[18] Carney L. G., Hill R. M.: Human tear pH. Diurnal variations. Archives of Ophthalmology, **94**, 821–824 (1976).
DOI: 10.1001/archopht.1976.03910030405011

[19] Baeyens V., Gurny R.: Chemical and physical parameters of tears relevant for the design of ocular drug delivery formulations. Pharmaceutica Acta Helvetiae, **72**, 191–202 (1997).
DOI: 10.1016/S0031-6865(97)00021-6

[20] Jaros P. A., Coles W. H.: Ocular surface pH in rosacea. CLAO Journal, **9**, 333–336 (1983).

[21] Norn M. S.: Tear fluid pH in normals, contact lens wearers, and pathological cases. Acta Ophthalmologica, **66**, 485–489 (1988).
DOI: 10.1111/j.1755-3768.1988.tb04368.x

[22] Bawa P., Pillay V., Choonara Y. E., du Toit L. C.: Stimuli-responsive polymers and their applications in drug delivery. Biomedical Materials, **4**, 022001/1–022001/15 (2009).
DOI: 10.1088/1748-6041/4/2/022001

[23] París R., Quijada-Garrido I.: Temperature- and pH-responsive behaviour of poly(2-(2-methoxyethoxy)ethyl methacrylate-*co*-*N*,*N*-dimethylaminoethyl methacrylate) hydrogels. European Polymer Journal, **46**, 2156–2163 (2010).
DOI: 10.1016/j.eurpolymj.2010.09.004

[24] Emileh A., Vasheghani-Farahani E., Imani M.: Swelling behavior, mechanical properties and network parameters of pH- and temperature-sensitive hydrogels of poly((2-dimethyl amino) ethyl methacrylate-*co*-butyl methacrylate). European Polymer Journal, **43**, 1986–1995 (2007).
DOI: 10.1016/j.eurpolymj.2007.02.002

[25] Andrade-Vivero P., Fernandez-Gabriel E., Alvarez-Lorenzo C., Concheiro A.: Improving the loading and release of NSAIDs from pHEMA hydrogels by copolymerization with functionalized monomers. Journal of Pharmaceutical Sciences, **96**, 802–813 (2007).
DOI: 10.1002/jps.20761

[26] Amalvy J. I., Wanless E. J., Li Y., Michailidou V., Armes S. P., Duccini Y.: Synthesis and characterization of novel ph-responsive microgels based on tertiary amine methacrylates. Langmuir, **20**, 8992–8999 (2004).
DOI: 10.1021/la049156t

[27] Wang K., Fu S. Z., Gu Y. C., Xu X., Dong P. W., Guo G., Zhao X., Wei Y. Q., Qian Z. Y.: Synthesis and characterization of biodegradable pH-sensitive hydrogels based on poly(ε-caprolactone), methacrylic acid, and poly(ethylene glycol). Polymer Degradation and Stability, **94**, 730–737 (2009).
DOI: 10.1016/j.polymdegradstab.2008.12.013

[28] Faccia P. A., Amalvy J. I.: Synthesis, characterization, and swelling behavior of new pH-sensitive hydrogels derived from copolymers of 2-hydroxyethyl methacrylate and 2-(diisopropylamino)ethylmethacrylate. Journal of Applied Polymer Science, **127**, 1974–1980 (2013).
DOI: 10.1002/app.37576

[29] Firestone B. A., Dickason M. A., Tran T.: Solubility characteristics of three fluoroquinolone ophthalmic solutions in an *in vitro* tear model. International Journal of Pharmaceutics, **164**, 119–128 (1998).
DOI: 10.1016/S0378-5173(97)00427-4

[30] Milder B.: The lacrimal apparatus, in 'Adler's Physiology of the eye: Clinical application' (eds.: Moses R. A.) Mosby, St. Louis, 15–35 (1987).

[31] Xu X., Fu S., Wang K., Jia W., Guo G., Zheng X., Dong P., Guo Q., Qian Z.: Preparation and characterization of vitamin-12 loaded biodegradable pH-sensitive microgels. Journal of Microencapsulation, **26**, 642–648 (2009).
DOI: 10.3109/02652040802610827

[32] Desai S., Perkins J., Harrison B. S., Sankar J.: Understanding release kinetics of biopolymer drug delivery microcapsules for biomedical applications. Materials Science and Engineering: B, **168**, 127–131 (2010).
DOI: 10.1016/j.mseb.2009.11.006

[33] Ozay O.: Synthesis and characterization of novel pH-responsive poly(2-hydroxylethyl methacrylate-*co*-*N*-allylsuccinamic acid) hydrogels for drug delivery. Journal of Applied Polymer Science, **131**, 39660/1–39660/10 (2014).
DOI: 10.1002/app.39660

[34] Canto L. B., Pessan L. A.: Determination of the composition of styrene–glycidyl methacrylate copolymers by FTIR and titration. Polymer Testing, **21**, 35–38 (2002).
DOI: 10.1016/S0142-9418(01)00041-1

[35] Sato S., Kim S. W.: Macromolecular diffusion through polymer membranes. International Journal of Pharmaceutics, **22**, 229–255 (1984).
DOI: 10.1016/0378-5173(84)90024-3

[36] Varshosaz J., Koopaie N.: Cross-linked poly (vinyl alcohol) hydrogel: Study of swelling and drug release behaviour. Iranian Polymer Journal **11**, 123–131 (2002).

[37] Ritger P. L., Peppas N. A.: A simple equation for description of solute release II. Fickian and anomalous release from swellable devices. Journal of Controlled Release, **5**, 37–42 (1987).
DOI: 10.1016/0168-3659(87)90035-6

[38] Ritger P. L., Peppas N. A.: A simple equation for description of solute release I. Fickian and non-Fickian release from non-swellable devices in the form of slabs, spheres, cylinders or discs. Journal of Controlled Release, **5**, 23–36 (1987).
DOI: 10.1016/0168-3659(87)90034-4

[39] Bajpai A. K., Shukla S. K., Bhanu S., Kankane S.: Responsive polymers in controlled drug delivery. Progress in Polymer Science, **33**, 1088–1118 (2008).
DOI: 10.1016/j.progpolymsci.2008.07.005

[40] Karlgard C. C. S., Wong N. S., Jones L. W., Moresoli C.: *In vitro* uptake and release studies of ocular pharmaceutical agents by silicon-containing and p-HEMA hydrogel contact lens materials. International Journal of Pharmaceutics, **257**, 141–151 (2003).
DOI: 10.1016/S0378-5173(03)00124-8

[41] Brannon-Peppas L., Peppas N. A.: Equilibrium swelling behavior of pH-sensitive hydrogels. Chemical Engineering Science, **46**, 715–722 (1991).
DOI: 10.1016/0009-2509(91)80177-Z

[42] Chirila T. V., Chen Y-C., Griffin B. J., Constable I. J.: Hydrophilic sponges based on 2-hydroxyethyl methacrylate. I. Effect of monomer mixture composition on the pore size. Polymer International, **32**, 221–232 (1993).
DOI: 10.1002/pi.4990320303

[43] Nam K., Watanabe J., Ishihara K.: Modeling of swelling and drug release behavior of spontaneously forming hydrogels composed of phospholipid polymers. International Journal of Pharmaceutics, **275**, 259–269 (2004).
DOI: 10.1016/j.ijpharm.2004.02.009

[44] Pinzón N., Espinosa A., Perilla J., Hernáez E., Katime I.: A model for swelling and solute diffusion in water soluble polymers (in Spanish). Revista Iberoamericana de Polímeros, **3**, 38–54 (2002).

[45] Lowman A. M., Peppas N. A.: Encyclopedia of controlled drug delivery Vol 1. Wiley, New York (1999).

[46] Chen J., Park H., Park K.: Synthesis of superporous hydrogels: Hydrogels with fast swelling and superabsorbent properties. Journal of Biomedical Materials Research, **44**, 53–62 (1999).
DOI: 10.1002/(SICI)1097-4636(199901)44:1<53::AID-JBM6>3.0.CO;2-W

[47] Chen J., Park K.: Superporous hydrogels: Fast responsive hydrogel systems. Journal of Macromolecular Science Part A: Pure and Applied Chemistry, **36**, 917–930 (1999).
DOI: 10.1080/10601329908951189

[48] Tleugabulova D., Sui J., Ayers P. W., Brennan J. D.: Evidence for rigid binding of Rhodamine 6G to silica surfaces in aqueous solution based on fluorescence anisotropy decay analysis. Journal of Physical Chemistry B, **109**, 7850–7858 (2005).
DOI: 10.1021/jp045569r

[49] Jin L., Deng Y., Hu J., Wang C.: Preparation and characterization of core–shell polymer particles with protonizable shells prepared by oxyanionic polymerization. Journal of Polymer Science Part A: Polymer Chemistry, **42**, 6081–6088 (2004).
DOI: 10.1002/pola.20453

[50] Watanabe H., Hayazawa N., Inouye Y., Kawata S.: DFT vibrational calculations of Rhodamine 6G adsorbed on silver: Analysis of tip-enhanced Raman spectroscopy. Journal of Physical Chemistry B, **109**, 5012–5020 (2005).
DOI: 10.1021/jp045771u

[51] Tripathi S. K., Monga A., Saini G. S. S.: Characterization of thermally evaporated thin films of Rhodamine 6G. Smart Materials and Structures, **18**, 125012/1–125012/7 (2009).
DOI: 10.1088/0964-1726/18/12/125012

[52] Saini G. S., Kaur S., Tripathi S. K., Mahajan C. G., Thanga H. H., Verma A. L.: Spectroscopic studies of Rhodamine 6G dispersed in polymethylcyanoacrylate. Spectrochimica Acta Part A: Molecular and Biomolecular Spectroscopy, **61**, 653–658 (2005).
DOI: 10.1016/j.saa.2004.05.022

[53] Tomić S. L., Mićić M. M., Filipović J. M., Suljovrujić E. H.: Swelling and drug release behavior of poly(2-hydroxyethyl methacrylate/itaconic acid) copolymeric hydrogels obtained by gamma irradiation. Radiation Physics and Chemistry, **76**, 801–810 (2007).
DOI: 10.1016/j.radphyschem.2006.05.013

[54] Momose T., Ito N., Kanai A., Watanabe Y., Shibata M.: Adsorption of levocabastine eye drops by soft contact lenses and its effects in rabbit eyes. CLAO Journal, **23**, 96–99 (1997).

[55] Lumbroso P., Nhamias M., Nhamias S., Tranche P.: A preliminary study of the adsorption and release of preservatives by contact lenses and collagen shields. CLAO Journal, **22**, 61–63 (1996).

[56] Miranda M. N., García-Castiñeiras S.: Effects of pH and some common topical ophthalmic medications on the contact lens Permalens. CLAO Journal, **9**, 43–48 (1983).

[57] Gendron P-O., Avaltroni F., Wilkinson K. J.: Diffusion coefficients of several Rhodamine derivatives as determined by pulsed field gradient–nuclear magnetic resonance and fluorescence correlation spectroscopy. Journal of Fluorescence **18**, 1093–1101 (2008).
DOI: 10.1007/s10895-008-0357-7

eXPRESS Polymer Letters Vol.9, No.6 (2015) 567–581
Available online at www.expresspolymlett.com
DOI: 10.3144/expresspolymlett.2015.53

Effect of bisphenol-A on the structures and properties of phthalonitrile-based resin containing benzoxazine

M. Z. Xu[*], *K. Jia, X. B. Liu*

Research Branch of Functional Materials, Institute of Microelectronic & Solid State Electronic, High-Temperature Resistant Polymers and Composites Key Laboratory of Sichuan Province, University of Electronic Science and Technology of China, 610054 Chengdu, P. R. China

Received 4 November 2014; accepted in revised form 2 January 2015

Abstract. Phthalonitrile and benzoxazine have been considered as high-performance materials in the field of heterocyclic chemistry. The polymerization of phthalonitrile and benzoxazine accelerated by active phenolic hydroxyl has attracted wide interests. In this work, self-promoted polymerization behavior and processability of phthalonitrile containing benzoxazine (BA-ph) with bisphenol-A (BPA) were investigated. Results revealed that BA-ph/BPA exhibited representative double-stage curing behaviors corresponding to the ring-opening polymerization of benzoxazine rings and ring-formation polymerization of nitrile groups. Compared with that of BA-ph, processability of BA-ph/BPA was improved and could be tuned by varying BPA contents, processing temperature and time. Then BA-ph/BPA/glass fiber (GF) composite laminates were prepared. In comparison with that of BA-ph/GF laminates (542 MPa and 25.8 GPa), the flexural strength and modulus were up to 789 MPa and 23.6 GPa, respectively. Moreover, double T_gs were observed at temperature around 200~300°C and 300~380°C, indicating microphase separation during the polymerization of oxazine rings and nitrile groups, confirmed by the scanning electron microscopic (SEM) images. Thermal stabilities demonstrated that all BA-ph/BPA/GF composites exhibited high $T_{10\%}$ up to 510°C. The systematic study of BA-ph/BPA system could enrich our knowledge on phthalonitrile-based resins in industrial applications, especially in the areas which require excellent mechanical properties and high temperature resistance.

Keywords: *polymer composites, phthalonitrile, benzoxazine, interpenetrating network, cross-linking*

1. Introduction

Over the past decades, epoxy (EP), phenolic (PE) and benzoxazine (Bz) resins have been reported widely in the fabrication of GF-reinforced laminates due to their properties such as good wettability, nice processability and good chemical resistances [1–3]. While the common thermal properties (150~300°C) and low glass transition temperature (100~250°C) of the polymers have greatly limited their further applications in the fields of marine, aerospace and electronic packaging [3, 4]. As the only candidate to satisfy the flame standards of United States Navy (MIL-STD-2031), phthalonitrile resins have attracted increased attentions both in laboratory and industry areas, recently. However, high curing temperature (≥250°C), high postcuring temperature (≥375°C) and narrow processing window (≤30°C) have also greatly limited their wide applications [5, 6]. To solve these problems, phthalonitrile-based monomers with additional polymerisable groups such as amino, carboxyl, propargyl, oxazine, allyl, etc. were designed and synthesized to pursue self-promoted polymerization and a broad processing window for advanced applications [7–11].

It is well known that a simple and effective method is the incorporation of hydroxyl or amino groups

[*]Corresponding author, e-mail: lisa735994712@126.com

into the reactive phthalonitrile units. The hydroxy- or amino-functional phthalonitrile polymers were proved to cross-link by self-promoted curing [12, 13]. A kind of phthalonitrile containing benzoxazine resin (BA-ph) was designed and synthesized via a condensation reaction between amino-functional phthalonitrile and bisphenol A, shown in Figure 1 [14]. Owing to the active phenolic hydroxyls generated from ring-opening of benzoxazine, many advantages can be obtained. On the one hand, the active phenolic hydroxyls generated from ring-opening of benzoxazine can be used as a kind of curing agent to achieve the cross-linking networks, thus realizing the self-promoted copolymerization. On the other hand, the active phenolic hydroxyls allowed BA-ph to be used as hydroxyl-functional phthalonitrile to achieve good processability and desirable properties of the composites [14–16]. In addition, the initial curing temperature and postcuring temperature of BA-ph were 200~220 and 280°C, respectively, which significantly improved the processibility of phthalonitrile-based resins. However, the process temperatures were also quite high for the industry applications which required the composites fabricated in lower temperature (≤200°C). Additionally, it was obvious that the outstanding properties of phthalonitrile-based composites were attributed to the completed polymerization of nitrile groups. Previous reports indicated that a mass of nitrile groups remaining in the polymer composites. Thus, the properties of BA-ph polymers can be further improved via increasing the polymerization degree of nitrile groups.

The mechanism for benzoxazine ring curing involves ring opening by protonation of the oxygen atom to form an iminium ion and active hydroxy merits, then electrophilic aromatic substitution, which was earlier established by McDonagh and Smith that 3, 4-dihydro-2H-1, 3-benzoxazines exhibit ring/chain tautomerism when protonated by migration of the proton from the nitrogen to the oxygen atom [17]. Meanwhile, the phthalonitrile-based resins can be effectively catalyzed by the active hydroxyl to form phthalocyanine-dominated polymers. In terms of the given mechanism, bisphenol-A (BPA) was introduced in the BA-ph matrix which provided additional active hydroxyl.

In this study, to understand the catalysis behaviors of active hydroxy in the curing process of BA-ph resin, various molar ratios BPA were introduced. Curing behaviors and processability of BA-ph/BPA were investigated by differential scanning calorimetric (DSC) and dynamic rheological analysis (DRA). The structural transition of the BA-ph/BPA system in the polymerization process was observed by Fourier transform infrared spectrometer (FTIR) and scanning electron microscope (SEM) images. The possible reaction process between BA-ph and BPA was presented in Figures 2 and 3. Then, solution prepolymer method was employed to prepare the impregnating adhesive and GF-reinforced laminates were fabricated by heat compression molding at 160°C. The mechanical and thermal measurements have been performed to evaluate the effects of BPA on the composite laminates. Also, the significant enhancements of the mechanical properties for BA-ph/BPA/GF laminates have been discussed.

2. Experimental

2.1. Materials

Bisphenol-A, paraformaldehyde, 1, 4-dioxane, and toluene were obtained from Tianjin BODI Chemicals Co. Ltd., Tianjin, China. 4-Nitrophthalonitrile was obtained from Alpha Chemical (Dezhou) Co. Ltd., Shijiazhuang, China. Butanone was purchased from Tianjin Guangfu Fine Chemical Research Institute. 3-Aminophenoxyphthalonitrile (3-APN, T_m = 174°C) was obtained from Dymatic Special Chemicals co., ltd., Chengdu, China. The woven glass fiber fabric is E-glass cloth-7628 provided by Jiangxi Changjia

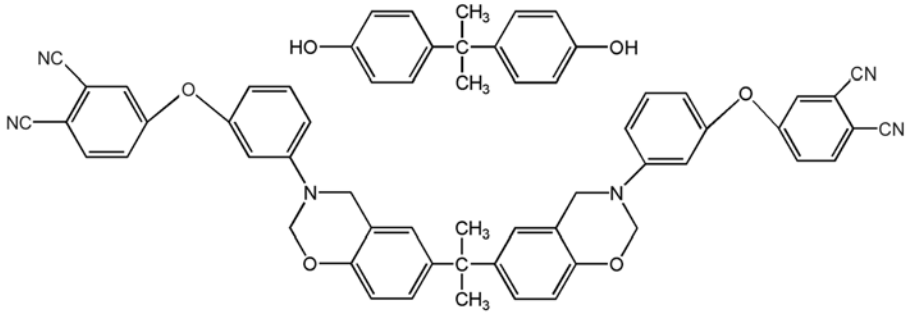

Figure 1. Structures of BPA and BA-ph monomer

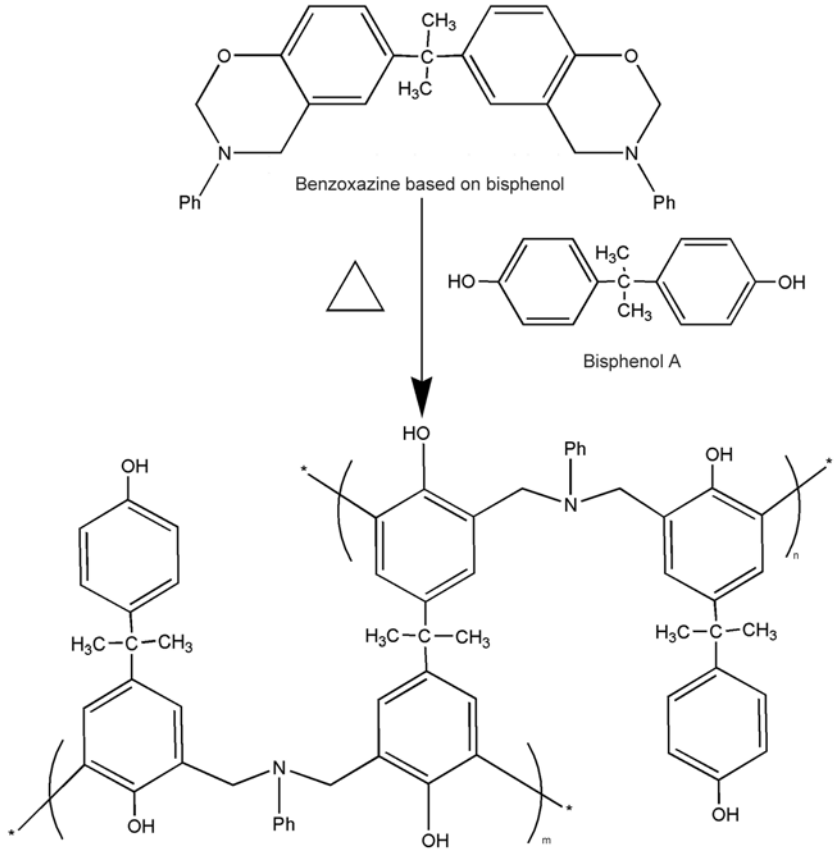

Figure 2. Reaction scheme for the AB-crosslinked polymerization of benzoxazine and BPA

glass fiber Co. Ltd., Jiangxi, China. The thickness of the fiber cloth was 0.188 mm and the weight was 210 g/m^2. All the reagents were of analytical grade and used without further purification.

2.2. Synthesis of phthalonitrile containing benzoxazine (BA-ph)

The synthetic route of BA-ph monomer was synthesized according to the reference [14, 18] reported before with minor modifications. In a typical experiment, 3-APN (47.00 g, 0.20 mol), bisphenol-A (22.80 g, 0.10 mol), paraformaldehyde (12.00 g, 0.40 mol) and 1, 4-Dioxane (60 mL) and toluene (10 mL) were mixed under a stirrer at a speed of 300 rpm. After being refluxed at 100°C for 5 h, the reaction mixture was treated by rotary evaporation processing. Then, the mixture completely dissolved in chloroform to remove the benzoxazine oligomer. Finally, the solution was slowly poured into the alkaline solution of sodium hydroxide (0.5 mol·L^{-1}) distilled water to remove the bisphenol-A residue and cooled to room temperature in the formation of a solid. The solid was filtered and washed five times with distilled water. Then the yellow solid was dried in a vacuum at 60°C overnight.

2.3. Preparation of BA-ph/BPA blends and impregnating adhesive

The BA-ph/BPA thermosetting blends with various molar ratios (BA-ph/BPA ratios: 2:1, 2:2, and 2:3) were prepared by physical blending at room temperature (25°C), labeled as BA-ph/BPA21, BA-ph/BPA22 and BA-ph/BPA23, respectively. As a reference, the pure BA-ph was prepared similarly.

The BA-ph/BPA impregnating adhesive with various content of BPA was prepared by solution prepolymer method in butanone at 80°C for 2 h. Then, the viscous solution was obtained.

2.4. Preparation of BA-ph/BPA/GF composite laminates

The preparation of the BA-ph/BPA/GF composite laminates was carried out as follows. GF cloth (20×20 cm^2) was brush-coated with the viscous solution obtained above and dried at room temperature for 24 h. The ratio was designed to give a prepreg of 40% copolymers and 60% GF by weight. Ten layers of GF prepreg cloth were placed in a stainless steel mold and hot-pressed under a pressure of 20 MPa at 160°C for 4 h. The laminates were natural cooled to room temperature and then solid poly-

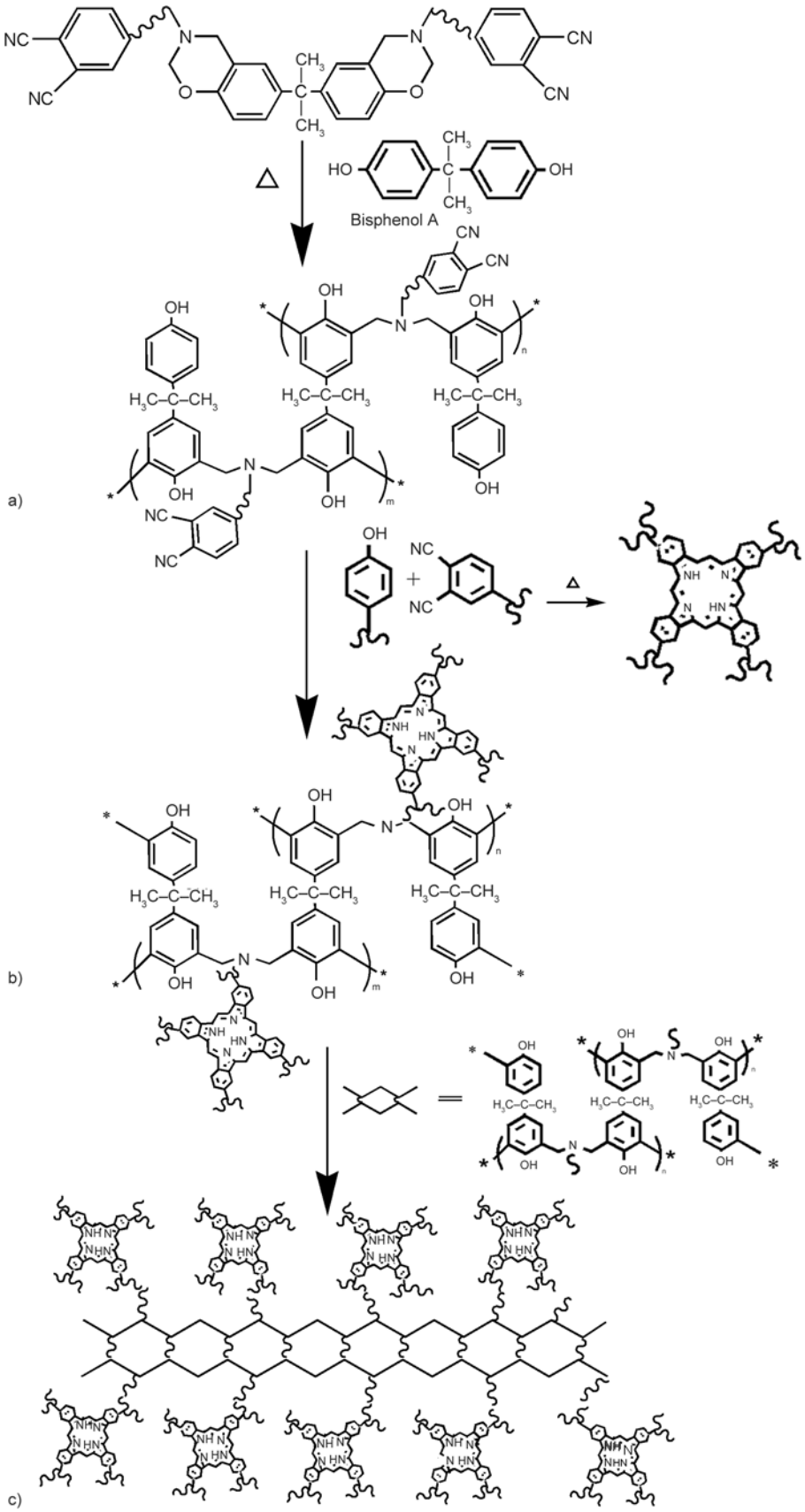

Figure 3. Reaction scheme for the polymerization of BA-ph: (a) linear linked of benoxazine, (b) ring-forming polymerization of nitrile groups and (c) possible structures of resultant polymers

merized at 200°C for 4 h, 240°C for 2 h and 280°C for 2 h in the oven, respectively. The final laminates were marked as BA-ph/BPA/GF21, BA-ph/BPA/GF22 and BA-ph/BPA/GF23, respectively.

2.5. Characterizations

Differential scanning calorimetric (DSC) analysis was performed by TA Instruments Modulated DSC-Q100 at a heating rate of 10°C/min and a nitrogen flow rate of 50 mL/min. The second DSC scans were performed for the according samples. Dynamic rheological analysis (DRA) was performed using TA Instruments Rheometer AR-G2 with a frequency of 1 Hz at different temperatures in air. The samples (0.5–1 g) were melted between 25 mm diameter parallel plates with an environmental testing chamber of the rheometer. FTIR spectra were recorded with Shimadzu FTIR8400S Fourier Transform Infrared spectrometer in KBr pellets between 4000 and 500 cm^{-1} in air. The flexural tests of the composite laminates were performed with a SANS CMT6104 series desktop electromechanical universal testing machine at room temperature. Flexural tests (three-point bending mode) were held according to the GB/T9341-2008 standard test method with a crosshead displacement speed of 10 mm/min and the test fixture was mounted in a 10 kN capacity. The samples (dimension: 80 mm ×15 mm×2 mm) were tested with a support span/sample thickness ratio of 15:1, and gained as average value for every three samples. Dynamic mechanical analysis (DMA) in a three-point-blending mode was performed on QDMA-800 dynamic mechanical analyzer (TA Instruments, USA) to determine the glass transition temperature (T_g). The storage modulus and tan delta were investigated at a frequency of 1 Hz and amplitude of 20 μm, and the samples (dimensions 30 mm×10 mm×2 mm) were heated from 50 to 400°C at a temperature ramp of 3°C/min. Thermal gravimetric analysis (TGA) was performed on a TA Instruments TGA Q50 with a heating rate of 20°C/min (under nitrogen or air) and a purge of 40 mL/min. The morphology of the fractured surfaces of the polymers were observed by SEM (JSM2 5900LV) operating at 20 kV.

3. Results and discussion

3.1. Curing behaviors of BA-ph/BPA blends

Model curing studies were conducted to character the curing behavior of phthalonitrile monomer with the curing agent of 2-hydroxydiphenylmethane [19]. Compounds with phenol hydroxyl were used as nucleophilic initiator to catalyze the reaction between nitrile groups of phthalonitrile monomer. This was driven by the fact that the nitrile groups can readily form the isoindoline, diimino, triazine and phthalocyanine with nucleophilic phenol groups [20].

The curing behaviors of BA-ph/BPA blends were studied by DSC analysis presented in Figure 4 and the main data were shown in Table 1. The typical curves of BA-ph and BPA monomer were shown in Figure 4b. It can be seen that the poignant endothermic transition observed at 156°C was assigned to the melting temperature (T_{melt}) of BPA monomer. However, the wide endothermic transition started from 200°C and peaked at 250°C was attributed to the evaporation of BPA monomer. In Figure 4b (curve a) for pristine BA-ph, the double exotherm bands were peaked at 230°C and 263°C, corresponding to the ring-opening polymerization of oxaznine rings and the ring-forming polymerization of nitrile groups, respectively [14, 15]. With the introduction of BPA, the exotherm bands shifted to a

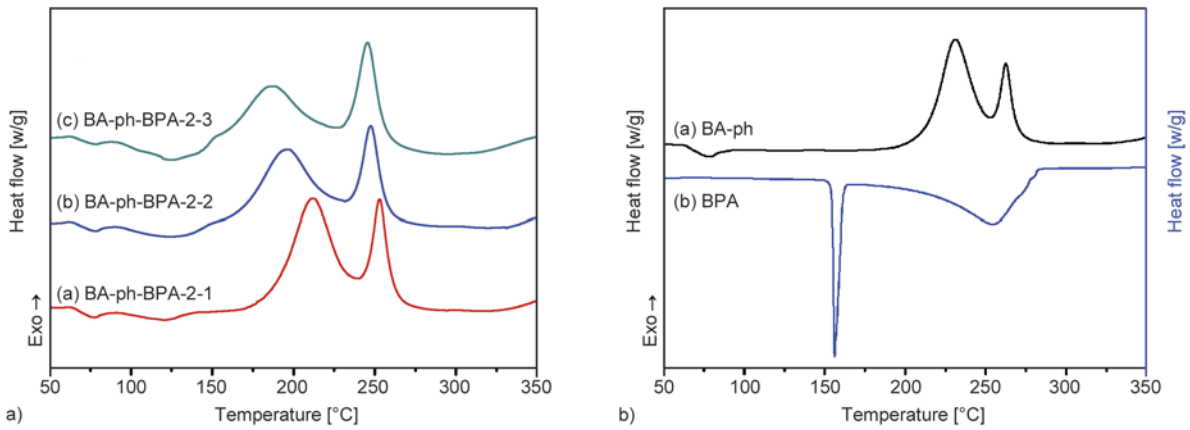

Figure 4. DSC curves of (a): BA-ph/BPA blends with various contents of BPA and (b): BA-ph and BPA monomers

Table 1. Thermal properties of BA-ph/BPA system

Samples	T_m [°C]	T_i [°C]	T_{top_1} [°C]	T_{top_2} [°C]	ΔH_{curing_1} [J/g]	ΔH_{curing_2} [J/g]	Weight loss [%]
BPA	156	–	–	–	–	–	100
BA-ph	56.5	170	230	263	167.7	46.1	0.48
BA-ph-BPA21	79.2	125	210	253	201.5	69.3	1.86
BA-ph-BPA22	78.5	126	193	248	178.1	76.6	3.95
BA-ph-BPA23	77.8	123	183	246	172.8	98.3	9.65

lower temperature range, shown in Figure 4a. The peak temperatures of BA-ph/BPA systems were lowered to 183~210°C and the maximum was lowered to 246~253°C. The lowering of the temperature necessary for the ring-opening polymerization of BA-ph has considerable meaning because the high temperature necessary for the complete polymerization often cause problems and limits its applications. Additionally, the enthalpy of curing of BA-ph/BPA blends was different in comparison with that of pristine BA-ph, both for the ring-opening of oxazine rings and ring-forming of nitrile groups. The enthalpy for the ring-opening of oxazine rings successively decreased with increasing the BPA, shown in Table 1. It was related to the fact that the oxazine rings formed more easily Mannich bridge structures in the presence of phenol hydroxyl. References reported that the phenolic compounds with free ortho or para positions act as initiators for the ring-opening oligomerization of benzoxazine composites, and an aminoalkylation reaction occur preferentially at the ortho and para positions of phenols [20–23]. Thus, the phenol hydroxyl groups in BPA help the ring-opening reaction of oxazine rings through copolymerization with BA-ph, affording an AB-crosslinked polymer, shown in Figure 2.

Moreover, the initial curing temperature gradient between oxazine rings and nitrile groups has been enlarged with increasing the content of BPA, shown in Figure 4a. The difference of polymerization rate would result in a microphase separation between the components resulting from the polymerization of oxazine rings and nitrile groups, respectively. As shown in Figure 3, BPA firstly catalyzed the ring-opening polymerization of oxazine rings and the linear polybenzoxazine formed (Figure 3a). Then, the ring-forming polymerization of nitrile groups was triggered by the active hydroxyl provided both from the oxazine rings and BPA (Figure 3b). With increasing the temperature or prolonging the time, the phthalocyanine cycles self-aggregated and paralleled to the linear linked network of polybenzoxazine (Figure 3c).

To further study the curing behaviors of BA-ph/BPA blends, isothermal DSC curves as a function of time have also been investigated at 180°C. It can be seen in Figure 5 (curve a) that there was a weak and wide exothermic band appeared at about 15 min, which indicated the extremely low curing rate of pristine BA-ph at 180°C. Figure 5 (curve b and c) and (curve d) showed the curves of BA-ph/BPA blends with various contents of BPA. All the blends exhibited double exothermic peaks which resulted from the double curing reactions. For all of the blends, the first exothermic peaks occurred quickly at about 0.5~20 min and the second occurred at 30~60 min. As can be seen, with increasing the content of BPA, the intensity of the first exothermic peak increased significantly. The reason was that the ring-opening reaction reinforced by BPA monomer and the formation of the Mannich bridge structures via ring-opening polymerization was the first priority [11, 14, 16]. The second exothermic peak corresponded to the polymerization of nitrile groups catalyzed by the extra hydrogen provided from the ring-opening of oxazine rings and BPA. For the curve of BA-

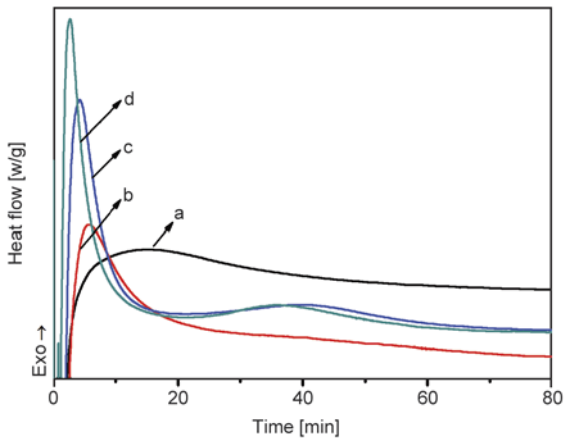

Figure 5. Time sweep DSC curves of BA-ph/BPA blends with various content of BPA: (a) BA-ph, (b) BA-ph/BPA21, (c) BA-ph/BPA22 and (d) BA-ph/BPA23

ph/BPA22 system, the second exothermic peak related to the polymerization of nitrile groups was proportional in comparison with that of BA-ph/BPA23 and stronger obviously than that of BA-ph/BPA21. In all, the polymerization of BA-ph could be significantly catalyzed by BPA and polymerization of the blends could be easily triggered at lower temperatures and controlled by varying the content of BPA. Additionally, with increasing the content of BA-ph, curing temperature gradient between oxazine rings and nitrile groups has been explicated.

3.2. Processability of BA-ph/BPA blends

The rheological behavior, a key factor in predicting processability, was studied by measuring viscosity changes accompanying the self-promoted curing reaction of the BA-ph/BPA blends. In Figure 6, the complex viscosity (η*) of BA-ph/BPA blends, as well as that of BA-ph, was determined as a function of temperature from 50 to 300°C. In each case, a decrease was observed in viscosity and a minimum melt viscosity of 1–6 Pa·s was observed for the blends. The low viscosity was maintained in the temperature range from 80~180°C, suggesting good processability of BA-ph/BPA systems. A rapid increase of η* was observed at about 180~200°C for all BA-ph/BPA blends. Moreover, the increase of η* was observed at lower temperatures with increasing the amount of BPA.

To further determine the processing temperature and time for BA-ph/BPA blends, the η* change of the BA-ph/BPA22 blend was measured as a function of time at various temperatures, shown in Figure 7. The curves indicated that the viscosity increased with the increase of temperature. As expected, high temperature had a great tendency to accelerate the polymerization reaction of BA-ph/BPA blends. It can be seen that the η* at different temperatures were relatively low and stable before the final curing reaction occurred. However, after the curing reaction started, the η* increased dramatically [24]. Namely, the increase of η* for BA-ph/BPA22 blend at 170 and 180°C took a rather short time (12 and 6 min), revealing that curing reaction carried out rapidly. Thus, 160°C was a proper processing temperature for BA-ph/BPA copolymers.

For comparison, isothermal viscosity measurements were recorded on the BA-ph/BPA blends at 160°C as a function of time to investigate the effect of BPA content on the processability. As depicted in Figure 8, it can be seen that all of the BA-ph/BPA blends exhibited relatively low initial η* and the initial η*

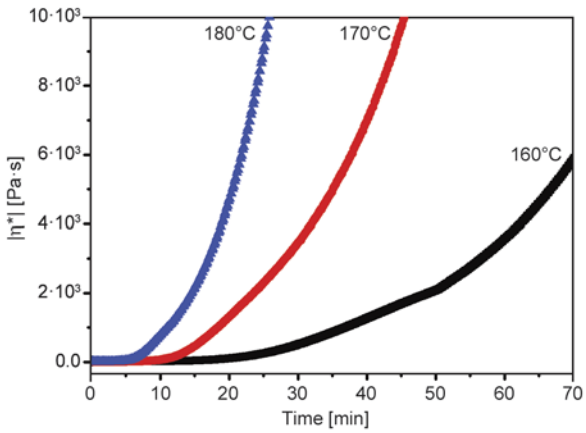

Figure 7. Complex viscosity (η*) as a function of time at various temperatures for the BA-ph/BPA22 system

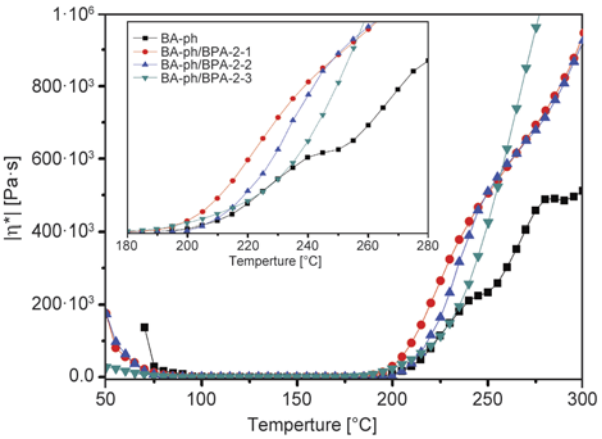

Figure 6. Complex viscosity (η*) as a function of temperature for BA-ph/BPA system with various content of BPA

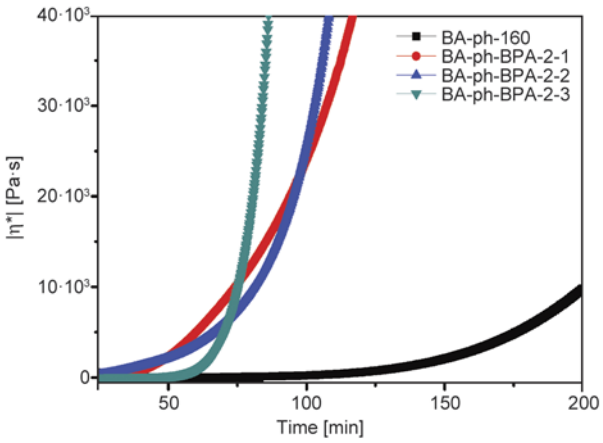

Figure 8. Complex viscosity (η*) as a function of time at 160°C for the BA-ph/BPA system with various content of BPA

of BA-ph/BPA blends decreased with increasing the amount of BPA. A complex melt viscosity around 3 Pa·s was observed for all of the blends at 160°C, initially, and then exhibited a dramatic increasing viscosity. The complex viscosity of BA-ph/BPA21, BA-ph/BPA22 and BA-ph/BPA23 blends increased to 5000 Pa·s in about 57, 64 and 70 min, respectively. Moreover, BA-ph/BPA21, BA-ph/BPA22 and BA-ph/BPA23 blends show different modes with the extension of testing time. The complex viscosity increased rapidly until the complex viscosity of BA-ph/BPA was 12000 Pa·s. Then, the increasing trend of complex viscosity was coincident with the increasing content of BPA. The sectionalized increasing of complex viscosity suggested the double-stage polymerization attributed to the ring-opening polymerization of oxazine rings and the ring-forming polymerization of nitrile groups accelerated by hydroxyl provided by BPA and ring-opening of oxazine rings at elevated temperature. These were in good agreement with the results of DSC. In all, results revealed that the influence of BPA content on the rate of the copolymerization was evident and the blends had the desirable processing temperature and gelation time [25]. Based on these rheological results, the blends exhibited the desirable polymerization rate and a wide processing window, which are important to their applications in resin transfer molding or resin infusion processes.

3.3. Structures of BA-ph/BPA pre-polymers and polymers

To confirm the structural transition of the composites, the structures of BA-ph/BPA pre-polymers obtained after being heated at 160°C and BA-ph/BPA22 polymers heated at 200, 240 and 280°C were investigated by FTIR spectra, respectively, as shown in Figure 9 and Figure 10. In Figure 9, the intensity characteristic absorption band at 1478 cm^{-1} was assigned to the in-plane C–H stretching of the tetra-substituted benzene, indicating that the methylene bridges formed in the free ortho positions of the phenolic structures [26, 27]. Meanwhile, the characteristic band of oxazine at around 967 cm^{-1} did not appear in the spectra, confirming oxazine rings were involved into the polymerization at 160°C. Meanwhile, the peaks observed at 1164 and 1114 cm^{-1} were corresponded to the frame vibration of phthalocyanine, and peaks at 1620 and 1283 cm^{-1} were assigned to the stretching vibration

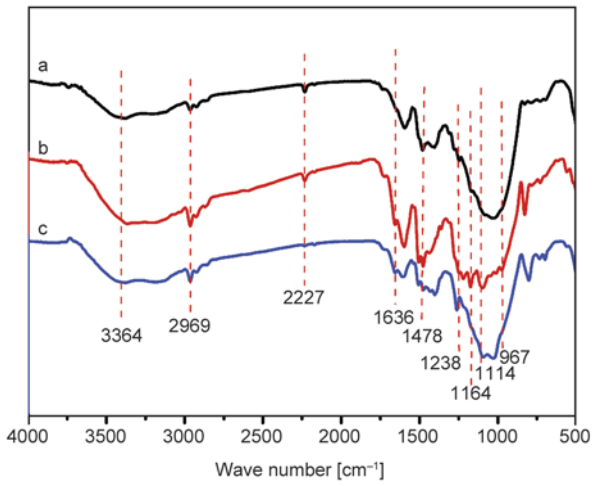

Figure 9. FTIR spectra of BA-ph/BPA system with various content of BPA heat treated at 160°C: (a) BA-ph/BPA21, (b) BA-ph/BPA22 and (c) BA-ph/BPA23

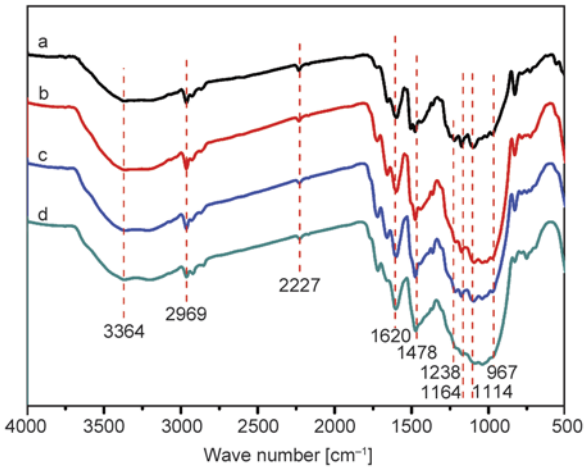

Figure 10. FTIR spectra of BA-ph/BPA22 system heat treated at various temperatures: (a) 160°C, (b) 200°C, (c) 240°C and (d) 280°C

of C=N and C–N=, respectively [28, 29]. Additionally, the aforementioned characteristics and the low intensity absorption band at 2227 cm^{-1} corresponding to nitrile groups, indicated the high polymerization degree of nitrile groups at 160°C. Moreover, the absorption intensity of nitrile groups decreased with increasing the content of BPA, suggesting the obvious catalysis. The wide and intensive absorption band at around 3364 cm^{-1} corresponding to the association state of hydroxyl were observed in all of the samples, reported previously [15, 16]. The absorption peak at 2969 cm-1 was assigned to the stretching vibration of $–CH_3$ and no obvious changes were observed.

Figure 10 showed the FTIR spectra of BA-ph/BPA22 polymers obtained after being heated at 160, 200,

240 and 280°C, respectively. It was obvious that the characteristic absorption bands at 2227 cm^{-1} of the BA-ph/BPA22 polymers were evidently weakened, and the characteristic absorption band at 1620 and 1238 cm^{-1} increased with increasing the treated temperature. The intensive absorption band at 3364 cm^{-1} indicated the existence of association hydroxyl in BA-ph/BPA systems. With increasing the treatment temperature, it was obvious that the absorption intensity decreased slightly, suggesting that elevated temperature damaged the association hydrogen bond.

3.4. Mechanical properties of BA-ph/BPA/GF composite laminates

In the previous parts, copolymerizing behaviors and processability of BA-ph/BPA blends were investigated. These investigations can provide us with effective molding procedures to prepare GF-based BA-ph/BPA composite laminates. The mechanical properties of resulting BA-ph/BPA/GF composite laminates with various BPA contents were shown in Figures 11 and 12, in which properties of BA-ph/GF were also presented. Overall, for individual BA-ph/BPA/GF composite laminate, the flexural properties were dramatically increased with the treated temperature increase and then decreased slightly. The flexural strength and flexural modulus of BA-ph/GF composite laminate were increased with increasing the temperature and up to 542 MPa and 25.8 GPa at the completed polymerization temperature of 280°C, respectively. BA-ph/BPA/GF21 composite laminate treated at 160°C exhibited high flexural strength of 632 MPa and high flexural modulus of 23.6 GPa. Raising treatment temperatures, flexural strength of BA-ph/BPA/GF21 composite laminate increased to 786, 711 and 639 MPa at 200, 240 and 280°C, respectively. Analogously, the flexural strength of BA-ph/BPA/GF22 and BA-ph/BPA/GF23 composite laminate increased to 737 and 753 MPa at 200°C and decreased to 665 and 408 MPa at 280°C, respectively. The significant increase of flexural strength was attributed to the introducing of BPA which accelerated the polymerization of BA-ph resulting in an improved cross-linking degree. In addition, the association hydroxyl in the polymers proved by FTIR may be conducive to the improved flexural strength. However, the slight decrease of strength may be resulting from the volatilization of surplus BPA and the damage of

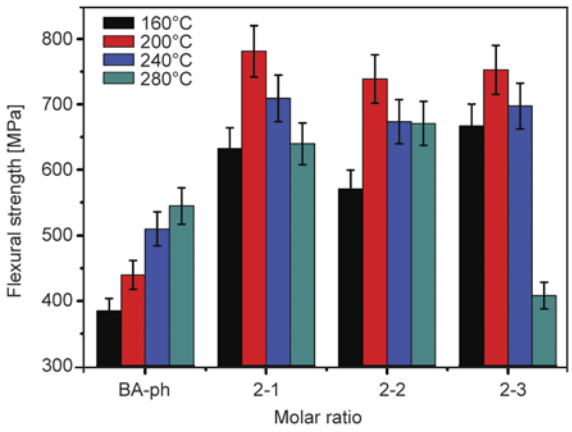

Figure 11. Flexural strength of BA-ph/BPA/GF system with various content of BPA

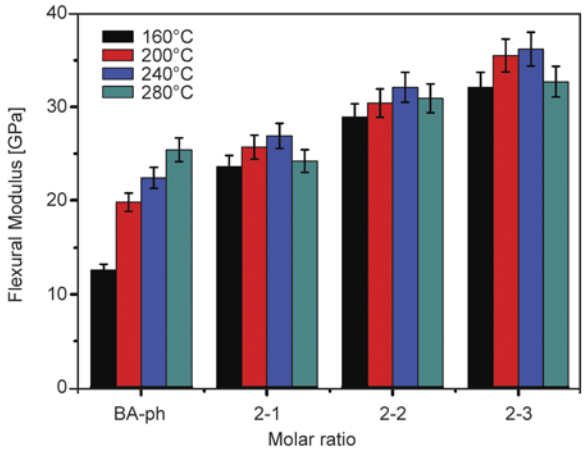

Figure 12. Flexural modulus of BA-ph/BPA/GF system with various content of BPA

hydrogen bond at elevated temperature, which was verified by the steep decline of the flexural strength for BA-ph/BPA/GF23 composite laminate. Additionally, the flexural modulus also showed regular increase or decrease with increasing or decreasing the BPA. In comparison with those of composite laminates reported previously, BA-ph/BPA/GF composite laminates which just underwent the heat treatment at 160°C for 4 h exhibited excellent mechanical properties. For thermosetting resin, long time curing and elevated temperature treatment were necessary. In the previous work, BA-ph/GF systems were treated for 11 h and the temperature was up to 280°C [15, 16]. Phthalocyanine/GF systems were generally treated at 320°C for 2 or 4 h to obtain the laminates with good properties. For other thermosetting resins, such as epoxy resins, though did not require the treatment of high temperature and long time, the properties of EP/GF composite laminates were usually barely satisfactory. Yang *et al*. [30] have prepared EP/GF composite laminates with three kinds

of GFs: plain weave fabric GF and biaxial or uniaxial stitched plain weave fabrics GF; and the corresponding flexural strengths of resulted EP/GF composite laminates were 370, 233 and 326 MPa with fiber volume of 56, 56 and 57%, respectively. Mouritz *et al*. [31] also reported that EP/GF composite laminates exhibited a relatively low mechanical performance with the flexural strength of 212MPa and flexural modulus of 12.9 GPa, with the fiber volume of 34%.

Generally, mechanical properties of polymer/GF composite laminates depended on the properties of each primary component, the nature of the interface, and the locus of filler-matrix interaction between the matrix resins and GFs [32]. In our BA-ph/BPA/GF systems, the good mechanical properties could be attributed to multiple factors. These mechanical properties are, on the one hand, attributed to primary component of GF and matrices themselves, while BA-ph was also traded for their good mechanical performances. On the other hand, the existence of association hydrogen bond which resulted from the polymerization of BA-ph/BPA blends was also a key factor. Furthermore, the polymerization of the matrices was significantly catalyzed by BPA, thus, the mechanical properties can be attributed to the highly crosslinked matrices. The exothermic enthalpy of the composites with various BPA and treated at various temperatures were summarized in Table 2. Results indicated that the conversion of oxazine rings and nitrile groups increased with increasing BPA or temperature, confirming the high crosslinking degree and the improved mechanical properties.

3.5. Thermal stabilities of the BA-ph/BPA/GF composite laminates

The thermal decomposition of the BA-ph/BPA/GF composite laminates was also examined by TGA (Figure 13 and 14) and the main results were summarized in Table 3 and 4, in which the initial degradation temperature (T_i), the temperatures at weight loss of 5% ($T_{5\%}$) and 10% ($T_{10\%}$) were displayed. Overall, thermal stabilities of BA-ph/BPA/GF composites in N_2 increased with raising the treatment temperature, attributed to the thermally induced polymerization and improved cross-linking density. Additionally, the catalysis of BPA was conducive to the further polymerization of BA-ph. Due to the volatilization of BPA at elevated temperature, the

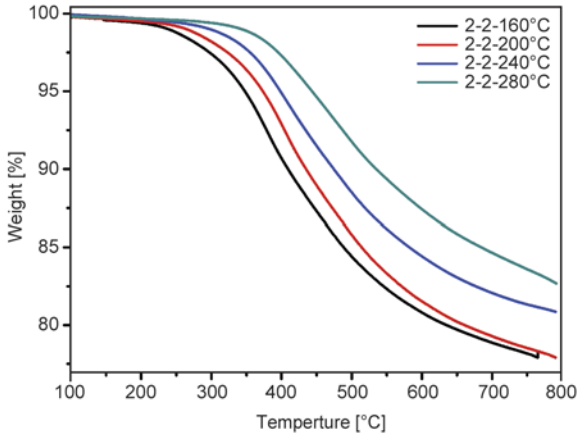

Figure 13. TGA curves of BA-ph/BPA22 system heat treated at various temperatures in nitrogen

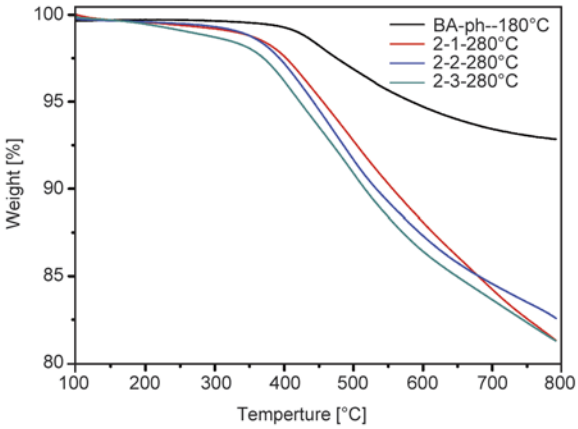

Figure 14. TGA curves of BA-ph/BPA system with various content of BPA heat treated at 280°C

Table 2. Exothermic enthalpy of various BA-ph/BPA composites heated treated at various temperatures

	160°C	200°C	240°C	280°C
BA-ph-BPA21	25.8	10.7	8.2	7.2
BA-ph-BPA22	19.3	8.1	6.2	5.9
BA-ph-BPA23	16.5	6.9	4.0	3.2

Table 3. Thermal stabilities of BA-ph/BPA/GF22 laminates heated at various temperatures

Samples	T_i	$T_{5\%}$	$T_{10\%}$
160°C	300.6	365.2	444.2
200°C	321.4	372.8	435.2
240°C	339.7	397.2	474.2
280°C	364.9	445.5	537.7

Table 4. Thermal stabilities of BA-ph/BPA/GF systems with various content of BPA heated at 280°C

Samples	T_i	$T_{5\%}$	$T_{10\%}$
BA-ph	456.0	589.0	–
BA-ph-BPA21	365.8	452.6	553.2
BA-ph-BPA22	364.9	445.5	537.7
BA-ph-BPA23	352.5	422.8	516.7

further improvement of thermal stabilities was restricted by the content of BPA. Nevertheless, all BA-ph/BPA/GF composites could stand high $T_{10\%}$ up to 510°C in N_2. Compared with other state-of-the-art thermosetting composite laminates, the BA-ph/BPA/GF composite laminates exhibited excellent thermal stabilities. The phthalonitrile-based composites or laminates [26, 27], by comparison, showed as high T_i and $T_{5\%}$ as BA-ph/BPA/GF systems. However, these composites have to be cured at elevated temperatures (over 350°C) for a very long time (24 h or even more), which would be hard in the practical processing. The thermosetting polyimide-based composite laminates, on the other hand, were durable for a long time at 343°C, but these laminates showed relatively low mechanical properties (flexural strength: 345 MPa; flexural modulus: 20.7G Pa) compared with BA-ph/BPA/GF systems (flexural strength: 781 MPa; flexural modulus: 23 GPa). The other laminates did not maintain the same degree of thermal stability [34] as BA-ph/BPA/GF systems. Meanwhile, the high-temperature machining increased the difficulty of processing and limited their potential applications.

3.6. Dynamic thermomechanical analysis of the BA-ph/BPA/GF composite laminates

In the previous parts, mechanical properties and thermal stabilities of BA-ph/BPA/GF laminates were investigated. Results indicated that the laminates shown outstanding mechanical properties treated at 200°C, suggesting the considerably high cross-linking. Dynamic mechanical studies were conducted to evaluate the changes in the sample modulus as a function of temperature and determinate the T_g of the polymers after being treated at 200°C. From these studies, storage modulus and tan delta plots generated on BA-ph/BPA/GF polymers versus temperature were presented in Figure 15 and 16, respectively, and the results of T_g were exhibited in Table 5. In Figure 15, the modulus for BA-ph/BPA/GF22 changed from 32 500 to 5000 MPa when heated from 50 to 400°C. The initial modulus of BA-ph/BPA/GF22 and BA-ph/BPA/GF23 were approximate (32 280 MPa and 30 570 MPa) and higher than that of BA-ph/BPA/GF21 (26 580 MPa), indicating the high cross-linking density of the laminates. For all of the samples, the decline of modulus was segmented, the first large modulus changes were observed at about 180~250°C and the second were

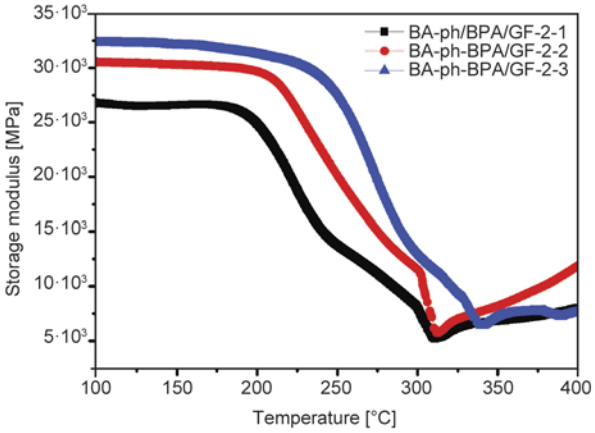

Figure 15. Storage modulus (G') of BA-ph/BPA/GF system with various content of BPA

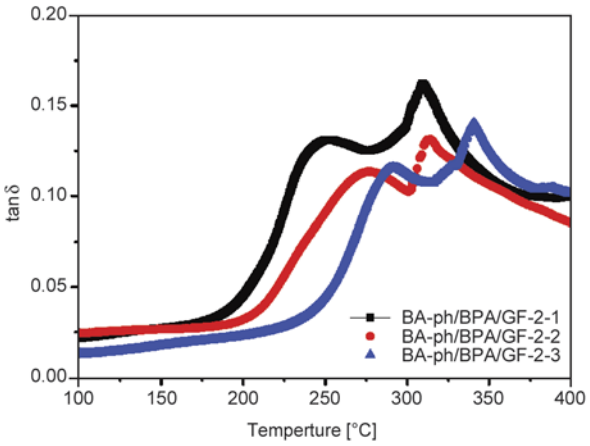

Figure 16. Damping factor (tan δ) of BA-ph/BPA/GF system with various content of BPA

Table 5. Glass transition temperature of BA-ph/BPA/GF laminates heated 200°C

Samples	T_{g_1} [°C]	T_{g_2} [°C]
BA-ph/GF	–	287
BA-ph/BPA/GF21	248	311
BA-ph/BPA/GF22	277	314
BA-ph/BPA/GF23	293	342

about 250~350°C. The data showed that the transformation temperature range increased with the increasing of BPA, attributed to the increased cross-linking density. The sectionalized decline of modulus suggested the microphase separation which resulted from the out-of-step polymerization of oxazine rings and nitrile groups at the presence of BPA.

The T_g was obtained from the maximum of tan δ in a plot of tan δ versus temperature. As noted in Figure 16, two obvious relaxation peaks were observed in each plot. The tan delta peaks (200~300°C) of all BA-ph/BPA/GF were attributed to the Mannich

bridge structures generated by ring-opening of oxazine rings catalyzed by BPA. On heating to 400°C, the tan delta peaks occurred at the range of 300~370°C, which was ascribed to the relaxation of aromatic heterocycte produced by the ring-forming polymerization of nitrile groups. Obviously, both the relaxation peaks shifted to higher temperature with increasing the content of BPA. Meanwhile, the space of the double peaks decreased with the content of BPA increasing. One possible explanation of these results was that the cross-linking degree of both oxazine rings and nitrile groups had been improved by the assistance of BPA, affording a reaction-induced microphase separation. As was well known, the T_g of polymers depends on the rigidity of the molecular chains and the cross-linking degree [35–40]. It can be seen in Table 5 that the T_{g1} of the samples were up to 240°C, which were superior to the traditional epoxy, phenolics and polybenzoxazines resin [36–40]. The T_{g2} of the samples were up to 340°C, which were comparable to that of phthalonitrile-based polymers cured at elevated temperature with longer time [2, 7, 8]. Also, a semi empirical equation has been used for calculating cross-link density of highly cross-linked systems [41, 42] shown in Equation (1):

$$\log_{10}G' = 7 + X_{density} \quad (1)$$

where G' is the storage modulus of the cured blends in the rubbery plateau region in dynes/cm^2 above T_g (i.e. T_g + 40°C), $X_{density}$ is the cross-link density of the polymers. According to the equation, the crosslinking density of various BA-ph/BPA polymers was presented in Table 6. It can be seen that all of the polymers exhibited high crosslinking degree (12 000~13 000 mol/m^3) which may confirm the good mechanical properties and glass transition temperatures. Besides, the increase of mechanical properties and glass transition temperatures can also be attributed to the high crosslinking degree. The outstanding T_g was mainly attributed to the high crosslinking degree of ring-opening polymerization of benzoxazine and heterocyclization of nitrile groups, which greatly limited the motion of the molecular chains.

3.7. Phase morphology of the BA-ph/BPA composite

SEM images of BA-ph/BPA22 polymers heat treated at various temperatures were presented in Figure 17. The images showed the evolution of the phase morphology as the cure advanced for BA-ph/BPA22 composites. After being treated at 160°C, the reaction (ring-opening polymerization and formation of interlinked network) leads to a homogeneous phase (Figure 17a). As the temperature was raised, formation of homopolymer of phthalocyanine occurs parallel to linked network formation of polybenzoxaine. Minor tendency for phase separation is observed at this stage (Figure 17b and 17c). Spherical nodules are visible, which can be ascribed to the phthalocyanine rings dispersed in polybenzoxazine linked network. With increasing the temperature, the severity of phase separation is diminished because of the formation of inter linked network as the major phase (Figure 17d).

4. Conclusions

Copolymerization behaviors and processability of BA-ph/BPA systems were investigated. The structures of the polymers were confirmed and the possible curing reactions were discussed. Results demonstrated that the polymerization of the BA-ph/BPA blends were representative double-stage curing model. The components of the polymers depended on the relative content of BA-ph and BPA. The results of processability indicated polymerization of BA-ph/BPA blends was progressing in the ranges from 160 to 200°C and the polymerization of nitrile groups can be reduced to 160°C. The GF-filled BA-ph/BPA composite laminates were prepared and their mechanical and thermal properties were investigated. The flexural strength of BA-ph/BPA/GF composites was 789 MPa, which was superior to that of BA-ph/GF composites (542 MPa), although the modulus (23.6 GPa) decreased in compared with that of BA-ph/GF composites (25.8 GPa). Such mechani-

Table 6. Crosslinking density of BA-Ph/BPA polymers with various content of BPA

Samples	T_g [°C]	Glass modulus at ambient temperature [GPa]	Crosslink density [mol/m^3]
BA-ph/BPA/GF-21	311	26.5	12700
BA-ph/BPA/GF-22	314	30.6	13380
BA-ph/BPA/GF-23	342	32.3	13300

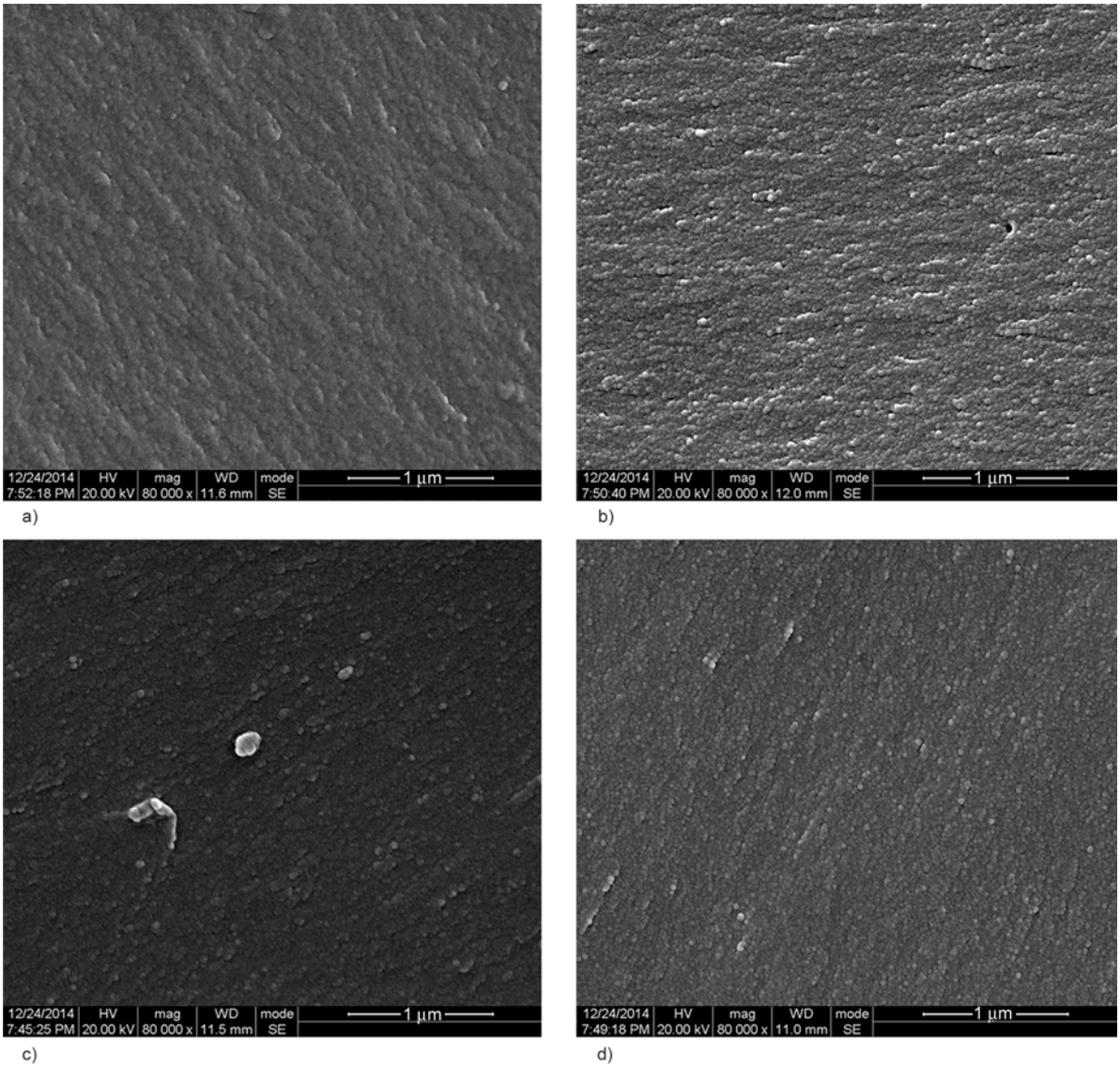

Figure 17. SEM images of BA-ph/BPA22 composites heat treated at various temperatures: (a) 160°C, (b) 200°C, (c) 240°C and (d) 280°C

cal enhancements can be attributed to the catalysis of BPA on the matrices and the abundant hydrogen bond. Additionally, for BA-ph/BPA/GF laminates, two T_g's were observed, suggesting the microphase separation of BA-ph/BPA polymers because of the out-of-step polymerization of oxazine rings and nitrile groups, which was also confirmed by the SEM images. Thermal stabilities revealed that all of the BA-ph/BPA/GF composites could stand high $T_{10\%}$ up to 510°C in N_2. These characteristics could enable the BA-ph/BPA/GF composites to find uses under some critical circumstances with requirements of excellent mechanical properties and high temperature resistance. Moreover, an idea has been suggested in this work to prepare a semi-IPN type polymer.

Acknowledgements

The authors wish to thank for financial support of this work from the National Natural Science Foundation of China (No. 51173021, 51373028) and '863' National Major Program of High Technology (2012AA03A212).

References

[1] Nagai A., Eguchi S., Ishii T., Ogata M., Nishi K.: Encapsulating material design of epoxy molding compounds for high reliability semiconductor packaging. Polymer News, **21**, 44–52 (1996).

[2] Guo H., Lei Y., Zhao X., Yang X., Zhao R., Liu X.: Curing behaviors and properties of novolac/bisphthalonitrile blends. Journal of Applied Polymer Science, **125**, 649–656 (2012).
DOI: 10.1002/app.36335

[3] Jin L., Agag T., Ishida H.: Bis(benzoxazine-maleimide)s as a novel class of high performance resin: Synthesis and properties. European Polymer Journal, **46**, 354–363 (2010).
DOI: 10.1016/j.eurpolymj.2009.09.013

[4] Takeichi T., Kawauchi T., Agag T.: High performance polybenzoxazines as a novel type of phenolic resin. Polymer Journal, **40**, 1121–1131 (2008).
DOI: 10.1295/polymj.PJ2008072

[5] Laskoski M., Dominguez D. D., Keller T. M.: Synthesis and properties of a bisphenol A based phthalonitrile resin. Journal of Polymer Science Part A: Polymer Chemistry, **43**, 4136–4143 (2005).
DOI: 10.1002/pola.20901

[6] Dominguez D. D., Keller T. M.: Low-melting phthalonitrile oligomers: Preparation, polymerization and polymer properties. High Performance Polymer, **18**, 283–304 (2006).
DOI: 10.1177/0954008306060143

[7] Keller T. M., Dominguez D. D.: High temperature resorcinol-based phthalonitrile polymer. Polymer, **46**, 4614–4618 (2005).
DOI: 10.1016/j.polymer.2005.03.068

[8] Dominguez D. D., Keller T. M.: Properties of phthalonitrile monomer blends and thermosetting phthalonitrile copolymers. Polymer, **48**, 91–97 (2007).
DOI: 10.1016/j.polymer.2006.11.003

[9] Laskoski M., Keller T. M., Qadri S. B.: Direct conversion of highly aromatic phthalonitrile thermosetting resins into carbon nanotube containing solids. Polymer, **48**, 7484–7489 (2007).
DOI: 10.1016/j.polymer.2007.11.003

[10] Laskoski M., Dominguez D. D., Keller T. M.: Synthesis and properties of aromatic ether phosphine oxide containing oligomeric phthalonitrile resins with improved oxidative stability. Polymer, **48**, 6234–6240 (2007)
DOI: 10.1016/j.polymer.2007.08.028

[11] Cao G. P., Chen W. J., Wei J. J., Li W. T., Liu X. B.: Synthesis and characterization of a novel bisphthalonitrile containing benzoxazine. Express Polymer Letters, **1**, 512–518 (2007).
DOI: 10.3144/expresspolymlett.2007.73

[12] Sumner M. J., Sankarapandian M., McGrath J. E., Riffle J. S., Sorathia U.: Flame retardant novolac–bisphthalonitrile structural thermosets. Polymer, **43**, 5069–5076 (2002)
DOI: 10.1016/S0032-3861(02)00354-3

[13] Zeng K., Hong H., Zhou S. H., Wu D. M., Miao P., Huang Z., Yang G.: A new soluble aramide with pendant phthalonitrile units and polymer property enhancement by nitrile cure reactions. Polymer, **50**, 5002–5006 (2009).
DOI: 10.1016/j.polymer.2009.08.033

[14] Xu M., Yang X., Zhao R., Liu X.: Copolymerizing behavior and processability of benzoxazine/epoxy systems and their applications for glass fiber composite laminates. Journal of Applied Polymer Science, **128**, 1176–1184 (2013).
DOI: 10.1002/app.38422

[15] Xu M., Hu J., Zou X., Liu M., Dong S., Zou Y., Liu X.: Mechanical and thermal enhancements of benzoxazine-based GF composite laminated by *in situ* reaction with carboxyl functionalized CNTs. Journal of Applied Polymer Science, **129**, 2629–2637 (2013).
DOI: 10.1002/app.38988

[16] Xu M. Z., Liu M. D., Dong S. H., Qiu G. Y., Liu X. B.: Active diluents effects of 4-nonylphenoxy-1, 2-dinitrilbenzene on phthalonitrile containing benzoxazine and their copolymerization behaviors. Express Polymer Letters, **7**, 984–995 (2013).
DOI: 10.3144/expresspolymlett.2013.97

[17] McDonagh A. F., Smith H. E.: Ring-chain tautomerism of derivatives of o-hydroxybenzylamine with aldehydes and ketones. The nuclear magnetic resonance spectra of immonium ions. Journal of Organic Chemistry, **33**, 8–12 (1968).
DOI: 10.1021/jo01265a002

[18] Ishida H., Ohba S.: Synthesis and characterization of maleimide and norbornene functionalized benzoxazines. Polymer, **46**, 5588–5595 (2005).
DOI: 10.1016/j.polymer.2005.04.080

[19] Keller T. M., Griffith J. R.: Polyphthalocyanine resins. U.S. Patent 4234712 A, USA (1980).

[20] Keller T. M.: Phenolic-cured phthalonitrile resins. U.S. Patent 4410676 A, USA (1983).

[21] Burke W. J., Mortenson Glennie E. L., Weatherbee C.: Condensation of halophenols with formaldehyde and primary amines. Journal of Organic Chemistry, **29**, 909–912 (1964).
DOI: 10.1021/jo01027a038

[22] Burke W. J., Bishop J. L., Mortensen Glennie E. L., Bauer W. N.: A new aminoalkylation reaction. condensation of phenols with dihydro-1,3-aroxazines. Journal of Organic Chemistry, **30**, 3423–3427 (1965).
DOI: 10.1021/jo01021a037

[23] Riess G., Schwob J. M., Guth G., Roche M., Laude B.: Ring opening polymerization of benzoxazines – A new route to phenolic resins. Advances in Polymer Synthesis, Polymer Science and Technology, **31**, 27–39 (1985).
DOI: 10.1007/978-1-4613-2121-7_2

[24] Dominguez D. D., Keller T. M.: Phthalonitrile-epoxy blends: Cure behavior and copolymer properties. Journal of Applied Polymer Science, **110**, 2504–2515 (2008).
DOI: 10.1002/app.28817

[25] Laza J. M., Vilas J. L., Mijangos F., Rodríguez M., León L. M.: Analysis of the crosslinking process of epoxy–phenolic mixtures by thermal scanning rheometry. Journal of Applied Polymer Science, **98**, 818–824 (2005).
DOI: 10.1002/app.22106

[26] Ning X., Ishida H.: Phenolic materials via ring-opening polymerization: Synthesis and characterization of bisphenol-A based benzoxazines and their polymers. Journal of Polymer Science Part A: Polymer Chemistry, **32**, 1121–1129 (1994).
DOI: 10.1002/pola.1994.080320614

[27] Agag T., Takeichi T.: Novel benzoxazine monomers containing *p*-phenyl propargyl ether: Polymerization of monomers and properties of polybenzoxazines. Macromolecules, **34**, 7257–7262 (2001)
DOI: 10.1021/ma0107915

[28] Young J-N., Chang T-C., Tsai S-C., Yang L., Yu S. J.: Preparation of a nonleaching, recoverable and recyclable palladium-complex catalyst for Heck coupling reactions by immobilization on Au nanoparticles. Journal of Catalysis, **272**, 253–261 (2010)
DOI: 10.1016/j.jcat.2010.04.005

[29] Ogino C., Kanehira K., Sasai R., Sonezakai S., Shimizu N.: Recognition and effective degradation of 17β-estradiol by anti-estradiol-antibody-immobilized TiO_2 nanoparticles. Journal of Bioscience and Bioengineering, **104**, 339–342 (2007)
DOI: 10.1263/jbb.104.339

[30] Yang B., Kozey V., Adanur S., Kumar S.: Bending, compression, and shear behavior of woven glass fiber–epoxy composites. Composites Part B: Engineering, **31**, 715–724 (2000).
DOI: 10.1016/S1359-8368(99)00052-9

[31] Mouritz A. P., Mathys Z., Gardiner C. P.: Thermomechanical modelling the fire properties of fibre–polymer composites. Composites Part B: Engineering, **35**, 467–474 (2004).
DOI: 10.1016/j.compositesb.2003.09.005

[32] Prashantha K., Soulestin J., Lacrampe M. F., Claes M., Dupin G., Krawczak P.: Multi-walled carbon nanotube filled polypropylene nanocomposites based on masterbatch route: Improvement of dispersion and mechanical properties through PP-g-MA addition. Express Polymer Letters, **2**, 735–745 (2008).
DOI: 10.3144/expresspolymlett.2008.87

[33] Keller T. M.: Phthalonitrile-based high temperature resin. Journal of Polymer Science Part A: Polymer Chemistry, **26**, 3199–3212 (1988).
DOI: 10.1002/pola.1988.080261207

[34] Kuznetsov A. A., Semenova G. K.: Perspective thermally stable thermoset binders for polymer composite materials. Russian Journal of General Chemistry, **80**, 2170–2180 (2010).
DOI: 10.1134/S1070363210100464

[35] Chow T. S.: Molecular interpretation of the glass transition temperature of polymer-diluent systems. Macromolecules, **13**, 362–364 (1980)
DOI: 10.1021/ma60074a029

[36] Hancock B. C., Zografi G.: The relationship between the glass transition temperature and the water content of amorphous pharmaceutical solids. Pharmaceutical Research, **11**, 471–477 (1994).
DOI: 10.1023/A:1018941810744

[37] Forrest J. A., Dalnoki-Veress K., Stevens J. R., Dutcher J. R.: Effect of free surfaces on the glass transition temperature of thin polymer films. Physical Review Letters, **7**, 2002–2005 (1996).
DOI: 10.1103/PhysRevLett.77.2002

[38] Forrest J. A., Dalnoki-Veress K., Dutcher J. R.: Interface and chain confinement effects on the glass transition temperature of thin polymer films. Physical Review E, **56**, 5705–5716 (1997).
DOI: 10.1103/PhysRevE.56.5705

[39] Allaoui A., El Bounia N.: How carbon nanotubes affect the cure kinetics and glass transition temperature of their epoxy composites? – A review. Express Polymer Letters, **3**, 588–594 (2009).
DOI: 10.3144/expresspolymlett.2009.73

[40] Kimura H., Ohtsuka K., Matsumoto A.: Curing reaction of bisphenol-A based benzoxazine with cyanate ester resin and the properties of the cured thermosetting resin. Express Polymer Letters, **5**, 1113–1122 (2011).
DOI: 10.3144/expresspolymlett.2011.108

[41] Ward I. M., Hadley D. W.: An introduction to the mechanical properties of solid polymers. Wiley, New York (1993).

[42] Santhosh Kumar K. S., Reghunadhan Nair C. P., Ninan K. N.: Investigations on the cure chemistry and polymer properties of benzoxazine–cyanate ester blends. European Polymer Journal, **45**, 494–502 (2009)
DOI: 10.1016/j.eurpolymj.2008.11.001